Cranfield University

Salah I. AlSwailem

Application of Robust Control in Unmanned Vehicle Flight Control System Design

College of Aeronautics

PhD Thesis

PhD Thesis

Academic Year 2003-2004

Salah I. AlSwailem*

Application of Robust Control in Unmanned Vehicle Flight Control System Design

Supervisor:

Mike V. Cook

March 2004

Submitted for the Degree of
Doctor in Philosophy

Abstract

The robust loop-shaping control methodology is applied in the flight control system design of the Cranfield A3 Observer unmanned, unstable, catapult launched air vehicle. Detailed linear models for the full operational flight envelope of the air vehicle are developed. The nominal and worst-case models are determined using the ν-gap metric. The effect of neglecting subsystems such as actuators and/or computation delays on modelling uncertainty is determined using the ν-gap metric and shown to be significant.

Detailed designs for the longitudinal, lateral, and the combined full dynamics TDF controllers were carried out. The Hanus command signal conditioning technique is also implemented to overcome actuator saturation and windup. The robust control system is then successfully evaluated in the high fidelity 6DOF non-linear simulation to assess its capability of launch stabilization in extreme cross-wind conditions, control effectiveness in climb, and navigation precision through the prescribed 3D flight path in level cruise. Robust performance and stability of the single-point non-scheduled control law is also demonstrated throughout the full operational flight envelope the air vehicle is capable of and for all flight phases and beyond, to severe launch conditions, such as 33knots crosswind and exaggerated CG shifts.

The robust TDF control law is finally compared with the classical PMC law where the actual number of variables to be manipulated manually in the design process are shown to be much less, due to the scheduling process elimination, although the size of the final controller was much higher. The robust control law performance superiority is demonstrated in the non-linear simulation for the full flight envelope and in extreme flight conditions.

*s_alswailem@yahoo.co.uk

All gratefulness and praises be to Allah, God of Adam, Abraham, Moses, Jesus, and Mohammad. Peace be upon them all.

Acknowledgements

Throughout the years of this research, I was fortunate to get the help and support of many people in the UK, to some of whom I would like to express my appreciation here. First, my thanks to my current supervisor, Mike Cook, for his advice, support, and appreciated effort of proof-reading this thesis. My thanks also go to my former supervisor, Peter Thomasson, for his advice and valuable assistance in understanding the flight dynamics and control of Cranfield XRAE-1 and A3 Observer UAVs and their detailed non-linear simulation. Equally, my thanks go to *Cranfield Aerospace*, namely to Andy Walster in the Control Systems Group, for the thorough introduction to the operational aspects of the A3 Observer UAV, and for taking some of his precious time to implement and evaluate the robust controller in the real-time GCS and proof-reading this thesis. My thanks also go to Tony Steer for reviewing the last two chapters of the thesis.

Also, I would like to express my appreciation to Prof. Keith Glover of Cambridge University, the UK pioneer of robust control and LSDP applied in this thesis, for his advice, materials, and my welcome to attend his robust control graduate course.

My thanks also go to *Bonus Aviation*, namely to my flying instructors: David Topp and Kevin Harris, with whom I obtained my Private Pilot License and enriched my knowledge with real experience and practice in many disciplines in the aeronautical arena including flight dynamics, control, navigation, instrumentation, communication, meteorology, and flight management.

Last but not least, I would like to express my gratitude to Cranfield Islamic Society that made living in Cranfield a pleasant experience.

Table of Contents

Symbols

$\mathcal{H}_\infty$: The symbol $\mathcal{H}$ comes from the "Hardy space"; $\mathcal{H}_\infty$ is the set of transfer functions G, with $\|G\|_\infty < \infty$. Or simply, the set of *stable* and *proper* transfer functions.

$\mathcal{RL}_\infty$: The space for all real-rational transfer function matrices which have no poles on the imaginary axis.

$\mathcal{RH}_\infty$: All transfer function matrices in $\mathcal{RL}_\infty$ which have no poles in $Re(s) > 0$.

$\in$: Is an element of

:= : Is defined to be

A^T : Transpose of matrix A

A^* : Complex conjugate (Hermitian) transpose of matrix A

$\|G\|_H$: Hankel norm of G

$\|G\|_\infty : \sup_\omega \bar{\sigma}(G(j\omega))$

$\sup_\omega(G(\omega))$: supremum (lowest upper bound) of G over ω

Δ: Uncertainty for MIMO system model

$A^\#$: Pseudoinverse of A

σ(s): Principal gain (singular value)

$\bar{\sigma}(s), \underline{\sigma}(s)$: Largest and smallest singular values

Definitions

Controllable system: *iff* every mode is controllable.

Detectable system: *iff* every *unstable* mode is observable.

Internally stable closed-loop system: *Iff* the transfer function is asymptotically stable.

Nominal Performance (NP): System satisfy the performance specifications with no model uncertainty.

Nominal Stability (NS): System is stable with no model uncertainty.

Observable system: *iff* every mode is observable.

Proper transfer function $G(s)$:

- *strictly proper*: If $G(s) \to D = 0$ as $s \to \infty$
- *semi-proper* or *bi-proper*: If $G(s) \to D \neq 0$ as $s \to \infty$
- *proper*: If *strictly* or *semi-proper*
- *improper*: If $G(s) \to \infty$ as $s \to \infty$

Robust Performance (RP): System satisfy the performance specifications for nominal and all perturbed models up to the worst-case model uncertainty.

Robust Stability (RS): System is stable for nominal and all perturbed models up to the worst-case model uncertainty.

Stabilizable system: *iff* every *unstable* mode is controllable.

Unitary: A square matrix with orthogonal columns in $\mathcal{R}$ and satisfies: $U^*U = I = UU^*$.

Well-posed closed-loop system: If the transfer function matrix exist and is *proper*.

Acronyms

2DOF: Two Degrees-of-Freedom dynamics. See also **TDF**

3D: Three dimensions: x,y, and z.

6DOF: Six Degrees-of-Freedom dynamics

ACSL: Advanced Continuous Simulation Language

DERA: MoD Defence Evaluation and Research Agency. Now QinetiQ

FCS : Flight Control System

FCSD : Flight Control System Design

GARTEUR: Group for Aeronautical Research and Technology in Europe

GCARE, GFARE: Generalized Control/Filter Algebraic Equation

ISTAR: Intelligence, Surveillance, and Tactical Reconnaissance

LQG : Linear Quadratic Gaussian

LSDP : Robust Control Loop-Shaping Design Procedure

LTR : Loop Transfer Recovery

MBPC: Model-Based Predictive Control

MIMO: Multi-Input Multi-Output

MOPS: Multi-objective parameter synthesis

PMC: Precision Manoeuvre Control

QFT: Quantitative Feedback Theory

RIDE: Robust Inverse Dynamics Estimation control technique

S/H: Sample and hold

SISO: Single-Input Single-Output

TDF: Two Degrees-of-Freedom controller design. See also **2DOF**

UAV : Unmanned Air Vehicle

Chapter 1

Introduction

1.1 Introduction

The development of high performance unmanned aerospace vehicles will see an increasing need to perform offensive flight missions where the dynamics of the vehicle are not well known. This, coupled with the requirement for performance close to stability limits, gives the concept of *model uncertainty* an important role in the development of flight control systems for such vehicles.

Essentially, an aircraft mathematical model is an approximation of the real vehicle dynamics which is generally accepted and worked around in the development of a flight control system. However, in the situations mentioned above, *model uncertainty* may have profound effects on the aircraft performance and stability. This is particularly true when the aircraft is intentionally designed to be open loop unstable or to have a very low stability margin as in the case of the Cranfield A3 Observer UAV.

A major problem facing Flight Control System(FCS) designers is uncertainty in

modelling not only the vehicle itself, but also the environment in which it must operate. Gain scheduling is often necessary because of the variation of the characteristics for which the control laws must guarantee stability and performance. Such a technique is costly for two reasons: the control law must be designed at each design point, and a great deal of assessment is required to insure adequate stability and performance at off-design points.[1]

Recent advances in control theory research have given rise to a number of novel robust control techniques specifically developed for dealing with model uncertainties and parameter variations[2-4]. These new techniques offer potential benefits to a control law designer for modern aircraft in the following ways:

- Multivariable systems can be handled in a concise methodical framework, thus removing the need for the sequential loop closure approach, and reducing the design effort required. Hence it can handle stability augmentation and flight-path guidance and navigation at a single level.

- Robust control laws which cover larger regions of the flight envelope around a design point can be derived more efficiently. This offers the potential for reducing the number of design points required, simplifying if not eliminating the gain schedule, and reducing the amount of assessment required at off-design points.

- Robust control theory can utilise available information about model uncertainty and performance and stability requirements. Moreover, some robust control methods can even make use of much classical control design knowledge and many classical techniques and rules in the absence of mathematical definitions of model uncertainty and/or disturbance. This is especially true for the design method used in this thesis as will be shown through-out.

The main consequence of these benefits is that a FCSD based on robust control techniques may yield a reduction in the design effort required, time-to-market and design costs.[1]

Robust control theory has evolved with powerful techniques to optimise performance, without sacrificing stability, in the presence of uncertainty.

1.2 A3 Observer Concept UAV

The Cranfield A3 Observer is an unmanned air vehicle designed as part of the Observer Intelligence, Surveillance, and Tactical Reconnaissance (ISTAR) UAV demonstrator system that resulted from DERA (now QinetiQ) research aimed at UK MoD requirements for small, automated, brigade-level system capable of operation by a single unskilled operator[5]. Figure 1.1 shows an early version of the air vehicle in a launch position on the catapult at one of MoD's firing ranges.

Figure 1.1: A3 Observer UAV

The airframe consists of a bullet-shaped fuselage with pusher engine; mid-mounted, anhedral delta wing with sweptback winglets at tips; inset rudder in central fin; one pair

of elevators at inboard wing trailing edge; another pair of ailerons at the outboard wing trailing edge; with all composite structure.

The aircraft exploits the *gust insensitive* configuration developed from earlier work[6]. As a result it is dynamically unstable about all axes but is required to fly precision manoeuvres in 3D space. It is under full authority autonomous control from catapult launch to parachute touch down, with no human involvement in the control loop. Stabilization, navigation, and control are done via onboard sensors involving attitude and rate gyros, air data, and GPS. The air-borne full authority multi-microprocessor controller executes the control and navigation algorithms autonomously based on onboard pre-programmed, and/or ground-station real-time, flight-plans and commands[7, 8].

1.3 Research objectives

The objectives of this work are to apply a *Robust Control* methodology to the design of a multivariable FCS for Cranfield A3 Observer UAV that is capable of:

- Stabilizing the UAV in flight against external disturbances, such as gusts and turbulence, and parameter variations due to different flight conditions and uncertainty in the model.

- Executing and following ground real-time control commands.

- Autonomously guiding the vehicle on a prescribed flight path defined in 3D space using on-board GPS/INS.

It is first required to select a proper methodology that is suitable for the above application and would have the chance for success in real world implementation. This methodology is required to be simple, effective, and practical. It is also required to have

solid and well-developed theoretical background and good history of real applications. In the next section, a brief review of the available modern and robust control methodologies is presented and the appropriate method is selected.

1.4 Literature Review

A large number of MIMO robust control design methods have been developed over the past thirty years including:

- Eigenstructure Assignment
- Non-linear Dynamic Inversion
- Robust Inverse Dynamics Estimation
- Multi-Objective Parameter Synthesis
- Quantitative Feedback Theory
- Linear Quadratic Optimal Control
- Predictive Control
- $\mathcal{H}_\infty$ Mixed Sensitivity
- $\mathcal{H}_\infty$ Loop Shaping
- μ-Synthesis

The main common objective between these techniques is to achieve advantages over classical methods by improved performance, efficiency, and design simplification utilizing available technology.

Recent years have seen a noticeable increase in the application of Robust control in the design of many aviation systems including fighters, unmanned vehicles, missiles, and space vehicles. An important project was undertaken by GARTEUR ACTION GROUP(AG08)[1] where a Robust Flight Control Design Challenge was performed in

order to demonstrate how Robust Control can be applied to realistic problems. This design challenge was based on (a) The Research Civil Aircraft Model (RCAM)[9-12] and considered a civil aircraft during final approach, (b) Implementation of a wide envelope flight control law for the High Incident Research Model (HIRM)[13-17]. The report evaluated over twelve techniques including most of the above mentioned ones.

The GARTEUR ACTION GROUP(AG08) Robust Flight Control Design Challenge report[1] has concluded the following: "To some extent, the Design Challenge has proven that modern techniques can be used to design controllers for realistic problems. Additionally, it has confirmed that requirements for industrial application of new techniques are quite severe. From an industrial point of view, desirable features of any technique can be assumed to be: transparency, simplicity, quality, accuracy, fidelity, reliability, implementability, predictability and generality. Even though the presented methods have much potential in the field of improved robustness, better performance, de-coupled control and simplification of the design process, some of them do not yet have the maturity required for industrialization. Even mature methods need to be carefully integrated into the industrial design process to fully address the complexities associated with modern aircraft. One of the main problems encountered remains the complexity of the proposed control solutions, which is partly driven by the choice of the control architecture. This is a crucial activity in the design process, which is not yet taken into account sufficiently by the theoretical community."

The following survey is mainly extracted from this project report and covers most of the techniques used in the aerospace industry.

1.4.1 Eigenstructure Assignment

Eigenstructure Assignment is basically an extension of the well-known pole-placement method. It allows the designer to assign the closed-loop eigenvalues (poles) and additionally, to assign the eigenvectors or parts of them, within certain limits. By the assignment of eigenvectors, the zeros of the transfer functions can be influenced and coupling and decoupling of states and modes can be addressed directly. Although the

standard technique takes performance and decoupling into account, it does not address robustness. Eigenstructure assignment is most useful as a tool within a fuller design environment, thus allowing the attainment of good performance, decoupling and robustness in the resulting control system.

1.4.2 Non-linear Dynamic Inversion

Non-linear dynamic inversion uses non-linear dynamic models and full-state feedback to globally linearise the dynamics of selected controlled variables. Simple controllers can then be designed to regulate these variables with desirable closed loop dynamics. The basic feature of feedback linearization or dynamic inversion is the transformation of the original non-linear control system into a linear and controllable system via a non-linear state space change of coordinates and a non-linear static state feedback control law. The solution of this problem relies on the non-singularity of the so-called decoupling matrix. When this condition is not satisfied, a dynamic state feedback control law can be investigated.

An inherent feature of most dynamic inversion schemes is that the open-loop transmission zeroes become poles of the zero dynamics, which are theoretically unobservable in the controlled outputs. If these poles are unstable or very poorly damped they will adversely affect the closed loop. This issue is usually worked around by either approximating the offending non-minimum phase output by ignoring the derivative terms in a large zero or by redefining the output using a regulated variable, which approximates this output but is minimum phase. Both of these approaches produce inexact decoupling of the original outputs despite the fact that the regulated variables are decoupled[18].

Theory of feedback linearization is still gradually developing. The design method requires, more or less, accurate knowledge of the state of the system, while no satisfactory theory for the design of the non-linear observers is available. A suitable non-linear analogue of the separation principle still needs to be developed. One possibility of improvements is that of combining the design technique with appropriate

robust techniques which could take into account unknown parameters and unmodelled dynamics.

1.4.3 Robust Inverse Dynamics Estimation

Robust Inverse Dynamics Estimation (RIDE) has developed from two other methods: the Salford Singular Perturbation Method and Pseudo-Derivative Feedback. Both of these methods use the same type of multivariable Proportional plus Integral (PI) controller structure but use a high gain to provide the desired decoupling and closed-loop dynamics. RIDE is a development of both these methods which replaces the high gain with an estimate of the inverse dynamics of the aircraft with respect to the controlled outputs. This inverse input gives RIDE strong similarities to Non-linear Dynamic Inversion and is similar to the equivalent control found in Variable Structure Control. RIDE does not take into account explicitly any actuator or sensor dynamics during the design phase. It assumes that the dynamics of the actuators and sensors will be sufficiently fast to maintain the desired performance[15].

Due to the simplicity of RIDE, it does not provide a comprehensive solution promised by other more complex methods. RIDE does not provide explicit guarantees in terms of either stability or performance robustness. It is also limited in terms of the amount of specification data which can be incorporated directly in the design stage. Therefore separate analysis is required once the initial design has been done, to see if the controller meets the specification.

1.4.4 Multi-Objective Parameter Synthesis

Multi-objective parameter synthesis (MOPS) is a general technique which complements a chosen control law synthesis technique[19]. Having chosen an application-specific control law structure with parameterisation, or having chosen a general control synthesis technique with its analytically given parameterisation, the free design parameters (e.g. the weights) are computed by a min-max parameter optimisation set up. The designer formulates this set up by specifying the design goals as a set of well defined computational criteria, which can be a function of stability parameters (e.g.

eigenvalues), and time- and frequency response characteristics (e.g. step-response overshoot and settling time, control rates, bandwidth, stability margins etc). By this multi-criteria formulation all the various conflicting design goals are taken care of individually, but are compromised concurrently by a weighted min-max parameter optimisation. In particular, robust-control requirements with respect to variations in structured parameter sets and operating conditions can be taken care of by a multi-model formulation which encompasses the worst-case design conditions.

1.4.5 Quantitative Feedback Theory

Quantitative Feedback Theory (QFT) is a classical frequency domain control system design methodology that was developed by [20]. It is centred around design using Nichols chart and uses a TDF structure for the controller. The method is restricted to a single loop at a time while assumptions are made about other loops. It has been successfully used in the design of UAV FCS[21, 22].

1.4.6 Linear Quadratic Gaussian and Loop Transfer Recovery

Linear quadratic optimal control dates back at least to the Fifties. The fundamentals of this theory can be found in the Special Issue on the LQG problem[23] which appeared as an IEEE Transaction on Automatic Control in 1971. This control technique allows the designer to take into account the amplitude of the control inputs and the settling time of the state variables. When considering infinite horizon optimisation and provided that the weighting matrices are suitably chosen, the resulting closed-loop system exhibits guaranteed multivariable stability margins. Many applications of the LQ theory have been performed in the aeronautical field. It has been recently applied to UAV FCSD[24]. When the complete state is not available for measurement and some or all of the measures are affected by noise, one can use the Kalman optimal filtering theory (which turns out to be the dual of the LQ optimal control theory) to design an observer of the state variables[25]. However the robustness margins are no longer guaranteed in the presence of an observer. If sensor noise is absent or one does not care about it, it is possible to use the degree of freedom on the design of the observer to recover the LQ robustness margins. This is the Loop Transfer Recovery (LTR) technique[26], which,

however, can be applied only when the aircraft model is minimum phase.

1.4.7 Predictive Control

Predictive Control requires the on-line solution of a constrained optimisation problem. This makes it an unlikely candidate for flight control. It explicitly allows for hard constraints, and it can anticipate control commands if the flight trajectory is known in advance. This makes it interesting for flight control, particularly if higher-level control functionality is considered. Predictive Control is distinguished from other control methodologies by the following three key ideas:

- An explicit 'internal model' is used to obtain predictions of system behaviour over some future time interval, assuming some trajectory of control variables.
- The control variable trajectory is chosen by optimising some aspect of system behaviour over this interval.
- Only an initial segment of the optimised control trajectory is implemented; the whole cycle of prediction and optimisation is repeated, typically over an interval of the same length. The necessary computations are performed on-line.

The optimisation problem solved can include constraints, which can be used to represent equipment limits such as slew rates and limited authority control surfaces, and operating/safety limits such as limits on roll angle, descent rate, etc.

Predictive control has up till now been applied mostly in the process industries, where the explicit specification of constraints allows operation closer to constraints than standard controllers would permit, and hence operation at more profitable conditions.

In [12], model-based predictive control (MBPC) was combined with $\mathcal{H}_\infty$ loop-shaping as a method for designing autopilots for civil aircraft. The $\mathcal{H}_\infty$ loop-shaping controller provided stability augmentation and guidance. The MBPC controller acted as a flight

manager. The design procedure developed was tested by designing an autopilot for the Research Civil Aircraft Model (RCAM) used in the GARTEUR design challenge.

1.4.8 $\mathcal{H}_\infty$ Mixed Sensitivity

$\mathcal{H}_\infty$ Mixed Sensitivity method is based on the $\mathcal{H}_\infty$ optimisation problem. It uses input and output frequency weights to minimize the ∞-norm of the closed-loop output sensitivity function S_o.

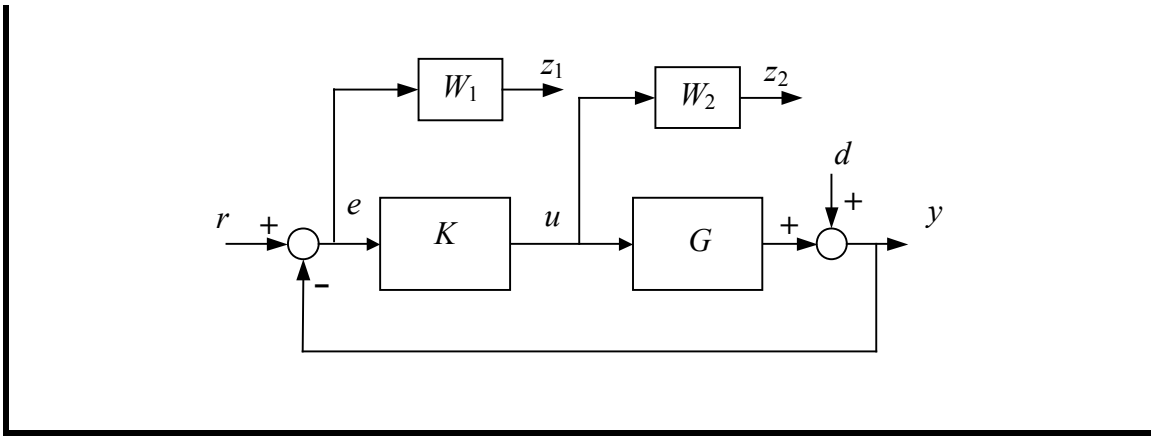

Figure 1.2: $\mathcal{H}_\infty$ Mixed Sensitivity closed-loop feedback system with weights

Figure 1.2 shows a closed loop feedback system with reference input r, output y, output disturbance d, error signal e, control signal u and the weights W_1 and W_2. To achieve small tracking error, good transient behaviour and high bandwidth the output sensitivity needs to be small at low frequencies which can be achieved by designing K to have high gain at these frequencies. In order to meet the low and high frequency conditions, the design will incorporate frequency dependent weights. These weights W_1 and W_2 can be chosen to give the bounds on the terms S_o and KS_o required to achieve the required high and low frequency gains. In fact W_1 needs to be a low pass filter whilst W_2 needs to be a high pass filter. Broadly speaking, W_1 and W_2 determine the performance and robustness properties respectively. Weight selection can be made to account for model uncertainty. If model uncertainty is unspecified, then the weight selection is broadly defined by robustness and performance requirements. The $\mathcal{H}_\infty$ optimisation can then be solved to find a stabilising controller K which is proper and minimises the supremum

(lowest upper bound) over frequency of the maximum singular value of the transfer function from the reference inputs to the output errors.

The pole-zero cancellation phenomenon can occur in the mixed sensitivity technique. Also, the $\mathcal{H}_\infty$ optimisation solution is an iterative process which iteratively searches for the optimum solution.

1.4.9 $\mathcal{H}_\infty$ Loop-Shaping

$\mathcal{H}_\infty$ loop-shaping is also part of the $\mathcal{H}_\infty$ optimisation problem. It was developed by McFarlane and Glover[27]. It is an intuitive method for designing robust controllers as the notions of classical loop-shaping readily carry through. The designer can specify closed loop requirements such as disturbance and noise rejection by shaping the open-loop gains. An important feature of $\mathcal{H}_\infty$ loop-shaping is that it enables the designer to push for the best achievable closed loop performance subject to a required level of robustness. This is because the designer has control over the cross-over frequencies of the loop gain singular values.

In general, when setting up a robust control problem a decision has to be made about the type of uncertainty to be used. This can be difficult as it requires good knowledge of the system model. The robust stability to coprime factor uncertainty, which this method is based on, requires no assumptions to be made about the open-loop stability of the perturbed system model. Coprime factor uncertainty is a general type of uncertainty similar to the single-input single-output (SISO) gain and phase margins. When there is little detailed knowledge about the uncertainty present in a system model $\mathcal{H}_\infty$ loop-shaping is a good method for designing robust controllers.

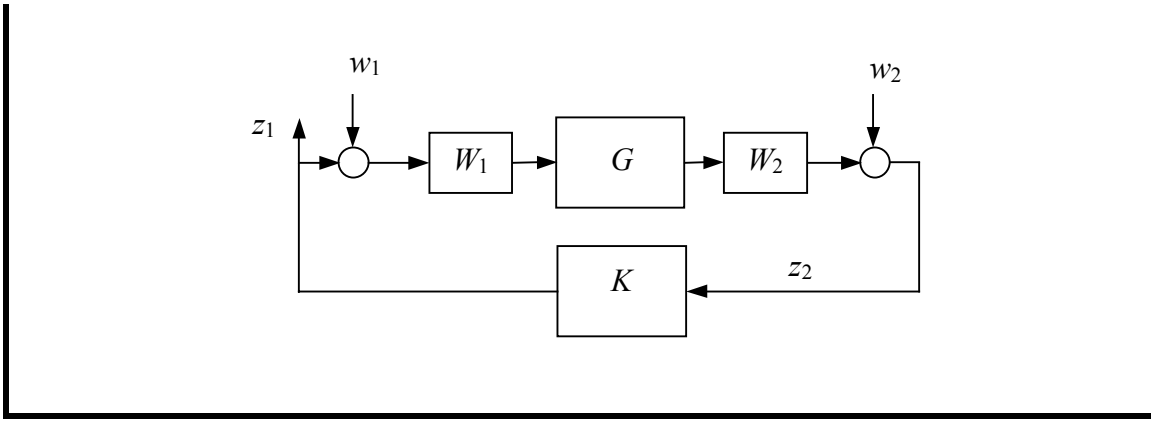

Figure 1.3: $\mathcal{H}_\infty$ loop-shaping standard block diagram

Performance is specified by shaping the singular values of the system model G with weights W_1 and W_2 as shown in Figure 1.3. It is proved that there are no left half plane pole/zero cancellations between controller K and the shaped model $G_s=W_1\ G\ W_2$. This is because K can be written as an exact observer plus state feedback. Hence $\mathcal{H}_\infty$ loop-shaping controllers can be gain scheduled. Left half plane pole/zero cancellations are undesirable as they can limit the achievable robust performance. The cost function minimised provides the robust stability and the solution requires no iteration.

The loop-shaping design method has been used to design robust controllers for several real aerospace projects: The DERA(i.e. QinetiQ) VAAC research Harrier[2, 28]; the Westland Lynx[29], Bell 205 helicopters.[30] The gain scheduled controller designed in[2] for the Harrier aircraft, which was flight tested in December 1993, was the first $\mathcal{H}_\infty$ controller to be flight tested on a real aircraft. Recently it was also applied in an unmanned robotic helicopter [31].

1.4.10 μ-Synthesis and Analysis

μ-Synthesis is an extension to the $\mathcal{H}_\infty$ optimal control technique. μ-Analysis is a method used in measuring the robustness of a system and this has been combined with the $\mathcal{H}_\infty$ optimal control technique in an attempt to *structure* the *uncertainty* in the system model and design a controller which is robust to a more realistic class of perturbations, thus being less conservative and having more flexibility to achieve a higher level of

performance. The method requires detailed *structured uncertainly* knowledge and description. It also requires iterative cycles to the optimum solution. Also, the method generates a high-order controller compared to other $\mathcal{H}_\infty$ optimal control based techniques. However the method has been widely applied in the aerospace field[14, 32-35]

1.5 Methodology Selected

In this project, $\mathcal{H}_\infty$ optimisation with Loop-Shaping Design Procedure(LSDP), which was proposed by Glover and McFarlane[27, 36, 37], is going to be implemented. It has been found to have the following features:

- Based on powerful mathematical background
- Systematic and simple application procedures
- Good history of real applications
- Clear and logical design steps that are similar to classical methods
- Developed and applied by leading British professionals for the last decade
- Well-developed tools and published literature
- Modified and extended for different application situations

Chapter 2

Loop Shaping Design Techniques

In this chapter, the robust Loop Shaping Design Procedure(LSDP) selected in Chapter **1** will be presented in more detail. A simple application example of the longitudinal FCSD of the Cranfield XRAE1 UAV will be introduced. Finally, important extensions to the method that deal with real application implementation issues, such as gain scheduling, actuator saturation, and two degrees-of-freedom design, will be discussed.

2.1 Introduction

The main objective of loop shaping design methodology is to produce a controller that guarantees robust stability against normalized coprime factor uncertainty. This form of uncertainty was used by Glover and McFarlane[27, 36, 37] to obtain an exact solution to the robust stabilization problem. As with all $\mathcal{H}_\infty$ methods, the mathematics used to develop this technique is somewhat involved, and the full description of it is not essential to understand the design process. Thus, only the main results will be presented below. The original work of Glover and McFarlane[27, 36, 37] and [38] can be referred to for more details.

2.2 Uncertainty Representation

Uncertainty for MIMO system model Δ is an unknown perturbation or deviation from the nominal model that satisfies $\Delta \in \mathcal{RH}_\infty$. The size of Δ can be measured using its singular values. There are two types of Δ defined in Robust Control: structured that represents parametric variations in model dynamics, and unstructured that represents unmodelled dynamics. The main three ways the unstructured Δ can be used within a system nominal model G and the perturbed model G_Δ as shown in Figure 2.1 are:

a. Additive: $G_\Delta = G + \Delta_a$: such as airframe flexible modes.

b. Multiplicative at the input: $G_\Delta = G\,[I + \Delta_i\,]$: such as actuator dynamics.

c. Multiplicative at the output: $G_\Delta = [I + \Delta_o\,]\,G$: such as sensor dynamics.

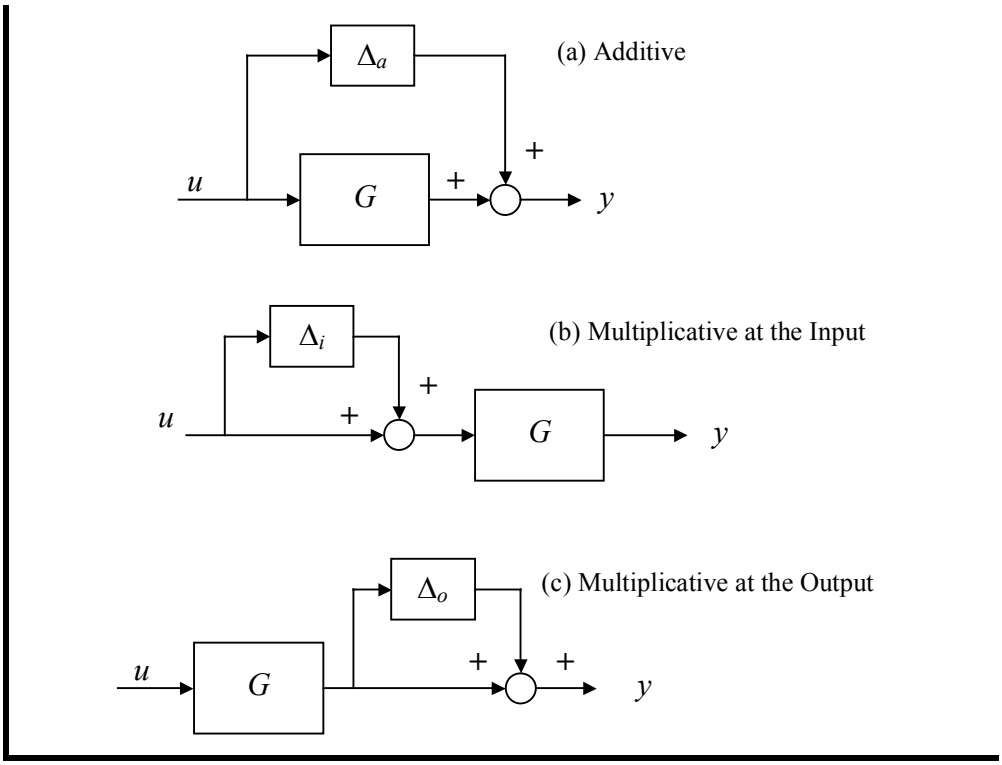

Figure 2.1: Unstructured Uncertainties

2.3 Coprime Factor Uncertainty Representation

An alternative uncertainty description, used in LSDP, is the coprime factor uncertainty.

To illustrate the concept behind this type, consider the linear model transfer function G is factored as $G = M^{-1} N$, where N and M are stable, normalized left coprime transfer functions, i.e. there exist $U, V \in \mathcal{RH}_\infty$ such that

$$\left.\begin{aligned} MV - NU &= I \\ NN^* + MM^* &= I \end{aligned}\right| \qquad \textbf{2.1}$$

This representation is particularly useful because it is possible to represent an unstable transfer function by two stable factors; the coprime factor representation contains no unstable hidden modes. Then we consider the perturbation about G as the set of system models

$$G_\Delta := \left\{ \left(M + \Delta_M\right)^{-1} \left(N + \Delta_N\right) : \left\| \left[\Delta_M \Delta_N\right] \right\|_\infty < \varepsilon \right\} \qquad \textbf{2.2}$$

where Δ_M, Δ_N are unknown stable real-rational transfer functions, i.e. $\Delta_M, \Delta_N \in \mathcal{RH}_\infty$, that represent unstructured additive uncertainty in the nominal model G and $\varepsilon > 0$ is the stability margin, as shown in Figure 2.2 below.

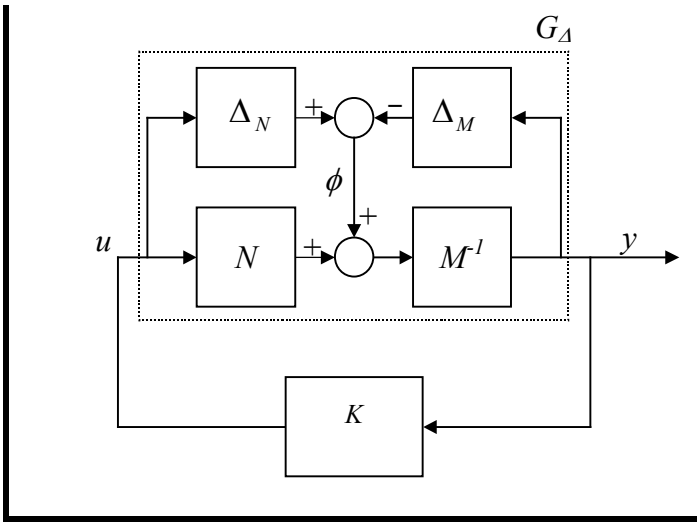

Figure 2.2: Normalized left coprime factor uncertainty description

2.4 Robust Stabilization

Given the system nominal model G above with the described uncertainty, the robust stabilization problem is to find a realizable, stable controller K which stabilizes all models in G_Δ. Such controller will satisfy the above requirements provided that

$$\left\| \begin{bmatrix} K \\ I \end{bmatrix} (I - GK)^{-1} M^{-1} \right\|_\infty \leq \frac{1}{\varepsilon} =: \gamma \qquad \textbf{2.3}$$

which is the $\mathcal{H}_\infty$ norm from ϕ to $[\, u \;\; y \,]^T$ [1]. Again, Glover and McFarlane have shown that, if the above normalized coprime uncertainty is used, the optimal values of ε_{max} and γ_{min} can be found directly and without iteration from the following relation

$$\varepsilon_{\max}^{-1} = \sqrt{1 - \left\| [\, N \;, M \,] \right\|_H^2} = (1 + \rho(XZ))^{1/2} \qquad \textbf{2.4}$$

where ρ is the spectral radius (maximum eigenvalues), Z and X are the solutions to the Generalized Control Algebraic Riccati Equation (GCARE) and the Generalized Filter Algebraic Riccati Equation (GFARE):

$$\left.\begin{aligned} (A - BS^{-1}D^TC)Z + Z(A - BS^{-1}D^TC)^T - ZC^TR^{-1}CZ + BS^{-1}B^T = 0 \\ (A - BS^{-1}D^TC)^T X + X(A - BS^{-1}D^TC) - XBS^{-1}B^TX + C^TR^{-1}C = 0 \end{aligned}\right| \qquad \textbf{2.5}$$

where

$$S = I + D^TD$$
$$R = I + DD^T$$

Thus, the robust stabilization problem of finding K and ε_{max} reduces to the solution of the two Riccati equations in 2.5 simultaneously[36]. For a particular $\gamma > \gamma_{\min}$, K is given by

$$K \overset{s}{=} \left[\begin{array}{c|c} A + BF + \gamma^2 (L^T)^{-1} Z C^T (C + DF) & \gamma^2 (L^T)^{-1} Z C^T \\ \hline B^T X & -D^T \end{array}\right] \quad \textbf{2.6}$$

where

$$\begin{aligned} F &= -S^{-1}(D^T C + B^T X) \\ L &= (1-\gamma^2) I + XZ \end{aligned} \quad \textbf{2.7}$$

and (A, B, C, D) are the minimum realization of G. Note that, if $\gamma = \gamma_{\min}$, L in Equation 2.7 becomes

$$L = -\rho(XZ) I + XZ \quad \textbf{2.8}$$

which is singular, hence Equation 2.6 cannot be implemented[39], but can ultimately be solved using the descriptor system[40, 41].

2.5 Loop Shaping Design Procedure(LSDP)

The above loop shaping design method alone does not give FCS designers room for specifying performance requirements. The key point here is that, if the designer shapes the model G with pre- and post-compensators for performance, as in classical control, then applies the above robust stabilization on the shaped model, an effective design would be achieved.

Thus, LSDP is basically a two stage process. First, the open-loop system nominal linear model is augmented by pre- and post-compensators to give a desired shape to the singular values of the open-loop frequency response, i.e. high gain at low frequency for good command tracking and low gain at high frequency for noise and disturbance rejection. The nominal model G and shaping functions W_1 and W_2 are then combined to form the shaped model G_s where

$$G_s = W_2\, G\, W_1 \qquad \textbf{2.9}$$

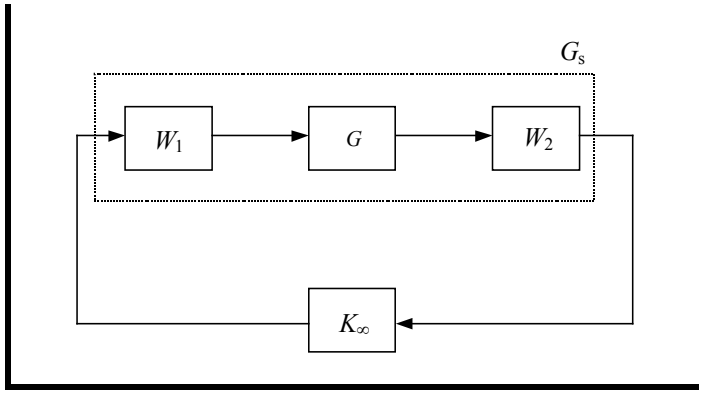

Figure 2.3: G **is shaped by** W_1 **and** W_2 **and stabilized by** K_∞

The resulting shaped system, G_s, is then "robustly" stabilized with respect to the left coprime factor uncertainty using $\mathcal{H}_\infty$ optimisation and the stabilizing central controller, K_∞ , is synthesized as shown in Figure 2.3 above. The final feedback controller K is then constructed by combining K_∞ with the shaping functions W_1 and W_2 , as shown in Figure 2.4 below, such that

$$K = W_1\, K_\infty\, W_2 \qquad \textbf{2.10}$$

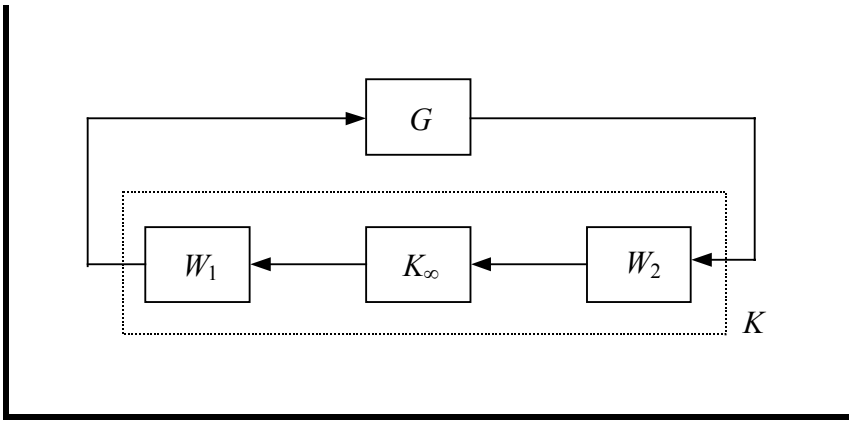

Figure 2.4: Final controller K **is constructed by combining** K_∞ **with** W_1 **and** W_2

The general steps for designing the FCS for the UAV can be summarized as follows:

1. Develop nominal linear model G, define uncertainties, set robust stability and performance requirements.

2. Analyse model frequency/time response. Design shaping filters W_1 and W_2 to meet robust performance requirements and build the shaped system model G_s.

3. Calculate controller gain K using LSDP technique:

   - Solve the equations GCARE and GFARE using the shaped system model G_s.
   - Calculate the optimum ε_{max} and γ_{min} using the above results.
   - Choose a value of $\gamma > \gamma_{min}$, because as $\gamma \rightarrow \gamma_{min}$, some eigenvalues of the controller $\rightarrow \infty$.
   - Calculate a sub-optimal central controller K_∞ using the above value of γ and the results from GCARE and GFARE.
   - Finally, construct the controller $K = W_1 K_\infty W_2$.

4. Analyse controller in LTI systems.

5. Evaluate final controller in full 6DOF; iterate if necessary.

2.6 Application Example

Figure 2.5: XRAE1 Gust Insensitive UAV

In this section an example of the design of the longitudinal controller will be applied to the XRAE1 UAV[42] shown in Figure 2.5 above. The longitudinal model of the

XRAE1 can be represented by the following perturbed linear state-space equations:

$$\dot{x} = Ax + Bu_c + Eg$$
$$y_m = Cx$$

$$\begin{Bmatrix} \dot{u} \\ \dot{w} \\ \dot{q} \\ \dot{\theta} \\ \dot{h} \\ \dot{\eta} \\ \ddot{\eta} \\ \dot{\theta}_f \end{Bmatrix} = \begin{bmatrix} x_u & x_w & x_q & x_\theta & 0 & x_\eta & 0 & 0 \\ z_u & z_w & z_q & z_\theta & 0 & z_\eta & 0 & 0 \\ m_u & m_w & m_q & m_\theta & 0 & m_\eta & 0 & 0 \\ 0 & 0 & 1 & 0 & 0 & 0 & 0 & 0 \\ 0 & -1 & 0 & U & 0 & 0 & 0 & 0 \\ 0 & 0 & 0 & 0 & 0 & 0 & 1 & 0 \\ 0 & 0 & 0 & 0 & 0 & -\omega_a^2 & -2\zeta_a\omega_a & 0 \\ 0 & 0 & 0 & 0 & 0 & 0 & 0 & -1/T_h \end{bmatrix} \begin{Bmatrix} u \\ w \\ q \\ \theta \\ h \\ \eta \\ \dot{\eta} \\ \theta_f \end{Bmatrix} + \begin{bmatrix} 0 & x_\tau & 0 \\ 0 & z_\tau & 0 \\ 0 & m_\tau & 0 \\ 0 & 0 & 0 \\ 0 & 0 & 0 \\ 0 & 0 & 0 \\ \omega_a^2 & 0 & 0 \\ 0 & 0 & 1/T_h \end{bmatrix} \begin{Bmatrix} \eta_D \\ \tau \\ h_D \end{Bmatrix} + \begin{bmatrix} x_u & x_w \\ z_u & z_w \\ m_u & m_w \\ 0 & 0 \\ 0 & 0 \\ 0 & 0 \\ 0 & 0 \\ 0 & 0 \end{bmatrix} \begin{Bmatrix} u_g \\ w_g \end{Bmatrix} \quad \textbf{2.11}$$

$$\begin{Bmatrix} u \\ q \\ \theta \\ h \\ \theta_f \end{Bmatrix} = \begin{bmatrix} 1 & 0 & 0 & 0 & 0 & 0 & 0 & 0 \\ 0 & 0 & 1 & 0 & 0 & 0 & 0 & 0 \\ 0 & 0 & 0 & 1 & 0 & 0 & 0 & 0 \\ 0 & 0 & 0 & 0 & 1 & 0 & 0 & 0 \\ 0 & 0 & 0 & 0 & 0 & 0 & 0 & 1 \end{bmatrix} \begin{Bmatrix} u \\ w \\ q \\ \theta \\ h \\ \eta \\ \dot{\eta} \\ \theta_f \end{Bmatrix}$$

where

θ_f : filtered pitch attitude demand

ω_a , ζ_a: actuator approx. natural frequency and damping ratio

T_h : height sensor filter time constant

η_D , h_D : demanded perturbed elevator deflection and height

u_g, w_g : gust exogenous disturbances

2.6.1 Gust Insensitive Configuration

From Equation 2.11, it is clear that the rotational gust insensitive configuration requires making both pitch dynamic coefficients m_u and m_w null or relatively small. Furthermore, the vehicle must not provide a significant path gain which excites the elevator η_D or the engine throttle τ in response to the gust inputs u_g and w_g [42]. That implies minimizing attitude angle and airspeed feedback gains k_θ and k_u respectively.

2.6.2 Original Controller Design

The original controller was designed using classical proportional constant gain techniques. The general configuration could be represented by an output feedback control law

$$u_c = K(y_r - y_m)$$

$$\begin{Bmatrix} \eta_D \\ \tau \\ h_D \end{Bmatrix} = \begin{bmatrix} 0 & k_q & k_\theta & 0 & -m_{\theta_D} \\ k_u & 0 & 0 & 0 & 0 \\ 0 & 0 & 0 & k_h & 0 \end{bmatrix} \begin{Bmatrix} u \\ q \\ \theta \\ h \\ \theta_f \end{Bmatrix} \quad \textbf{2.12}$$

where, K is the controller feedback gain. The controller was implemented as a regulator as shown in Figure 2.6 , where

$$G = \left[\begin{array}{c|c} A & B \\ \hline C & 0 \end{array}\right]$$

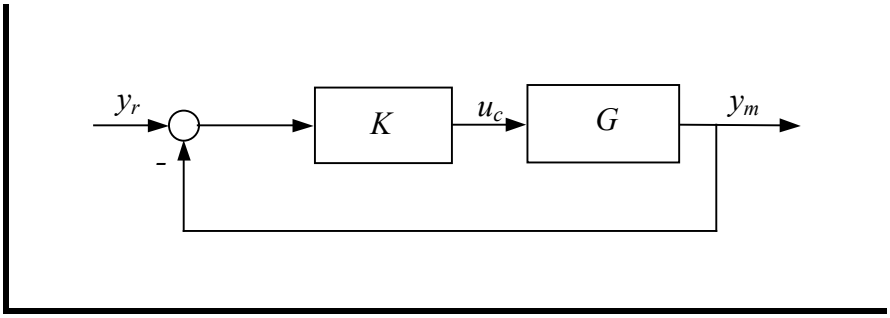

Figure 2.6: Original controller implementation

2.6.3 Longitudinal Linear Model Development

Before starting the robust design, the longitudinal linear model is first developed based on the ACSL non-linear simulation[43]. The linear coefficients are derived from ACSL, then the required modifications and simplifications on the model are made. The longitudinal linear model is presented by,

$$\begin{Bmatrix} \dot{u} \\ \dot{w} \\ \dot{q} \\ \dot{\theta} \\ \dot{h} \\ \dot{\eta} \\ \ddot{\eta} \\ \dot{rpm} \\ \dot{\tau} \\ \ddot{\tau} \end{Bmatrix} = \begin{bmatrix} x_u & x_w & x_q & x_\theta & 0 & x_\eta & 0 & x_\omega & 0 & 0 \\ z_u & z_w & z_q & z_\theta & 0 & z_\eta & 0 & z_\omega & 0 & 0 \\ m_u & m_w & m_q & m_\theta & 0 & m_\eta & 0 & m_\omega & 0 & 0 \\ 0 & 0 & 1 & 0 & 0 & 0 & 0 & 0 & 0 & 0 \\ 0 & -1 & 0 & U & 0 & 0 & 0 & 0 & 0 & 0 \\ 0 & 0 & 0 & 0 & 0 & 0 & 1 & 0 & 0 & 0 \\ 0 & 0 & 0 & 0 & 0 & -\omega_a^2 & -2\zeta_a\omega_a & 0 & 0 & 0 \\ N_u & 0 & 0 & 0 & 0 & 0 & 0 & N_\omega & N_\tau & 0 \\ 0 & 0 & 0 & 0 & 0 & 0 & 0 & 0 & 0 & 1 \\ 0 & 0 & 0 & 0 & 0 & 0 & 0 & 0 & -\omega_a^2 & -2\zeta_a\omega_a \end{bmatrix} \begin{Bmatrix} u \\ w \\ q \\ \theta \\ h \\ \eta \\ \dot{\eta} \\ rpm \\ \tau \\ \dot{\tau} \end{Bmatrix} + \begin{bmatrix} 0 & 0 \\ 0 & 0 \\ 0 & 0 \\ 0 & 0 \\ 0 & 0 \\ 0 & 0 \\ \omega_a^2 & 0 \\ 0 & 0 \\ 0 & 0 \\ 0 & \omega_a^2 \end{bmatrix} \begin{Bmatrix} \eta \\ \tau \end{Bmatrix}_D$$

$$\begin{Bmatrix} u \\ q \\ \theta \\ h \end{Bmatrix}_m = \begin{bmatrix} 1 & 0 & 0 & 0 & 0 & 0 & 0 & 0 & 0 & 0 \\ 0 & 0 & 1 & 0 & 0 & 0 & 0 & 0 & 0 & 0 \\ 0 & 0 & 0 & 1 & 0 & 0 & 0 & 0 & 0 & 0 \\ 0 & 0 & 0 & 0 & 1 & 0 & 0 & 0 & 0 & 0 \end{bmatrix} \begin{Bmatrix} u \\ w \\ q \\ \theta \\ h \\ \eta \\ \dot{\eta} \\ rpm \\ \tau \\ \dot{\tau} \end{Bmatrix} \qquad \textbf{2.13}$$

2.6.4 Robust Controller Design

In general, the main procedure in LSDP was followed in the design process. The principal steps are described in the following sections.

2.6.4.1 Input and Output Scaling

Here *G*, defined by Equation 2.13, is scaled according to the desired output decoupling. At the input, the system model is scaled according to relative actuators usage and capability. The scaled system model is defined as:

$$G_c = W_{1c}\, G\, W_{2c} \qquad \textbf{2.14}$$

where W_{1c} and W_{2c} are the input and output scaling matrices and defined as,

$$W_{1c} = \texttt{diag[}\pi\texttt{/180 1]},\ W_{2c} = \texttt{diag[1 }\pi\texttt{/180 }\pi\texttt{/180 1]}$$

2.6.4.2 Shape System Model Open-Loop SV

The scaled system model G_c is then shaped using pre- and post-weights W_{1s} and W_{2s} as

$$G_s = W_{1s}\, G_c\, W_{2s} \qquad \textbf{2.15}$$

W_{1s} was chosen to include integrators to boost the low frequency gain. This ensures zero steady-state tracking error, disturbance rejection, and output decoupling. W_{2s} was chosen for noise rejection, i.e. low pass filter for high frequency damping.

$$W_{1s} = \frac{s+1}{s} I_{2\times 2}, \quad W_{2s} = \frac{1}{.2s+1} I_{4\times 4} \qquad \textbf{2.16}$$

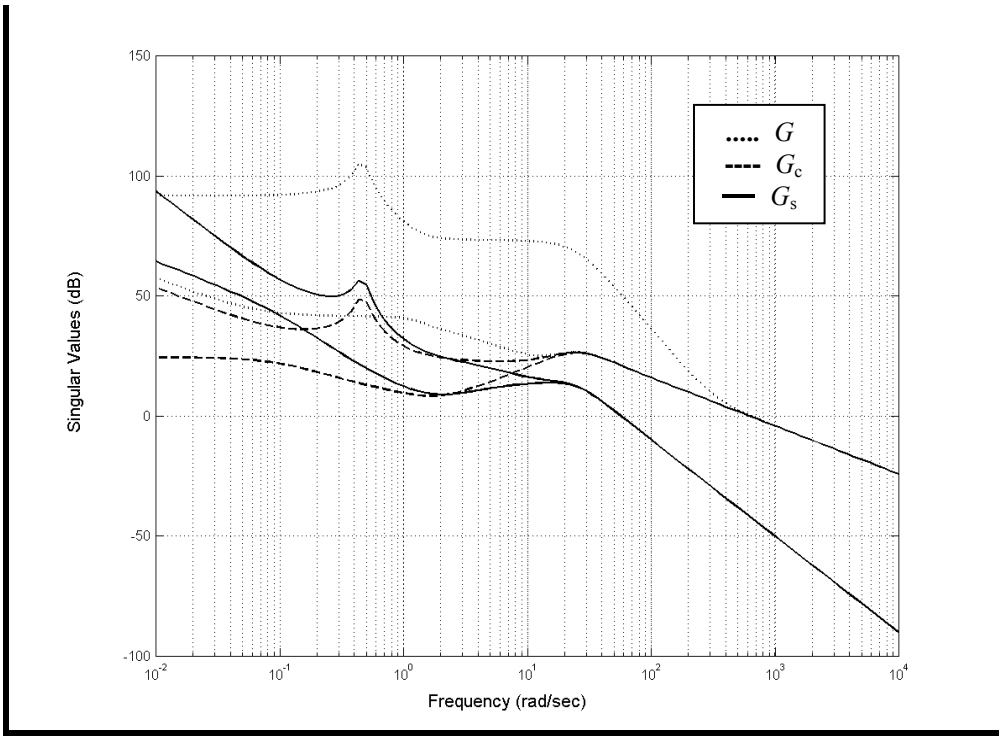

Figure 2.7: Effect of scaling and shaping on Open-loop SV

Figure 2.7 above, shows how the open loop singular values of the system model G have been modified, first by scaling and then by shaping.

2.6.4.3 Robust Stabilization

Using normalized coprime factorisation uncertainty, the scaled and shaped system

model G_s is used to find the controller K_∞ as shown in Figure 2.8 below.

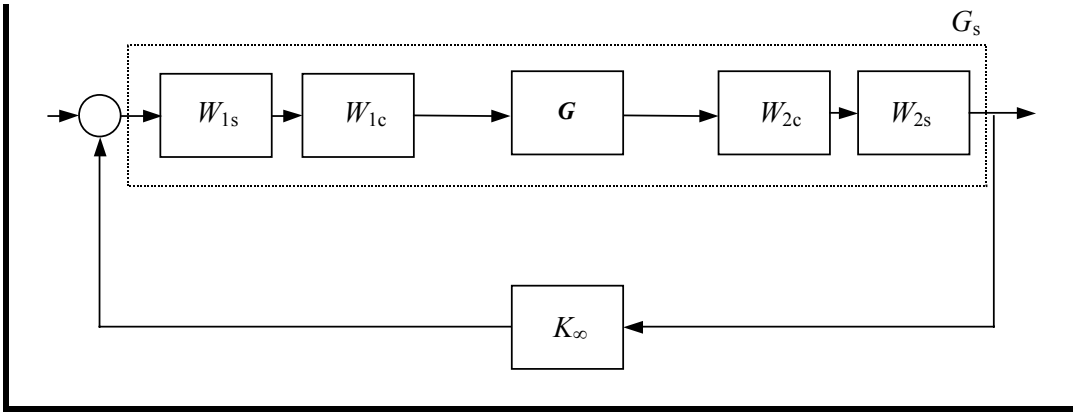

Figure 2.8: Stabilizing controller for shaped model

The resulting sub-optimal robust stability margin was: $\varepsilon = 0.355$, $\gamma = 2.81$. The design is usually considered successful if $\varepsilon > 0.25$ (or $\gamma < 4$)[39].

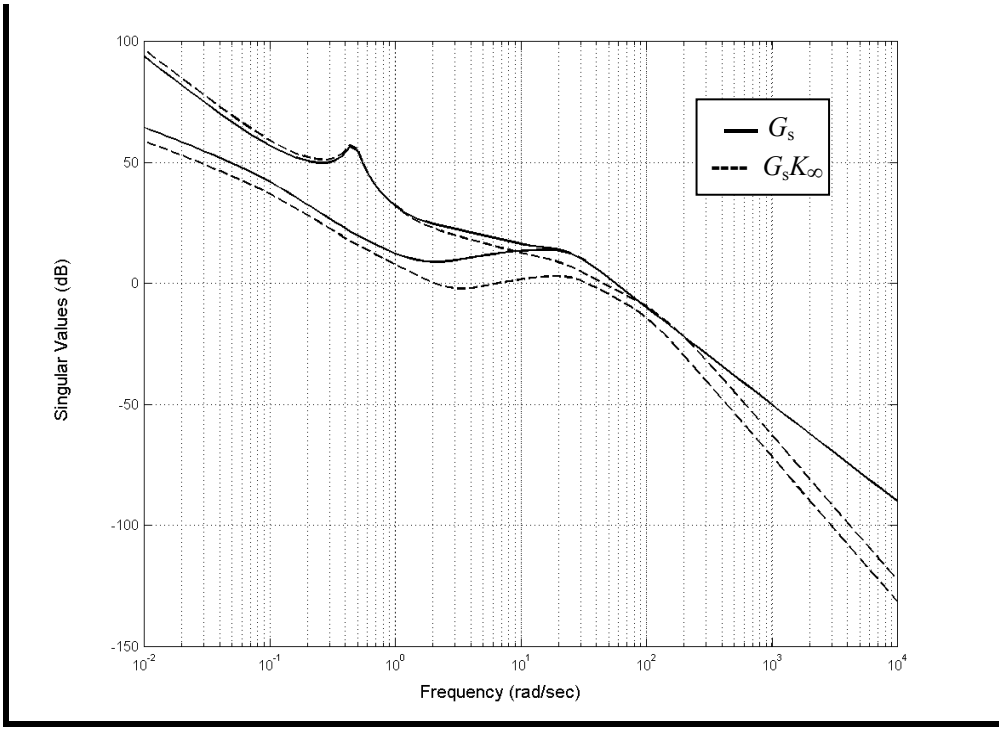

Figure 2.9: Controller effect on shaped model open-loop SV

Figure 2.9 above shows how K_∞ has altered the open loop system G_s singular values by

slightly reducing slope at crossover and reducing the high frequency gain.

2.6.4.4 Controller Implementation

The controller can be implemented in several ways, in the forward path, in the feedback path, or in the observer form. It was found that the configuration in Figure 2.10 below gives better response than the feedback or feed-forward configurations [2, 39]. This is because the reference commands do not directly excite the dynamics of the controller K_s, which would result in large overshoots. The constant prefilter K_{pr} ensures a steady-state unity gain between y_r and y_m and is given by

$$K_{pr} = K_\infty(0)W_{2s}(0)W_{1c} \qquad \textbf{2.17}$$

where $K_\infty(0)$ and $W_{2s}(0)$ are the DC gains of the respective systems.

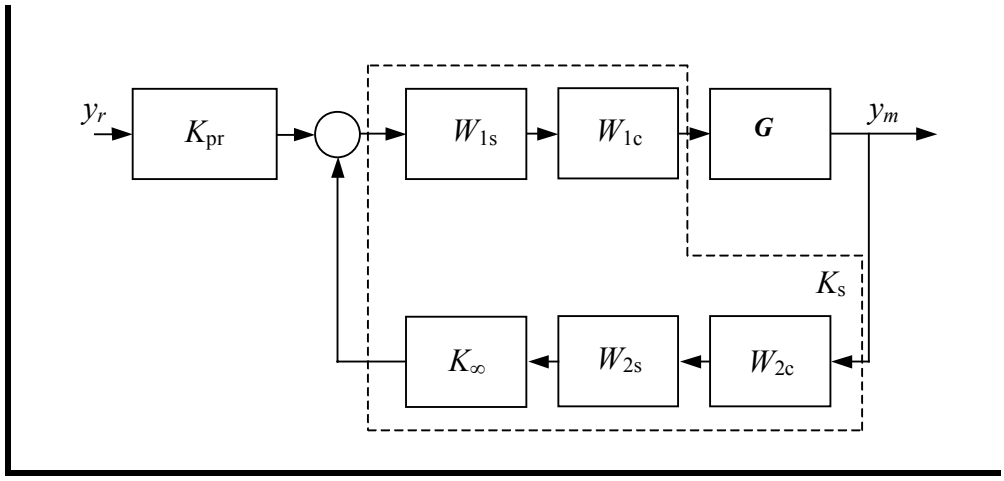

Figure 2.10: Robust controller implementation

2.6.4.5 Linear Analysis

Using the linear model of the aircraft, the longitudinal pitch dynamics were analysed by performing a step response on the elevator input as a $1m$ height command. The following figures show the initial results of the robust controller response compared the original classical controller.

Figure 2.11 below, shows how the robust controller was able to improve the height h

step response and decoupling with airspeed u, while using less elevator η effort. Note that the elevator time line response is 1sec to emphasize the initial response.

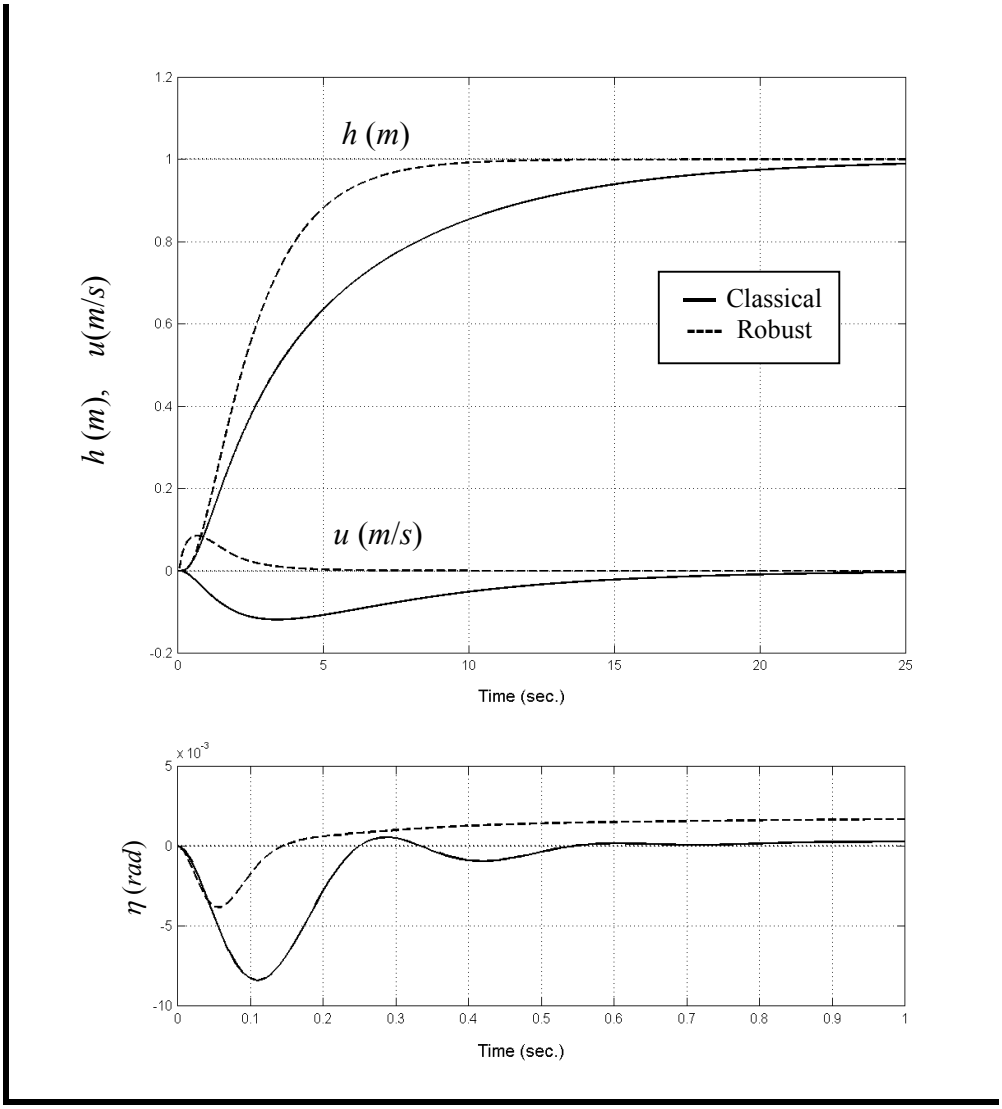

Figure 2.11: Height step response comparison

2.7 Observer-Form Controller Structure

$\mathcal{H}_\infty$ loop-shaping controller exhibits a separation structure in the controller[44]. This structure has several important advantages such as gain-scheduling and anti-windup implementation as shown by[45]. A brief description is given below and the interested reader can refer to [46-49] for more details.

If we assume that the system model is strictly proper, with a stabilizable and detectable state-space realization,

$$G_s = C_s(sI - A_s)^{-1}B_s \overset{s}{=} \left[\begin{array}{c|c} A_s & B_s \\ \hline C_s & 0 \end{array}\right] \qquad \textbf{2.18}$$

then the loop-shaping controller can be realized as an observer, as in Figure 2.12 below, for the shaped system model plus a state-feedback control law such as

$$\begin{aligned} \dot{\hat{x}}_s &= A_s\hat{x}_s + H_s(C_s\hat{x}_s - y_s) + B_s u_s \\ u_s &= F_s\hat{x}_s \end{aligned} \qquad \textbf{2.19}$$

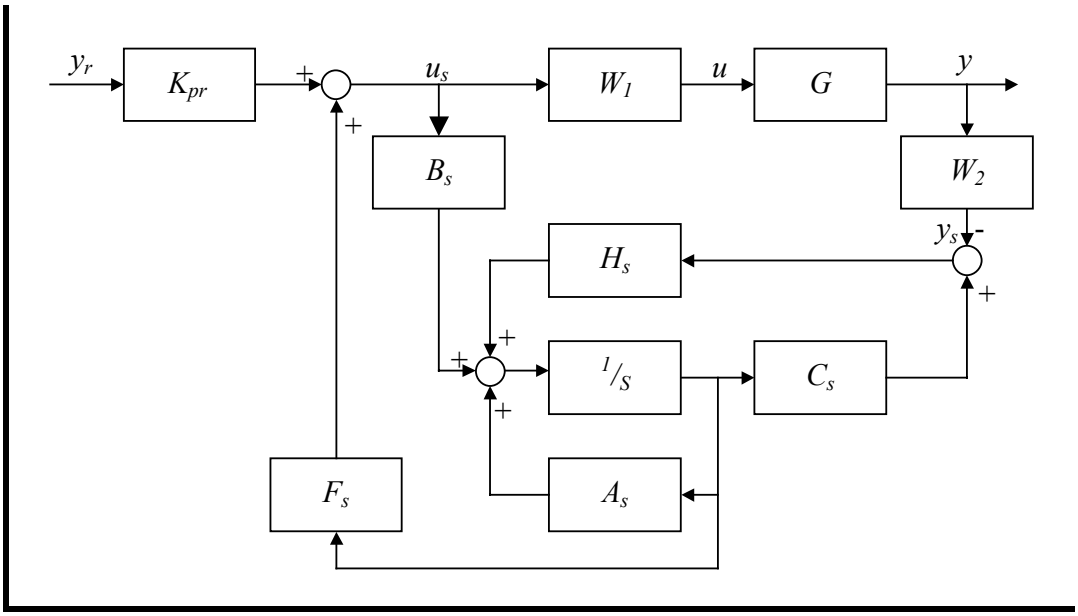

Figure 2.12: Observer-form Controller

where $\hat{x}_s$ is the observer state, u_s and y_s are the model input and output respectively, and

$$\begin{aligned} H_s &= -Z_s C_s^T \\ F_s &= -B_s^T \left[I - \gamma^{-2} I - \gamma^{-2} X_s Z_s \right]^{-1} X_s \end{aligned} \qquad \textbf{2.20}$$

where Z_s and X_s are the appropriate solutions to the GCARE and GFARE equations[39]. Note that the observer form in Figure 2.12 above also gives a well behaved tracking response. This is because the reference signal y_r is injected in such a way that

$$y = N y_r \qquad \textbf{2.21}$$

where N is the numerator of the normalized right coprime factorisation of G defined in Equation 2.1, which is robust to small perturbations in G and has a bandwidth approximately equal to the open-loop bandwidth of G [50].

2.8 Two Degrees-of-Freedom Design

The $\mathcal{H}_\infty$ loop-shaping design procedure of McFarlane and Glover [27, 37] is considered as a one degree-of-freedom design. Although a simple constant prefilter can be implemented for zero steady-state error, for many tracking problems this will not be sufficient and a dynamic two degrees-of-freedom (TDF) design is required. The TDF controller shown in Figure 2.13 allows one to improve performance by treating disturbance rejection and command tracking separately to some degree. A brief description of the method will follow. More details about this method are given in[51, 52].

If the controller is partitioned to $K_s = [\, K_1 \;\; K_2 \,]$, as in Figure 2.13, it can be seen that the controller command is given by

$$u = \begin{bmatrix} K_1 & K_2 \end{bmatrix} \begin{bmatrix} \beta \\ y \end{bmatrix} \qquad \textbf{2.22}$$

where K_1 and K_2 in Figure 2.13 are the demand and feedback controllers. The demand controller K_1 is to ensure that

$$\left\| W_o T_{y\beta} - W_{2s} T_{ref} \right\| \le \gamma \rho^{-2} \qquad \textbf{2.23}$$

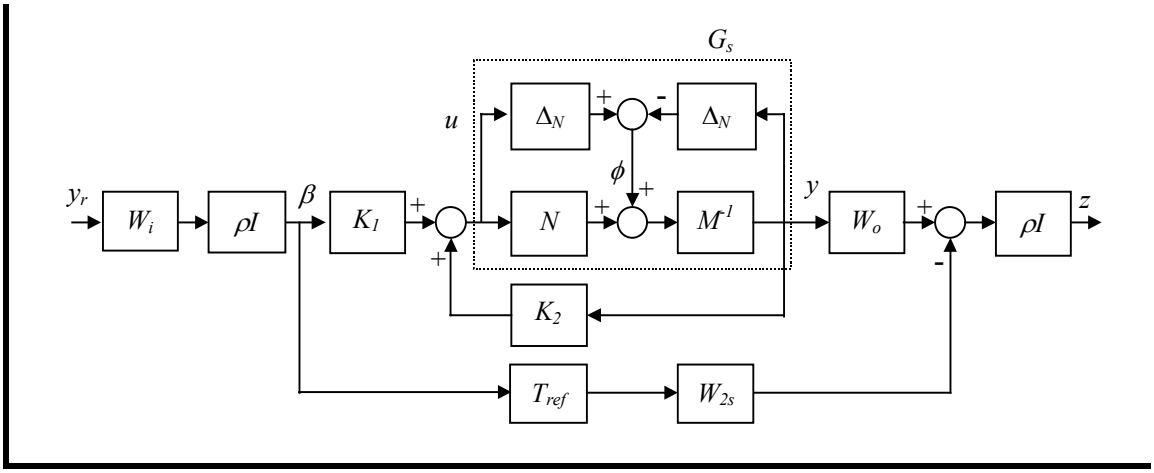

Figure 2.13: Two degrees-of-freedom Configuration

where

$$T_{y\beta} = (I - G K_2)^{-1} G K_1 \qquad \textbf{2.24}$$

is the closed loop transfer function: y/β and the transfer function T_{ref} is the model chosen to have the required time response performance. The scaling factor $\rho > 1$ is a scalar parameter that can be increased to place more emphasis on model matching in the optimisation at the expense of robustness. Note that if ρ is set to zero, the TDF controller reduces to the ordinary robust stability problem. The input pre-weight W_i is to insure that the closed-loop transfer function: y_r / z matches the desired model T_{ref} at steady-state and is given by,

$$W_i \triangleq \left[W_o \left(I - G_s(0) K_2(0) \right)^{-1} G_s(0)\, K_1(0) \right]^{-1} T_{ref} \qquad \textbf{2.25}$$

W_o is the output selection matrix which selects from the output measurement y the variables to be controlled and included in the model matching optimisation part. This implies that W_o rows are less than or equal to its columns. W_{2ref} contains the weights of the selected outputs to be matched from the full output weighting W_2 . The TDF system in Figure 2.13 above, can be put in a generalized transfer function form P as,

$$\begin{bmatrix} u \\ y \\ e \\ \beta \\ y \end{bmatrix} = \begin{bmatrix} P_{11} & P_{12} \\ P_{21} & P_{22} \end{bmatrix} \begin{bmatrix} r \\ \phi \\ u \end{bmatrix} = \left[\begin{array}{cc:c} 0 & 0 & I \\ 0 & M_s^{-1} & G_s \\ \hdashline -\rho^2 W_{2s} T_{ref} & \rho M_s^{-1} & \rho G_s \\ \hdashline 0 & 0 & 0 \\ 0 & M_s^{-1} & G_s \end{array}\right] \begin{bmatrix} r \\ \phi \\ u \end{bmatrix} \quad \textbf{2.26}$$

With the shaped model G_s and the reference model T_{ref} , with the addition of W_{2s}, have the following state-space realizations,

$$G_s \overset{s}{=} \begin{bmatrix} A_s & B_s \\ C_s & D_s \end{bmatrix}$$

$$W_{2ref} T_{ref} \overset{s}{=} \begin{bmatrix} A_r & B_r \\ C_r & D_r \end{bmatrix}$$

the generalized P , with the addition of W_o , can be realized as,

$$P = \left[\begin{array}{cc|cc:c} A_s & 0 & 0 & (B_s D_s^T + Z_s C_s^T) R_s^{-1/2} & B_s \\ 0 & A_r & B_r & 0 & 0 \\ \hline 0 & 0 & 0 & 0 & I \\ C_s & 0 & 0 & R_s^{1/2} & D_s \\ \rho W_o C_s & -\rho^2 C_r & -\rho^2 D_r & \rho W_o R_s^{1/2} & \rho W_o D_s \\ \hdashline 0 & 0 & \rho I & 0 & 0 \\ C_s & 0 & 0 & R_s^{1/2} & D_s \end{array}\right] \quad \textbf{2.27}$$

where $R_s = I + D_s D_s^T$. Note that Z_s is the solution of the GCARE in Equations 2.5. Equation 2.27 can then be solved using the standard $\mathcal{H}_\infty$ method and γ-iteration as shown in[39, 51, 53]. Please refer to these references for more details.

2.9 Actuator Saturation and Anti-Windup

Multivariable systems present a real problem when actuators saturate. This is because the loop-gain has both magnitude and direction both of which are affected by the saturation. The loss in directionality can mean loss of decoupling between the controlled

outputs. The situation gets even worse if more than one actuator saturates at the same time.[2] Several techniques exist for the design of multivariable anti-windup compensators[54-58]. The Observer and Hanus approach provides a reliable way of affecting de-saturation and has been tested in real flights[45].

2.9.1 Hanus Self-conditioning Anti-Windup

In $\mathcal{H}_\infty$ loop-shaping the pre-compensator weight W_1 would normally include integral action in order to reject low frequency disturbances and uncertainty. However, in the case of actuator saturation, the integrators will continue to integrate their input and hence cause windup problems. Let,

$$W_1 \overset{s}{=} \left[\begin{array}{c|c} A_w & B_w \\ \hline C_w & D_w \end{array}\right] \qquad \textbf{2.28}$$

The Hanus or self-conditioned form of W_1 is[54],

$$W_{1f} = \left[\begin{array}{c|cc} A_w - B_w D_w^{-1} C_w & 0 & B_w D_w^{-1} \\ \hline C_w & D_w & 0 \end{array}\right] \qquad \textbf{2.29}$$

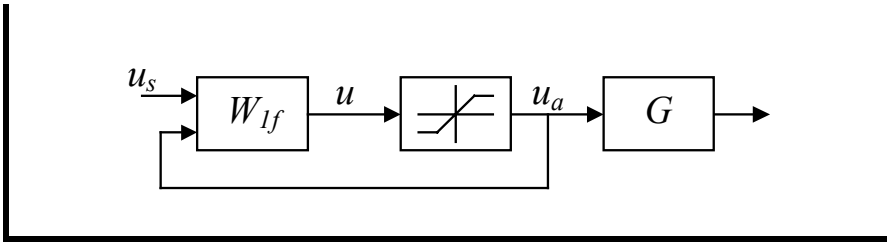

Figure 2.14: Hanus Self-conditioning Implementation

The Hanus form as implemented in Figure 2.14 prevents windup by keeping the states of W_{1f} consistent with the actual system model at all times. When there is no saturation $u_a = u$, the dynamics of W_{1f} will not be affected. When $u_a \neq u$ the dynamics are inverted and driven by u_a so that the states remain consistent with the actual limited input u_a [39].

2.9.2 Combined Hanus and Observer-form Structure

By combining the Hanus self-conditioning and the observer form, the actual system model input u_a is used to drive both of the self-conditioned pre-weight W_{1f} and the observer as shown in Figure 2.15. Thus the controller states remain consistent with the system model states, while the Hanus form keeps W_{1f} from winding up at saturation. Note that W_1 needs to be semi-proper to be invertible.

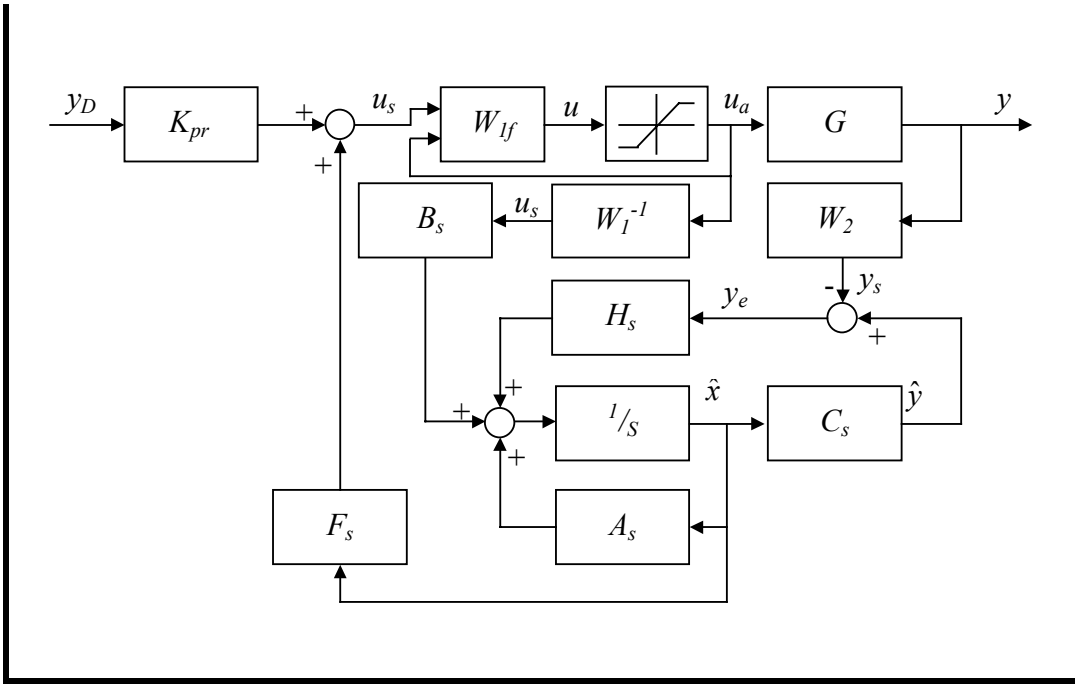

Figure 2.15: Hanus anti-windup implementation in Observer-structure

2.10 The ν-Gap Metric

Most of the robust control design techniques assume that there is some description of the system model uncertainty (i.e., there is a measure of the distance from the nominal system model to the set of models that represent the uncertainty). This measure is usually chosen to be a metric or a norm. However, the operator norm can be a poor measure of the distance between systems in respect to feedback control system design[38, 59]. The gap[59] and ν-gap[50, 60, 61] metrics were introduced as being more appropriate for the study of uncertainty in the feedback systems.

The ν-gap metric measures the distance between systems in terms of how their differences can effect closed-loop performance. In general, if the ν-gap distance between two models is small then any controller which performs well with one model will also perform well with the other. The ν-gap metric also allows measuring the distance between models with different numbers of right half plane poles.

Given the nominal system model G_0 and a perturbed model G_1, the ν-gap metric is defined as,

$$\delta_\nu(G_0, G_1) := \begin{cases} \left\| (I + G_1 G_1^*)^{-1/2} (G_1 - G_0)(I + G_0 G_0^*)^{-1/2} \right\|_\infty, & \text{if } \eta[G_1, -G_0^*] = \eta[G_0, -G_0^*] \\ 1, & \text{otherwise} \end{cases} \quad \textbf{2.30}$$

where $\eta[G, K]$ denotes the number of open-loop RHP poles of $[G, K]$: the positive feedback system model G and controller K. $\eta[G_0, -G_0^*]$ can be shown to equal the *degree* of G_0; the condition $\eta[G_1, -G_0^*] = \eta[G_0, -G_0^*]$ is defined as the *winding number* condition. For more details refer to[38, 50, 61].

In summary, the ν-gap technique computes the distance between two system models and gives a numerical value of

$$0 \le \delta_\nu(G_0, G_1) \le 1 \quad \textbf{2.31}$$

Smaller numbers correspond to G_0 and G_1 being more similar, with $\delta_\nu(G_0, G_1) = 0$ only if $G_0 = G_1$.

Another important definition which is related to the ν-gap metric is the generalized stability margin(*SM*),

$$SM = b(G,K) := \begin{cases} \left\| \begin{bmatrix} I \\ K \end{bmatrix} (I - GK)^{-1} \begin{bmatrix} I & G \end{bmatrix} \right\|_{\infty}^{-1}, & \text{if } [G,K] \text{ is stable} \\ 0, & \text{otherwise.} \end{cases} \quad \textbf{2.32}$$

This measure of stability is large(good) when the norm is small, and small(bad) when the norm is large, where for any G and K,

$$0 \le b(G,K) \le 1$$

For the above metric the following robust performance result holds,

$$\arcsin b(G_1,K) \ge \arcsin b(G_0,K) - \arcsin \delta_v(G_0,G_1) \quad \textbf{2.33}$$

The interpretation of this result is that, if a nominal plant G_0 is stabilized by controller K, with $b(G_0, K)$, then the SM, when G_0 is perturbed to G_1, is degraded by no more than the formula in Equation 2.33. Note that $1/b(G,K)$ is also the signal gain from disturbances on the model input and output to the input and output of the controller. The stability margin in Equation 2.32 can loosely be related to the classical gain and phase margins as,

$$GM \ge \frac{1+SM}{1-SM}, \; PM \ge 2\arcsin SM \quad \textbf{2.34}$$

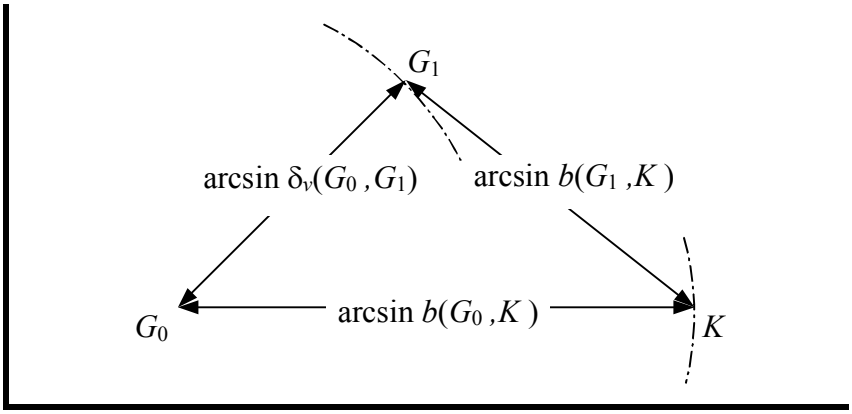

Figure 2.16: The triangle inequality for b and δ_v

Equation 2.33 can also be interpreted in terms of Figure 2.16 above. That is, if we associate the systems G_0, G_1, and K with points in the plane, the inequality in Equation 2.33 is just expressing a triangle inequality[50]. Figure 2.16 can also be interpreted as: If K stabilizes G_0 with $b(G_0, K) > \delta_v(G_0, G_1)$, then K is guaranteed to stabilize G_1.

The ν-gap is always less than or equal to the gap, so its predictions using the above robustness result are tighter. To make use of the *v*-gap metric in robust design, weighting functions need to be introduced. In the above robustness result, G needs to be replaced by $G_s = W_2 G W_1$ and K by $W_1^{-1} K W_2^{-1}$ (similarly for G_0 and G_1). This makes the weighting functions compatible with the weighting structure in the loop shaping synthesis.[53]

Chapter 3

A3 Observer Non-Linear Simulation

In this chapter, the full non-linear six degrees-of freedom model simulation of the A3 Observer UAV will be introduced including airframe, engine and propeller, and actuators. The existing flight control system will also be described including axial airspeed, longitudinal, and lateral control loops. Finally, the simplified navigation system that was implemented in the non-linear simulation and includes cross-track error from current flight path segment will be discussed.

3.1 Introduction

Most flight control system design techniques are model-based. This implies the necessity for the development of an adequate mathematical model of the system to be controlled. This is an important preliminary task since the performance and robustness of the controller will depend on how accurate and representative the model is for the real system on which the design is based.

There are, in general, two types of modelling of aerospace vehicles. The first is the high fidelity, six degrees-of-freedom, non-linear and detailed model which is developed to simulate the real system response as accurately as possible. These models include as many subsystems as possible, such as actuator dynamics, amplitude and rate limiters, gyros, engine/propeller, control delays and discretization, structure dynamics, atmospheric external disturbances, and sensor measurement noise. Such simulation models are developed to evaluate the whole system performance in realistic environments and are essential for pre/post-flight simulations where some modelling parameters are only mathematical estimates, or wind-tunnel measurements, and need to be fine-tuned with real system dynamic behaviour in order to match their actual response. These simulation models are also important for the validation of the control systems and are usually based on simplified models of the vehicle which are described next.

The second kind of air vehicle mathematical modelling is the simplified model that serves specific applications. Such models emphasize the dynamics and behaviour of particular interest and simplify or, if possible, neglect the effects of the less important subsystem components. These simplified models are usually used in the control system design process. The main characteristics of such models are simplicity, linearity and functional visibility, while maintaining the desired level of response fidelity.

3.2 ACSL Simulation

The A3 non-linear model simulation was developed using the Advanced Continuous Simulation(ACSL) programming language[43]. The program has evolved from previous works on the XRAE1 UAV[6, 62-64]. Due to the nature of the A3 Observer project, no documentations were available for public release at the time of writing this thesis. In the following paragraphs, a brief description of the non-linear simulation model will be given. More details can be acquired from *Cranfield Aerospace Ltd* or the Flight Dynamics Group in School of Engineering. Figure 3.1 shows a functional block diagram of the ACSL non-linear model simulation.

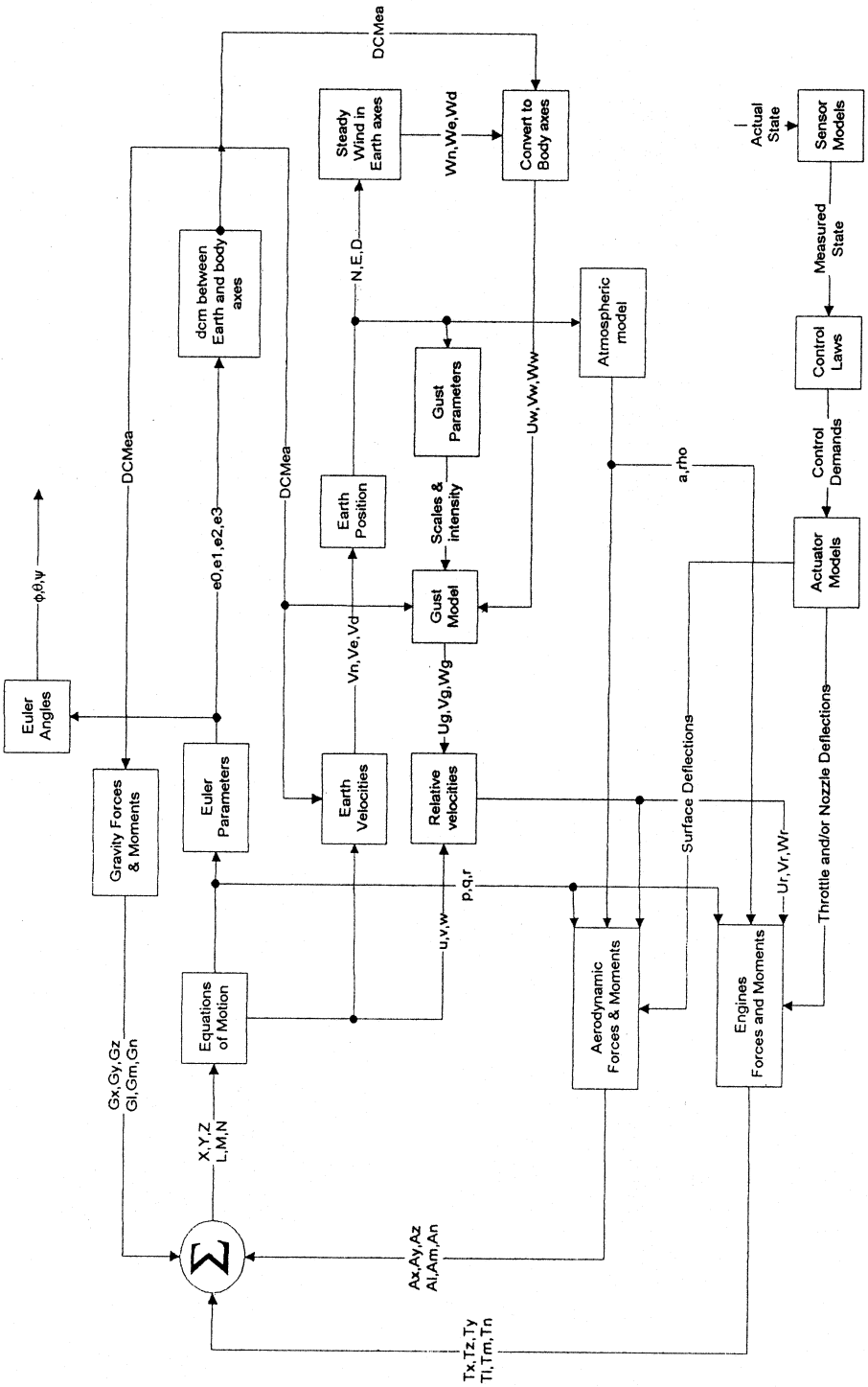

Figure 3.1: Non-linear Model Simulation Block Diagram

Figure 3.2: The A3 Observer in launch position at an MoD firing range

3.2.1 Main Assumptions

The air vehicle is modelled as a standard six degrees-of-freedom system with the following main assumptions:

- Airframe is a rigid body with a fixed centre of gravity(CG) position.
- Vehicle has a centred longitudinal plane of symmetry that passes though the CG.
- Vehicle weight and moments of inertia are fixed time invariant quantities.
- Earth is flat and fixed in space, and atmosphere is fixed with respect to earth.
- Perfect sensor dynamics apart from amplitude limits, quantization effects, and bias errors.

3.2.2 System Axes and Transformation

Body axis origin is 530*mm* ahead of the trailing edge and on the fuselage centre line and not positioned at the CG of the airframe. This was because the variation of CG position would be simplified by requiring only one definition of the aerodynamic data, while the

mass and inertia matrices are transformed from the CG position in the x- and y-axes back to the origin[63].

The body rotation rates *p*, *q*, *r* were not integrated directly to find, roll, pitch, and yaw. This is due to the large angular displacements involved. Instead, the Euler Symmetric Parameters (Quaternion)[65, 66] were used to find both the Euler angles and the Direction Cosine Matrix(DCM) between the body axes and the earth fixed axes. It is then used to transform the body axis velocity components to earth axes to give the earth reference velocities. These velocities can then be integrated to obtain the air vehicle position in space.

$$X_B = \text{DCM}\ X_E \qquad \textbf{3.1}$$

$$\begin{bmatrix} x_B \\ y_B \\ z_B \end{bmatrix} = \begin{bmatrix} e_0^2+e_1^2-e_2^2-e_3^2 & 2(e_1e_2+e_0e_3) & 2(e_1e_3-e_0e_2) \\ 2(e_1e_2-e_0e_3) & e_0^2-e_1^2+e_2^2-e_3^2 & 2(e_2e_3+e_0e_1) \\ 2(e_1e_3+e_0e_2) & 2(e_2e_3-e_0e_1) & e_0^2-e_1^2-e_2^2+e_3^2 \end{bmatrix} \begin{bmatrix} x_E \\ y_E \\ z_E \end{bmatrix} \qquad \textbf{3.2}$$

The quaternions are solved using the following dynamic equations:

$$\begin{bmatrix} \dot{e}_0 \\ \dot{e}_1 \\ \dot{e}_2 \\ \dot{e}_3 \end{bmatrix} = \frac{1}{2} \begin{bmatrix} 0 & -p & -q & -r \\ p & 0 & r & -q \\ q & -r & 0 & p \\ r & q & -p & 0 \end{bmatrix} \begin{bmatrix} e_0 \\ e_1 \\ e_2 \\ e_3 \end{bmatrix} \qquad \textbf{3.3}$$

Note that the quaternions are normalized, i.e. $e_0^2 + e_1^2 + e_2^2 + e_3^2 = 1$.

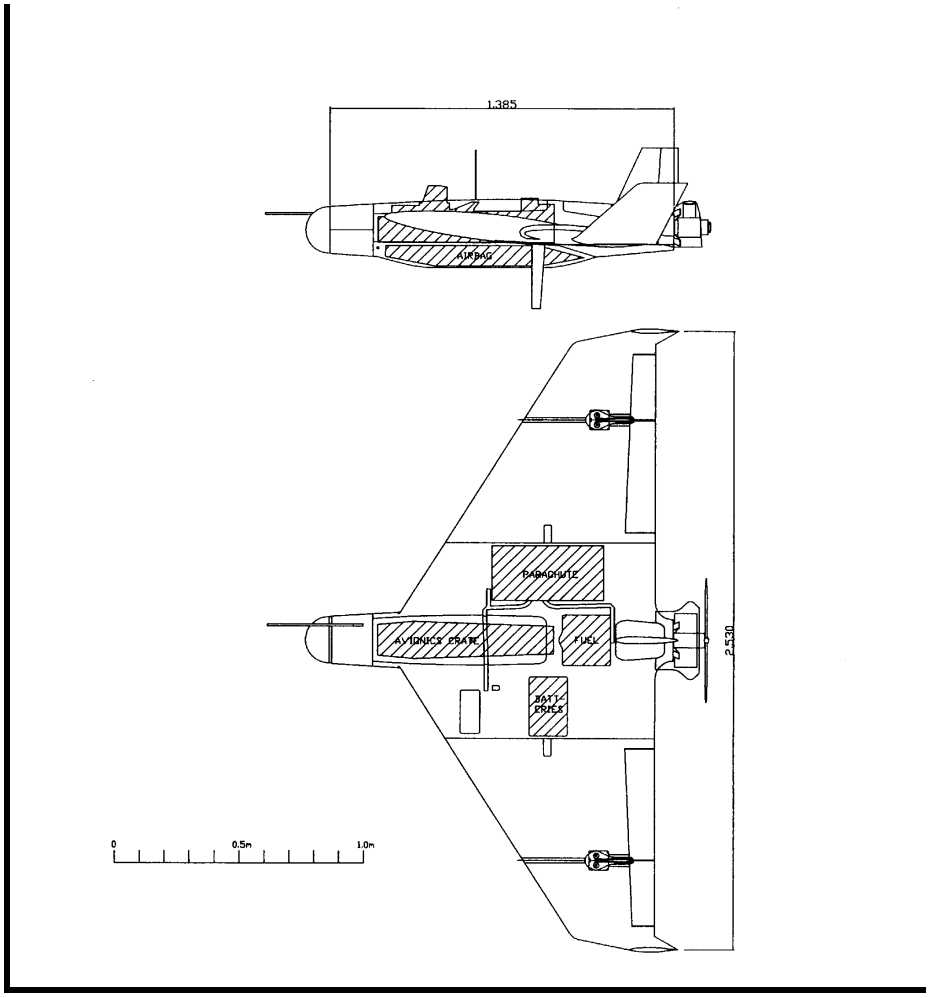

Figure 3.3: The A3 Observer Airframe

3.2.3 Airframe Dynamics

The vehicle airframe shown in Figure 3.3 exploits the *Gust Insensitive* configuration. The advantage of such configuration is to be insensitive in angular motion to exogenous disturbances such as gust wind. This can be accomplished by making the dimensional rotational dynamic derivatives null or very small by means of CG position, anhedral wing angle, etc. The major contributing coefficients that were modified are[7, 64]:

- Rolling moment due to side slip l_v was neutralized by adding as much anhedral as practical on the delta wing.
- Yawing moment due to sideslip n_v was reduced by using wing tips to counter

that due to wing body.

- Pitching moment due to forward speed m_u was reduced by making the vertical separation between the CG and the thrust and drag lines as small as possible. This in turn reduced the pitching moment due to thrust m_t .
- Pitching moment due to heave velocity m_w was reduced by moving CG position longitudinally aft to neutral point.

This however resulted in a vehicle that has marginal or neutral dynamic stability about all three axes. This implied that it lacked natural stability and restoring moments that would return the aircraft to a level flight after a disturbance in bank or heading. Instead the aircraft would simply sideslip and keep a fixed heading angle with respect to the flight path.

3.2.4 Equations of Motion

Air vehicle equations of motion are derived from Newton's Second Law of Motion. They basically describe the dynamic behaviour of the air vehicle as a rigid body moving through the atmosphere. These equations lie in the heart of any air vehicle simulation and are detailed in many standard text books such as [65, 67-69].

The following equations of motion were implemented in the ACSL simulation and expressed in the body-axes frame[62, 63]. The translational equations were given in the following form:

$$F = M_a \dot{x}_F = \sum F$$

$$\begin{bmatrix} F_x \\ F_y \\ F_z \end{bmatrix} = \begin{bmatrix} m_x & 0 & 0 \\ 0 & m_y & 0 \\ 0 & 0 & m_x \end{bmatrix} \begin{Bmatrix} \dot{u} \\ \dot{v} \\ \dot{w} \end{Bmatrix} = \begin{bmatrix} F_x \\ F_y \\ F_z \end{bmatrix}_D + \begin{bmatrix} F_x \\ F_y \\ F_z \end{bmatrix}_A + \begin{bmatrix} F_x \\ F_y \\ F_z \end{bmatrix}_G + \begin{bmatrix} F_x \\ F_y \\ F_z \end{bmatrix}_T + \begin{bmatrix} F_x \\ F_y \\ F_z \end{bmatrix}_C \quad \textbf{3.4}$$

where,

x_F : translational state

M_a : mass matrix

$[F]_D$: linear dynamics vector

$[F]_A$: aerodynamic forces vector

$[F]_G$: gravitational forces vector

$[F]_T$: thrust forces vector

$[F]_C$: catapult launch forces vector

The rotational equations were given in the following form:

$$T = I_a \dot{x}_M = \sum T$$

$$\begin{bmatrix} L \\ M \\ N \end{bmatrix} = \begin{bmatrix} I_{xx} & 0 & -I_{xz} \\ 0 & I_{yy} & 0 \\ -I_{xz} & 0 & I_{zz} \end{bmatrix} \begin{Bmatrix} \dot{p} \\ \dot{q} \\ \dot{r} \end{Bmatrix} = \begin{bmatrix} L \\ M \\ N \end{bmatrix}_D + \begin{bmatrix} L \\ M \\ N \end{bmatrix}_A + \begin{bmatrix} L \\ M \\ N \end{bmatrix}_G + \begin{bmatrix} L \\ M \\ N \end{bmatrix}_T + \begin{bmatrix} L \\ M \\ N \end{bmatrix}_C \quad \textbf{3.5}$$

where,

x_M : rotational state vector

I_a : inertia matrix for symmetric airframe

$[T]_D$: angular dynamics vector

$[T]_A$: aerodynamic moments vector

$[T]_G$: gravitational moments vector

$[T]_T$: thrust forces vector

$[T]_C$: catapult launch moments vector

Note that, as mentioned earlier in §3.2.2, the mass and inertia matrices were expressed in the origin of the body-axes frame and need to be transformed back from the different CG positions. This has introduced extra terms between the linear and angular dynamic

states as follows:

$$\begin{bmatrix} M_a & D_c^T \\ D_c & J_a \end{bmatrix} \begin{bmatrix} \dot{x}_F \\ \dot{x}_M \end{bmatrix} = \left\{ \begin{bmatrix} F \\ T \end{bmatrix}_D^O + \begin{bmatrix} F \\ T \end{bmatrix}_A + \begin{bmatrix} F \\ T \end{bmatrix}_G^O + \begin{bmatrix} F \\ T \end{bmatrix}_T + \begin{bmatrix} F \\ T \end{bmatrix}_C \right\} \quad \textbf{3.6}$$

where D_c is the recalculated transformation from the CG position, and J_a is the transformed inertia matrix I_a at the origin. The vectors with superscript O have been also transformed from the CG to the origin. The combined state vector $[x_F\ x_M]^T$ is obtained explicitly by multiplying both sides of Equation 3.6 by the inverse of the combined mass-inertia matrix, and then the state variables are obtained by numerical integration of the resulting following equations[62, 63],

$$\begin{bmatrix} \dot{x}_F \\ \dot{x}_M \end{bmatrix} = \begin{bmatrix} M_a & D_c^T \\ D_c & J_a \end{bmatrix}^{-1} \left\{ \begin{bmatrix} F \\ T \end{bmatrix}_D^O + \begin{bmatrix} F \\ T \end{bmatrix}_A + \begin{bmatrix} F \\ T \end{bmatrix}_G^O + \begin{bmatrix} F \\ T \end{bmatrix}_T + \begin{bmatrix} F \\ T \end{bmatrix}_C \right\} \quad \textbf{3.7}$$

3.3 Engine and Propeller Models

The thrust is produced by a wooden two-blade 20x12 inch propeller fitted on the ML-88 twin-cylinder two-stroke engine that produces 4.6kW. Similar to the XRAE1 work[62, 63], the propeller was modelled using a combination of momentum theory, blade element theory, and wind tunnel/real flight data. The propeller thrust is defined as:

$$T_P = K_T \rho\, n_E^2 D_P^4 \quad \textbf{3.8}$$

and engine/propeller rotational dynamics (rev/sec)

$$\dot{n}_E = {P_E - P_P} \Big/ {4\pi^2 I_E n_E} \quad \textbf{3.9}$$

propeller absorbed power

$$P_P = K_P P_E n_E^3 D_P^5 \quad \textbf{3.10}$$

K_T and K_P are the propeller thrust and power coefficients respectively

$$K_T = table(J),\ K_P = table(J) \quad 3.11$$

J is the propeller advance ratio

$$J = V / n_E D_P \quad \textbf{3.12}$$

The ML-88 engine dynamic characteristics were expressed as a set of relations in table forms that combine wind tunnel and real flight tests data. Engine Torque

$$Torque_E = P_E / 2\pi n_E \quad \textbf{3.13}$$

and engine power is given by the table

$$P_E = table(\tau, n_E)\ ,\ \tau : \text{throttle setting (0-1)}$$

and given:

ρ : air density

I_E : engine/propeller moment of inertia

D_P : propeller diameter

Note that the engine rotations n_E is defined in rev/sec in the above equations, but in the actual ACSL simulation it was defined as N_E in rpm where

$$N_E = 60\ n_E$$

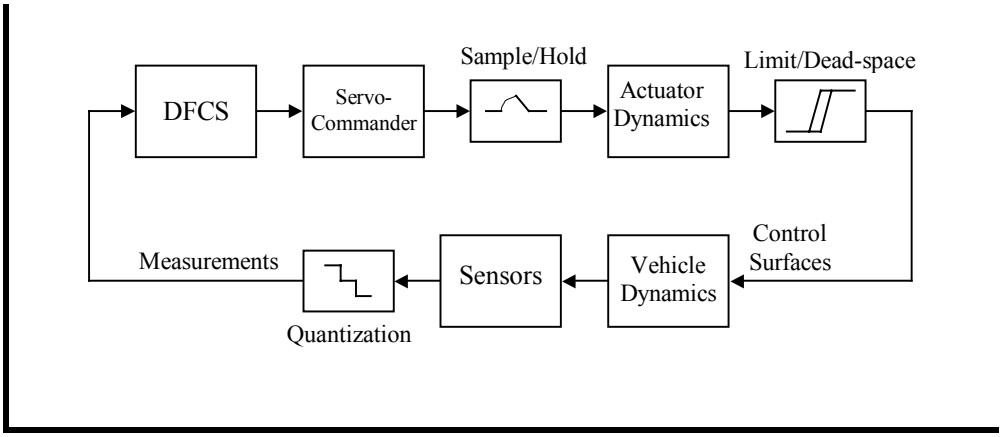

Figure 3.4: DFCS time-delays, limits, dead-space, and quantization discontinuities modelling

3.4 Actuators Dynamic Modelling

The final A3 configuration has five independent control surfaces, each controlled by a separate actuator plus the engine throttle actuator:

- Two ailerons: port and starboard with positive sign downward
- Two elevators: port and starboard with positive sign downward
- One rudder: dorsal fin with positive sign to port

All above control surface actuators were identical, and were modelled as an ideal second order system,

$$\frac{\delta}{\delta_c} = \frac{\omega_a^2}{s^2 + 2\zeta_a s + \omega_a^2} \qquad \textbf{3.14}$$

with the following characteristics:

$$\omega_a = 65 r/s$$
$$\zeta_a = .7$$

Also amplitude, rate, limits and dead-space were modelled as

$$|\delta| \le |\delta_{\max}|$$
$$|\dot{\delta}| \le |\dot{\delta}_{\max}|$$
$$\delta \pm \delta_{ds}$$

Table 3.1: Actuators physical limits used in ACSL

Actuator	Position Limit $\delta_{\max}$ (*rad*)	Dead-space δ_{ds} (*rad*)	Slew Rate Limit $\dot{\delta}_{\max}$ (*rad/s*)
Elevator	±0.262	0.0013	±1.4
Aileron	±0.262	0.0013	±1.55
Rudder	±0.349	0.0013	±1.16
Throttle	10%-100%	-	-

The nonlinearities in Table 3.1 were implemented in the ACSL simulation using the BOUND function for the limits and DEAD for dead-space as shown in Figure 3.4 above.

The engine throttle actuator dynamics were neglected due to the considerably slower airspeed response, which will be verified in the Robust control design in Chapter 5.

3.5 Computation Delays

The digital flight control system(DFCS) on-board processor runs at 62.5 Hz which translates to 16 milliseconds(*ms*) delay. Connected in series with the controller is the servo-motor commander which translates the controller position commands to pulse width modulated(PWM) signals for each actuator with an average delay of 4 *ms*. The effective sample and hold delay of 50% of the combined delays is also taken into account. The total delay adds up to:

$$(16 + 4) \text{ x } 1.5 = 30 \text{ } ms$$

The time delay was modelled in the ACSL simulation program using the DISCRETE function.

3.6 Sensors' Dynamics

The sensors used on-board the air vehicle include:

- Magnetometer: magnetic heading
- Vertical gyro: pitch and yaw angles
- Rate gyro: pitch, yaw, and roll rates
- Airspeed sensor: total airspeed
- Barometric pressure sensor: altitude
- Engine RPM
- GPS signal: height, true heading, 3D position, cross-track error

All of the above sensors were assumed perfect apart from amplitude bounds, quantization, and bias where applicable.

3.7 Continuous Modelling Approximation

The ACSL simulation language has the capability of producing a perturbed linear model about an operating test point from the non-linear simulation for the control design. The discontinuity in the actuators, measurement quantization and bounds, and the delays in the DFCS need to be removed for such a process. Dead-space, limits, and quantization effects were found to have limited influence on the overall system dynamics so they can safely be removed. On the other hand, the DFCS computation time delay has been found to have a significant effect on the vehicle dynamic response and cannot be ignored. The computation time delay, Δ (ms), has a continuous transfer function of $e^{-s\Delta}$ which has a magnitude of 1 and a phase of $-\omega\Delta$. But such function is not rational, and a controller will be difficult to synthesize. Thus it is more appropriate to approximate the delay with a rational function. For this purpose, Padé approximation which matches the first two terms of the Taylor's series expansion of $e^{-s\Delta}$ was used:

$$\frac{D_{out}}{D_{in}} = \frac{\Delta^2 s^2 - 6\Delta s + 12}{\Delta^2 s^2 + 6\Delta s + 12} \qquad \textbf{3.15}$$

This Padé delay approximation was applied to each control output that drives an actuator pair, i.e. elevator starboard/port and aileron starboard/port pairs, while the rudder dorsal fin had one actuator and Padé function. Again, the engine actuator dynamics were neglected but the computation delay was not. So the Padé function was added to the engine throttle control.

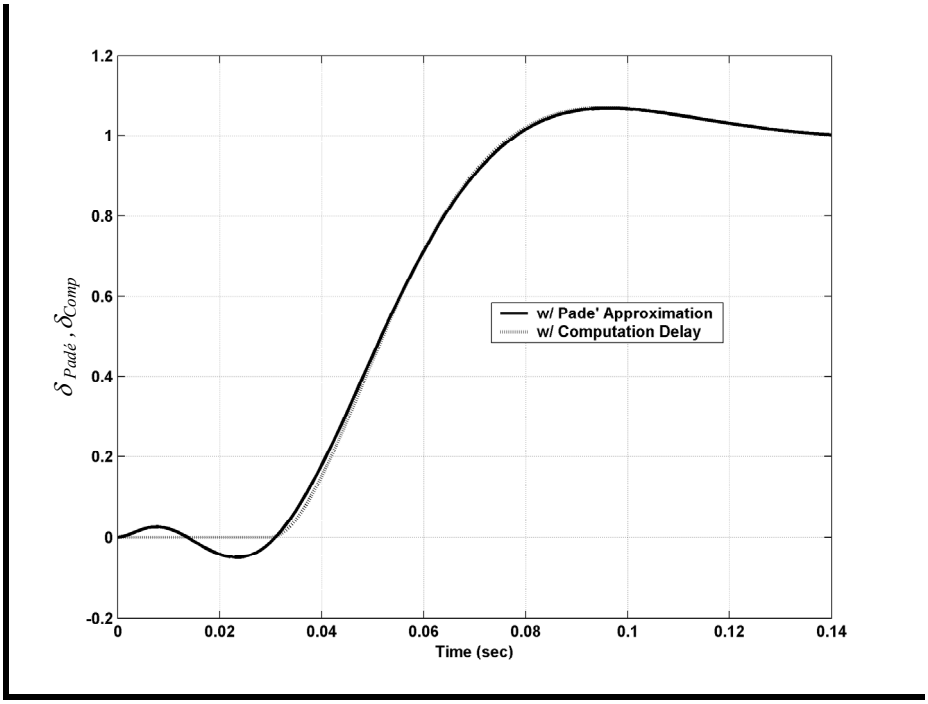

Figure 3.5: Padé approximation of computation delay step response

The effect of the second-order Padé delay of 30 *ms* on actuator step response compared with the real computation delay is shown in Figure 3.5, where the Padé delay shows very good approximation of the actual delay response.

The FCS was also modelled as a continuous system by solving at each time-step of the simulation. The overall continuous simulation system schematic is shown in Figure 3.6.

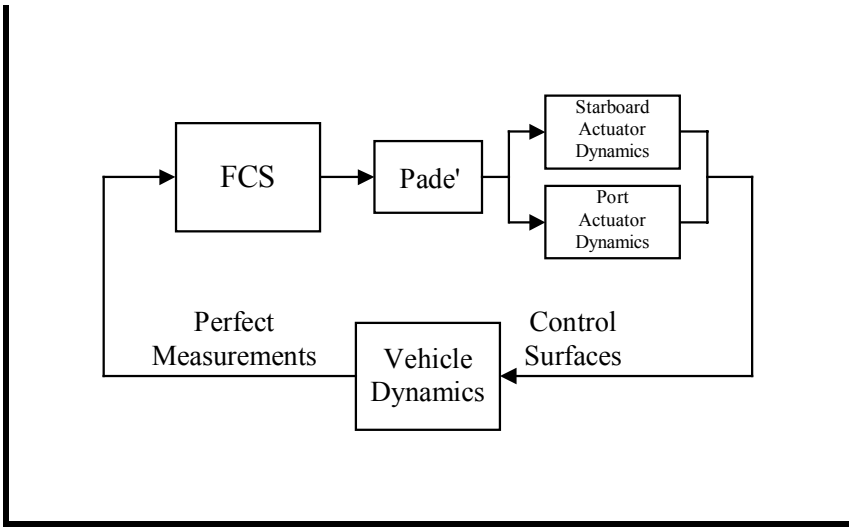

Figure 3.6: Continuous modelling for linear analysis

3.8 A3 Current Classical Flight Control System

The A3 current classical FCS was a development of the previous work on the XRAE1 UAV[42]. Although considerable modifications have been made, the main system structure remains similar to the original design. It has been code-named PMC: Precision Manoeuvre Controller. Detailed description of the PMC can be found in[8].

Briefly, the PMC consists of three main outer loops:

1. Axial: speed / throttle
2. Longitudinal: height / elevator
3. Lateral: loop: heading / aileron

Although the controller is based on linear analysis, the implementation includes several non-linear terms that compensate mainly for the coupling and speed effects as will be shown next.

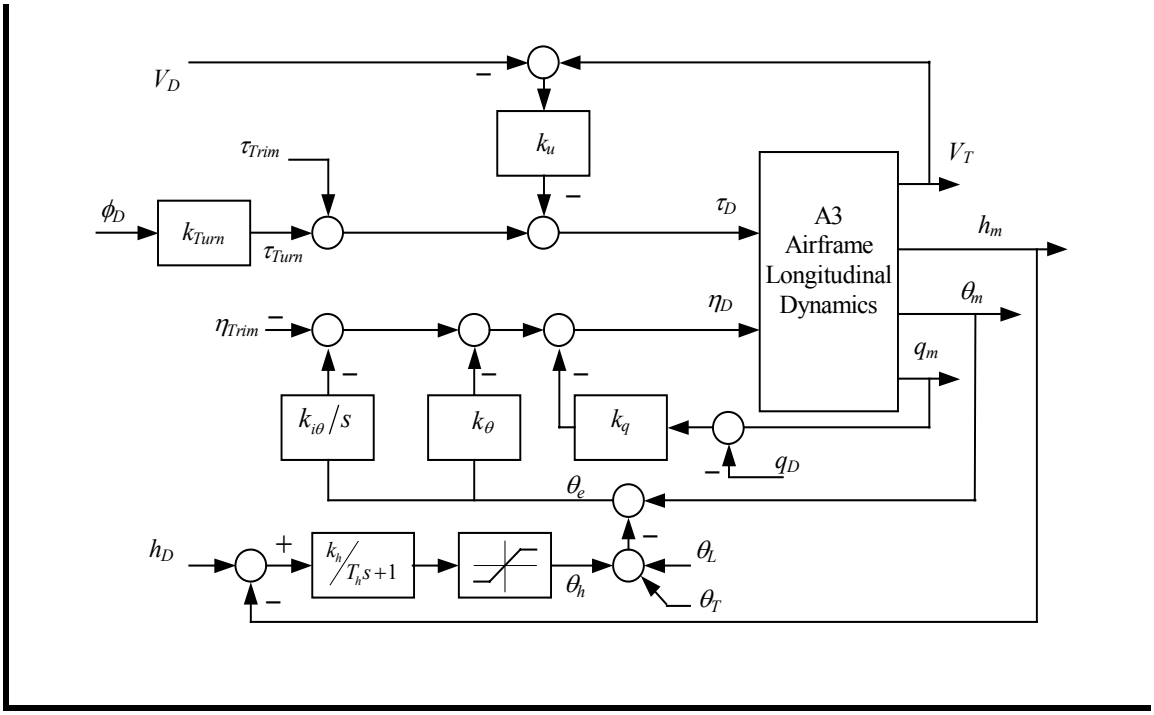

Figure 3.7: A3 Axial and Longitudinal PMC

3.8.1 Axial / Speed Control

The main speed control consists of a simple proportional feedback gain loop as shown in Figure 3.7, but takes into account airspeed and lateral coupling effects:

$$\tau_D = -k_u u_e + \tau_{Trim}(V_T) + \tau_{Turn}(|\phi_D|), \qquad \textbf{3.16}$$

where

τ_D is throttle demand: $\tau_D \geq \tau_{min}$, full throttle 100% = 1

$\tau_{\min}$ is minimum throttle demand to avoid engine cut-off: 0.08

k_u is speed control proportional gain: 0.2

u_e is the measured speed error: $u_e = V_T - V_D$

τ_{Trim} is throttle trim bias, scheduled as a function of total airspeed, V_T

V_T is measured total airspeed with a lower limit, $V_T \geq V_{\min}$= 10 *m/s*, to avoid numerical faults.

V_D is demanded airspeed: 25-55 *m*/*s*,

$\tau_{Turn}(|\phi_D|)$ is lateral decoupling bias, scheduled as a function of the absolute value of the roll angle demand $|\phi_D|$.

3.8.2 Longitudinal Control System

The longitudinal control system, also shown in Figure 3.7, consists of the following main loops:

1. Pitch rate feedback loop for stability:

$$\left.\begin{aligned} \eta_q &= -k_q(V_T)q_e \\ q_e &= q_m - q_D \\ q_D &= \frac{g}{V_T}\sin\phi_m \tan\phi_m \end{aligned}\right| \qquad \textbf{3.17}$$

where q_D is the demanded steady turn pitch rate[68].

2. Pitch angle feedback loop for control with an integrator for zero steady-state error:

$$\left.\begin{aligned} \eta_\theta(s) &= -\left[k_\theta(V_T) + \frac{k_{i\theta}}{s}\right]\theta_e(s) \\ \theta_e &= \theta_m - \theta_D, \quad \theta_D = \theta_h + \theta_L(V_T) + \theta_T(\phi_m) \\ \theta_h(s) &= \frac{k_h(V_T)}{T_h s + 1} h_e(s), \quad h_e = h_D - h_m \end{aligned}\right| \qquad \textbf{3.18}$$

where θ_m is the measured pitch angle. θ_D is the demanded pitch which comprises: height error pitch demand θ_h with a low-pass filter for pitch rate damping, level pitch demand θ_L which is a non-linear function of total airspeed, and turn pitch demand θ_T which is a non-linear function of roll angle ϕ_m. h_m and h_D are the measured and demanded heights respectively.

The final elevator demand comprises:

$$\eta_D = \eta_q + \eta_\theta + \eta_{Trim}(V_T) \qquad \textbf{3.19}$$

where $\eta_{Trim}(V_T)$ is elevator trim bias for level flights scheduled with total airspeed V_T.

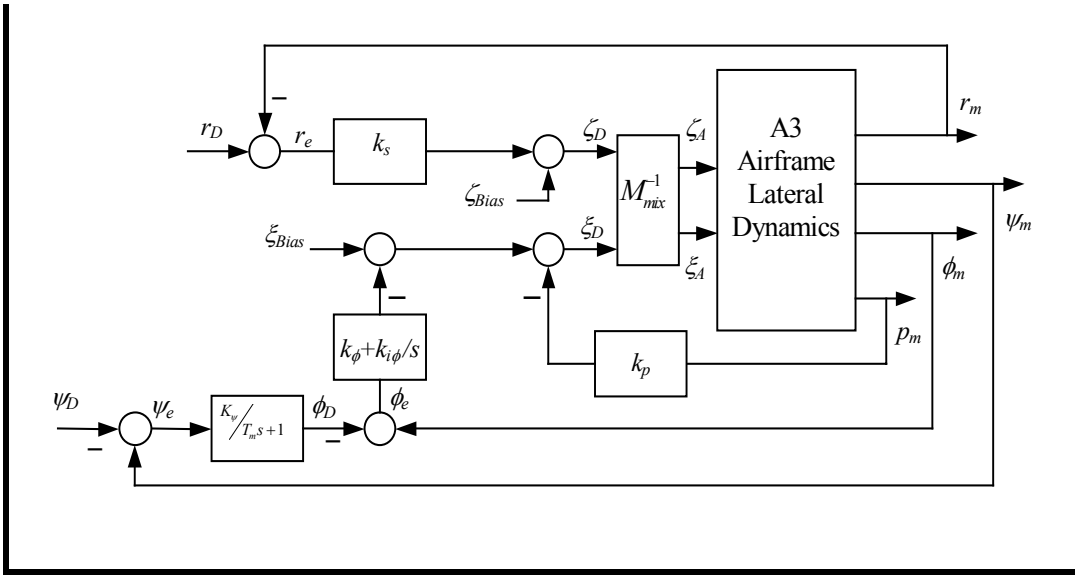

Figure 3.8: A3 Lateral Flight Control System

3.8.3 Lateral Control System

The lateral control system is shown in Figure 3.8. It mainly consists of the following control loops:

1. Roll rate feedback loop for stability:

$$\xi_p = -k_p(V_T)\,p_m \qquad \textbf{3.20}$$

2. Roll angle feedback loop for control with an integrator for zero steady-state error:

$$\left.\begin{aligned}\xi_{\phi}(s) &= -\left[k_{\phi}(V_T) + \frac{k_{i\phi}(V_T)}{s}\right]\phi_e(s) \\ \phi_e &= \left(\phi_m - \phi_D\right)\end{aligned}\right| \qquad \textbf{3.21}$$

3. Outer-loop heading-to-roll demand with low-pass filter for measurement noise:

$$\left.\begin{aligned}\phi_D(s) &= \frac{k_{\psi}}{T_m s + 1}\psi_e(s) \\ \psi_e &= \psi_m - \psi_D\end{aligned}\right| \qquad \textbf{3.22}$$

The total aileron demand becomes

$$\xi_D = \xi_p + \xi_{\phi} \qquad \textbf{3.23}$$

4. Yaw rate feedback loop for coordinated turns:

$$\left.\begin{aligned}\zeta_D &= -k_s(V_T)\left(r_m - r_D\right) \\ r_D &= \frac{g\sin\phi\cos\theta}{V_T}\end{aligned}\right| \qquad \textbf{3.24}$$

where r_D is the demanded yaw for coordinated turns[68]. The input biases, ζ_{Bias} and ξ_{Bias} in Figure 3.8, are used by ACSL simulation to construct the perturbed linear model as will be shown in Chapter 4.

3.8.4 Decoupling and scaling

Due to the clear coupling between aileron and rudder in yaw, it was necessary to decouple the two channels for effective SISO design. Defining the mixing matrix M_{mix} between actual and demanded signals as follows[7, 70]:

$$\begin{Bmatrix} \eta \\ \xi \\ \zeta \end{Bmatrix}_D = M_{mix} \begin{Bmatrix} \eta \\ \xi \\ \zeta \end{Bmatrix}_A \Rightarrow \begin{Bmatrix} \eta \\ \xi \\ \zeta \end{Bmatrix}_A = M_{mix}^{-1} \begin{Bmatrix} \eta \\ \xi \\ \zeta \end{Bmatrix}_D \quad \textbf{3.25}$$

$$M_{mix} = M_c \times M_s = \begin{bmatrix} S_\eta & 0 & 0 \\ 0 & S_\xi & W_\zeta^\xi S_\zeta \\ 0 & W_\xi^\zeta S_\xi & S_\zeta \end{bmatrix} \quad \textbf{3.26}$$

where M_c defined as

$$M_c = \begin{bmatrix} 1 & 0 & 0 \\ 0 & 1 & W_\zeta^\xi \\ 0 & W_\xi^\zeta & 1 \end{bmatrix} = \begin{bmatrix} 1 & 0 & 0 \\ 0 & 1 & l_\zeta / l_\xi \\ 0 & n_\xi / n_\zeta & 1 \end{bmatrix} \quad \textbf{3.27}$$

is the static decoupling matrix for p/ξ and r/ζ loops, where l_ξ and l_ζ are the yaw aerodynamic dimensional derivatives for aileron and rudder; n_ξ and n_ζ are the roll aerodynamic dimensional derivatives for aileron and rudder. M_s is the scaling matrix defined as

$$M_s = \begin{bmatrix} S_\eta & 0 & 0 \\ 0 & S_\xi & 0 \\ 0 & 0 & S_\zeta \end{bmatrix} = \begin{bmatrix} \eta_{D_{FS}} / \eta_{A_{FS}} & 0 & 0 \\ 0 & \xi_{D_{FS}} / \xi_{A_{FS}} & 0 \\ 0 & 0 & \zeta_{D_{FS}} / \zeta_{A_{FS}} \end{bmatrix} \quad \textbf{3.28}$$

where $\eta_{D_{FS}}$ and $\eta_{A_{FS}}$ are the full-scale demanded and actual elevator signals; $\xi_{D_{FS}}$ and $\xi_{A_{FS}}$ are the full-scale demanded and actual aileron signals; $\zeta_{D_{FS}}$ and $\zeta_{A_{FS}}$ are the full-scale demanded and actual rudder signals. Note that M_{mix} is numerically inverted before it is used in the ACSL simulation.

3.9 Navigation System

The A3 navigation system has the capability to navigate the vehicle autonomously in the 3D space, given a route of waypoints and their coordinates and heights, using the

onboard GPS and other sensors[8]. In the ACSL simulation, basic navigation is implemented. This includes heading ψ_D , cross-track error y_X , and height h_D only.

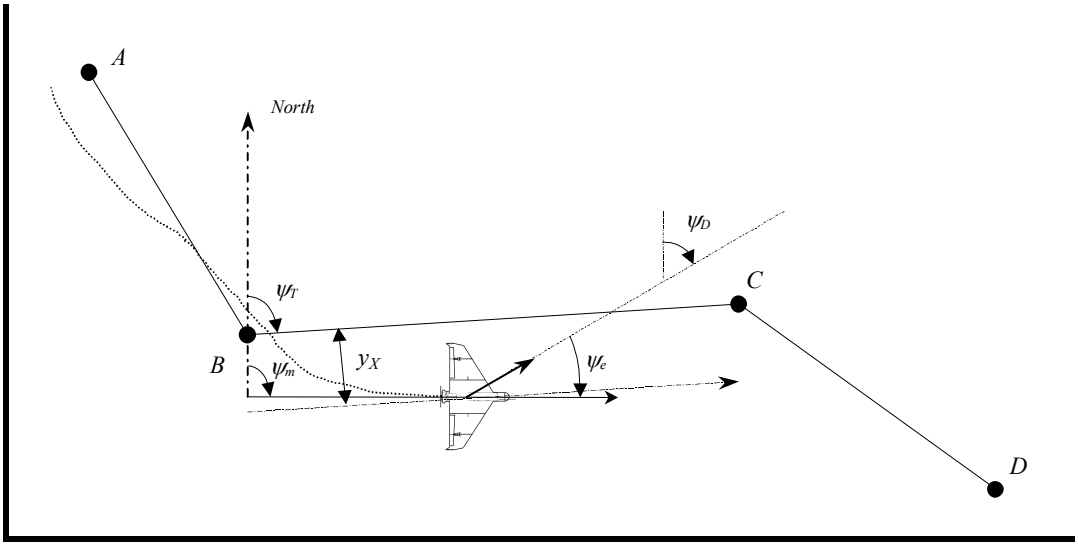

Figure 3.9: A3 Basic 2D Navigation

In 'en route' navigation mode, the vehicle is required to fly along flight path segments between defined waypoints as shown in Figure 3.9. In this mode the navigation law required to null the cross-track y_X while minimizing the heading error is defined as:

$$\phi_D(s) = \frac{k_\psi}{T_m s + 1}\left(\psi_e(s) + k_y y_X(s)\right)$$
$$\psi_e = \psi_m - \psi_T \qquad \textbf{3.29}$$

where ψ_T is the desired track of the current leg between ***B*** and ***C*** waypoints. ψ_m is the vehicle heading which is equal to the current track relative to the ground in still air. Note how heading demand is transformed into roll demand in Equation 3.29 which is handled by the lateral control system. The cross-track error control gain k_y is calculated such that if $y_X = 500m$ then the absolute heading error would not exceed 80 degrees, i.e.

$$k_y = 80 / 500 = 0.16 \text{ deg/m} = 0.0028 \text{ rad/m}$$

Finally, height error is handled by the longitudinal control system, where the demanded height is the level of the current flight path segment.

The actual navigation system on the Observer has the capability to estimate wind speed and direction using a GPS calculated velocity vector, measured airspeed, and vehicle magnetic heading and takes these into account in the above calculations. All these factors were neglected in the ACSL simulation for simplicity.

Chapter 4

Linear Modelling and Analysis

In this chapter, the derivation of the linear control models from the non-linear ACSL simulation will be presented and discussed. Also, a linear representation of the A3 current classical control law will be introduced. Finally, the linear models will be compared with the non-linear simulation for validation and justification.

4.1 Introduction

As described in Chapter **3**, linear models are usually built to serve specific applications. They emphasize the dynamics and behaviour of the particular interest and simplify or, if possible, neglect the effects of the less important subsystem components. These models should be simple, functionally visible, and at the same time have the desired level of response fidelity[67]. There is, however, a trade-off between accuracy and simplicity. A complicated high-order model that is very accurate may result in a huge controller which is not practical for real-time application. On the other hand, a controller designed with an over simplified model may fail in the real system. Due to the fact that the simplified vehicle models will never be a perfect match with the non-linear six degrees-

of-freedom models, not to mention the real-life system, the increasing demands for robust controllers has been the drive for many FCS designs in the last three decades.

4.2 Small Perturbation Linearization

In general, state derivatives and outputs are non-linear functions of states and inputs:

$$\dot{x} = f(x,u)$$
$$y = g(x,u)$$

At steady-state:

$$\dot{x}_o = f(x_o,u_o)$$
$$y_o = g(x_o,u_o)$$

Applying small perturbation from steady-state:

$$x = x_o + \delta x,\ u = u_o + \delta u$$
$$\dot{x} = \dot{x}_o + \delta\dot{x} + \dot{u}_o + \delta\dot{u} = f(x_o + \delta x\ ,\ u_o + \delta u)$$

$$y = y_o + \delta y = g(x_o + \delta x\ ,\ u_o + \delta u)$$

Expanding and taking the first term of the Taylor series:

$$\dot{x} = f(x_o) + \frac{\partial f}{\partial x}\delta x + \frac{\partial f}{\partial u}\delta u + \cdots$$
$$\delta\dot{x} = \frac{\partial f}{\partial x}\delta x + \frac{\partial f}{\partial u}\delta u = A\delta x + B\delta u$$

$$y = g(x_o) + \frac{\partial g}{\partial x}\delta y + \frac{\partial g}{\partial u}\delta y + \cdots$$
$$\delta y = \frac{\partial g}{\partial x}\delta y + \frac{\partial g}{\partial u}\delta y = C\delta x + D\delta u$$

Expanding the linear perturbed system:

$$\begin{Bmatrix} \delta\dot{x}_1 \\ \delta\dot{x}_2 \\ \vdots \\ \delta\dot{x}_n \end{Bmatrix} = \begin{bmatrix} \frac{\partial f_1}{\partial x_1} & \frac{\partial f_1}{\partial x_2} & \cdots & \frac{\partial f_1}{\partial x_n} \\ \frac{\partial f_2}{\partial x_1} & \frac{\partial f_2}{\partial x_2} & \cdots & \frac{\partial f_2}{\partial x_n} \\ \vdots & \vdots & \ddots & \vdots \\ \frac{\partial f_n}{\partial x_1} & \frac{\partial f_n}{\partial x_2} & \cdots & \frac{\partial f_n}{\partial x_n} \end{bmatrix} \begin{Bmatrix} \delta x_1 \\ \delta x_2 \\ \vdots \\ \delta x_n \end{Bmatrix} + \begin{bmatrix} \frac{\partial f_1}{\partial u_1} & \frac{\partial f_1}{\partial u_2} & \cdots & \frac{\partial f_1}{\partial u_n} \\ \frac{\partial f_2}{\partial u_1} & \frac{\partial f_2}{\partial u_2} & \cdots & \frac{\partial f_2}{\partial u_n} \\ \vdots & \vdots & \ddots & \vdots \\ \frac{\partial f_n}{\partial u_1} & \frac{\partial f_n}{\partial u_2} & \cdots & \frac{\partial f_n}{\partial u_n} \end{bmatrix} \begin{Bmatrix} \delta u_1 \\ \delta u_2 \\ \vdots \\ \delta u_n \end{Bmatrix} \quad \textbf{4.1}$$

$$\begin{Bmatrix} \delta y_1 \\ \delta y_2 \\ \vdots \\ \delta y_n \end{Bmatrix} = \begin{bmatrix} \frac{\partial g_1}{\partial x_1} & \frac{\partial g_1}{\partial x_2} & \cdots & \frac{\partial g_1}{\partial x_n} \\ \frac{\partial g_2}{\partial x_1} & \frac{\partial g_2}{\partial x_2} & \cdots & \frac{\partial g_2}{\partial x_n} \\ \vdots & \vdots & \ddots & \vdots \\ \frac{\partial g_n}{\partial x_1} & \frac{\partial g_n}{\partial x_2} & \cdots & \frac{\partial g_n}{\partial x_n} \end{bmatrix} \begin{Bmatrix} \delta x_1 \\ \delta x_2 \\ \vdots \\ \delta x_n \end{Bmatrix} + \begin{bmatrix} \frac{\partial g_1}{\partial u_1} & \frac{\partial g_1}{\partial u_2} & \cdots & \frac{\partial g_1}{\partial u_n} \\ \frac{\partial g_2}{\partial u_1} & \frac{\partial g_2}{\partial u_2} & \cdots & \frac{\partial g_2}{\partial u_n} \\ \vdots & \vdots & \ddots & \vdots \\ \frac{\partial g_n}{\partial u_1} & \frac{\partial g_n}{\partial u_2} & \cdots & \frac{\partial g_n}{\partial u_n} \end{bmatrix} \begin{Bmatrix} \delta u_1 \\ \delta u_2 \\ \vdots \\ \delta u_n \end{Bmatrix} \quad \textbf{4.2}$$

Let $x = \delta x$, $u = \delta u$, and $y = \delta y$:

$$\begin{aligned} \dot{x} &= Ax + Bu \\ y &= Cx + Du \end{aligned} \quad \textbf{4.3}$$

which represent the standard state-space form of the linear system. The transfer function matrix of the above realization can written as:

$$G(s) = D + C(sI - A)^{-1}B \overset{s}{=} \left[\begin{array}{c|c} A & B \\ \hline C & D \end{array}\right] \quad \textbf{4.4}$$

ACSL simulation is capable of producing the above state-space matrices $\{A, B, C, D\}$ numerically. It can also export them to MATLAB for linear analysis and controller

design as will be shown later.

4.3 Airframe Dynamics

The airframe is usually divided into two subsystems: axial/longitudinal and lateral/directional. This division is based on the decoupling assumption between the two linear perturbed subsystems about their trim-equilibrium.

4.3.1 Axial/Longitudinal System

The axial system: $\{u, N_E\}$ which represent the perturbed states of axial speed and engine rpm is usually combined with the longitudinal system: $\{u, w, q, \theta, h\}$, which represent the perturbed states of axial speed, heave motion, pitch rate, pitch angle, and flight path height above ground respectively. The combined axial/longitudinal system can be represented by the following linear dynamic equations[68]:

$$\begin{Bmatrix} \dot{u} \\ \dot{w} \\ \dot{q} \\ \dot{\theta} \\ \dot{h} \\ \dot{N}_E \end{Bmatrix} = \begin{bmatrix} x_u & x_w & x_q - W_0 & -g\cos\Theta_0 & 0 & x_N \\ z_u & z_w & z_q + U_0 & -g\sin\Theta_0 & 0 & 0 \\ m_u & m_w & m_q & 0 & 0 & 0 \\ 0 & 0 & 1 & 0 & 0 & 0 \\ \sin\Theta_0 & -\cos\Theta_0 & 0 & U_0\cos\Theta_0 & 0 & 0 \\ e_u & e_w & 0 & 0 & 0 & e_N \end{bmatrix} \begin{Bmatrix} u \\ w \\ q \\ \theta \\ h \\ N_E \end{Bmatrix} + \begin{bmatrix} 0 & x_\eta & x_\eta \\ 0 & z_\eta & z_\eta \\ 0 & m_\eta & m_\eta \\ 0 & 0 & 0 \\ 0 & 0 & 0 \\ e_\tau & 0 & 0 \end{bmatrix} \begin{Bmatrix} \tau_A \\ \eta_{A_{SB}} \\ \eta_{A_P} \end{Bmatrix} \quad \textbf{4.5}$$

The perturbed linear model states are defined as:

$$u = \mathbf{u} - U_0, \quad w = \mathbf{w} - W_0, \quad q = \mathbf{q}, \quad \theta = \boldsymbol{\theta} - \Theta_0, \quad h = \mathbf{h} - H_o, \quad N_E = \mathbf{N}_E - \mathbf{N}_{E0} \quad \textbf{4.6}$$

where $\{U_0, W_0, \Theta_0, H_0, N_{E0}\}$ are the body-axis nominal equilibrium values of airspeed, vertical heave, pitch angle, air vehicle height, and engine rpm respectively. The bold variables $\{\mathbf{u}, \mathbf{w}, \mathbf{q}, \boldsymbol{\theta}, \mathbf{h}, \mathbf{N}_E\}$ are the unperturbed true respective states. $\{\tau_A, \eta_{A_{SB}}, \eta_{A_P}\}$ are the control positions of throttle, starboard elevator, and port elevator respectively.

If the starboard/port elevator pair are not to be controlled individually, they can be

represented as a single control surface with doubled aerodynamic force and one actuator. This will help reduce the number of equations when modelling the actuator dynamics later on. The longitudinal control matrix can be modified as follows:

$$\begin{Bmatrix} \dot{u} \\ \dot{w} \\ \dot{q} \\ \dot{\theta} \\ \dot{h} \\ \dot{N}_E \end{Bmatrix} = \begin{bmatrix} x_u & x_w & x_q - W_0 & -g\cos\Theta_0 & 0 & x_N \\ z_u & z_w & z_q + U_0 & -g\sin\Theta_0 & 0 & 0 \\ m_u & m_w & m_q & 0 & 0 & 0 \\ 0 & 0 & 1 & 0 & 0 & 0 \\ \sin\Theta_0 & -\cos\Theta_0 & 0 & U_0\cos\Theta_0 & 0 & 0 \\ e_u & e_w & 0 & 0 & 0 & e_N \end{bmatrix} \begin{Bmatrix} u \\ w \\ q \\ \theta \\ h \\ N_E \end{Bmatrix} + \begin{bmatrix} 0 & 2x_\eta \\ 0 & 2z_\eta \\ 0 & 2m_\eta \\ 0 & 0 \\ 0 & 0 \\ e_\tau & 0 \end{bmatrix} \begin{Bmatrix} \tau_A \\ \eta_A \end{Bmatrix} \quad \textbf{4.7}$$

The output measurement equations can be represented by:

$$\begin{Bmatrix} u_e \\ q_e \\ \theta_e \\ h_e \end{Bmatrix} = \begin{bmatrix} \cos\Theta_0 & \sin\Theta_0 & [-\sin\Theta_0] & 0 & 0 & 0 \\ 0 & 0 & 1 & 0 & 0 & 0 \\ 0 & 0 & 0 & 1 & 0 & 0 \\ 0 & 0 & 0 & 0 & 1+\sin\Theta_0 & 0 \end{bmatrix} \begin{Bmatrix} u \\ w \\ q \\ \theta \\ h \\ N_E \end{Bmatrix} \quad \textbf{4.8}$$

The transfer function of the above realization can written as:

$$G_{Rz}(s) = \left[\begin{array}{c|c} A_{Rz} & B_{Rz} \\ \hline C_{Rz} & 0 \end{array}\right]$$

where the subscript '*Rz* ' stands for the simplified or *R*educed-order model, i.e. without the actuator and Padé delay, for the longitudinal *z*-plane dynamics.

4.3.2 Lateral/Directional System

The lateral/directional system: $\{v, p, r, \phi, \psi, y_x\}$ represent the perturbed states of lateral sideslip, roll rate, yaw rate, roll angle, yaw/heading, and the flight path cross track error respectively. The linear dynamic system is represented by the following equations:

$$\begin{Bmatrix} \dot{v} \\ \dot{p} \\ \dot{r} \\ \dot{\phi} \\ \dot{\psi} \\ \dot{y}_x \end{Bmatrix} = \begin{bmatrix} y_v & y_p + W_0 & y_r - U_0 & g\cos\Theta_0 & 0 & 0 \\ l_v & l_p & l_r & 0 & 0 & 0 \\ n_v & n_p & n_r & 0 & 0 & 0 \\ 0 & \sec\Theta_0 & \tan\Theta_0 & 0 & 0 & 0 \\ 0 & 0 & \sec\Theta_0 & 0 & 0 & 0 \\ 1 & 0 & 0 & -U_0\sin\Theta_0 & U_0\cos\Theta_0 & 0 \end{bmatrix} \begin{Bmatrix} v \\ p \\ r \\ \phi \\ \psi \\ y_x \end{Bmatrix} + \begin{bmatrix} y_\xi & -y_\xi & y_\zeta \\ l_\xi & -l_\xi & l_\zeta \\ n_\xi & -n_\xi & n_\zeta \\ 0 & 0 & 0 \\ 0 & 0 & 0 \\ 0 & 0 & 0 \end{bmatrix} \begin{Bmatrix} \xi_{A_{SB}} \\ \xi_{A_P} \\ \zeta_A \end{Bmatrix} \quad \textbf{4.9}$$

The perturbed linear model states are defined as:

$$p = \mathbf{p}, \quad r = \mathbf{r}, \quad \phi = \boldsymbol{\phi} - \Phi_0, \quad \psi = \boldsymbol{\psi} - \Psi_T - \Psi_0, \quad y_X = \mathbf{y}_X \qquad \textbf{4.10}$$

where the bold variables $\{\mathbf{v}, \mathbf{p}, \mathbf{r}, \boldsymbol{\phi}, \boldsymbol{\psi}, \mathbf{y}_x\}$ are the unperturbed true respective states. Ψ_T is the current fight path segment track and it equals zero for North heading. $\{\xi_{A_{SB}}, \xi_{A_P}, \zeta_A\}$ are the controls of starboard/port ailerons, and dorsal rudder.

If the starboard/port aileron pair are not to be controlled individually, they can also be represented as a single control surface with doubled aerodynamic force and one actuator. This will also reduce the number of equations when modelling the actuator dynamics. The lateral/directional control matrix can be modified as follows:

$$\begin{Bmatrix} \dot{v} \\ \dot{p} \\ \dot{r} \\ \dot{\phi} \\ \dot{\psi} \\ \dot{y}_x \end{Bmatrix} = \begin{bmatrix} y_v & y_p + W_0 & y_r - U_0 & g\cos\Theta_0 & 0 & 0 \\ l_v & l_p & l_r & 0 & 0 & 0 \\ n_v & n_p & n_r & 0 & 0 & 0 \\ 0 & \sec\Theta_0 & \tan\Theta_0 & 0 & 0 & 0 \\ 0 & 0 & \sec\Theta_0 & 0 & 0 & 0 \\ 1 & 0 & 0 & -U_0\sin\Theta_0 & U_0\cos\Theta_0 & 0 \end{bmatrix} \begin{Bmatrix} v \\ p \\ r \\ \phi \\ \psi \\ y_x \end{Bmatrix} + \begin{bmatrix} 2y_\xi & y_\zeta \\ 2l_\xi & l_\zeta \\ 2n_\xi & n_\zeta \\ 0 & 0 \\ 0 & 0 \\ 0 & 0 \end{bmatrix} \begin{Bmatrix} \xi_A \\ \zeta_A \end{Bmatrix} \quad \textbf{4.11}$$

The output measurement equations is given by:

$$\begin{Bmatrix} p_e \\ r_e \\ \phi_e \\ \psi_e \\ y_x \end{Bmatrix} = \begin{bmatrix} 0 & 1 & 0 & 0 & 0 & 0 \\ 0 & 0 & 1 & 0 & 0 & 0 \\ 0 & 0 & 0 & 1 & 0 & 0 \\ 0 & 0 & 0 & 0 & 1 & 0 \\ 0 & 0 & 0 & 0 & 0 & 1 \end{bmatrix} \begin{Bmatrix} v \\ p \\ r \\ \phi \\ \psi \\ y_x \end{Bmatrix} \quad \textbf{4.12}$$

The transfer function of the above realization can written as:

$$G_{Ry}(s) = \left[\begin{array}{c|c} A_{Ry} & B_{Ry} \\ \hline C_{Ry} & 0 \end{array}\right]$$

where the subscripts 'y ' stand for the lateral/directional **y**-plane dynamics.

4.4 Actuator Dynamics and Computation Delay

The actuator dynamics were represented by linear second order systems in §3.4. A total of five actuators: two for ailerons, two for elevators, and one for rudder dorsal fin are modelled by ten first order differential equations. These equations are linear and do not need to be modified in anyway. The computation delay, as discussed in §3.5, was modelled by a Padé approximation of each output channel of the control system., i.e. for each actuator pair. These equations were also linear and can be implemented directly into the linear dynamic system of the air vehicle. Note that the linear model controls are perturbed about their nominal trim values as follows:

$$\begin{aligned} \tau_A &= \boldsymbol{\tau} - \tau_{Trim}, \tau_{Trim} > 0 \\ \eta_A &= \boldsymbol{\eta} - \eta_{Trim}, \eta_{Trim} \neq 0 \\ \xi_A &= \boldsymbol{\xi}, \xi_{Trim} \approx 0 \\ \zeta_A &= \boldsymbol{\zeta}, \zeta_{Trim} \approx 0 \end{aligned} \quad \textbf{4.13}$$

where $\boldsymbol{\tau}, \boldsymbol{\eta}, \boldsymbol{\xi}, \boldsymbol{\zeta}$ are the actual respective controls. For the elevator, including the actuator dynamics combined with the Padé delay we have:

$$\begin{Bmatrix} \eta_{A_{SB}} \\ \eta_{A_P} \end{Bmatrix} = \begin{bmatrix} \left.\dfrac{\omega_a^2}{s^2+2\zeta_a s+\omega_a^2}\right|_{SB} \\ \left.\dfrac{\omega_a^2}{s^2+2\zeta_a s+\omega_a^2}\right|_{P} \end{bmatrix} \frac{s^2-2\zeta_\Delta\omega_\Delta s+\omega_\Delta^2}{s^2+2\zeta_\Delta\omega_\Delta s+\omega_\Delta^2}\eta_D \qquad \textbf{4.14}$$

where η_D is the demanded elevator position. In state-space:

$$\begin{Bmatrix} \dot{\eta}_{A_{SB}} \\ \ddot{\eta}_{A_{SB}} \\ \dot{\eta}_{A_P} \\ \ddot{\eta}_{A_P} \\ \dot{D}_\eta \\ \ddot{D}_\eta \end{Bmatrix} = \begin{bmatrix} 0 & 1 & 0 & 0 & 0 & 0 \\ -\omega_a^2 & -2\zeta_a\omega_a & 0 & 0 & 0 & \omega_a^2 \\ 0 & 0 & 0 & 1 & 0 & 0 \\ 0 & 0 & -\omega_a^2 & -2\zeta_a\omega_a & 0 & \omega_a^2 \\ 0 & 0 & 0 & 0 & 0 & 1 \\ 0 & 0 & 0 & 0 & -\omega_\Delta^2 & -2\zeta_\Delta\omega_\Delta \end{bmatrix} \begin{Bmatrix} \eta_{A_{SB}} \\ \dot{\eta}_{A_{SB}} \\ \eta_{A_P} \\ \dot{\eta}_{A_P} \\ D_\eta \\ \dot{D}_\eta \end{Bmatrix} + \begin{bmatrix} 0 \\ \omega_a^2 \\ 0 \\ \omega_a^2 \\ 0 \\ -4\zeta_\Delta\omega_\Delta \end{bmatrix} \{\ \eta_D\} \qquad \textbf{4.15}$$

Or, for a single pair, it can be represented as a single actuator as:

$$\begin{Bmatrix} \dot{\eta}_A \\ \ddot{\eta}_A \\ \dot{D}_\eta \\ \ddot{D}_\eta \end{Bmatrix} = \begin{bmatrix} 0 & 1 & 0 & 0 \\ -\omega_a^2 & -2\zeta_a\omega_a & 0 & \omega_a^2 \\ 0 & 0 & 0 & 1 \\ 0 & 0 & -\omega_\Delta^2 & -2\zeta_\Delta\omega_\Delta \end{bmatrix} \begin{Bmatrix} \eta_A \\ \dot{\eta}_A \\ D_\eta \\ \dot{D}_\eta \end{Bmatrix} + \begin{bmatrix} 0 \\ \omega_a^2 \\ 0 \\ -4\zeta_\Delta\omega_\Delta \end{bmatrix} \{\ \eta_D\} \qquad \textbf{4.16}$$

For the throttle, only Padé delay is modelled as:

$$\tau_A = \frac{s^2-2\zeta_\Delta\omega_\Delta s+\omega_\Delta^2}{s^2+2\zeta_\Delta\omega_\Delta s+\omega_\Delta^2}\tau_D \qquad \textbf{4.17}$$

where τ_D is the demanded throttle position. In state-space:

$$\begin{Bmatrix} \dot{D}_\tau \\ \ddot{D}_\tau \end{Bmatrix} = \begin{bmatrix} 0 & 1 \\ -\omega_\Delta^2 & -2\zeta_\Delta\omega_\Delta \end{bmatrix} \begin{Bmatrix} D_\tau \\ \dot{D}_\tau \end{Bmatrix} + \begin{bmatrix} 0 \\ -4\zeta_\Delta\omega_\Delta \end{bmatrix} \{\ \tau_D\} \qquad \textbf{4.18}$$
$$\tau_A = \dot{D}_\tau$$

where

$$\zeta_\Delta = \frac{3}{\sqrt{12}} = .867 \quad \omega_\Delta = \sqrt{12}/\Delta \; rad/s$$
$$\zeta_a = .65 \qquad\qquad \omega_a = 41 \; rad/s$$

For the ailerons, the actuator dynamics with the Padé delay are represented as:

$$\begin{Bmatrix} \xi_{A_{SB}} \\ \xi_{A_P} \end{Bmatrix} = \begin{bmatrix} \left.\dfrac{\omega_a^2}{s^2 + 2\zeta_a s + \omega_a^2}\right|_{SB} \\ -\left.\dfrac{\omega_a^2}{s^2 + 2\zeta_a s + \omega_a^2}\right|_{P} \end{bmatrix} \frac{s^2 - 2\zeta_\Delta \omega_\Delta s + \omega_\Delta^2}{s^2 + 2\zeta_\Delta \omega_\Delta s + \omega_\Delta^2} \xi_D \qquad \textbf{4.19}$$

where ξ_D is the demanded aileron position. In state-space:

$$\begin{Bmatrix} \dot{\xi}_{A_{SB}} \\ \ddot{\xi}_{A_{SB}} \\ \dot{\xi}_{A_P} \\ \ddot{\xi}_{A_P} \\ \dot{D}_\xi \\ \ddot{D}_\xi \end{Bmatrix} = \begin{bmatrix} 0 & 1 & 0 & 0 & 0 & 0 \\ -\omega_a^2 & -2\zeta_a\omega_a & 0 & 0 & 0 & \omega_a^2 \\ 0 & 0 & 0 & 1 & 0 & 0 \\ 0 & 0 & -\omega_a^2 & -2\zeta_a\omega_a & 0 & \omega_a^2 \\ 0 & 0 & 0 & 0 & 0 & 1 \\ 0 & 0 & 0 & 0 & -\omega_\Delta^2 & -2\zeta_\Delta\omega_\Delta \end{bmatrix} \begin{Bmatrix} \xi_{A_{SB}} \\ \dot{\xi}_{A_{SB}} \\ \xi_{A_P} \\ \dot{\xi}_{A_P} \\ D_\xi \\ \dot{D}_\xi \end{Bmatrix} + \begin{bmatrix} 0 \\ \omega_a^2 \\ 0 \\ -\omega_a^2 \\ 0 \\ -4\zeta_\Delta\omega_\Delta \end{bmatrix} \{\xi_D\} \qquad \textbf{4.20}$$

Or, for a single pair, it can be represented with a single actuator as:

$$\begin{Bmatrix} \dot{\xi}_A \\ \ddot{\xi}_A \\ \dot{D}_\xi \\ \ddot{D}_\xi \end{Bmatrix} = \begin{bmatrix} 0 & 1 & 0 & 0 \\ -\omega_a^2 & -2\zeta_a\omega_a & 0 & \omega_a^2 \\ 0 & 0 & 0 & 1 \\ 0 & 0 & -\omega_\Delta^2 & -2\zeta_\Delta\omega_\Delta \end{bmatrix} \begin{Bmatrix} \xi_A \\ \dot{\xi}_A \\ D_\xi \\ \dot{D}_\xi \end{Bmatrix} + \begin{bmatrix} 0 \\ \omega_a^2 \\ 0 \\ -4\zeta_\Delta\omega_\Delta \end{bmatrix} \{\xi_D\} \qquad \textbf{4.21}$$

For the rudder, the actuator dynamics with the Padé delay are given by:

$$\left\{\zeta_{A_{SB}}\right\} = \left(\frac{\omega_a^2}{s^2 + 2\zeta_a s + \omega_a^2}\right)\left(\frac{s^2 - 2\zeta_\Delta \omega_\Delta s + \omega_\Delta^2}{s^2 + 2\zeta_\Delta \omega_\Delta s + \omega_\Delta^2}\right)\zeta_D \qquad \textbf{4.22}$$

where ζ_D is the demanded rudder position. In state-space:

$$\begin{Bmatrix} \dot{\zeta}_A \\ \ddot{\zeta}_A \\ \dot{D}_\zeta \\ \ddot{D}_\zeta \end{Bmatrix} = \begin{bmatrix} 0 & 1 & 0 & 0 \\ -\omega_a^2 & -2\zeta_a\omega_a & 0 & \omega_a^2 \\ 0 & 0 & 0 & 1 \\ 0 & 0 & -\omega_\Delta^2 & -2\zeta_\Delta\omega_\Delta \end{bmatrix} \begin{Bmatrix} \zeta_A \\ \dot{\zeta}_A \\ D_\zeta \\ \dot{D}_\zeta \end{Bmatrix} + \begin{bmatrix} 0 \\ \omega_a^2 \\ 0 \\ -4\zeta_\Delta\omega_\Delta \end{bmatrix} \{\zeta_D\} \qquad \textbf{4.23}$$

4.5 Numerical Linearization

Although the linear models of the airframe dynamics presented in §4.3 are considered good analytical approximations, the capability of the ACSL simulation language to numerically calculate the perturbed linear system matrices {*A*, *B*, *C*, *D*} from the full non-linear coupled system produces more accurate linear systems with significantly less effort. This is especially true when there is considerable coupling in the system, such as in the A3 air vehicle. The following procedure was followed to obtain the linear system matrices from the ACSL non-linear simulation:

1- Remove all discrete, limit, and dead-space functions.

2- Use the Padé continuous approximation of the computation delay.

3- Add trim bias to control variables to enable analysis without control.

4- Run simulation with full control until steady-state is reached at nominal speed.

5- Disconnect all controller commands and disable mixing.

6- Define state, control, and output variables for the linear system.

7- Initialise control bias with last run trim values especially for throttle and elevator.

8- Use 'ANALYZE' command to calculate the perturbed linear system.

9- Use 'JACOBIAN' to export linear system matrices {A, B, C, D} to MATLAB.

10- Repeat with different flight conditions.

Also, for linear modelling, it is more convenient to work with Euler angles in the DCM instead of the quaternion. This has the advantages of reducing the coupling and non-linear effects and gives clearer and more logical linear model representation. Moreover, linear models are built around small angle approximation assumption which reduces the quaternion necessity. The Euler angles can then be updated from the angular velocities using the standard dynamic equations:

$$\begin{aligned}\dot{\phi} &= P + Q\tan\theta\sin\phi + R\tan\theta\cos\phi \\ \dot{\theta} &= Q\cos\phi - R\sin\phi \\ \dot{\psi} &= Q\left(\frac{\sin\phi}{\cos\theta}\right) + R\left(\frac{\cos\phi}{\cos\theta}\right)\end{aligned} \qquad \textbf{4.24}$$

4.5.1 Axial/Longitudinal Model

Following the above procedures, the decoupled axial/longitudinal linear dynamic model generated by ACSL was:

$$\begin{Bmatrix} \dot{u} \\ \dot{w} \\ \dot{q} \\ \dot{\theta} \\ \dot{h} \\ \dot{N}_E \end{Bmatrix} = \begin{bmatrix} -0.146 & -0.016 & 0.557 & -9.809 & 0 & 0.001 \\ -0.63 & -4.487 & 34.57 & 0.161 & 0 & 0 \\ 0.001 & 0.039 & -0.894 & 0 & 0 & 0 \\ 0 & 0 & 1 & 0 & 0 & 0 \\ -0.016 & -1 & 0 & 35.2 & 0 & 0 \\ 665.7 & -6.89 & 0 & 0 & 0 & -8.57 \end{bmatrix} \begin{Bmatrix} u \\ w \\ q \\ \theta \\ h \\ N_E \end{Bmatrix} + \begin{bmatrix} 0 & -1.368 \\ 0 & -19.96 \\ 0 & -15.96 \\ 0 & 0 \\ 0 & 0 \\ 45910 & 0 \end{bmatrix} \begin{Bmatrix} \tau_A \\ \eta_A \end{Bmatrix} \qquad \textbf{4.25}$$

with the output measurement equation:

$$\begin{Bmatrix} u_e \\ q_e \\ \theta_e \\ h_e \end{Bmatrix} = \begin{bmatrix} 1 & -0.014 & 0.019 & 0 & 0 & 0 \\ 0 & 0 & 1.002 & 0 & 0 & 0 \\ 0 & 0 & 0 & 0.997 & 0 & 0 \\ 0 & 0 & 0 & 0 & 0.984 & 0 \end{bmatrix} \begin{Bmatrix} u \\ w \\ q \\ \theta \\ h \\ N_E \end{Bmatrix} \quad \textbf{4.26}$$

The linear model nominal trim values are:

$$\begin{array}{lll} U_0 = 35.2 \text{ m/s} & \Theta_0 = -.016 \text{ rad} & \tau_{Trim} = 15.9\% \\ W_0 = -.567 \text{ m/s} & N_{E0} = 5833 \text{ rpm} & \eta_{Trim} = -.049 \text{ rad} \end{array}$$

Note how the air vehicle is flying with a negative nominal pitch angle $\Theta_0 < 0$. Also, air vehicle nominal height H_0 can take any value since it does not affect the dynamics of the model.

The transfer function of the above model is given by:

$$G_{35Rz}(s) = \left[\begin{array}{c|c} A_{35Rz} & B_{35Rz} \\ \hline C_{35Rz} & 0 \end{array}\right] \quad \textbf{4.27}$$

where the subscript '35' stands for the nominal airspeed of 35 *m/s* .

The elevator actuator dynamics and Padé approximation of computation delays for the throttle and elevator channels were modelled as linear systems and have the following dynamic equations

$$\begin{Bmatrix} \dot{D}_\tau \\ \ddot{D}_\tau \\ \dot{\eta}_A \\ \ddot{\eta}_A \\ \dot{D}_\eta \\ \ddot{D}_\eta \end{Bmatrix} = \begin{bmatrix} 0 & 1 & 0 & 0 & 0 & 0 \\ -13333 & -200 & 0 & 0 & 0 & 0 \\ 0 & 0 & 0 & 1 & 0 & 0 \\ 0 & 0 & -3982 & -82.03 & 0 & 3982 \\ 0 & 0 & 0 & 0 & 0 & 1 \\ 0 & 0 & 0 & 0 & -13333 & -200 \end{bmatrix} \begin{Bmatrix} D_\tau \\ \dot{D}_\tau \\ \eta_A \\ \dot{\eta}_A \\ D_\eta \\ \dot{D}_\eta \end{Bmatrix} + \begin{bmatrix} 0 & 0 \\ -400 & 0 \\ 0 & 0 \\ 0 & 3982 \\ 0 & 0 \\ 0 & -400 \end{bmatrix} \begin{Bmatrix} \tau_D \\ \eta_D \end{Bmatrix} \quad \textbf{4.28}$$

The transfer function of the longitudinal model with the actuator and Padé delay is given by:

$$G_{35Az}(s) = \left[\begin{array}{c|c} A_{35Az} & B_{35Az} \\ \hline C_{35Az} & 0 \end{array}\right] \quad \textbf{4.29}$$

where the subscript '*A*' indicates the addition of the actuator and Padé delay in the dynamic model.

4.5.2 Lateral/Directional Model

The decoupled lateral/directional linear dynamic model generated by ACSL was:

$$\begin{Bmatrix} \dot{v} \\ \dot{p} \\ \dot{r} \\ \dot{\phi} \\ \dot{\psi} \\ \dot{y}_x \end{Bmatrix} = \begin{bmatrix} -0.359 & -0.502 & -34.9 & 9.809 & 0 & 0 \\ -6.722 & -7.044 & 1.432 & 0 & 0 & 0 \\ 0.269 & 0.051 & -0.159 & 0 & 0 & 0 \\ 0 & 1 & -0.016 & 0 & 0 & 0 \\ 0 & 0 & 1 & 0 & 0 & 0 \\ 1 & 0 & 0 & 0.567 & 35.2 & 0 \end{bmatrix} \begin{Bmatrix} v \\ p \\ r \\ \phi \\ \psi \\ y_x \end{Bmatrix} + \begin{bmatrix} -1.772 & 1.337 \\ -69.93 & 4.263 \\ 2.331 & -2.023 \\ 0 & 0 \\ 0 & 0 \\ 0 & 0 \end{bmatrix} \begin{Bmatrix} \xi_A \\ \zeta_A \end{Bmatrix} \quad \textbf{4.30}$$

with the output measurement equation:

$$\begin{Bmatrix} p_e \\ r_e \\ \phi_e \\ \psi_e \\ y_x \end{Bmatrix} = \begin{bmatrix} 0 & 1.002 & 0 & 0 & 0 & 0 \\ 0 & 0 & 1.002 & 0 & 0 & 0 \\ 0 & 0 & 0 & .997 & 0 & 0 \\ 0 & 0 & 0 & 0 & .997 & 0 \\ 0 & 0 & 0 & 0 & 0 & 1 \end{bmatrix} \begin{Bmatrix} v \\ p \\ r \\ \phi \\ \psi \\ y_x \end{Bmatrix} \quad \textbf{4.31}$$

The linear model nominal and trim values are:

$$V_0 = .035\,\text{m/s} \approx 0 \qquad \Phi_0 = .0007\,\text{rad} \approx 0 \qquad \xi_{Trim} = .003\,\text{rad} \approx 0$$
$$\Psi_T = 0\ (\text{North}) \qquad \Psi_0 = -.001\,\text{rad} \approx 0 \qquad \zeta_{Trim} = .0087\,\text{rad} \approx 0$$

The transfer function of the above model is given by:

$$G_{35Ry}(s) = \left[\begin{array}{c|c} A_{35Ry} & B_{35Ry} \\ \hline C_{35Ry} & 0 \end{array}\right] \quad \textbf{4.32}$$

The aileron and rudder actuators dynamics with their respective Padé delays were modelled as linear systems and have the following numerical dynamic equations:

$$\begin{Bmatrix} \dot{\xi}_A \\ \ddot{\xi}_A \\ \dot{D}_\xi \\ \ddot{D}_\xi \\ \dot{\zeta}_A \\ \ddot{\zeta}_A \\ \dot{D}_\zeta \\ \ddot{D}_\zeta \end{Bmatrix} = \begin{bmatrix} 0 & 1 & 0 & 0 & 0 & 0 & 0 & 0 \\ -3982 & -82.03 & 0 & 3982 & 0 & 0 & 0 & 0 \\ 0 & 0 & 0 & 1 & 0 & 0 & 0 & 0 \\ 0 & 0 & -13333 & -200 & 0 & 0 & 0 & 0 \\ 0 & 0 & 0 & 0 & 0 & 1 & 0 & 0 \\ 0 & 0 & 0 & 0 & -3982 & -82.03 & 0 & 3982 \\ 0 & 0 & 0 & 0 & 0 & 0 & 0 & 1 \\ 0 & 0 & 0 & 0 & 0 & 0 & -13333 & -200 \end{bmatrix} \begin{Bmatrix} \xi_A \\ \dot{\xi}_A \\ D_\xi \\ \dot{D}_\xi \\ \zeta_A \\ \dot{\zeta}_A \\ D_\zeta \\ \dot{D}_\zeta \end{Bmatrix} + \begin{bmatrix} 0 & 0 \\ 3982 & 0 \\ 0 & 0 \\ -400 & 0 \\ 0 & 0 \\ 0 & 3982 \\ 0 & 0 \\ 0 & -400 \end{bmatrix} \begin{Bmatrix} \xi_D \\ \zeta_D \end{Bmatrix} \quad \textbf{4.33}$$

The transfer function of the longitudinal model with the actuator and Padé delay is given by:

$$G_{35Ay}(s) = \left[\begin{array}{c|c} A_{35Ay} & B_{35Ay} \\ \hline C_{35Ay} & 0 \end{array}\right] \qquad \textbf{4.34}$$

4.5.3 Dynamic Coupling

Although decoupling between linear longitudinal and lateral dynamics is a valid assumption due to symmetry in airframe, there exist in reality some coupling that could be significant due to flight and trim conditions. If the combined longitudinal and lateral dynamics are defined as:

$$\begin{Bmatrix} \dot{x}_{35Rz} \\ \dot{x}_{35Ry} \end{Bmatrix} = \begin{bmatrix} A_{35Rz} & A_{C35Ry} \\ A_{C35Rz} & A_{35Ry} \end{bmatrix} \begin{Bmatrix} x_{35Rz} \\ x_{35Ry} \end{Bmatrix} + \begin{bmatrix} B_{35Rz} & B_{C35Ry} \\ B_{C35Rz} & B_{35Ry} \end{bmatrix} \begin{Bmatrix} u_{35Rz} \\ u_{35Ry} \end{Bmatrix}$$
$$\begin{Bmatrix} y_{35Rz} \\ y_{35Ry} \end{Bmatrix} = \begin{bmatrix} C_{35Rz} & 0 \\ 0 & C_{35Ry} \end{bmatrix} \begin{Bmatrix} x_{35Rz} \\ x_{35Ry} \end{Bmatrix}$$

which can be represented by the transfer function:

$$G_{35R}(s) = \left[\begin{array}{c|c} A_{35R} & B_{35R} \\ \hline C_{35R} & 0 \end{array}\right] \qquad \textbf{4.35}$$

The dynamic coupling can be expressed as:

$$\begin{aligned} \dot{x}_{35Rz} &= A_{C35Ry} x_{35Ry} + B_{C35Ry} u_{35Ry} \\ \dot{x}_{35Ry} &= A_{C35Rz} x_{35Rz} + B_{C35Rz} u_{35Rz} \end{aligned} \qquad \textbf{4.36}$$

The above equations are derived numerically with ACSL with the following results:

$$\begin{Bmatrix} \dot{u} \\ \dot{w} \\ \dot{q} \\ \dot{\theta} \\ \dot{h} \\ \dot{N}_E \end{Bmatrix} = \begin{bmatrix} 0 & 0 & 0.035 & 0 & 0 & 0 \\ 0 & -0.035 & 0 & -.0087 & 0 & 0 \\ 0 & 0 & 0 & 0 & 0 & 0 \\ 0 & 0 & -.0007 & 0 & 0 & 0 \\ -.0007 & 0 & 0 & -.036 & 0 & 0 \\ 0 & 0 & 0 & 0 & 0 & 0 \end{bmatrix} \begin{Bmatrix} v \\ p \\ r \\ \phi \\ \psi \\ y_x \end{Bmatrix} + \begin{bmatrix} 0 & 0 \\ 0 & 0 \\ 0 & 0 \\ 0 & 0 \\ 0 & 0 \\ 0 & 0 \end{bmatrix} \begin{Bmatrix} \xi_A \\ \zeta_A \end{Bmatrix} \quad \textbf{4.37}$$

$$\begin{Bmatrix} \dot{v} \\ \dot{p} \\ \dot{r} \\ \dot{\phi} \\ \dot{\psi} \\ \dot{y}_x \end{Bmatrix} = \begin{bmatrix} 0 & 0 & 0 & 0 & 0 & 0 \\ -.0185 & -.0036 & 0 & 0 & 0 & 0 \\ 0.0003 & -.002 & 0 & 0 & 0 & 0 \\ 0 & 0 & 0 & 0 & 0 & 0 \\ 0 & 0 & .0007 & 0 & 0 & 0 \\ -.001 & -.0007 & 0 & 0 & 0 & 0 \end{bmatrix} \begin{Bmatrix} u \\ w \\ q \\ \theta \\ h \\ N_E \end{Bmatrix} + \begin{bmatrix} 0 & 0 \\ 2.295 & 0 \\ 0 & 0 \\ 0 & 0 \\ 0 & 0 \\ 0 & 0 \end{bmatrix} \begin{Bmatrix} \tau_A \\ \eta_A \end{Bmatrix} \quad \textbf{4.38}$$

The significant coupling between the roll rate p and the throttle setting τ_A comes mainly from airframe reaction to engine torque . The minor coupling coefficients are due to the steady-state condition, where it was not possible to zero the lateral/directional states and controls before perturbing the linear model. How significant this coupling is on the linear model accuracy and its effect on stability will be discussed next.

Neglecting the coupling between the two subsystems, the combined dynamic model is represented by:

$$\begin{Bmatrix} \dot{x}_{35Rz} \\ \dot{x}_{35Ry} \end{Bmatrix} = \begin{bmatrix} A_{35Rz} & 0 \\ 0 & A_{35Ry} \end{bmatrix} \begin{Bmatrix} x_{35Rz} \\ x_{35Ry} \end{Bmatrix} + \begin{bmatrix} B_{35Rz} & 0 \\ 0 & B_{35Ry} \end{bmatrix} \begin{Bmatrix} u_{35Rz} \\ u_{35Ry} \end{Bmatrix}$$
$$\begin{Bmatrix} y_{35Rz} \\ y_{35Ry} \end{Bmatrix} = \begin{bmatrix} C_{35Rz} & 0 \\ 0 & C_{35Ry} \end{bmatrix} \begin{Bmatrix} x_{35Rz} \\ x_{35Ry} \end{Bmatrix} \quad \textbf{4.39}$$

which can be represented by the transfer function:

$$G_{35RD}(s) = \left[\begin{array}{c|c} A_{35RD} & B_{35RD} \\ \hline C_{35RD} & 0 \end{array}\right] \quad \textbf{4.40}$$

When adding the actuator and Padé delay the model transfer function is given by:

$$G_{35AD}(s) = \left[\begin{array}{c|c} A_{35AD} & B_{35AD} \\ \hline C_{35AD} & 0 \end{array}\right] \qquad \textbf{4.41}$$

where the '*D*' in the subscript indicates the decoupling of the subsystems.

4.6 Dynamic Analysis

The A3 *gust insensitive* configuration has a notable influence on the air vehicle dynamics. Instability, sensitivity, and coupling are some of the effects such a configuration can introduce. In this section the air vehicle longitudinal and lateral/directional dynamics are examined and analysed.

4.6.1 Longitudinal Stability

From Equations 4.7 and 4.25 it can be observed that the bare airframe exhibits the following static stability characteristics:

- stable axial speed disturbance: $x_u < 0$.
- stable vertical speed disturbance: $z_w < 0$.
- asymmetric thrust: $m_u < 0$
- negative longitudinal stability margin: $m_w > 0$

The dynamic stability can be evaluated by analysing the system eigenvalues in the s-plane diagram.

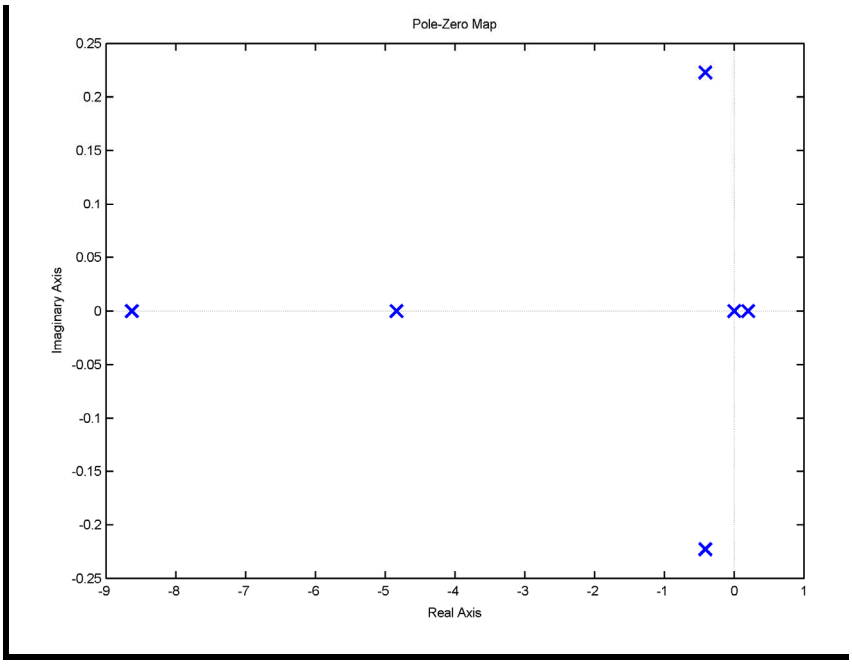

Figure 4.1: Longitudinal dynamics open-loop poles

Figure 4.1 shows the bare airframe poles that represent the roots of the system characteristic equation:

$$s\,(s + 8.631)\,(s + 4.832)\,(s - 0.2002)\,(s^2 + 0.8263s + 0.22) = 0 \qquad 4.42$$

The root at the origin represents the height mode. The high frequency pole at 8.63 *rad/s* is due to the engine dynamics. The slow unstable pole at 0.2 *rad/s* is the axial phugoid mode. The high frequency pole at 4.83 *rad/s* is the pitch short period mode. But the quadratic pair at 0.43 *rad/s* is a third oscillatory mode that resulted from the relaxed stability ($m_w \geq 0$). This mode is often encountered in combat aircraft and missiles where the CG is designed to lie aft of the neutral point (NP) to enhance manoeuvrability and not for gust insensitivity. As the CG moved further aft of the NP the value of m_w changes so that one of the real roots of the short period mode and one of the roots of the phugoid mode migrate in a complex pair corresponding to this third oscillatory mode. When this occurs, that mode will have the main influence upon the dynamic response of the FCSD. This has resulted in the slow real aperiodic unstable phugoid mode coupled with the high frequency real aperiodic short period mode[68].

The control actuators and computation delay have the following dynamics:

$$(s^2 +200s +13333)(s^2 +0.8263s +0.22)(s^2 +200s +13333) = 0 \qquad 4.43$$

As shown in Figure 4.2, the two quadratic pairs at 100 *rad/s* with 0.866 damping and the companion zeros are the computation delays for the throttle and elevator channels. The quadratic pair at 41 *rad/s* and 0.65 damping are the actuator dynamics.

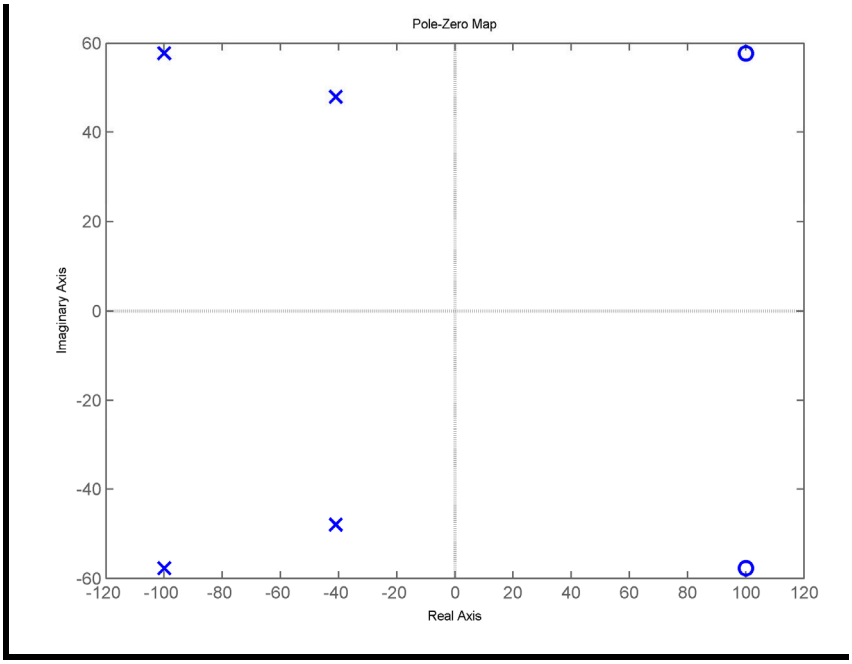

Figure 4.2: Longitudinal control actuator and delays poles and zeros

Although the closed-loop bandwidth is restricted by the RHP poles and zeros, for the longitudinal subsystem the RHP pole is very slow (0.2*rad/s*) and the zeros are very fast (100*rad/s*), which do not impose a serious limitation in the control system design.

4.6.2 Lateral/Directional Stability

From Equations 4.30 and 4.33, the lateral/directional static stability can be analysed as follows:

- stable sideslip motion: $y_v < 0$

- stable directional motion: $n_v > 0$
- positive stability margin and stable spiral mode: $l_v < 0$
- considerable *adverse yaw* in aileron controls: $| n_\xi | > | n_\zeta |$, $n_\xi > 0 > l_\xi$

The lateral/directional dynamic characteristic equation is given by:

$$s(s +8.17)(s +0.0584)(s –1.0e\text{-}4)(s2 \text{-}0.666\ s +14.64) \qquad \textbf{4.44}$$

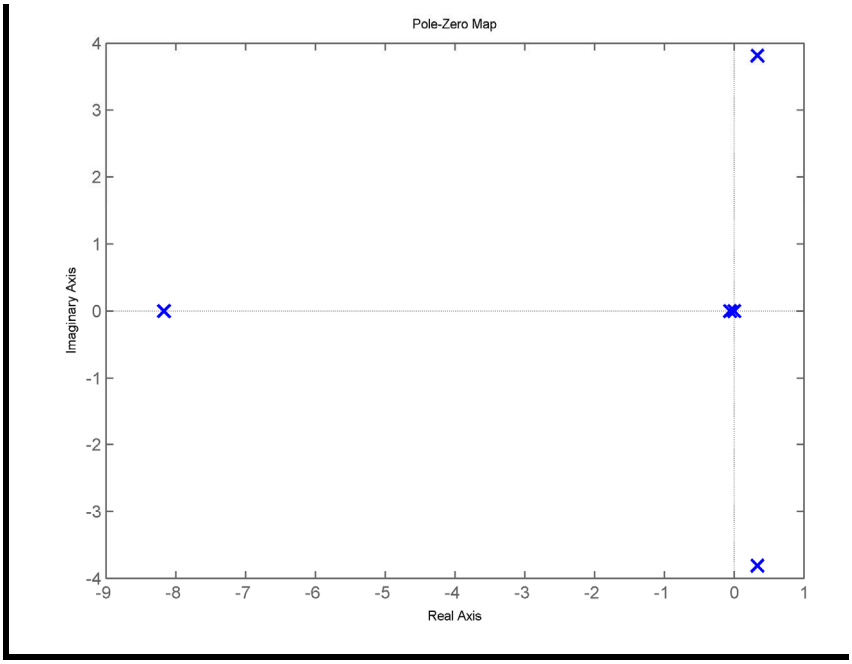

Figure 4.3: Lateral/directional dynamics open-loop poles

As shown in Figure 4.3, the two over-lapping poles at the origin are the cross-track and the heading/directional modes, the pole at 8.17 *rad/s* corresponds to the stable roll subsidence mode, the pole at 0.0584 is the stable *spiral* mode, and the quadratic term at 3.83 *rad/s* represent the unstable oscillatory *Dutch roll*.

Note that the unstable *Dutch roll* complex pair will impose a lower limit on the closed-loop bandwidth in the FCSD.

The lateral control actuators and computation delay have the following dynamics:

$$(s^2 + 0.8263s + 0.22)^2(s^2 + 200s + 13333)^2 = 0 \qquad 4.45$$

The aileron and rudder controls have identical dynamics as the elevator. Two quadratic pairs at 100*rad/s* with 0.866 damping and the companion RHP zeros are the computation delays, and two quadratic pairs at 41*rad/s* with 0.65 damping are the actuators dynamics.

4.6.3 Full Model Frequency Response

The open-loop frequency response analysis of the full linear model is performed in this section using the singular value decomposition(SVD). Singular values are used for gains and directionality analysis of square and non-square MIMO systems [39, 71]. For any system model $G(s)$ with m rows and l columns and $m \geq l$, the singular values are the positive square roots of the eigenvalues of $G^{\mathrm{H}}G$, where G^{H} is the complex conjugate transpose of G:

$$\sigma_i(G) = \sqrt{\lambda_i(G^H G)} \qquad \mathbf{4.46}$$

where $\sigma_1 \geq \sigma_2 \geq \ldots \geq \sigma_m$. σ_1 is the maximum singular value which is the largest gain for any input direction and denoted by $\bar{\sigma}$. σ_m is the minimum singular value which is the smallest gain for any input direction denoted by $\underline{\sigma}$. If we set $s = j\omega$ ($0 \leq \omega < \infty$), then the singular values of $G(j\omega)$ are functions of ω , and they are then called the *principal gains* of $G(s)$. The singular values of the linear models: $G_{35\mathrm{A}}$, $G_{35\mathrm{AD}}$, and $G_{35\mathrm{R}}$ are shown in Figure 4.4. The effects of the actuator dynamics are shown in the difference of the singular values of $G_{35\mathrm{A}}$ and $G_{35\mathrm{R}}$ at the high frequencies for all outputs. The effect of coupling is shown in the difference of the singular values of $G_{35\mathrm{A}}$ and $G_{35\mathrm{AD}}$ at low frequencies for roll and yaw, and high frequency at roll only. As discussed earlier, the major coupling comes from the engine torque effect on lateral roll at the high frequency and heading at the low frequency.

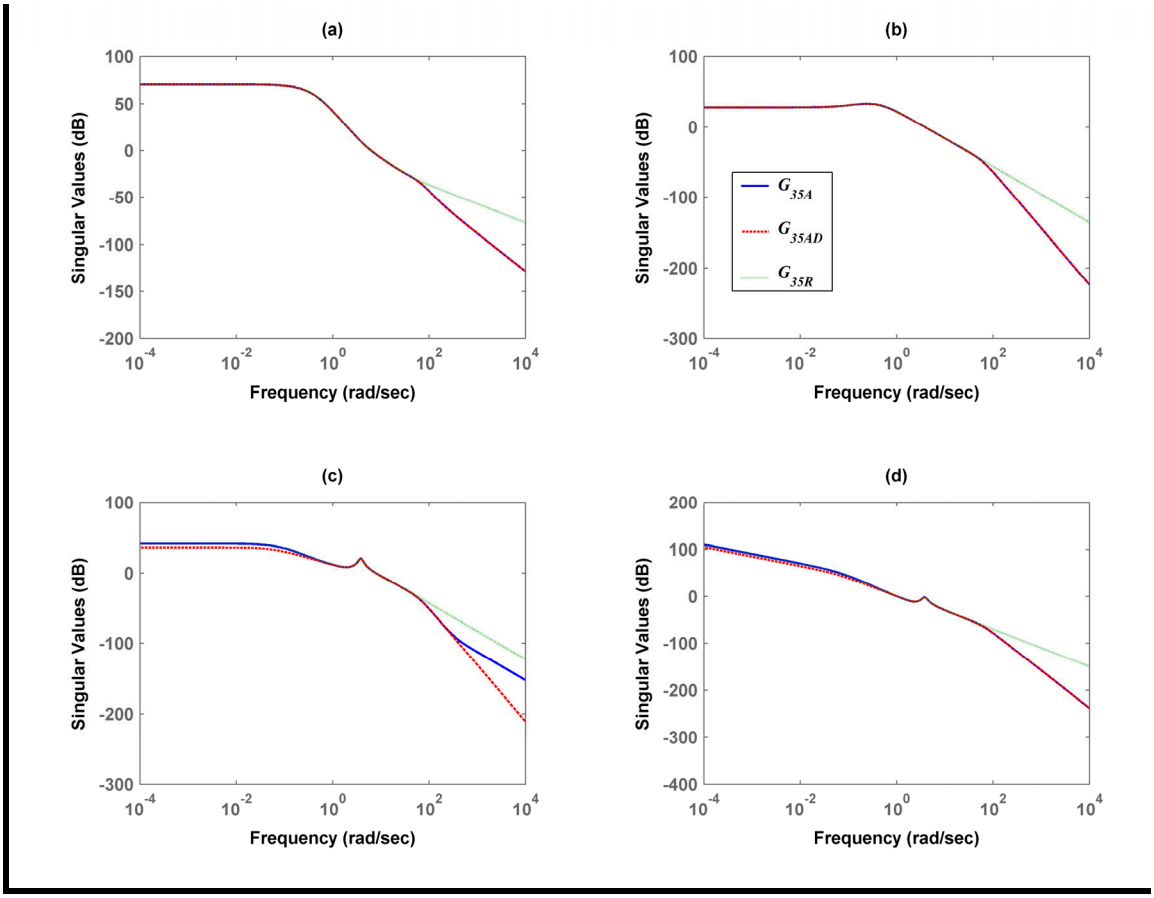

Figure 4.4: Linear models singular values comparison from all inputs to: (a) axial speed u, (b) pitch θ, (c) roll ϕ, and (d) yaw ψ

4.7 Classical PMC Linearization

To verify the air vehicle linear models, it was necessary to build a complete closed-loop linear system that included the classical PMC. Although the controller was linear, the implementation in the non-linear simulation was not totally linear. The required Linearization work was:

- all scheduled gains were set at the nominal speed U_0 = 35 m/s
- all limits were removed
- small angle approximations were applied

The governing PMC linear control equations become as follows:

$$\tau_D(s) = -k_u u_e(s)$$

$$\eta_D(s) = -\left\{ k_q q_e(s) + \left[k_\theta + \frac{k_{i\theta}}{s} \right] \left(\theta_e(s) + \frac{k_h}{T_h s + 1} h_e(s) \right) \right\}$$

$$\xi_D(s) = -\left\{ k_p p_e(s) + \left[k_\phi + \frac{k_{i\phi}}{s} \right] \left(\phi_e(s) - \frac{k_\psi}{T_m s + 1} \left(\psi_e(s) + k_y y_e(s) \right) \right) \right\}$$

$$\zeta_D(s) = -k_s \left(r_e(s) - \frac{g \cos \Theta_0}{U_0} \phi_e(s) \right)$$

In state-space realization

$$\begin{aligned} \dot{x}_c &= A_c x_c + B_c y_e \\ u_D &= C_c x_c + D_c y_e \end{aligned}$$

$$\begin{Bmatrix} \dot{\theta}_h \\ i\dot{\theta} \\ \dot{\psi}_f \\ i\dot{\phi} \end{Bmatrix} = \begin{bmatrix} -1/T_h & 0 & 0 & 0 \\ -1 & 0 & 0 & 0 \\ 0 & 0 & -1/T_m & 0 \\ 0 & 0 & -1 & 0 \end{bmatrix} \begin{Bmatrix} \theta_h \\ i\theta \\ \psi_f \\ i\phi \end{Bmatrix} + \begin{bmatrix} 0 & 0 & 0 & k_h/T_h & 0 & 0 & 0 & 0 & 0 \\ 0 & 0 & 1 & 0 & 0 & 0 & 0 & 0 & 0 \\ 0 & 0 & 0 & 0 & 0 & 0 & 0 & k_\psi/T_m & k_\psi k_y/T_m \\ 0 & 0 & 0 & 0 & 0 & 0 & 1 & 0 & 0 \end{bmatrix} \begin{Bmatrix} u_e \\ q_e \\ \theta_e \\ h_e \\ p_e \\ r_e \\ \phi_e \\ \psi_e \\ y_x \end{Bmatrix}$$

$$\begin{Bmatrix} \tau_D \\ \eta_D \\ \xi_D \\ \zeta_D \end{Bmatrix} = \begin{bmatrix} 0 & 0 & 0 & 0 \\ k_\theta & -k_{i\theta} & 0 & 0 \\ 0 & 0 & k_\phi & -k_{i\phi} \\ 0 & 0 & 0 & 0 \end{bmatrix} \begin{Bmatrix} \theta_h \\ i\theta \\ i\phi \\ \psi_f \end{Bmatrix} + \begin{bmatrix} -k_u & 0 & 0 & 0 & 0 & 0 & 0 & 0 & 0 \\ 0 & -k_q & -k_\theta & 0 & 0 & 0 & 0 & 0 & 0 \\ 0 & 0 & 0 & 0 & -k_p & 0 & -k_\phi & 0 & 0 \\ 0 & 0 & 0 & 0 & 0 & -k_s & k_s g \cos\Theta_0 / U_o & 0 & 0 \end{bmatrix} \begin{Bmatrix} u_e \\ q_e \\ \theta_e \\ h_e \\ p_e \\ r_e \\ \phi_e \\ \psi_e \\ y_x \end{Bmatrix}$$

Note that the controller input variables $\{u_e, q_e, \theta_e, h_e, p_e, r_e, \phi_e, \psi_e, y_x\}$ are the perturbed linear model outputs and not the actual air vehicle output measurements.

The PMC mixing matrix[7] is linear as shown in §**3.8.4**; it was computed as follows:

$$\begin{Bmatrix} \eta \\ \xi \\ \zeta \end{Bmatrix}_A = M_{mix}^{-1} \begin{Bmatrix} \eta \\ \xi \\ \zeta \end{Bmatrix}_D$$

$$M_{mix} = \begin{bmatrix} \eta_{D_{FS}}/\eta_{A_{FS}} & 0 & 0 \\ 0 & \xi_{D_{FS}}/\xi_{A_{FS}} & l_\zeta/l_\xi \times \zeta_{D_{FS}}/\zeta_{A_{FS}} \\ 0 & n_\xi/n_\zeta \times \xi_{D_{FS}}/\xi_{A_{FS}} & \zeta_{D_{FS}}/\zeta_{A_{FS}} \end{bmatrix} = \begin{bmatrix} 1 & 0 & 0 \\ 0 & 1 & -.15\times.75 \\ 0 & -2\times1 & .75 \end{bmatrix} \quad \textbf{4.47}$$

$$M_{mix}^{-1} = \begin{bmatrix} 1 & 0 & 0 \\ 0 & 1.429 & 0.214 \\ 0 & 3.81 & 1.905 \end{bmatrix}$$

Note that the scaling in Equation 4.47 is based on single actuator for each control signal with doubled force coefficient in the linear model as in Equations 4.7 and 4.11. If each control signal is driving two actuators, as in Equations 4.5 and 4.9, the scaling would then be halved.

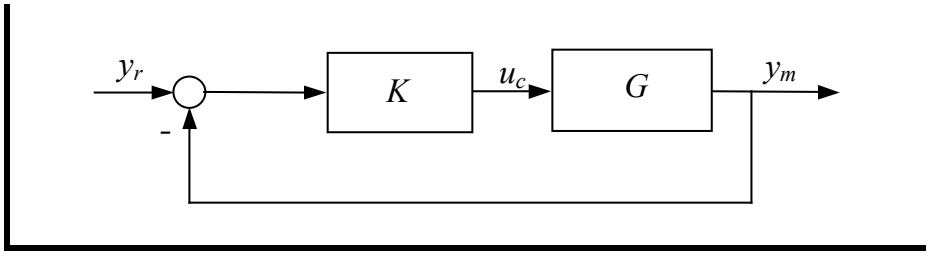

Figure 4.5: PMC implementation

Finally, the PMC was implemented in the forward path, as shown in Figure 4.5, as in the non-linear simulation. This means that it will act as a regulator trying to null the feedback inputs.

4.8 Linear Models Validation

In this section the derived linear models and the PMC law are validated and verified using the non-linear ACSL simulation. Basically a time step input response is used to compare the response of the non-linear and linear models. The linear models should match the non-linear simulation for small perturbations about the nominal flight condition at which the linear models were derived.

4.8.1 Linear Models Comparison

Here, the step responses of the different linear models are compared first. It was chosen to apply a simultaneous $20m$ step to both height and cross-track. This excites both longitudinal and lateral modes in addition to the coupling between them.

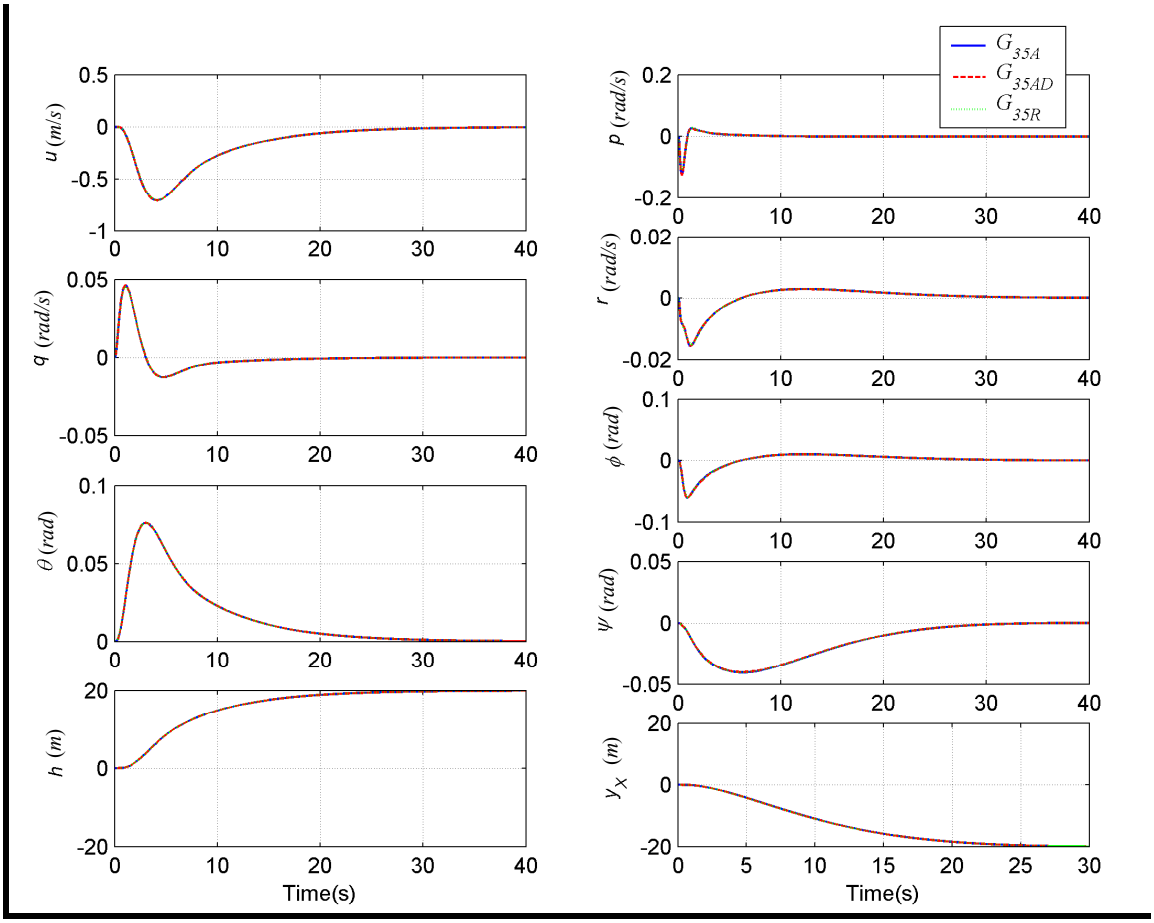

Figure 4.6: Linear models step response comparison

It can be seen from Figure 4.6 that all three models: G_{35A} , G_{35AD} , and G_{35R} show undistinguished response for the applied manoeuvre. This indicates that the actuator dynamics with the Padé delay and the coupling has limited effects on the overall low-frequency dynamic response of the system model. In the coming chapters this point will be discussed in more detail, to include the effects on robustness and stability.

4.8.2 Non-linear Simulation Comparison

Here, the above manoeuvre will be applied to the non-linear simulation model and compared with the linear response.

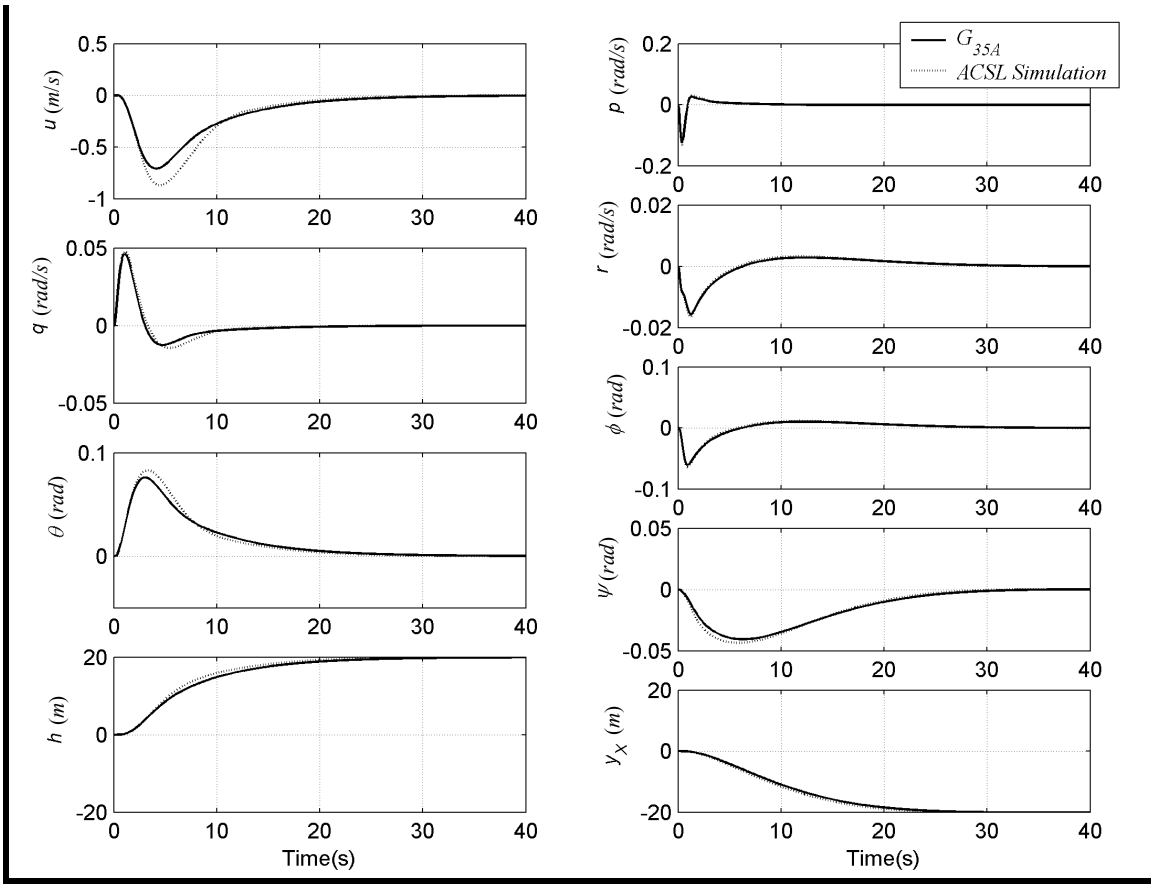

Figure 4.7: Non-linear simulation versus linear model response

The non-linear simulation response shown in Figure 4.7 demonstrates a significant similarity with the linear model. Although the step size was large, i.e. 20m for both height and cross-track, the frequencies involved are low. Also, the noticeable difference

in the axial speed is due to the high non-linearity involved in the engine and propeller dynamics. Note that the comparison here is made between the closed-loop systems that include the dynamic models and the PMC law, since both were linearised and simplified for the linear closed-loop system. Also note that the outputs of the non-linear simulation here are the perturbations from the nominal values and not the actual variables' magnitudes i.e.:

$$\begin{aligned} u &= \mathbf{u} - U_0, \quad q = \mathbf{q}, \quad \theta = \boldsymbol{\theta} - \Theta_0, \quad h = \mathbf{h} - H_o, \\ p &= \mathbf{p}, \qquad r = \mathbf{r}, \quad \phi = \boldsymbol{\phi} - \Phi_0, \quad \psi = \boldsymbol{\psi} - \Psi_T - \Psi_0, \quad y_X = \mathbf{y}_X \end{aligned} \tag{4.48}$$

The following nominal flight condition values were set:

$$\begin{aligned} U_0 &= 35.2 \text{ m/s} \quad \Theta_0 = -.016 \text{ rad} \quad H_o = 104 \text{ m} \\ \Phi_0 &= .0007 \text{rad} \quad \Psi_0 = -.001 \text{rad} \quad \Psi_T = 0 \text{ (North)} \end{aligned} \tag{4.49}$$

4.9 Nominal Design Model Selection

In this section, different flight envelope linear models will be built and compared, and a nominal model is selected for use in the control system design.

The major parameters variations that are taken into account for building these models are:

- Airspeed U:=35±10 *m/s*
- Axial CG position X_{CG}:=20 ± 10 *mm*

Table 4.1 shows the different flight envelope models and their respective airspeeds and CG positions. Note that Model 4 is the initial nominal model selected for the earlier linear analysis.

Table 4.1: A3 Flight envelope models

No	Model name (Long. / Lat.)	Airspeed (*m/s*)	CG axial position (*mm*)
1	G_{25Az} / G_{25Ay}	25	20
2	G_{25Pz} / G_{25Py}	25	30
3	G_{25Mz} / G_{25My}	25	10
4	G_{35Az} / G_{35Ay}	35	20
5	G_{35Pz} / G_{35Py}	35	30
6	G_{35Mz} / G_{35My}	35	10
7	G_{45Az} / G_{45Ay}	45	20
8	G_{45Pz} / G_{45Py}	45	30
9	G_{45Mz} / G_{45My}	45	10

4.9.1 Dynamic Analysis

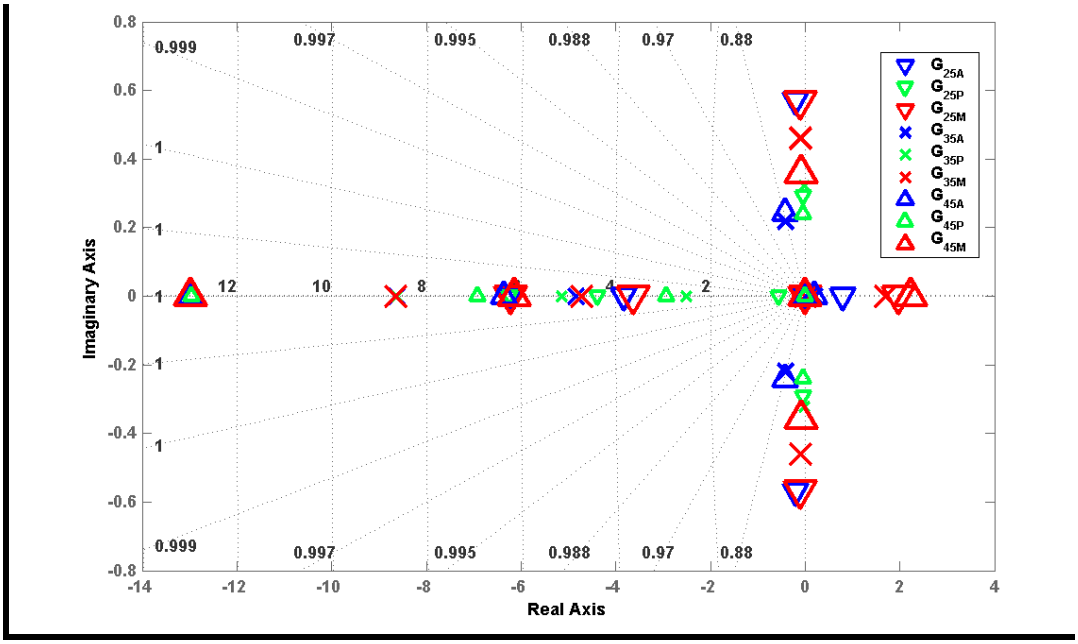

Figure 4.8: Longitudinal Models' Poles

Here, the poles of the longitudinal and lateral models listed in Table 4.1 are compared. Figure 4.8 shows how airspeed and CG shift have affected the dynamics of the longitudinal model. It can be seen from figure that increasing airspeed and moving the CG aft the nominal values stiffen and destabilize the model. On the other hand,

reducing airspeed and moving CG fore, destabilizes and make model more sluggish.

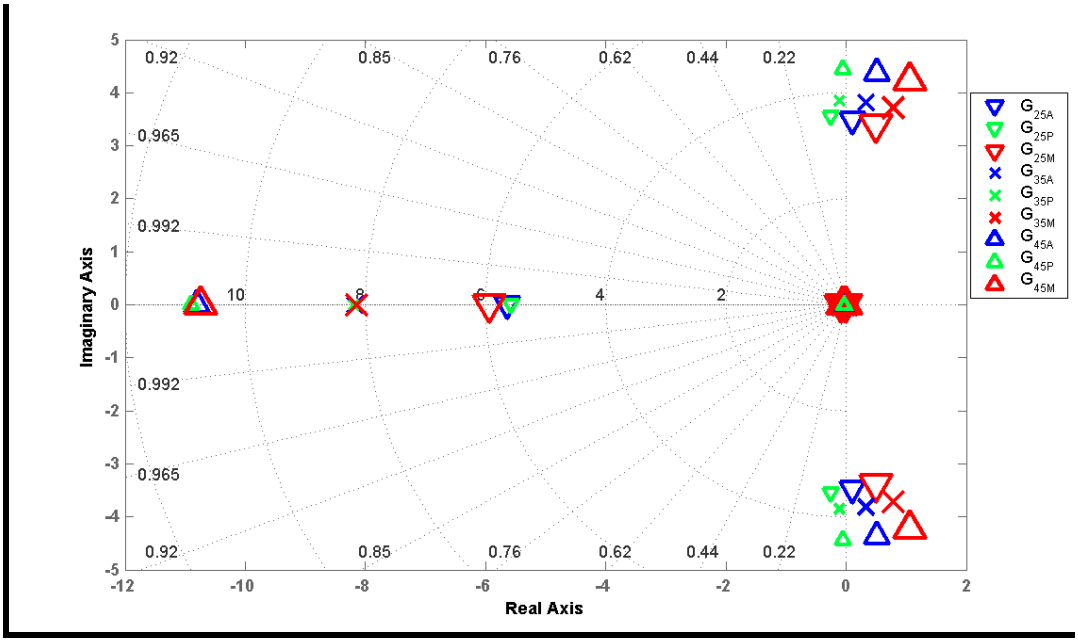

Figure 4.9 : Lateral Models Poles

Figure 4.9 above, also shows the effect of airspeed and CG shift on the dynamics of the lateral model. It can similarly be said that increasing airspeed and moving the CG aft stiffens and destabilizes the model. Also, reducing airspeed and moving CG forward, destabilizes the model and makes it more sluggish.

4.9.2 *ν*-Gap Analysis

In this section, the *ν*-gap metric[50, 60, 61] introduced in §2.10, will be used to "measure" the distance between the full operational flight envelope models, and calculate the minimum gap model that can represent the whole set with the minimum distance. Table 4.2 shows the maximum gap that each model has with the full set. It is clearly shown that G_{35A} does represent the best nominal model for the whole set for both longitudinal and lateral dynamics, with the least maximum gap, as expected.

Table 4.2 : v-Gap analysis of flight envelope models

Case	Model name (Long. / Lat.)	*v*-Gap (max.)
1	G_{25Az} / G_{25Ay}	0.550 / 0.799
2	G_{25Pz} / G_{25Py}	0.571 / 0.829
3	G_{25Mz} / G_{25My}	0.546 / 0.793
4	$\boldsymbol{G_{35Az}}^{\bullet}$ / $\boldsymbol{G_{35Ay}}^{\bullet}$	**0.381 / 0.554**
5	G_{35Pz} / G_{35Py}	0.399 / 0.567
6	G_{35Mz} / G_{35My}	0.409 / 0.618
7	G_{45Az} / G_{45Ay}	0.558 / 0.801
8	G_{45Pz} / G_{45Py}	0.549 / 0.794
9	G_{45Mz} / G_{45My}	0.571 / 0.828

$^{\bullet}$ Nominal models

The gap between the nominal models, G_{35Az} and G_{35Ay}, and the full set is shown in Table 4.3. It is clearly shown that the longitudinal models are less sensitive to CG and airspeed variation than the lateral, since their distances from the nominal are always less. It also shows that airspeed reduction (i.e. models with a P subscript) has more influence or larger distances than its increase (i.e. models with an M subscript) on both longitudinal and lateral dynamics.

Table 4.3 : Nominal models G_{35Az} / G_{35Ay} *v*-Gap analysis

Case	Model (Long. / Lat.)	*v*-Gap with G_{35Az} / G_{35Ay}
1	G_{25Az} / G_{25Ay}	0.367 / 0.533
2	$\boldsymbol{G_{25Pz}}^{\blacktriangledown}$ / $\boldsymbol{G_{25Py}}^{\blacktriangledown}$	**0.382 / 0.554**
3	G_{25Mz} / G_{25My}	0.364 / 0.521
4	$\boldsymbol{G_{35Az}}^{\bullet}$ / $\boldsymbol{G_{35Ay}}^{\bullet}$	**0 / 0**
5	G_{35Pz} / G_{35Py}	0.107 / 0.195
6	G_{35Mz} / G_{35My}	0.104 / 0.205
7	G_{45Az} / G_{45Ay}	0.261 / 0.415
8	G_{45Pz} / G_{45Py}	0.263 / 0.423
9	$\boldsymbol{G_{45Mz}}^{\blacktriangle}$ / $\boldsymbol{G_{45My}}^{\blacktriangle}$	**0.267 / 0.450**

$^{\bullet}$Nominal models $^{\blacktriangledown}$Lower worst-case $^{\blacktriangle}$Upper worst-case

Table 4.3 also shows that the lateral control system design will be more challenging than the longitudinal to work for the whole flight envelope that these models represent. Finally, Table 4.2 and Table 4.3 show that Case 2 and Case 9 represent the worst or extreme cases at both ends of the flight envelope as expected.

4.9.3 Worst-Case Models

It is appropriate to analyse the worst-case models in more details to draw the limits which the flight control system is expected to counter. Figure 4.10 below, shows how far the longitudinal model poles have travelled due to the airspeed and CG position variations for Cases 2 and 9 in Table 4.3.

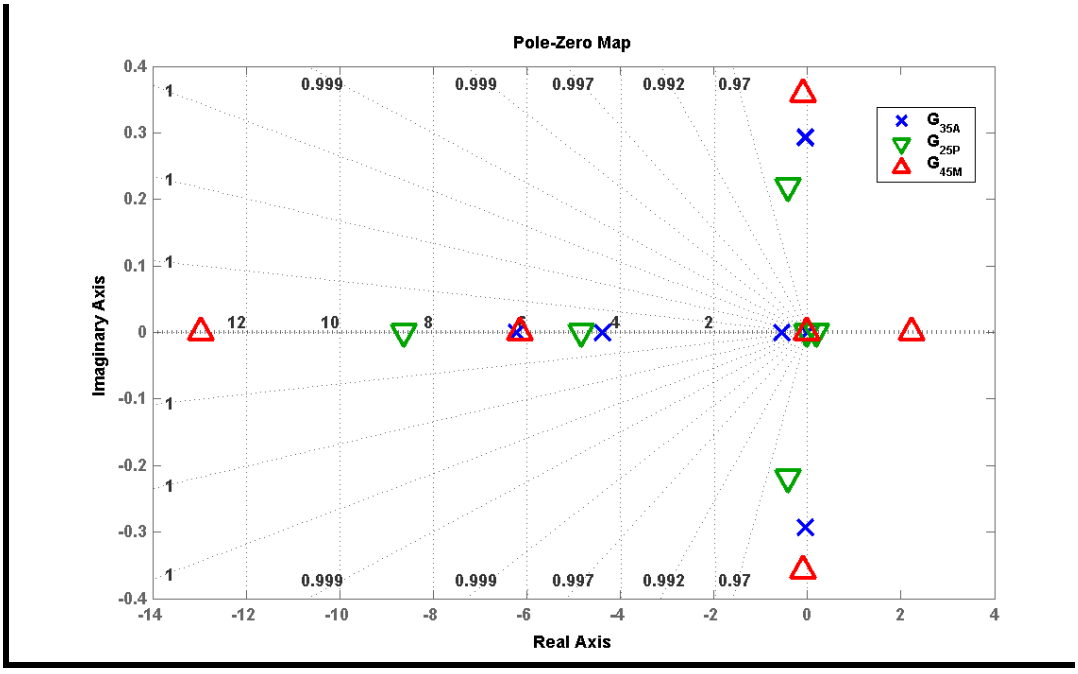

Figure 4.10: Worst-case longitudinal models poles comparison

Along with Table 4.4 below, the most significant effect is shown to be the increase in *phugoid* unstable mode frequency in Case 9, i.e. G_{45Mz}, to 2.23 *rad/s*. This will impose an important lower limit on the closed-loop bandwidth in the longitudinal control system design.

Table 4.4: Worst-case models longitudinal dynamic modes comparison

Dynamic Mode	G_{25Pz}▼ $\omega(rad/s)/\ \zeta$	G_{35Az}● $\omega(rad/s)/\ \zeta$	G_{45Mz}▲ $\omega(rad/s)/\ \zeta$
Engine dynamics	6.23	8.63	13.0
Short period	4.38	4.83	6.14
Phugoid	0.55	**0.2 RHP**	**2.23 RHP**
Third mode	0.296 / 0.132	0.468 / 0.88	0.366 / 0.22

●Nominal model ▼Lower worst-case ▲Upper worst-case

Table 4.5: Longitudinal nominal and worst-case models trim values

Dynamic Model	U_0 (m/s)	Θ_0 (rad)	τ_{Trim} $(\%)$	η_{Trim} (rad)
G_{25Pz}▼	25	0.06	10	-0.097
G_{35Az}●	35	-0.016	16	-0.049
G_{45Mz}▲	46	-0.045	35	-0.029

The longitudinal nominal and worst-case models flight trim values are given in Table 4.5. Note how the trim attitude angle Θ_0 is positive for the low airspeed model and negative for the nominal and high airspeed models. Note the wing incidence is $+3deg$ (i.e. $0.05rad$) with respect to the fuselage.

Figure 4.11 shows how the lateral model poles have been moved by the airspeed and CG position variations for Cases 2 and 9. Airspeed increase and CG aft shift have a clear destabilizing effect on the *Dutch roll* complex pair. While compared to Figure 4.9, roll mode pole was largely effected by CG shift.

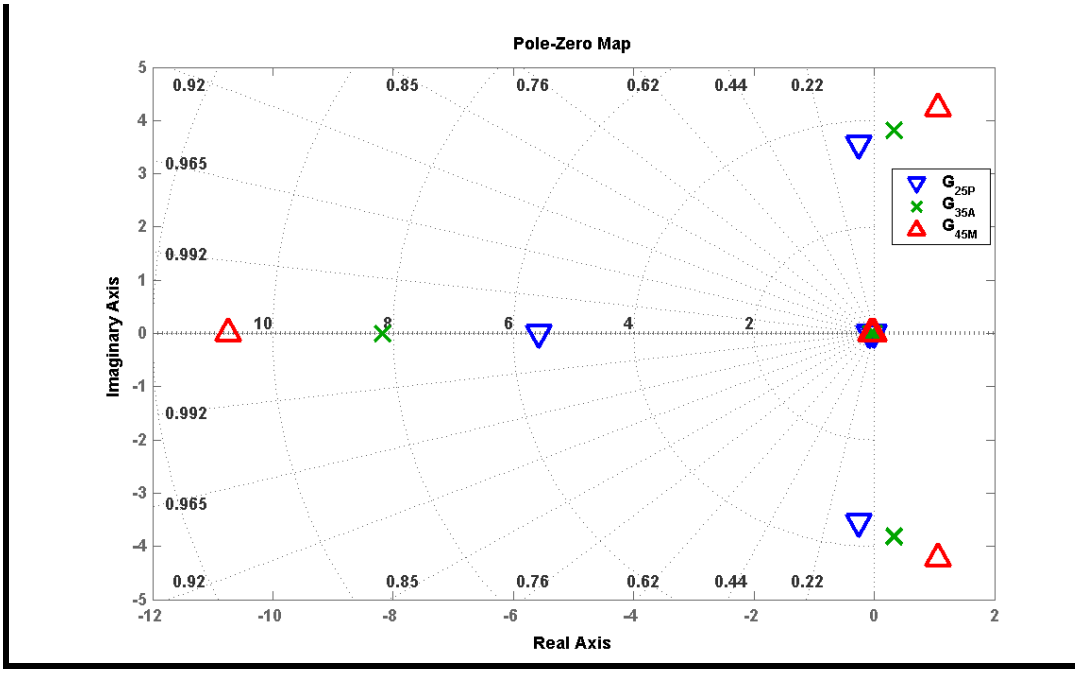

Figure 4.11: Worst-case lateral models comparison

Table 4.6 summarizes the changes to the open-loop lateral model poles. Note that destabilizing the *Dutch roll* frequency to 4.37*rad/s* in Case 9, i.e. G_{45My} , will also impose a lower limit on the closed-loop bandwidth in the lateral/directional control system design.

Table 4.6: Worst-case models lateral dynamic modes comparison

Dynamic Mode	G_{25Py} (ω / ζ)	G_{35Ay} (ω / ζ)	G_{45My} (ω / ζ)
Spiral mode	0.0762	0.0583	0.0416
Dutch roll	3.56/0.072	**3.83/0.087RHP**	**4.37/0.245RHP**
Roll subsidence	5.57	8.17	10.7

4.10 Chapter Summary

- Analytical and numerical linearization of the air vehicle non-linear dynamic model and the current flight control system was performed and presented.
- Longitudinal dynamic analysis showed considerable coupling between the phugoid and short period modes with the existence of a third oscillatory mode at $0.43 rad/s$ due to the relaxed stability condition ($m_w > 0$).
- Lateral dynamic analysis showed considerable *adverse yaw* in the aileron control and an unstable complex *Dutch roll* mode at $3.83 rad/s$ which will impose a lower limit on the closed-loop bandwidth in the FCSD.
- Dynamic coupling between longitudinal and lateral/directional modes, shown by the SV analysis, indicate that the coupling only affects heading and roll at the low frequency and roll alone at high frequency and comes mainly from airframe reaction to engine torque.
- Singular value analysis also showed that the effect of the actuator dynamics and the Padé delay are on the high frequency only and act as low-pass filters.
- Non-linear simulation comparison with linear model response showed very good match in both longitudinal and lateral/directional modes for the performed simultaneous $20m$ step manoeuvre for both height and cross-track demand.
- Multiple linear flight envelope models were developed for the variations in airspeed ($35\pm10 m/s$) and CG axial position ($20\pm10 mm$). It was shown that extreme/worst-case variation from nominal model were due to (a) airspeed increase plus aft CG shift, (b) airspeed reduction plus fore CG shift.
- Nominal model G_{35A} derived at $35m/s$ and with an X_{CG} at $20mm$ was proved to represent the full flight envelope models with the least maximum gap distance. Consequently, this model will be used for the fight control system design in the coming chapters.

Chapter 5

Longitudinal Flight Control System Design

It was concluded in Chapter 4 that decoupling of the longitudinal and lateral dynamics is a valid assumption. Thus in this chapter, the longitudinal flight control system design is described using the robust LSDP.

5.1 Linear Model Analysis

Before starting the robust loop shaping design procedure, the longitudinal linear model is analysed in more detail. First, the actuator dynamics and the computation delay effects on modelling accuracy are studied using the ν-gap metric. Next, the open-loop model singular values are investigated.

5.1.1 The ν-Gap Metric

It was shown in §4.8.1 that actuator dynamics and computation delays have little effects on the time response output of the step manoeuvre. The analysis was limited to the performed manoeuvre and did not give a precise indication of how these dynamics

effect the uncertainty and accuracy of the nominal control design model. In this section these dynamics are treated as uncertainties and their effects are analysed using the *ν*-gap metric introduced in §2.10.

Let the nominal air vehicle longitudinal dynamic model be G_{35Az} which includes the elevator actuator dynamics and the Padé continuous approximation of the computation delay and let the reduced order model be G_{35Rz}, which omits the actuator dynamics and the computation delay, and represent the perturbed model. Applying the *ν*-gap metric to the nominal and the perturbed models we can measure the 'distance' between the two models as follows

$$\delta_\nu(G_{35Az},G_{35Rz}) = 0.61$$

The above value can be interpreted as:

> *Neglecting the actuator dynamics and the computation delay will have a considerable effect on the longitudinal dynamic model accuracy.*

Note that the value 0 means the two systems are identical[50]. This very important result was not possible to achieve with the closed-loop time-domain nor the open-loop frequency-domain analysis of §4.8.1.

This powerful metric can also be used to examine the effects of the different dynamic components as they are neglected from the nominal dynamic model. Table 5.1 below, shows different cases of simplification and their effects.

It must be noted first that the non-linear dynamic model of the air vehicle in the ACSL simulation neglected the throttle actuator dynamics as mentioned in §3.4. This simplification is evaluated here by constructing a linear longitudinal model that includes the throttle actuator dynamics G_{35Azt}, then all of the simplifications are measured against this model which is shown on the last column in Table 5.1 alongside the nominal model that neglected the throttle dynamics (column four). Note also that the throttle actuator

characteristics (i.e. natural frequency and damping ratio) were not available, so it was modelled by a first-order transfer function with a time constant of 0.03 seconds as

$$TF = \frac{1}{0.03s + 1} \quad \textbf{5.1}$$

compared to the elevator actuator equivalent time constant of 0.02 seconds. This is because the throttle actuator has more torque than the elevator's and is slower in response as shown by their respective data-sheets[72].

Table 5.1: Simplification effects on nominal models' accuracy

Case	Actuator Dynamics Neglected	Computation Delay Neglected	ν-Gap Metric from Nominal Model G_{35Az}	ν-Gap Metric from Model w/ Throttle Dynamics G_{35Azt}
1	Elevator	None	0.32	0.32
2	None	Elevator	0.38	0.38
3	Elevator	Elevator	0.61	0.61
4	Throttle	None	0.00	0.085
5	None	Throttle	0.014	0.080
6	Throttle	Throttle	0.082	0.165
7	All	All	0.61	0.61

Table 5.1 can be interpreted as follows:

- Case 1: Elevator actuator dynamics have significant effect on modelling accuracy (0.32).
- Case 2: Elevator computation delay has more effect on modelling accuracy (0.38>0.32).
- Case 3: Elevator computation delay and actuator dynamics have the most significant effect on modelling accuracy (0.61) which necessitates that either one, but not both, may be neglected in the control design model.
- Case 4: Throttle actuator dynamics have much less effect on modelling accuracy

than the elevator dynamics (0.085 < 0.32), which may justify its elimination in the ACSL non-linear simulation.

- Case 5: Throttle computation delay has similar effect on modelling accuracy as actuator dynamics (0.082 ≅0.08) if neglected individually, which is also indicated by the small difference this case has with $\boldsymbol{G_{35Az}}$ (0.014).
- Case 6: Throttle computation delay and actuator dynamics have noticeable effect (0.165) on modelling accuracy which implies that both should not be neglected at the same time.
- Case 7: Neglecting both elevator and throttle actuator dynamics and their respective computation delays will not have more effect on modelling accuracy (0.61) than Case 3.

From the above analysis, it was decided to use G_{35Az} as the nominal design model for the longitudinal FCSD, even though it does not model the throttle actuator. This is because the final controller will be evaluated in the ACSL simulation which itself does not model the throttle actuator either. Let $G \equiv G_{35Az}$ in the context of this chapter.

5.1.2 Open-loop Singular Values

Here, the open-loop singular values of the nominal design model G_{35Az} are presented in some detail. Figure 5.1 shows the throttle input effect on all outputs individually, and Figure 5.2 shows the effect of elevator input on all outputs individually also. Note that these response curves are for single loops that are equivalent to the Bode gain plots.

The following observations can be made from Figure 5.1:

- Axial airspeed/throttle loop low gain across the low frequency band: this is justified by the fact that engine power was mainly designed to overcome drag and not to have a high speed acceleration capability at this cruise speed. This result also explains why neglecting the throttle actuator dynamics has less effect on modelling accuracy than the elevator actuator dynamics. Also, the loop has a

high gain at the high frequencies which needs to be reduced to eliminate unwanted engine throttle high frequency activity.

- Height/throttle loop high gain at low frequency: this fact was discussed in § 4.6.1, where axial and longitudinal dynamics were highly coupled due to relaxed stability configuration (i.e. gust-insensitivity).

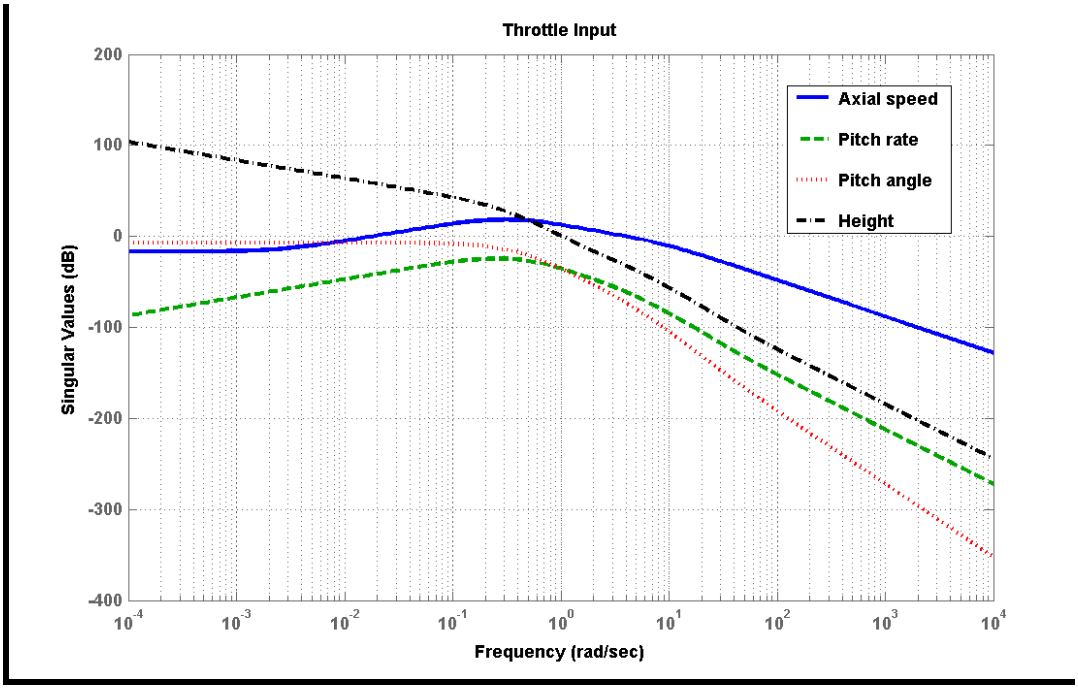

Figure 5.1: Open-loop singular values response of throttle input to each output

For Figure 5.2, the following can be observed:

- Axial speed/elevator loop higher gain than the throttle loop: this is also due to the coupling discussed just above.
- Height/elevator loop high gain/slope at low frequency: this is an indication of the integral effect it has.
- Pitch rate/elevator loop high gain at high frequency: this may introduce instability in the loop due to high frequency disturbance such as measurement noise.

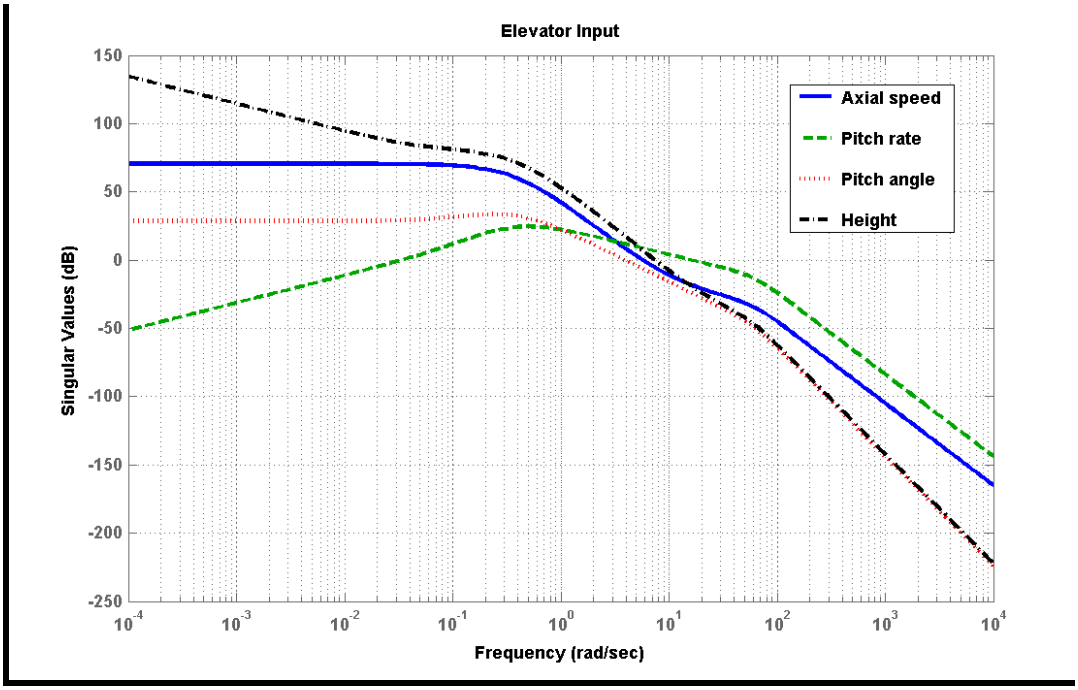

Figure 5.2: Open-loop singular values response of Elevator input to each output

5.2 Input / Output Scaling

The first step in LSDP is usually scaling of the inputs and outputs of the control system design model. This is an important step for practical applications that is sometimes ignored. Scaling generally improves the conditioning of the design problem and simplifies the weight selection process later on[39].

5.2.1 Input Scaling

For the inputs, each input is scaled to the maximum allowed value. Note that the linear model inputs are defined as the variation from the nominal trim values such as

$$\tau = \boldsymbol{\tau} - \tau_{Trim}$$
$$\eta = \boldsymbol{\eta} - \eta_{Trim}$$

So the range for each input variable is defined as

$$\begin{aligned} -\left|\boldsymbol{\tau}_{Min} - \tau_{Trim}\right| \le \tau \le +\left|\boldsymbol{\tau}_{Max} - \tau_{Trim}\right| \\ -\left|-\boldsymbol{\eta}_{Max} - \eta_{Trim}\right| \le \eta \le +\left|\boldsymbol{\eta}_{Max} - \eta_{Trim}\right| \end{aligned} \quad \textbf{5.2}$$

Given from Chapter 4

$$\begin{aligned} \tau_{Trim} &= 0.159\ (15.9\%) \\ \boldsymbol{\tau}_{Max} &= 1\ (100\%),\ \boldsymbol{\tau}_{Min} = 0.1\ (10\%) \\ \boldsymbol{\eta}_{Trim} &= 0.049\ rad \\ \boldsymbol{\eta}_{Max} &= \pm 0.262\ rad \end{aligned}$$

Thus, we have the following calculated limits for each input;

$$\begin{aligned} -0.059 \le \tau \le +0.841\ (\times 100\%) \\ -0.213 \le \eta \le +0.311\ rad \end{aligned} \quad \textbf{5.3}$$

Since the limits are not symmetric, the minimum values are taken for each case, although this may be conservative. For the throttle input, at higher speeds (i.e. 45-55 *m/s*) there would be little reserve, and it could reach full throttle easily. So using the lower limit seems more practical.

Thus, the initial input scaling matrix is chosen,

$$W_{1c} = \begin{bmatrix} 1/\tau & 0 \\ 0 & 1/\eta \end{bmatrix} \cong \begin{bmatrix} 17 & 0 \\ 0 & 5 \end{bmatrix} \quad \textbf{5.4}$$

Note that the above values are just initial guesses and could be varied in the tuning process of the controller.

5.2.2 Output Scaling

In a similar way, the outputs are scaled based on the maximum expected, or allowed, variation about the nominal. Initially the following maximum variations are chosen:

$$u = \pm 20\ m/s, \quad q = \pm 0.2\ rad/s, \quad \theta = \pm 0.2\ rad, \quad h = \pm 25\ m$$

The axial speed variation can be verified by the fact that the air vehicle will fly within this speed envelope using the nominal model based control system. The pitch rate scaling is a balance between stability and manoeuvrability, the well-known inverse relation. The pitch angle scaling is the main control variable and has a direct influence on control gain and effectiveness. The height variation is a logical limit that was set in the current control system to reduce saturation and windup, where in reality it can take any value. The initial output scaling matrix is thus calculated as

$$W_{2c} = \begin{bmatrix} 1/u & 0 & 0 & 0 \\ 0 & 1/q & 0 & 0 \\ 0 & 0 & 1/\theta & 0 \\ 0 & 0 & 0 & 1/h \end{bmatrix} \cong \begin{bmatrix} .05 & 0 & 0 & 0 \\ 0 & 5 & 0 & 0 \\ 0 & 0 & 5 & 0 \\ 0 & 0 & 0 & .04 \end{bmatrix} \qquad \textbf{5.5}$$

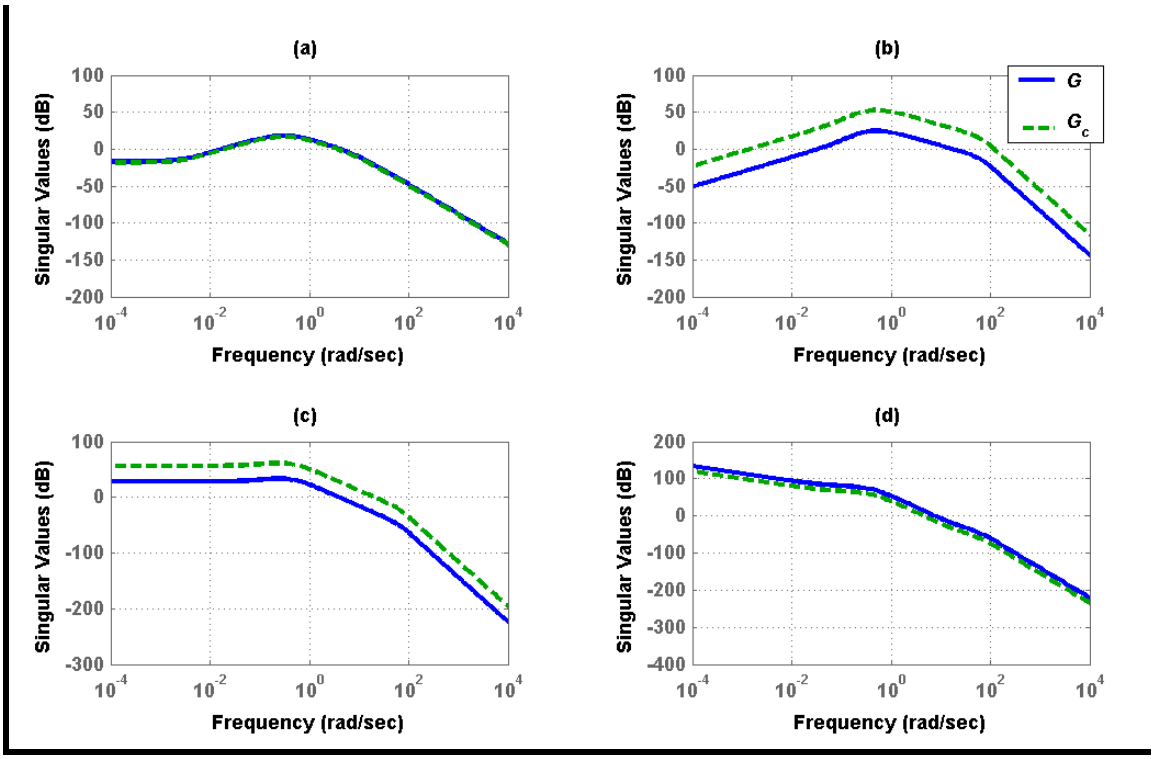

Figure 5.3: Scaling effect on longitudinal model open-loop singular values: (a) axial airspeed u/τ, (b) pitch rate q/η (c) pitch angle θ/η , (d) height h/η

The nominal design model, G, can then be scaled by the above matrices as follows:

$$G_c = W_{2c}\, G\, W_{1c} \qquad \textbf{5.6}$$

The effect of scaling on the open-loop singular values of G_c are shown in Figure 5.3. These initial results show the overall effect of scaling on each control loop. While axial speed loop gain, in Figure 5.3.a was not changed much, pitch rate and angle loops, in Figure 5.3.b-c have been increased, and flight path height loop overall gain was slightly reduced, as in Figure 5.3.d.

5.3 Shaping Weights

In this section, the shaping weights for the input and the output are selected. By multiplying the scaled model G_c by pre- and post-weights, the open-loop SVs can be shaped to meet the required performance specification. Given the input and output shaping weight matrices W_{1s} and W_{2s}, the shaped model is,

$$G_s = W_{2s}\, G_c\, W_{1s} \qquad \textbf{5.7}$$

Before describing the weight selection process, the general open-loop principal gain shape requirements are briefly reviewed[37-39, 71, 73]:

1- For performance, reduced tracking and minimum steady-state errors and reduced input sensitivity, the minimum principal gain should be large at low frequency ω_{low}, $\underline{\sigma}(G_s) >> 1$, with a sharp attenuation of at least -40dB/decade (slope of -2) or more.

2- For robustness and sensor noise rejection, the maximum principal gain should be as low as possible at high frequency ω_{high}, $\overline{\sigma}(G_W) << 1$, with a roll-off rate of -40dB/decade or more.

3- For stability, the frequency roll-off rate of the principal gains should reduce to approximately -20dB/decade (slope of -1) around gain cross-over frequency

ω_{cross} , at the required bandwidth.

The above requirements can be viewed graphically as bounds, on the open-loop principal gains, for the high and low frequencies as demonstrated in Figure 5.4.

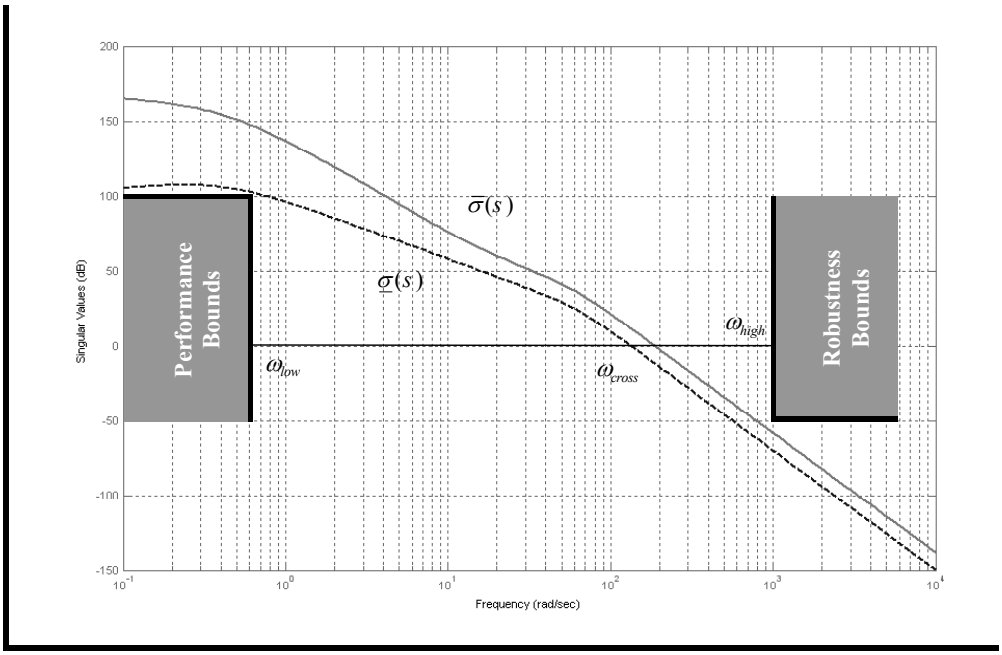

Figure 5.4: General open-loop principal gains shaping bounds

5.3.1 Input Shaping Weights

Input shaping weights usually contain functions such as integrators. Referring to Figure 5.3.a, the axial speed loop SV can be improved by adding an integrator pole to boost the low frequency gain and a zero to reduce roll-off rate at gain cross-over. Similarly, for the pitch control loop SV in Figure 5.3.b-d, an integrator would also improve performance especially for the pitch angle in Figure 5.3.c and a zero would help keep roll-off rate at gain cross-over low. The following input shaping weights were initially selected,

$$W_{1s} = \mathtt{diag}\left[\frac{s+.5}{s+.01} \quad \frac{s+1}{s+.01}\right] \qquad \textbf{5.8}$$

5.3.2 Output Shaping Weights

Output shaping weights usually contain functions such as low-pass filters. Initially, the following output weighting matrix was used,

$$W_{2s} = \mathrm{diag}\left[1 \quad .05\frac{s+.01}{s+1} \quad \frac{1}{.01s+1} \quad \frac{1}{.05s+1}\right] \tag{5.9}$$

For the axial speed SV, there was no need to add a low-pass filter. This is mainly because at launch, the controller is required to act quickly to increase throttle for the under-speed situation. For the pitch rate SV, it was required to reduce gain at both high and low frequency bands. So initially a band-pass filter was added that is the inverse of the input weight to overcome the integrator effect. For the pitch attitude SV, a simple low-pass filter was added to increase robustness and reject gyro measurement noise. Similarly, for the height loop, a simple low-pass filter was added to overcome height sensor quantization effect.

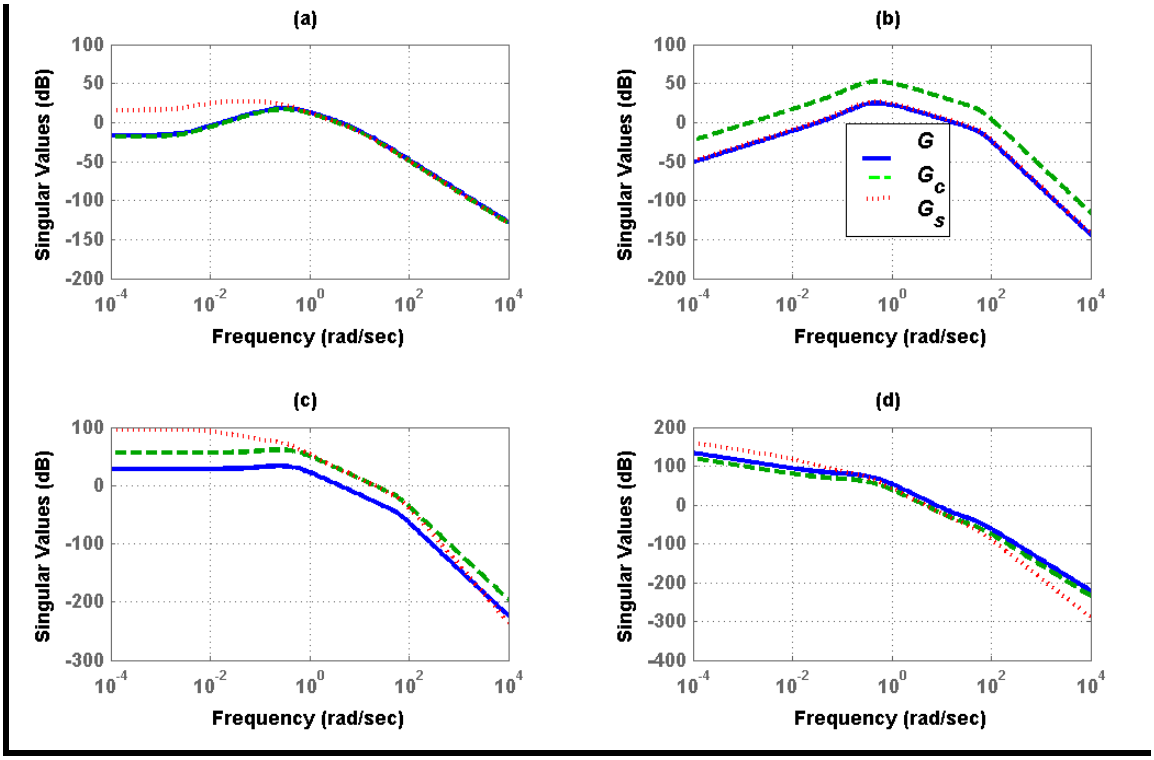

Figure 5.5: Scaling and shaping effects on model open-loop SVs
(a) airspeed u/τ, (b) pitch rate q/η (c) pitch angle θ/η , (d) height h/η

Figure 5.5 shows the effect of shaping weights on the original and scaled model open-loop SVs. The effect of integrators on axial speed SV is clear. Pitch attitude and height SVs also show the low-pass filter effect. Pitch rate SV shows how the band-pass filter cancels the integrator effect of the elevator input weight.

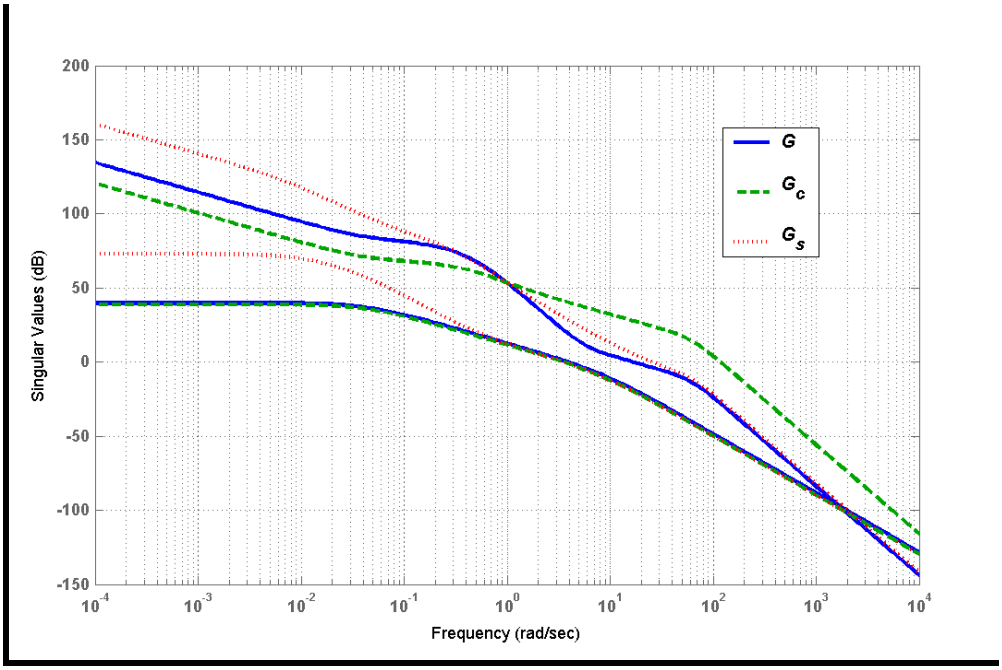

Figure 5.6: Scaling and shaping effects on model open-loop principal gains

Figure 5.6 shows the overall effect of scaling and shaping on the model open-loop principal gains (i.e. $\bar{\sigma}(s)$ and $\underline{\sigma}(s)$). Although it agrees with the results shown in Figure 5.5, it does not give the same details.

5.4 Alignment and Decoupling

Although the coupling between the longitudinal and lateral dynamics was shown, in Chapter 4, to be weak, the coupling between the axial and pitch modes was shown in § 4.6.1 and §5.1.2 to be significant. This leads to the consideration of alignment and decoupling of the longitudinal model.

SV *alignment* is the process of aligning the model open-loop singular values statically at

a certain frequency (or at DC), or dynamically at the full frequency range. In this section the constant static `align` algorithm in [71, 74-77] will be used. This algorithm calculates an approximate inverse of the design model at the selected frequency, and at the same time, it decouples the model at that frequency. It has been proven practical that aligning the SVs at the bandwidth frequency improves performance by reducing interaction which is normally greatest at this frequency[29, 39].

To align the SV, the `align` algorithm scales and decouples the model at the specified frequency ω_o . To align the shaped design model we have,

$$\begin{aligned} W_{a1}\big|_{2\times 2} &= \texttt{align}(G_s(\omega_o)\big|_{2\times 2}) \\ G_{a1}\big|_{4\times 2} &= G_s(\omega_o)\big|_{4\times 2} W_{a1}\big|_{2\times 2} \end{aligned} \qquad \textbf{5.10}$$

where G_{a1} is the aligned model with axial speed u and pitch attitude θ selected outputs only as indicated by $G_s\big|_{2\times 2}$ in Equation 5.10. Note that alignment can be applied to square and non-square models $G\big|_{m\times n}$ with $m \geq n$. Thus, applying the alignment algorithm to the full output model we have,

$$\begin{aligned} W_{a2}\big|_{2\times 4} &= \texttt{align}(G_s(\omega_o)\big|_{4\times 2}) \\ G_{a2}\big|_{4\times 4} &= G_s\big|_{4\times 2} W_{a2}\big|_{2\times 4} \end{aligned} \qquad \textbf{5.11}$$

Note that `align` should not be used when the condition number of the design model is high[39]. The previous scaling and shaping processes usually help to reduce the condition number at the model bandwidth. To prevent the `align` function from changing the scaling of the design model, W_{a1} can be modified as follows,

$$\begin{aligned} W_{a3} &= W_{a1}\,\texttt{diag}\,(W_{a1}^{-1}) \\ G_{a3}\big|_{4\times 2} &= G_s\big|_{4\times 2} W_{a3}\big|_{2\times 2} \end{aligned} \qquad \textbf{5.12}$$

This way, only decoupling takes effect on the aligned model. This decoupling technique

can only be applied to a square system, i.e. $m = n$. In this case, axial speed u and pitch attitude θ were selected for decoupling. Applying the `align` function at $\omega_o = 5 rad/s$ we have,

$$W_{a1} = \begin{bmatrix} -1.54 & 0.033 \\ 0 & 0.064 \end{bmatrix}$$
$$W_{a2} = \begin{bmatrix} -1.54 & 0.008 & 0.032 & 0.01 \\ 0 & 0.015 & 0.06 & -0.003 \end{bmatrix} \quad \textbf{5.13}$$
$$W_{a3} = \begin{bmatrix} 1.00 & 0.52 \\ 0 & 1.00 \end{bmatrix}$$

where W_{a1} is the alignment matrix for u and θ outputs, W_{a2} is the alignment for all outputs, and W_{a3} is the decoupling matrix for u and θ outputs. The numerical values of W_{a1} in Equation 5.13 indicate that to align the throttle input with the elevator at ω_o, it must be boosted 54% (i.e. 1.54). It also indicates that elevator input has negligible coupling with axial speed (i.e. 0) at ω_o, while throttle input has about 50% coupling with the pitch outputs (i.e. 0.033/0.064).

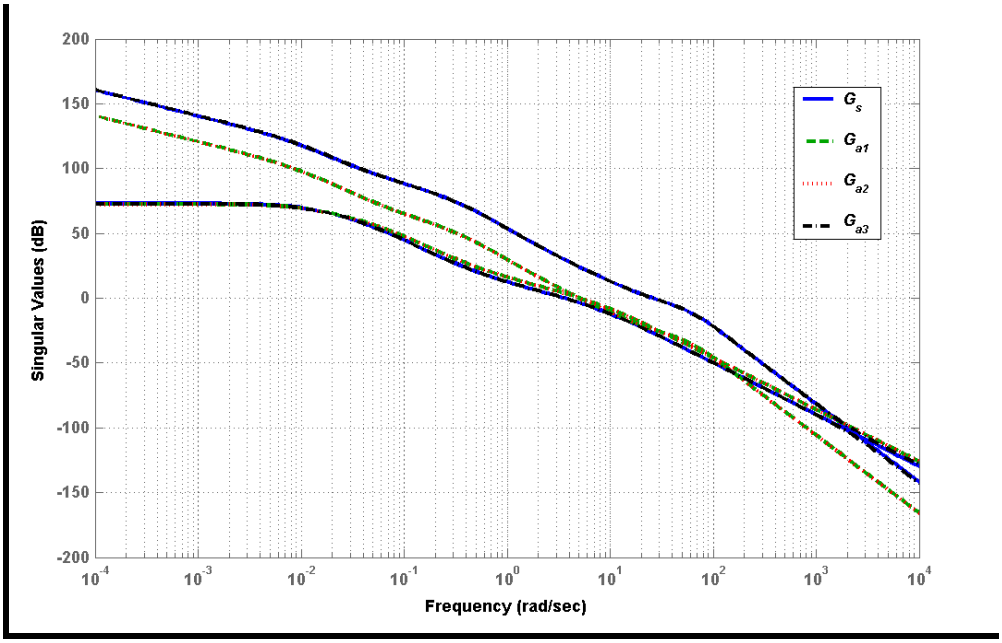

Figure 5.7: Alignment effect on shaped model principal SV
G_s and G_{a3} are over-lapping , G_{a1} and G_{a2} are over-lapping

Figure 5.7 shows the effect of alignment on the open-loop principal SV of the shaped model. See how the alignment was achieved by having both G_{a1} and G_{a2} principal gains, $\bar{\sigma}$ and $\underline{\sigma}$, coincide at around ω_o. Note that G_s and G_{a3} over-lapping implies that decoupling did not alter the system principal gains. Also, G_{a1} and G_{a2} over-lapping implies that aligning airspeed and pitch attitude in G_{a1} has the major effect on model principal SV compared to G_{a2} full alignment.

Figure 5.8 shows the effect of alignment on the individual outputs. It can be seen that alignment was achieved by reducing the overall gains of pitch dynamics and height and slightly boosting the airspeed gain. Note that G_s and G_{a3} are over-lapping in Figure 5.8.

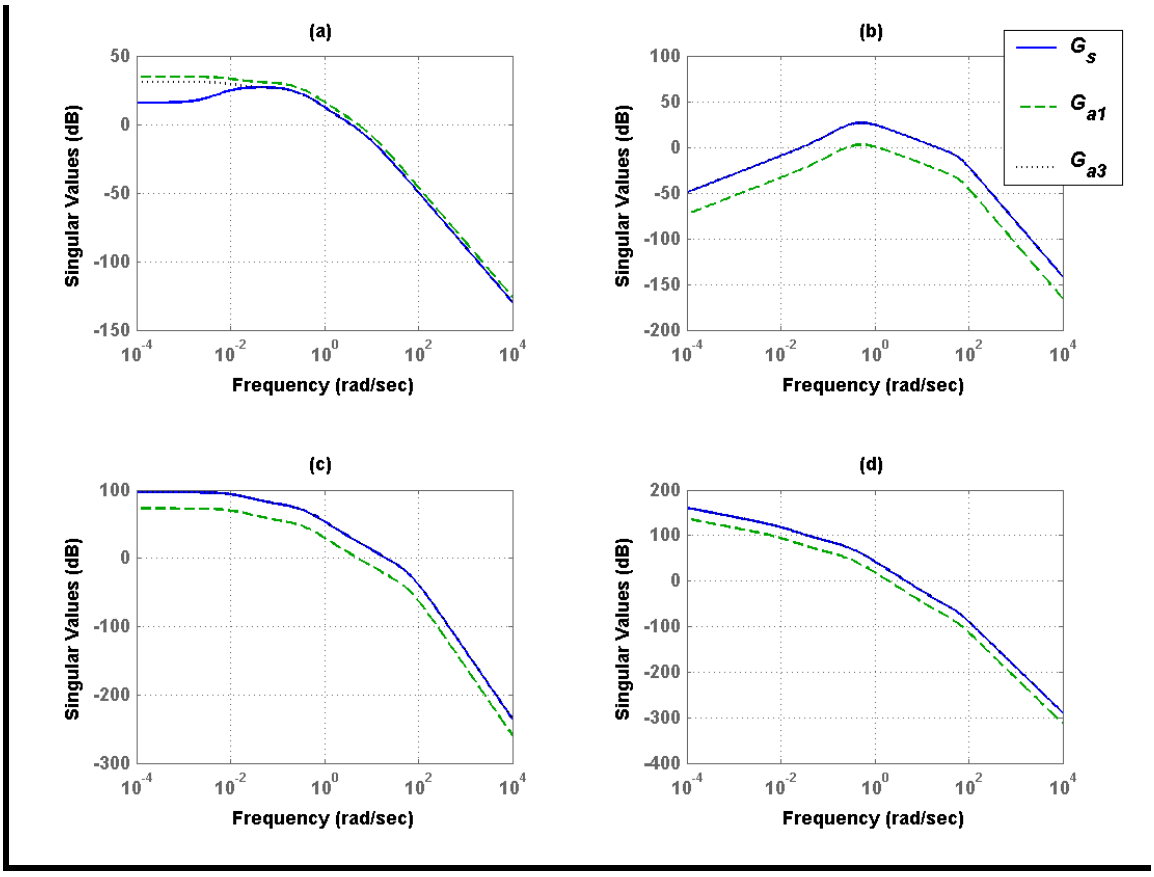

Figure 5.8: Alignment effect on each output of shaped model principal SV: (a) airspeed (b) pitch rate (c) pitch attitude (d) flight path height

5.5 Robust Stabilization

In this section, the scaled, shaped, and aligned model G_{a1} is robustly stabilized using Glover and McFarlane technique[27, 36, 37, 39], described in §2.4.

Let the final weighted model be,

$$G_w := G_{a1} = W_{2s}\, W_{2c}\, G\, W_{1c}\, W_{1s}\, W_{a1} \qquad \textbf{5.14}$$

The maximum stability margin ε_{max} is first calculated using MATLAB function `ncfsyn`[53]

$$[K_\infty, \varepsilon_{max}] = \texttt{ncfsyn}(G_w, 1) \qquad \textbf{5.15}$$

Note that the second input argument in Equation 5.15 (i.e. 1) is to indicate that the optimum solution, which gives $\varepsilon_{max} = 1/\gamma_{min}$, is solved. . The resulting controller has a maximum stability margin of:

$$\varepsilon_{max} = 0.3;\ \gamma_{min} = 3.34 \qquad \textbf{5.16}$$

where, as a rule of thumb, when $\varepsilon > 0.25$ or $\gamma < 4$, the design is usually successful[39].

Next, the sub-optimal solution for the robust stabilization problem is solved as discussed in §2.4. This is done by setting a sub-optimal value of $\gamma > \gamma_{min}$, say $\gamma = 1.1\gamma_{min}$, in the solution for the central controller K_s , in Equation 2.6 in §2.4. Thus, the function `ncfsyn` is used again as

$$[K_s, \varepsilon_{max}] = \texttt{ncfsyn}(G_w, 1.1) \qquad \textbf{5.17}$$

where the second input argument in Equation 5.17 (i.e. 1.1) is to indicate that the sub-optimal solution is solved with a 10% less performance than optimum.

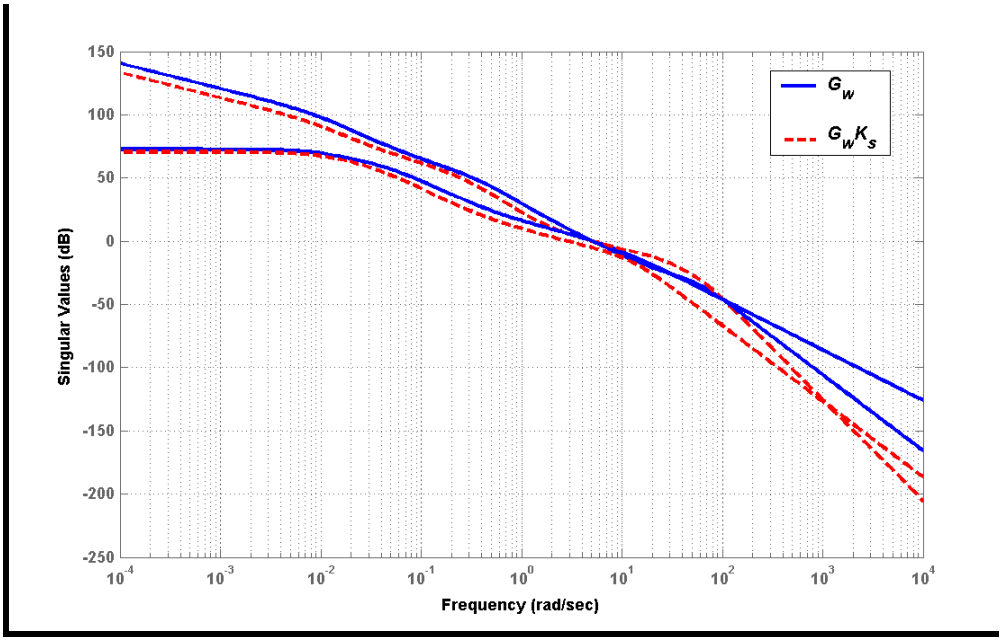

Figure 5.9: Controller effect on weighted model principal SVs

Figure 5.9 shows how the controller had slightly altered the shaped system principal SV. Mainly, the controller has,

- reduced over-all gain and bandwidth
- added low-pass filter for high frequency attenuation
- reduced gain cross-over slope

Figure 5.10 shows the effect of the controller on each output gain of the shaped/scaled model. Note how low-pass filters were added on all channels, while extra integration was only added to the airspeed loop at Figure 5.10.a. Figure 5.10.b shows how the controller reduced the attitude rate gain to improve stability. Also note that height loop gain cross-over frequency in Figure 5.10.d. was slightly reduced compared to the airspeed loop in Figure 5.10.a, while the attitude loop gain cross-over frequency in Figure 5.10.c was actually increased. This indicates that the stability is more sensitive to height loop bandwidth than the airspeed loop. Finally, the gain cross-over slope for each loop was also reduced as the principal gains have shown in Figure 5.9.

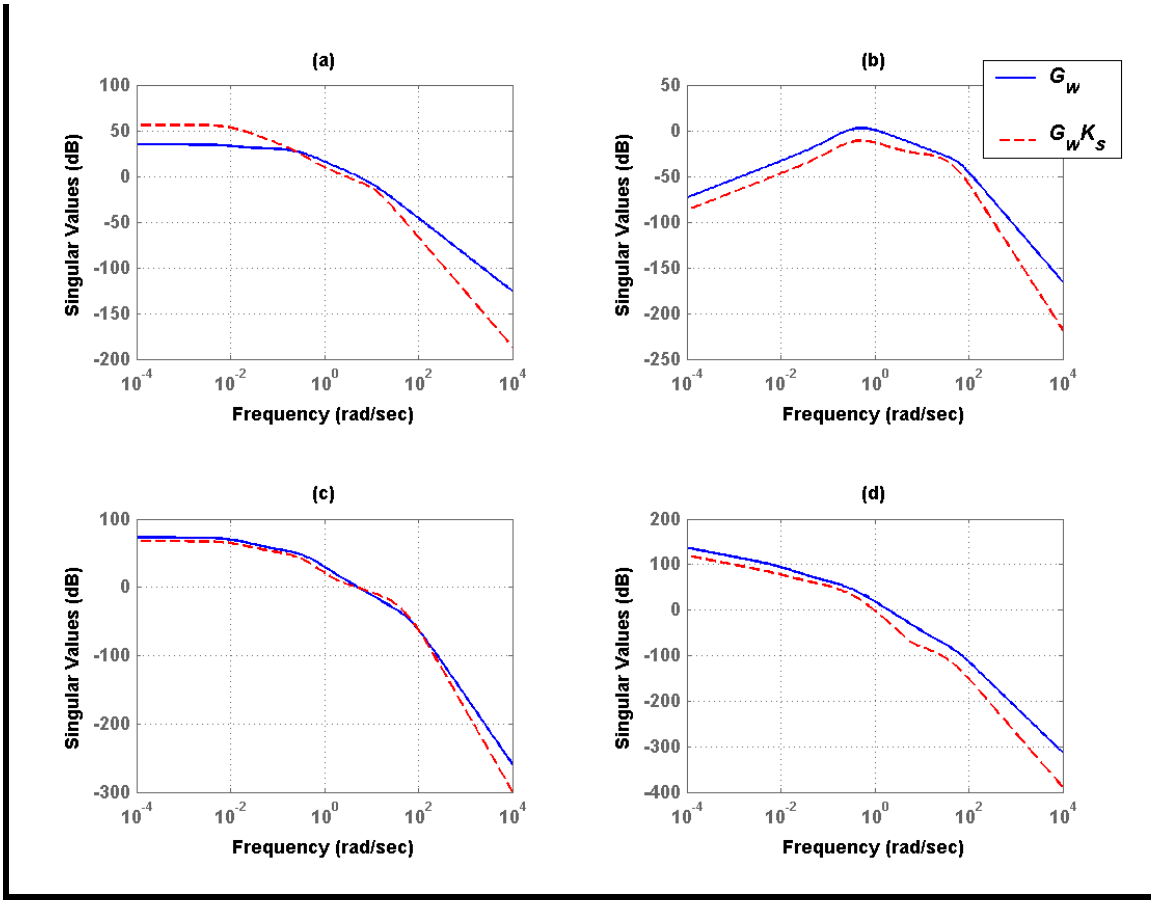

Figure 5.10:Controller effect on individual outputs of weighted model principal SVs : (a) airspeed (b) pitch rate (c) pitch attitude (d) flight path height

The stability margin(*SM*) introduced in §2.10, is now calculated for classical gain and phase margins comparison. Given the stability margin[50, 60]

$$SM = b(G_w, K_s) = \left\| \begin{bmatrix} I \\ K_s \end{bmatrix} \left(I - G_w K_s\right)^{-1} \begin{bmatrix} G_w & I \end{bmatrix} \right\|_\infty^{-1} = 0.274 \qquad \textbf{5.18}$$

the approximately equivalent classical gain and phase margin are

$$\begin{aligned} GM &\geq \frac{1+SM}{1-SM} = 4.88\,\text{dB}, \\ PM &\geq 2\arcsin(SM) = 31.78\,\text{deg} \end{aligned} \qquad \textbf{5.19}$$

Note that the values in Equation 5.19 are the guaranteed lower bounds of *GM* and *PM*.

5.6 Controller Implementation

Before evaluating the closed-loop system, it is important to discuss how the controller is implemented in the loop. It was shown in §2.7, that the observer-form structure implementation has several advantages including:

- gain-scheduling implementation capability
- anti-windup implementation capability
- well behaved tracking response[50, 60]

That makes it more appealing than the conventional implementation in the forward path, where the controller usually acts as a regulator rather than a command follower. So it was decided to implement the observer-form structure in this design phase, which is shown in Figure 2.12 and repeated here for clarity in Figure 5.11 below.

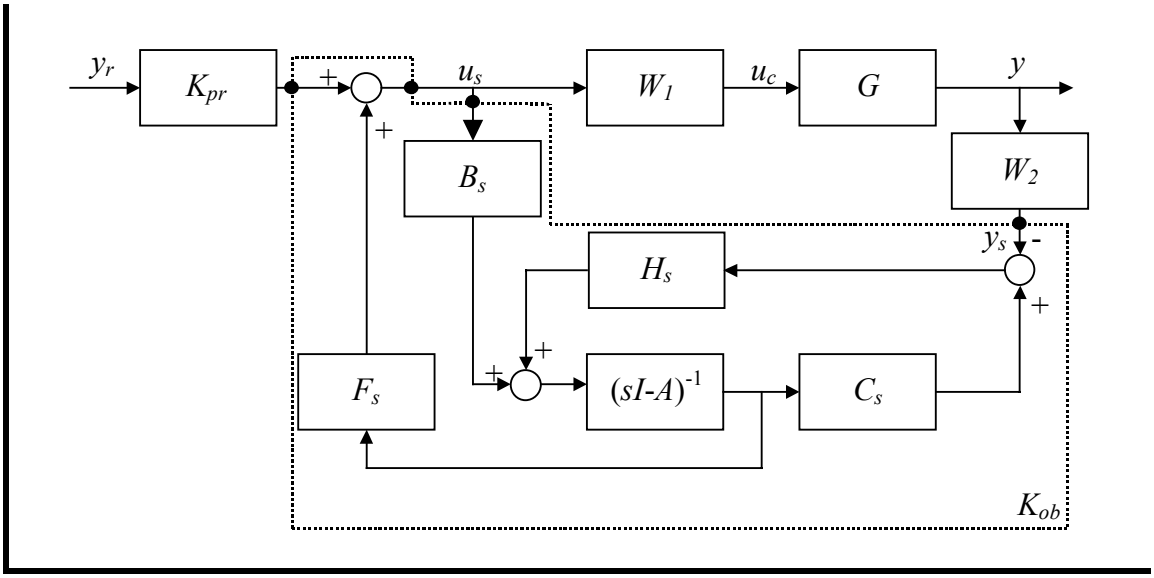

Figure 5.11: Observer-form controller K_{ob}

The following MATLAB function[53] produces the observer controller K_{ob}

$$[K_s, \varepsilon_{\max}, K_{ob}] = \texttt{ncfsyn}(G_w, 1.1, \texttt{'ref'}) \qquad \textbf{5.20}$$

The third input argument in Equation 5.20 is to include the extra command reference vector to obtain the observer-form controller. Note that K_{ob} has, as shown in Figure 5.11, three inputs: model output y_m , reference demand y_D , and control command u_s. Although K_{ob} output u_s is initially the same as the control command input, it has an advantage in the anti-windup implementation where the actual limited input will be used to drive the observer model, as will be shown later on. The command pre-weight K_{pr} in Figure 5.11 is used to insure unity gain at DC between command input and the controlled outputs which are airspeed and flight path height.

5.7 Controlled System Time Response

In this section, the step response of the initial robust controller is evaluated using the flight envelope nominal and worst-case air vehicle models.

5.7.1 Nominal Design Model Evaluation

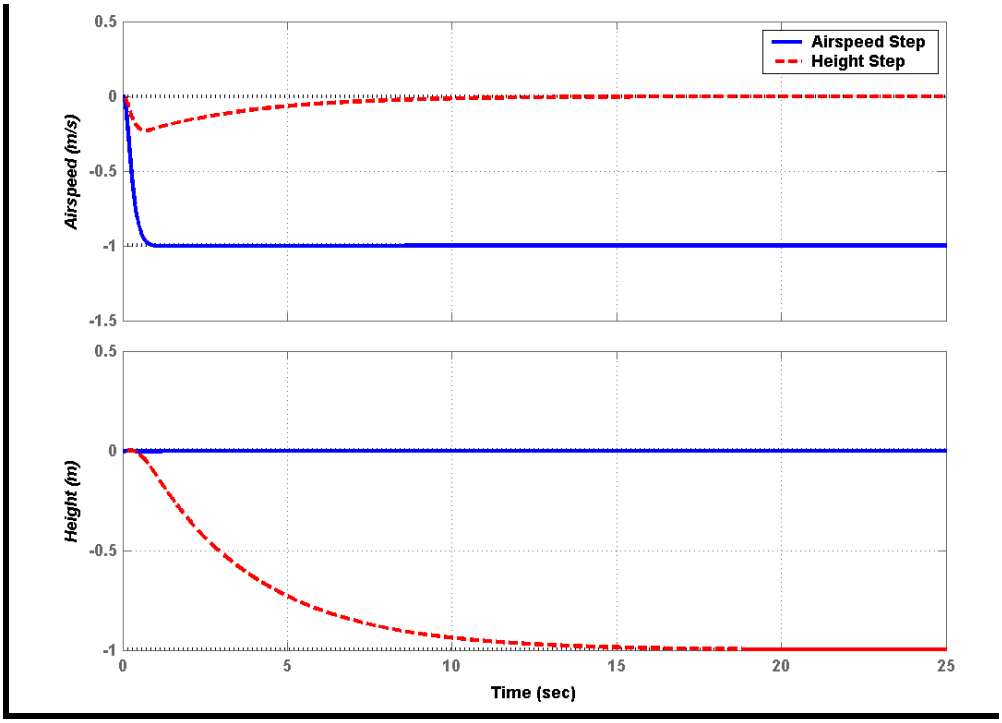

Figure 5.12: Controlled nominal system response to airspeed *u* and height *h* step demands

Figure 5.12 above, shows demanded airspeed and height response of the controlled nominal air vehicle model. As an initial design, the response demonstrates well-behaved characteristics while keeping a good decoupling level.

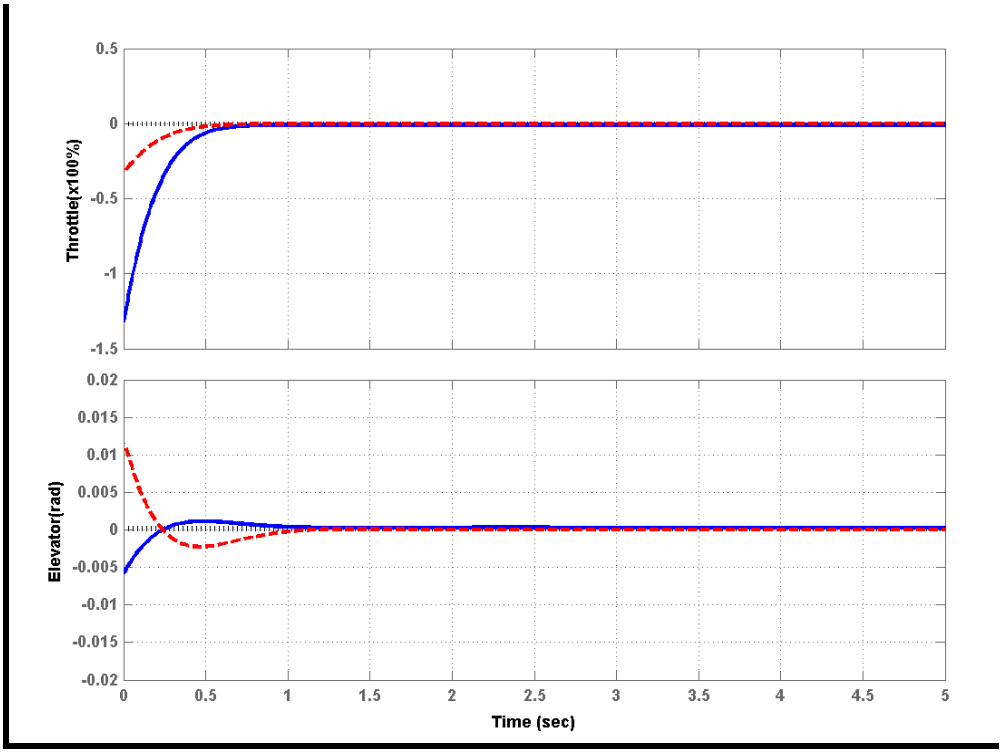

Figure 5.13: Controlled nominal system throttle τ and elevator η response to airspeed and height step demands

Actuator activities in Figure 5.13 show that throttle demand was extremely high and fast while trying to respond to the airspeed demand. This is a sign of actuator saturation and wind-up. If applied in the non-linear simulation or real system, it must be taken into consideration.

Figure 5.14 below, shows the pitch rate q and attitude θ response to the demanded airspeed and height steps. Initially, q response show no signs of instability and θ had acceptable amplitude.

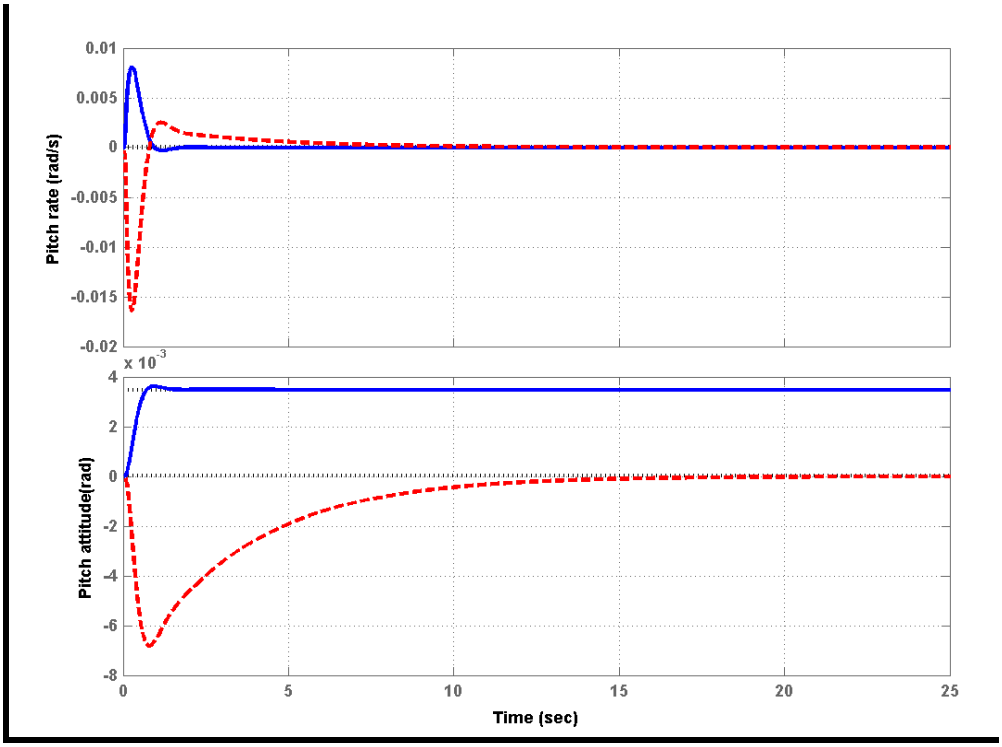

Figure 5.14:Controlled nominal system pitch attitude θ and rate q response to airspeed and height step demands

Recall that in Figure 5.10, it was shown that the robust stabilization controller reduced the bandwidth of the height loop more than the airspeed loop to ensure stability. This is clearly demonstrated in their time responses in Figure 5.12.

5.7.2 Flight Envelope Worst-Case Models Evaluation

The preliminary robust controller is evaluated here using the air vehicle worst-case flight envelope models developed in Chapter 4. The responses for a unit step demand of airspeed and height are shown in Figure 5.15. The results show that the demand tracking performance for the slow airspeed model $G_{25\mathrm{Pz}}$ degraded more severely than the high airspeed model $G_{45\mathrm{Mz}}$. This includes the steady-state values and the decoupling between the controlled variables, airspeed and height. Note that the pre-weight K_{pr} in Figure 5.11 is used to insure unity gain at DC between command input and the controlled outputs, was not recalculated for the worst-case models which greatly contributes to the large steady-state errors and coupling encountered here.

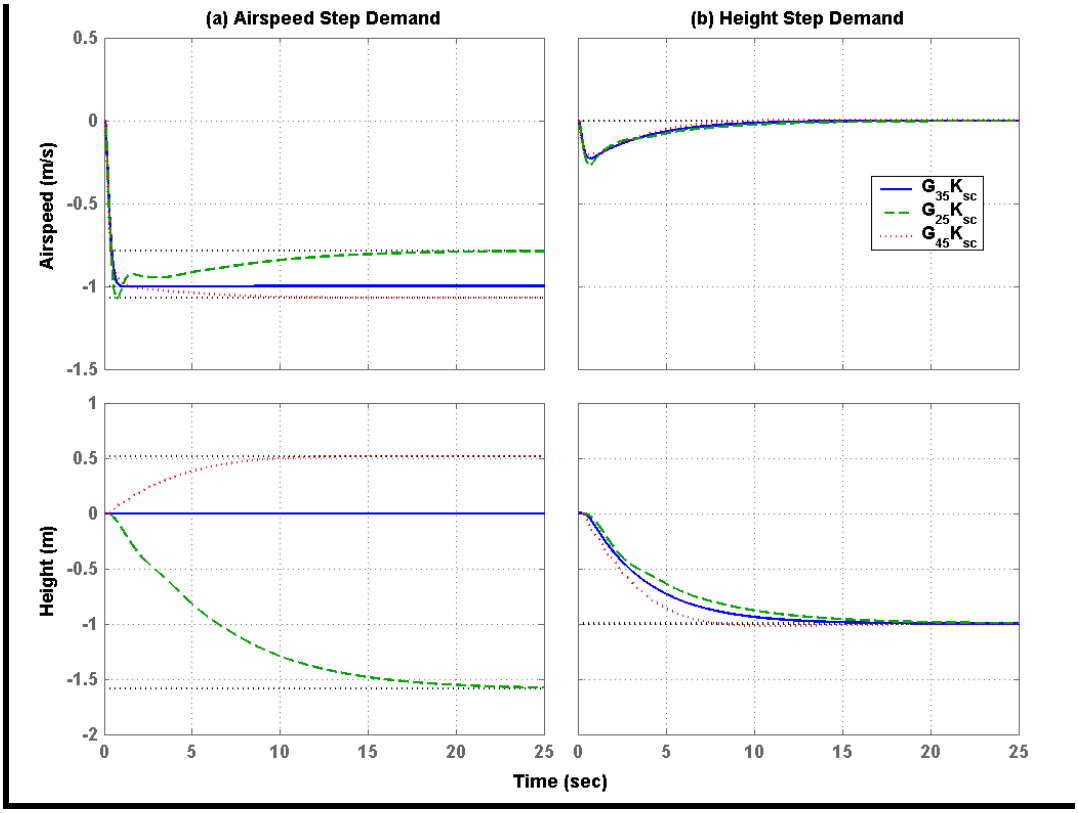

Figure 5.15: Control design evaluation with flight envelope nominal and worst-case models

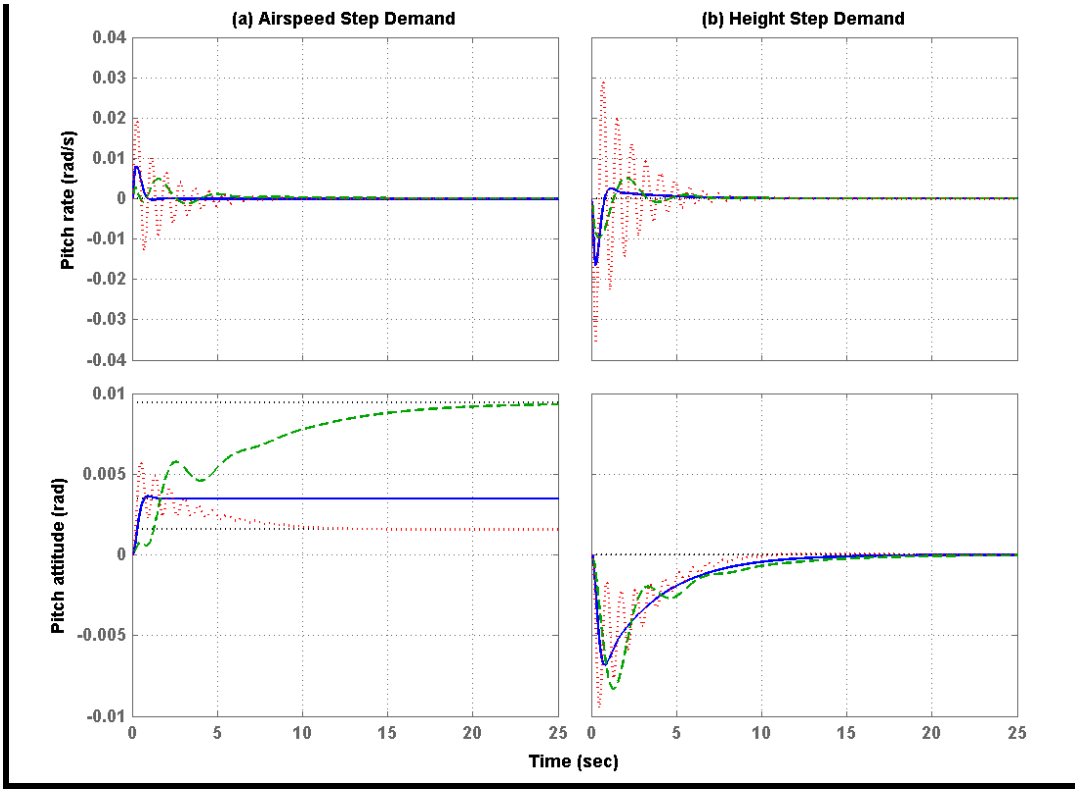

Figure 5.16: Control design evaluation with flight envelope nominal and worst-case models

The air vehicle attitude rate and angle response in Figure 5.16 and the actuators activities in Figure 5.17 show clear signs of instability in the high speed model and sluggishness in the low speed model as expected.

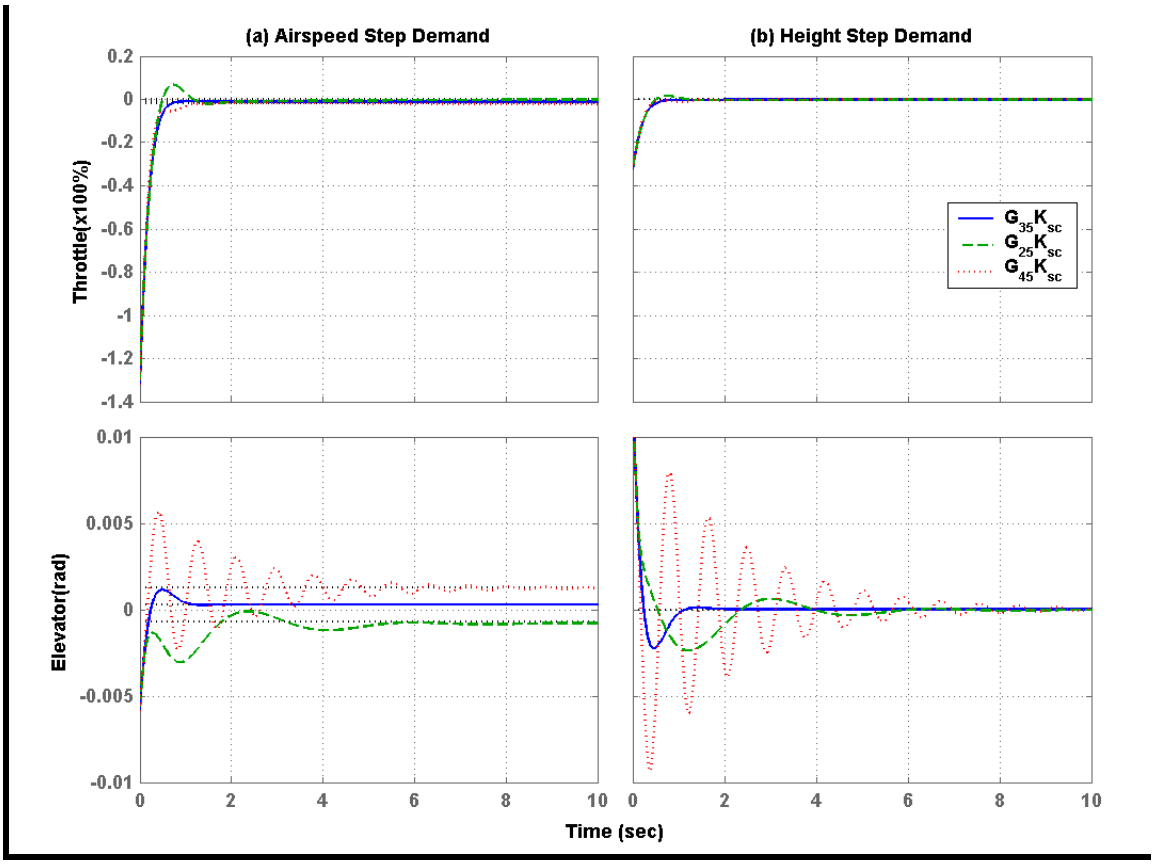

Figure 5.17: Throttle τ and elevator η activities of worst-case models response

Note that the throttle τ and elevator η activi1ty plots in Figure 5.17 show the first 10 seconds of response only where most of the activity takes place.

It is important here to recall the ν-gap distances these models have from the nominal model as discussed in §4.9.2. It was shown in Table 4.3, for the worst-case models: Case 2 and 9, their ν-gap distances from the nominal, which are repeated here in Table 5.2 for convenience.

Table 5.2 : Worst-case models *v*-gap distances from nominal

Case	Model	*v*-Gap from Nominal G
2	G_{25Pz}	**0.382**
9	G_{45Mz}	**0.267**

The values in Table 5.2 can be interpreted as follows: A robust controller K_s, designed with the nominal model G must have a *SM* $b(G,K_s)\geq 0.382$ for guaranteed stability of G_{25Pz} , and $b(G,K_s)\geq 0.267$ for guaranteed stability of G_{45Mz}. Recalling Equation 5.18, we have $b(G,K_s)=0.274$ and this fairly agrees with the step response results. That is, the low speed model G_{25Pz} performance was degraded more than the high speed model G_{45Mz} in terms of airspeed and height response. But the latter had high frequency signs of instability compared to the low speed model. Recall that it was shown in §4.9.2, and in Table 4.4, that the high speed model had moved the unstable *phugoid* mode pole from 0.2*rad*/*s* to 2.23*rad*/*s* in the RHP, while the low speed model G_{25Pz} pushed it into the stable LHP to 0.55*rad*/*s*.

5.8 Controller Modification

Before the controller is modified or adjusted, it is important to discuss the outcome of the results from the previous sections in general terms:

- Although the design procedure followed in the above sections did not produce a perfect controller, it has achieved a good initial system that could be fine tuned and adjusted for the particular situations and requirements.
- It was relatively a long process before knowing how well every decision and assumption in each step was. So it was thought more appropriate to modify the design procedure to be able to get some kind of insight at every design step. This is discussed in more detail later in this section.
- Having more information about the air vehicle flight envelope is essential to design a robust controller that will have acceptable performance throughout the whole envelope.

- The *v*-gap distance measurement is an important tool for understanding the behaviour of the controller design with the different models that represent the expected flight envelope.
- The classical effect of SISO unstable poles and zeros and how to deal with them is also valid for the MIMO design.

5.8.1 Design Procedure Modification

Here, a simple modification on the design procedure is introduced and applied to readjust and fine-tune the initial robust controller design.

5.8.1.1 Robust Stabilization Calculation

It is shown in Figure 5.9 and Figure 5.10 that the modifications the controller makes to the open-loop SV of the air vehicle model have important interpretations in regard to the robust stability requirements. Thus it was thought adequate to calculate the robust controller at each design stage (i.e. scaling, shaping, alignment etc.) and to plot the effect of the robust controller on the open-loop SV for each stage model. This gives strong indications on where the improvements should be and an evaluation at these early stages of design raises awareness of any stability problems that arise. Table 5.3 below shows how *SM*, calculated using Equations 5.18 and 5.19, was affected at each design stage. From Table 5.3 it is clear that the scaling step contributes inversely to the stability of the controlled system(i.e. 0.09<0.16), while shaping and alignment have recovered the *SM* rather nicely (i.e. 0.22>0.09 and 0.27>0.22).

Table 5.3 : Design stage effects on stability margins

Design Stage	Model used in Equation	*SM*	*GM* / *PM* dB / Deg
Basic Model	$b(G,K)$	0.16	2.74 / 18.02
Scaling	$b(G_c,K)$	0.09	1.54 / 10.13
Shaping	$b(G_s,K)$	0.22	3.81 / 24.94
Alignment	$b(G_{a1},K)$	0.27	4.88 / 31.78

5.8.1.2 Flight Envelope Models Utilization

When designing a flight control system for a certain flight envelope using the air vehicle models that represent that envelope, it is important to use the worst-case models in the design stages. This helps ensure that the controller designed will perform at acceptable levels in these flight conditions.

Table 5.4 : Worst-case models stability margins

Model	*SM*	*GM* / *PM* dB / Deg
$b(G_{25Pz},K_s)$	**0.15**	**2.69 / 17.66**
$b(G_{45Mz},K_s)$	**0.03**	**0.54 / 3.55**

Table 5.4 shows how the initial robust controller was predicted to perform on the worst-case flight envelope models. It is obvious from Table 5.4 that these values are essential in the design phase and would have predicted the poor performance in an early stage of the design process.

5.8.1.3 RHP-Poles and Zeros

RHP-poles and zeros play an important role in the design of any flight control system. Here, the classical rules of thumb will be reviewed as they are also valid for the robust control design[39]:

- For a real RHP-pole at $s=p$: the open-loop principal gain cross-over frequency should approximately $\omega_{cross} > 2p$. For imaginary RHP-poles $\omega_{cross} > |p|$.
- For a real RHP-zero at $s=z$: $\omega_{cross} < |z|/2$. For a complex pair:
  - i. $\omega_{cross} < |z|/4$ if $\mathrm{Re}(z) >> \mathrm{Im}(z)$
  - ii. $\omega_{cross} < |z|/2.8$ if $\mathrm{Re}(z) = \mathrm{Im}(z)$
  - iii. $\omega_{cross} < |z|$ if $\mathrm{Re}(z) >> \mathrm{Im}(z)$
- For a controller with the computation time delay approximated by a second order Padé function, which has a complex RHP-zero pair at 100 *rad/s* in this thesis, approximately $\omega_{cross} < |z|/3$.

- For a model that has both a RHP-pole at p and a RHP-zero at z, it must have $z>4p$ to be controlled by a stable controller (i.e. *strongly stabilizable*). Note that the gain cross-over frequency can approximately represent the closed-loop bandwidth in the above rules.

In light of the above rules, it is important to draw these limits using the worst-case flight envelope models to ensure proper controller performance and stability for the whole flight envelope.

5.8.2 Controller Adjustments

Here, the initial robust controller is modified and adjusted using the above techniques and rules. It must be admitted that the adjustment process was somewhat involved and the final results are presented here.

It was found that proper scaling, integral action, along with robust stabilization would produce a well-behaved robust controller, without the need to add low-pass filters where the robust stabilization process adds these filters to the design model to give the desired performance and stability as seen back in Figure 5.9. The final input/output scaling and shaping weights that were used are given by:

$$\begin{aligned} W_{1c} &= \mathtt{diag}\begin{bmatrix} 4 & .2 \end{bmatrix} \\ W_{2c} &= \mathtt{diag}\begin{bmatrix} .04 & 3 & 2 & .03 \end{bmatrix} \end{aligned} \tag{5.21}$$

$$\begin{aligned} W_{1s} &= \mathtt{diag}\left[\frac{s+.3}{s+.0001} \quad \frac{s+.1}{s+.0001} \right] \\ W_{2s} &= \mathtt{diag}\left[1 \quad \frac{s+.0001}{s+.1} \quad 1 \quad 1 \right] \end{aligned} \tag{5.22}$$

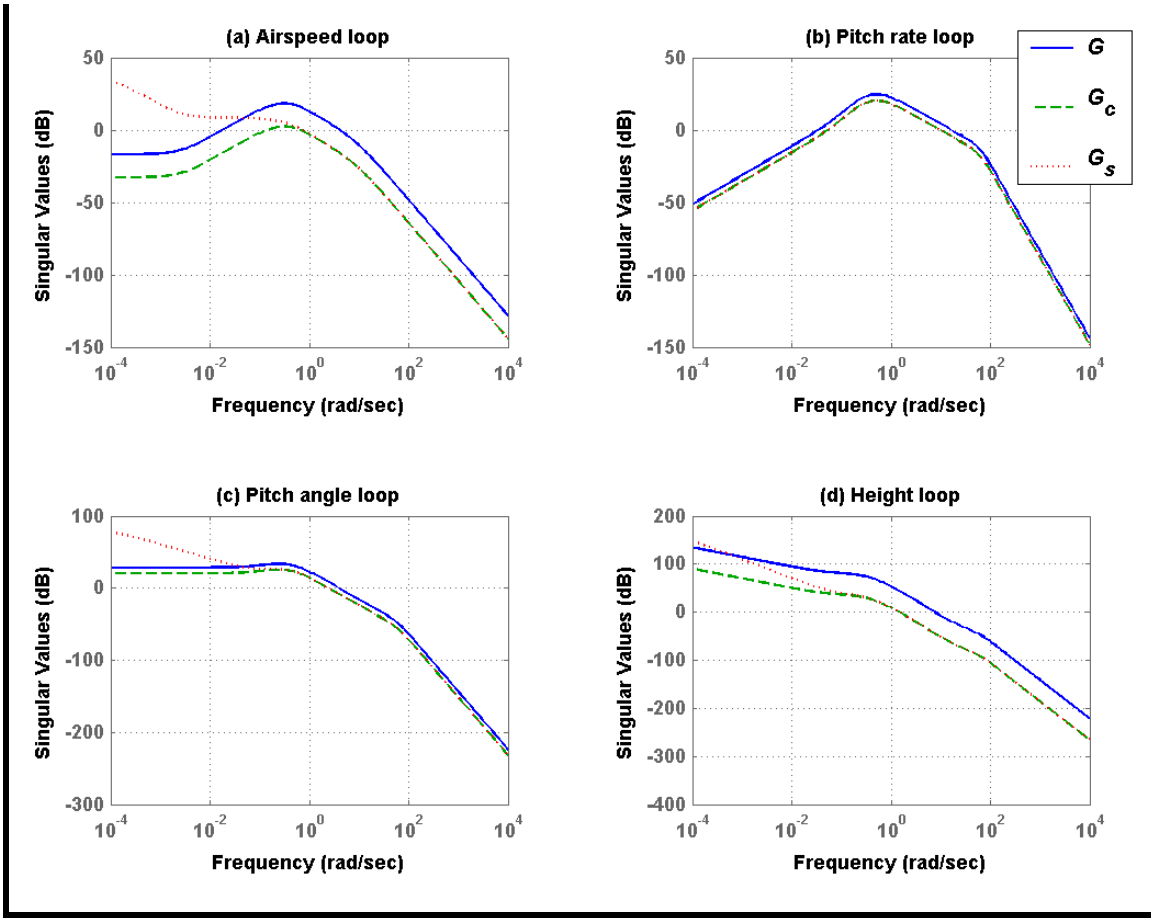

Figure 5.18: Scaling and shaping effect on model open-loop SVs: (a) airspeed loop u/τ (b) pitch rate loop q/η (c) pitch angle loop θ/η (d) height loop h/η

Figure 5.18 shows the scaling and shaping effects on the open-loop the air vehicle model. Notice how the main controlled output variable (i.e. airspeed and height) gains were reduced significantly compared to attitude rate and angle outputs while the integral weights boosted the low frequency gains.

The robust stabilization was done using the modified weighted model G_w,

$$G_w := G_s = W_{2s} W_{2c} G W_{1c} W_{1s} \qquad \textbf{5.23}$$

The achieved stabilities are shown in Table 5.6.

Table 5.5 : Controller stability margins

Design Stage	Model used in Equation	*SM*	*GM* / *PM* dB / Deg
Basic Model	$b(G,K)$	.16	2.74 / 18.0
Scaling	$b(G_c,K)$	.37	6.86 / 44.1
Shaping	$b(G_s,K)$	.36	6.48 / 41.8

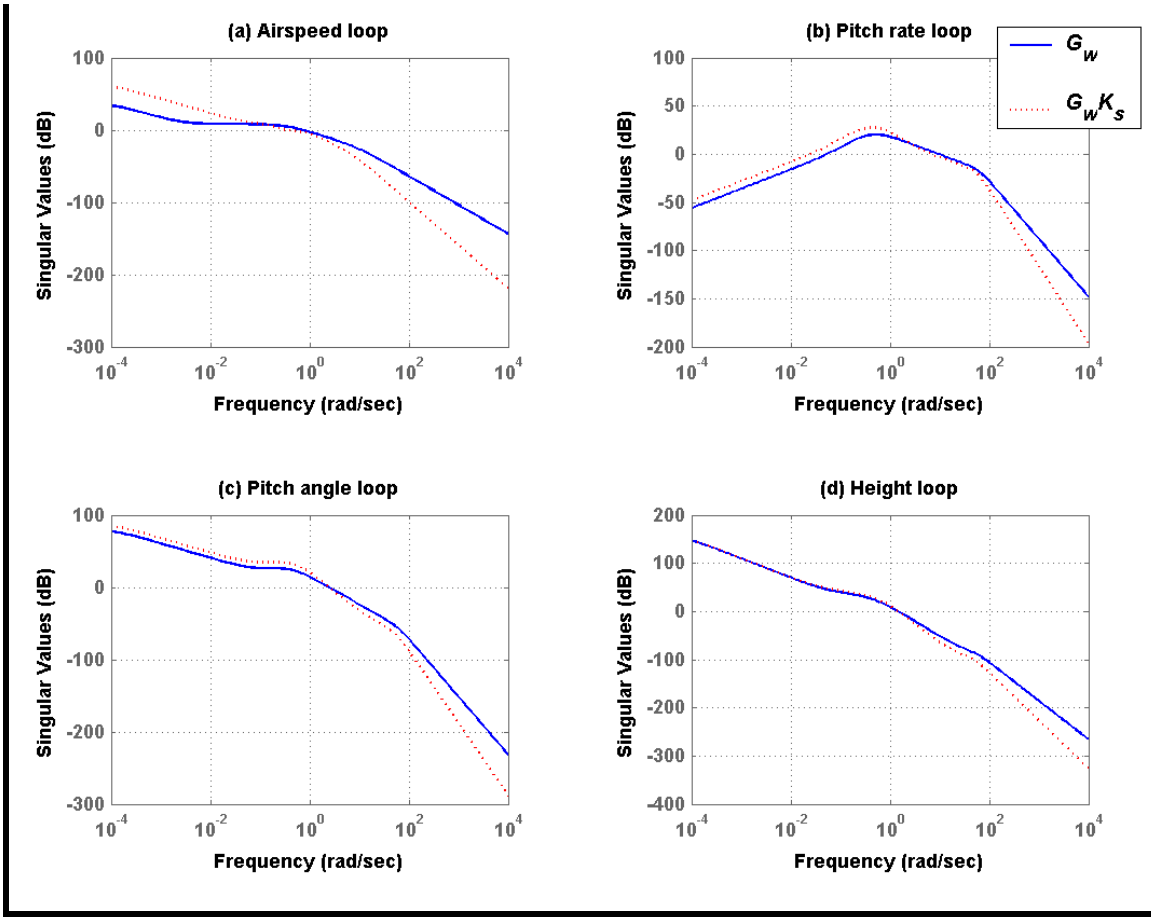

Figure 5.19: Controller effect on open-loop SV

The modified controller effect on the shaped model G_w open-loop SVs is shown in Figure 5.19. Notice the added integral action in the airspeed loop and the low-pass filter to all channels. The new controller worst-case models stability is shown in Table 5.6.

Table 5.6 : Controller worst-case models stability margins

Model	*SM*	*GM* / *PM* dB / Deg
$b(G_{25Pz},K_s)$	**0.30**	**5.3 / 34.5**
$b(G_{45Mz},K_s)$	**0.21**	**3.7 / 24.5**

The above results clearly show a real enhancement over the initial robust controller designed previously.

5.8.3 Controller Evaluation

Here, the modified controller will be evaluated using a simultaneous airspeed and height unit step demand using the nominal and the worst-case air vehicle models. This helps to excite the coupling between the two loops for evaluation. It is important to point out here that as the new controller was implemented in the observer form, as in Figure 5.11, the command pre-weight K_{pr} was recalculated using airspeed effect only. That is K_{pr} was recalculated at 25 and 45*m*/*s* but with the nominal X_{CG} position. This is justified by the fact that the command pre-weight K_{pr} can be scheduled for the airspeed in the non-linear simulation and real flights.

Figure 5.20 below shows the controlled system response to the simultaneous airspeed and height step demand. $G_{35}K_{sc}$ indicates the controlled nominal air vehicle model system. Similarly, $G_{25}K_{sc}$ and $G_{45}K_{sc}$ are the controlled worst-case systems. These results show that the controller is capable of controlling the air vehicle for the full flight envelope defined by the nominal and worst-case models. Controller robust tracking performance is evident throughout the full flight envelope.

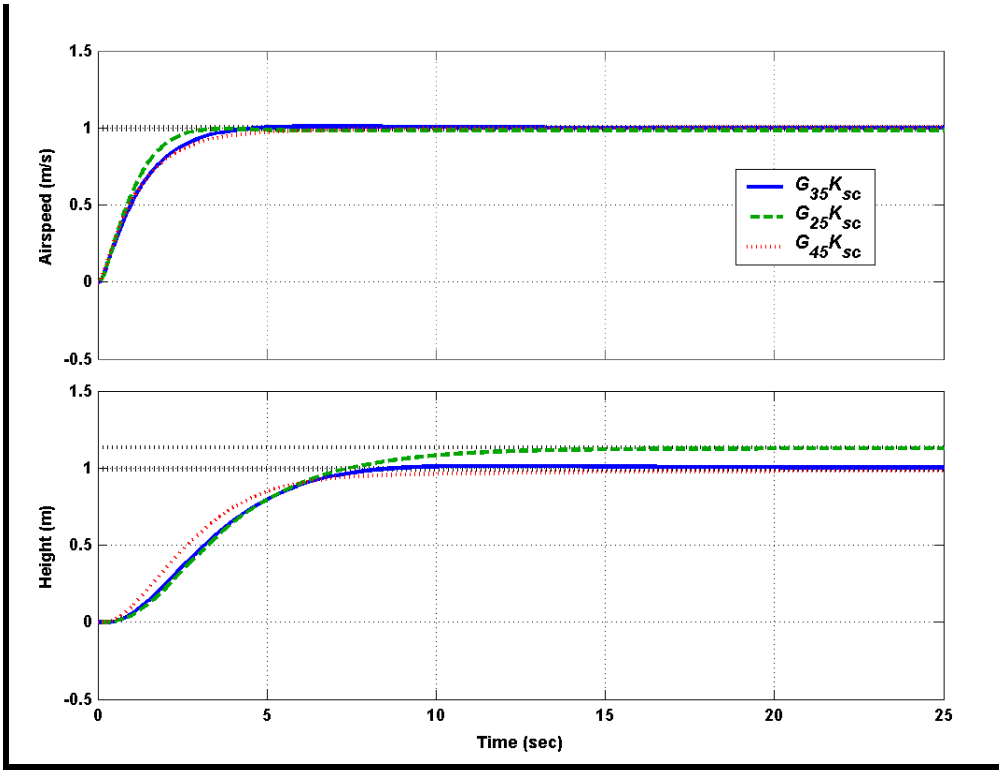

Figure 5.20: Controller response to simultaneous unit step demands of airspeed u and height h with nominal and worst-case models

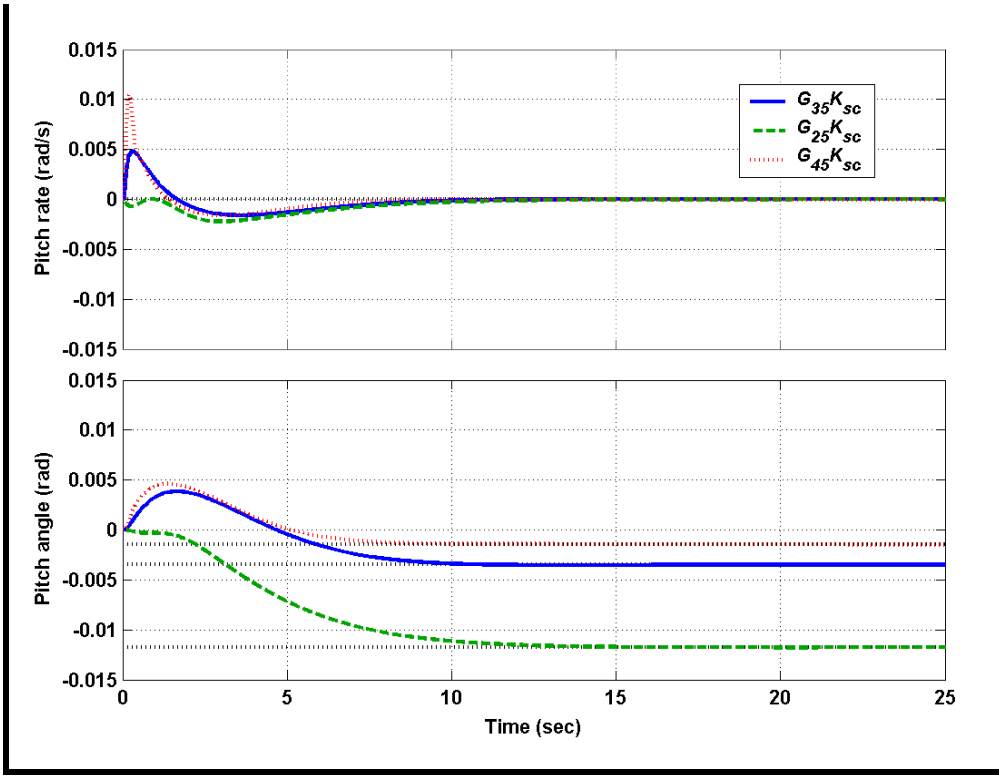

Figure 5.21:Pitch rate q and angle θ response of nominal and worst-case models

Figure 5.21 above shows the pitch rate q and angle θ response of nominal and worst-case models to the simultaneous airspeed and height unit step demand. These results clearly show the controller robust stability for the full flight envelope. Note that the steady-state values that the air vehicle attitude angles adapt in this manoeuvre are mainly due to the new airspeed that is reached. As the airspeed increases, the required angle of attack is reduced. Note also that all the outputs here are the perturbations from the trim values at each total airspeed. This is especially true for airspeed, attitude angle, and height outputs which would have significant trim values in the non-linear simulation and in real flights, as discussed in Chapter 4.

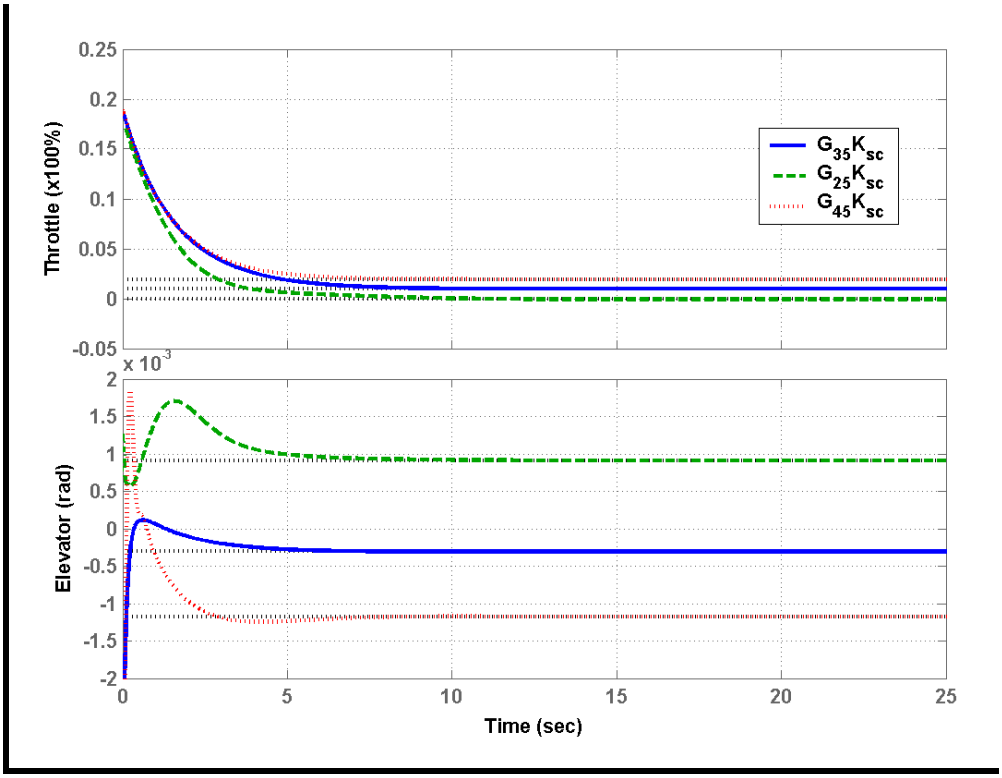

Figure 5.22: Throttle τ and elevator η response of nominal and worst-case models

Figure 5.22 shows the throttle τ and elevator η response to the simultaneous step demand. The results show adequate amplitudes for the manoeuvre performed. Note how the elevator trim changes to the new steady-state values, following the attitude angle trend in Figure 5.20. Again, the values shown here are the perturbations from the trim values at each airspeed which were shown in Chapter 4, and repeated here in Table 5.7

for clarity. These values will be adopted, as functions of airspeed, in the non-linear simulation and real flights.

Table 5.7: Nominal and worst-case models trim values

Dynamic Model	U_0 (m/s)	Θ_0 (rad)	τ_{Trim} $(\%)$	η_{Trim} (rad)
G_{25Pz}	25	0.06	10	-0.097
G_{35Az}	35	-0.016	16	-0.049
G_{45Mz}	45	-0.045	35	-0.029

5.9 Non-linear Simulation Evaluation

In this section the control system implementation in ACSL non-linear simulation is first discussed. Then, the performance is evaluated.

5.9.1 Controller Non-linear Implementation

The implementation process of any flight control system in the real and non-linear simulation environment is an essential task. A properly designed FCS in simplified linear environment could easily fail in real air vehicle and/or in non-linear simulation due to improper implementation. Here, the implementation process of the robust control system into the ACSL non-linear simulation environments is briefly discussed. The main implementation process steps are:

- Put the final controller in the state-space form:

$$\dot{x}_c = A_c x_c + B_c y_c$$
$$u_c = C_c x_c + D_c y_c$$

where the input vector y_c includes the measurement and demand vectors as: $y_c = [y_m \; y_D]$

- Discretize controller at the real control system processor frequency. In the ACSL non-linear simulation, the control system was modelled using the `DISCRETE` function with 16 *ms* interval which is equivalent to 62.5Hz. This was simply done using the MATLAB function `c2d`.

- Export the controller A, B, C, D matrices from MATLAB to ACSL using formatted ASCII files with a proper numerical format to be read accurately by ACSL. Note that real control system processors have limited word lengths, ACSL A3 non-linear simulation was built around single precision real variables. This meant that the exported stand-alone controller needs to be verified at that working precision. This was done by importing the controller back from ACSL to MATLAB and making the required tests and comparisons including the *v*-gap distance and the closed-loop time and frequency response until a satisfactory result was obtained with the right export numerical data format.

- Generate the required trim tables as functions of total airspeed in ACSL. These include throttle setting, elevator trim, attitude angle trim, and the command pre-weight K_{pr}. Note that X_{CG} was not part of the scheduling process. So any CG shift represents an unaccounted for uncertainty.

- Calculate the required linear feedback inputs to the new controller in ACSL on-line. These include measured and demanded airspeeds, measured attitude angle and measured and demanded heights with their respective signs.

- Implement the proper mixing strategy for the starboard and port actuators. For the longitudinal case, the elevator mixing was a simple unity vector,

$$\begin{Bmatrix} \eta_{SB} \\ \eta_P \end{Bmatrix}_A = M_{mix}^{-1} \{\eta\}_D = \begin{bmatrix} 1 & 1 \end{bmatrix}^T \eta_D$$

This is due to the fact that the controller was designed using a single actuator representation, as discussed in Chapter 4.

- Finally, ACSL capability was extended to be able to handle matrix operations more efficiently using its macro facility.

It must be stressed here again, that the implementation process was an involved time-consuming task. Simple improper implementation errors have been shown to cause chaotic effects on controller performance and response.

5.9.2 Controller Non-linear Evaluation

Here, the longitudinal controller is evaluated in the ACSL non-linear simulation. Initially, the controller was implemented in the forward path, i.e. it acts as a regulator, and the reference demands y_r act as a disturbance. This configuration had more stable response than the demanded input y_D configuration, which both are shown in Figure 5.23.

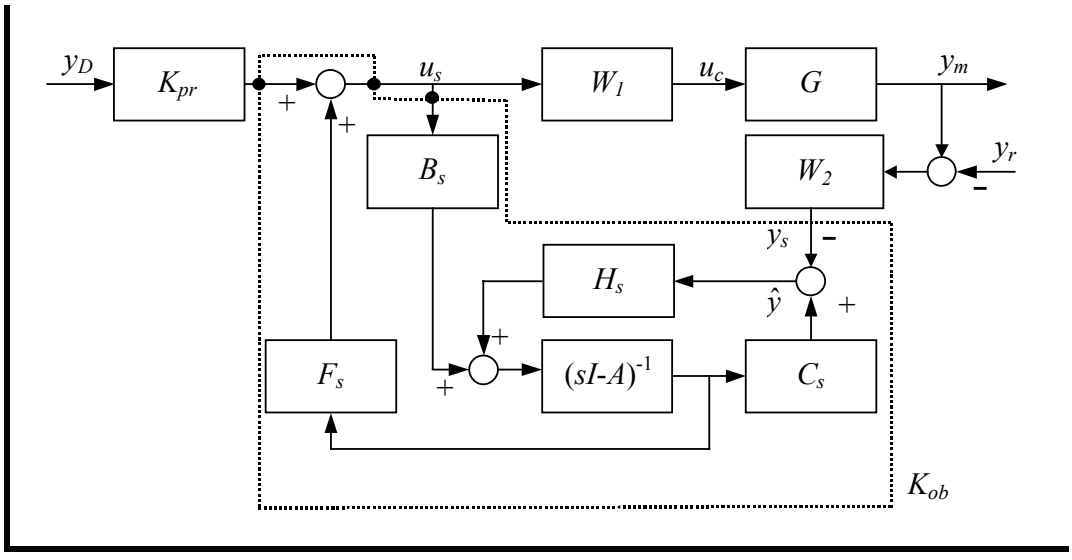

Figure 5.23: Controller demand and regulator inputs

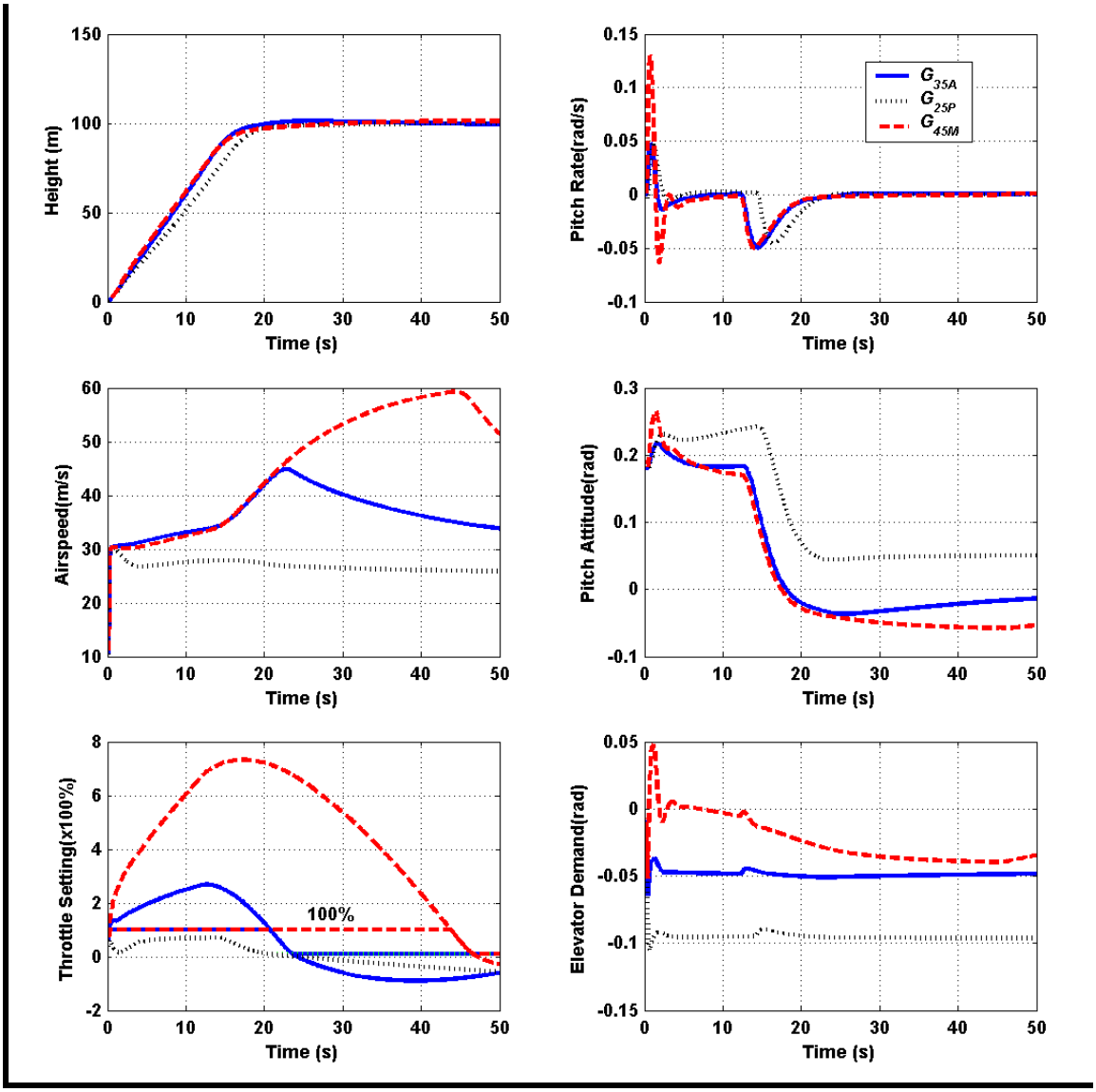

Figure 5.24: Initial Controller Response in the launch phase

The initial controller response in the launch phase is shown in Figure 5.24. Note that the launch phase is the most demanding stage of the controlled flight, where considerable and simultaneous changes in air vehicle dynamic parameters take place.

Figure 5.24 shows several important results:

1. Height response is fairly acceptable and as expected for the nominal and worst cases. While the low-speed worst-case model G_{25P} is a little lagging due to reduced airspeed and increased static stability.

2. Pitch rate activity at launch for the high-speed model G_{45M} is high as expected due to the reduced stability. Also, an undesirable initial elevator down demand was executed for this model run.
3. Pitch attitude and elevator steady-state trim values agree with the linear analysis.
4. Airspeed control shows an unacceptable response with high lag and overshoot. This is mainly due to the available throttle demand which has a threshold of 1 (i.e. full throttle of 100%). Note how the controller, as shown in the high-speed model response, exceeded this limit up to 8(800%!). Obviously, only full throttle of 100% was possible to execute. This throttle saturation situation led to the demand windup to the unrealistic 800% value.

Note that, while the airspeed control loop has a limited gain, it is required to have a wide-band response to act quickly at launch. These two contradicting requirements resulted in the saturation and windup of the throttle demand. Consequently, the Hanus anti-windup algorithm described in §2.9.1 and implemented in the observer-form in § 2.9.2, is introduced here, as shown in Figure 5.25, to help overcome the saturation and windup of the throttle demand.

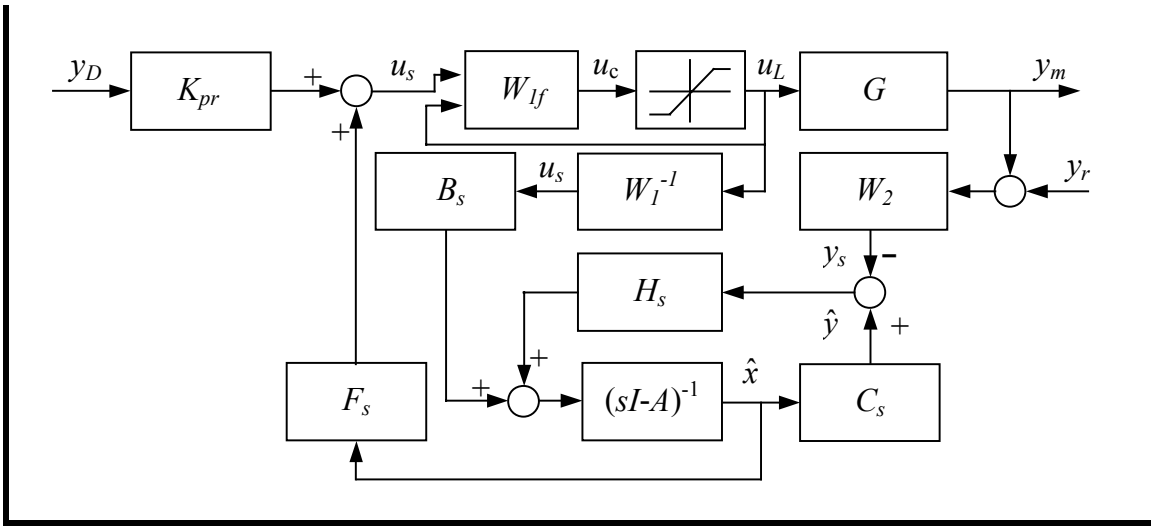

Figure 5.25: Observer-form with Hanus anti-windup

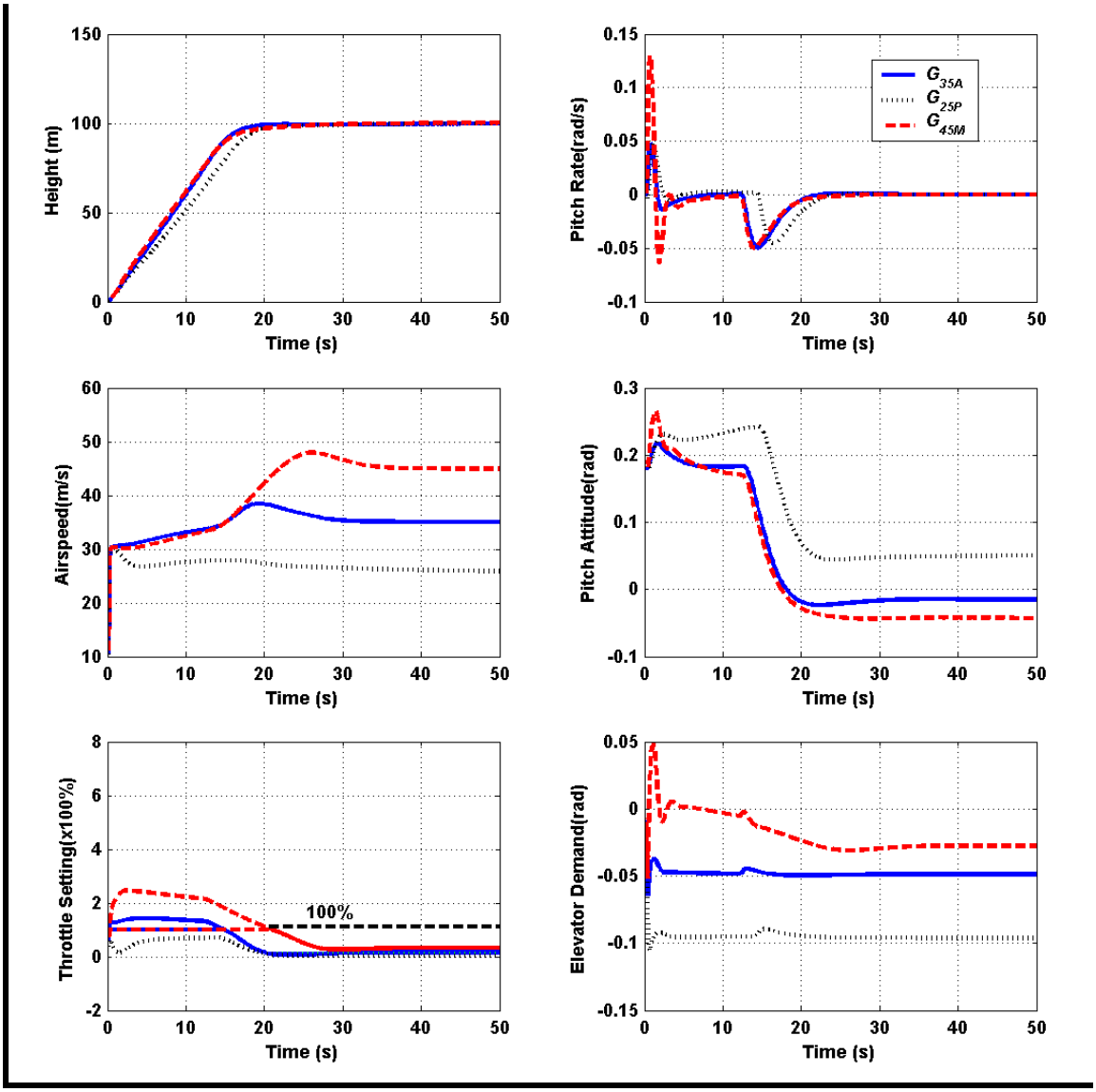

Figure 5.26: Anti-windup observer controller non-linear simulation

The modified controller performance is shown in Figure 5.26 for nominal and worst cases. Although the height response improvement is unnoticeable, the airspeed response is greatly improved. Even though the nominal and high speed models (i.e. G_{35A} and G_{45M}) have crossed the throttle threshold, they have reached the demanded airspeed within less than 30 seconds. Furthermore, G_{45M} required much less throttle demand using the Hanus anti-windup algorithm(i.e. 250% vs. 800%). Note that the coupling between the axial and longitudinal dynamics has been utilized by the controller by using throttle and elevator commands to track the height demand. Unlike the classical single-loop control design philosophy, multivariable designs can utilize such situations similar

to real manned aircraft pilots' climbing practice PAT: Power(throttle), Attitude(elevator) then Trim[78], while fine-tuning of the height tracking is done by elevator only.

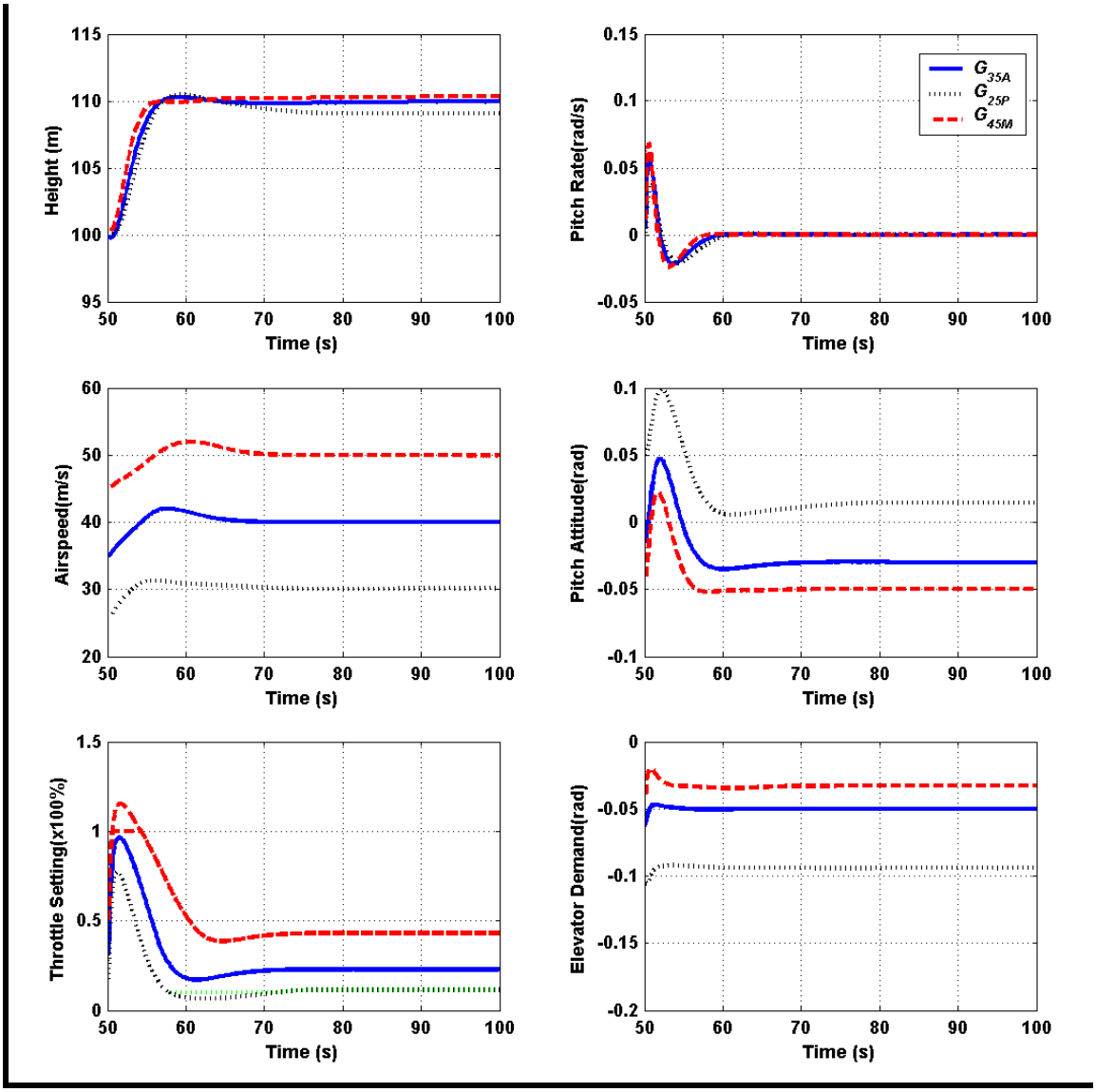

Figure 5.27: Non-linear simultaneous step response

Figure 5.27 shows the response to simultaneous steps to airspeed and height with Δu=5m/s and Δh=10m. These demands were executed after the air vehicle reached steady-state at 50s from launch, as shown in the time axis. Again, the response for the nominal and worst-case models is fairly reasonable and acceptable. Notice that the airspeed overshoot is due partly to the controller demand of throttle for height control.

5.10 Controller Order Reduction

One of the last processes in the flight control system design is the reduction of the control system order. It is well-known that modern control theories produce high order controllers compared to classical techniques. The $\mathcal{H}_\infty$ theory produces a controller that is the same order as the system model plus the added weights.

The controller order can be calculated as follows:

$$n_K = n_G + 2n_{W_1} + 2n_{W_2} \qquad \textbf{5.24}$$

Table 5.8 shows how the controller order is built-up. Note that the observer-form controller in Figure 5.25 included the inverse of the input weighting W_1, which also adds to the final stand-alone controller order as shown in Table 5.8 as well.

Table 5.8: Controller order build-up

Model	Order	Description	Controller Order
G	12	Air vehicle longitudinal model with single elevator actuator	=12
W_1	2	Input weighting (i.e. integrators etc.)	+2x2 =16
W_2	1	Output weighting (i.e. low-pass filters etc.)	+1x2 =18
W_1^{-1}	2	Inverse of input weighting for Observer-form feedback	+2 =20

Controller order reduction was done as follows:

- Calculate the balanced realization using the MATLAB `sysbal` function which also returns the Hankel SV of the system which can be examined for the order that the controller can be reduced to.
- Truncate the balanced system using MATLAB `strunc` function to the required order $<n_K$.

The reduced order controller is then tested as follows:

- Calculate the *v*-gap distance between the full and reduced order control systems.
- Compare the principal SV of the two systems.
- Compare closed-loop time responses with the air vehicle model.

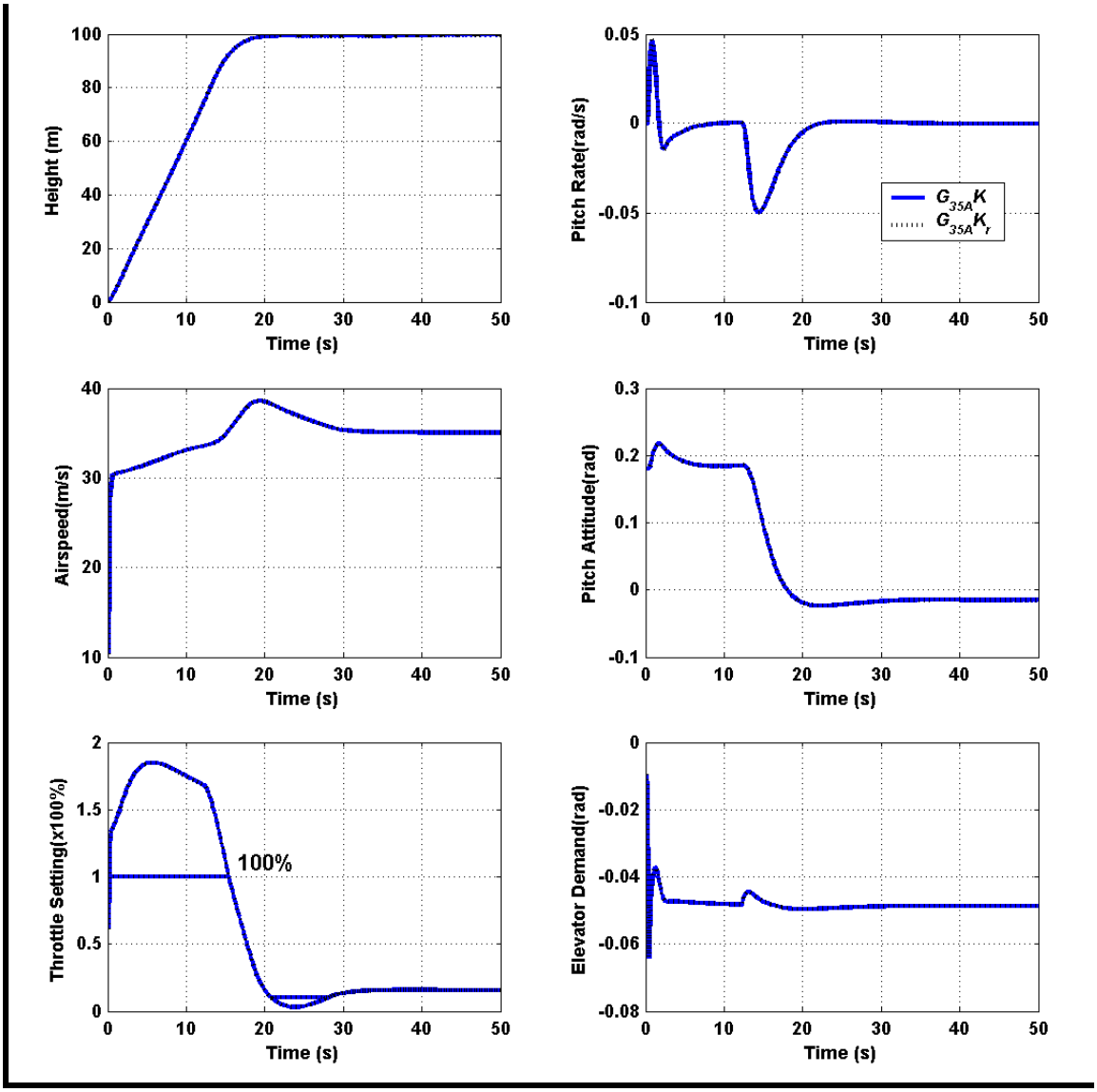

Figure 5.28: Full and reduced order controllers (K_{zob}, K_{zobr}) non-linear simulation response

Applying the above steps, the 20th order observer-form controller with anti-windup was possible to reduce to a 10th order system with the following results:

- Maximum Hankel SV truncated = 0.004
- Full- and reduced-order systems ν-gap distance = 0.0057
- Non-linear simulation time response curves were indistinguishable as shown in Figure 5.28.

5.10.1 Controller Maximum Condition Tests

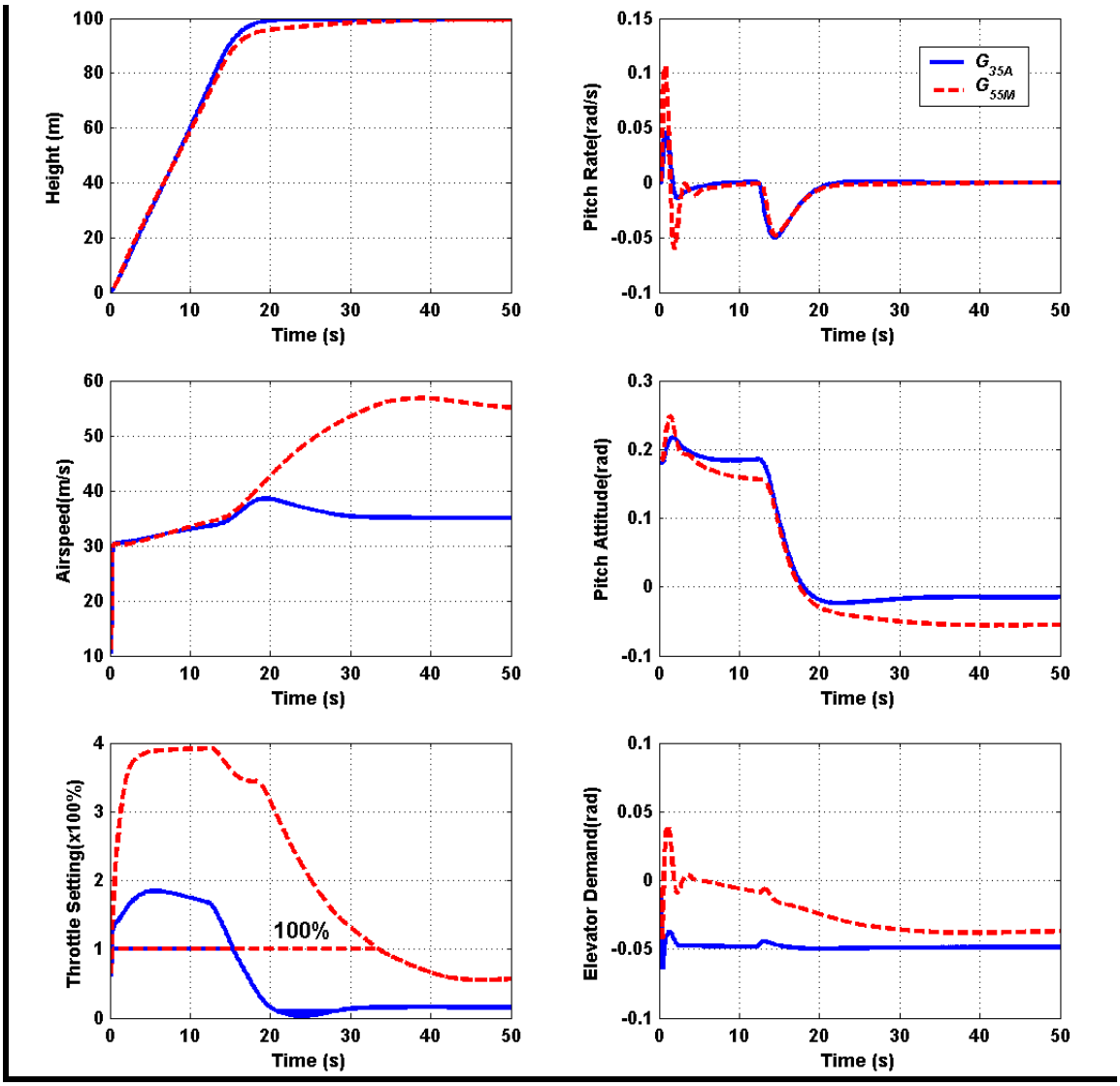

Figure 5.29: Maximum limit controller test in launch phase

Here, the final reduced order controller is evaluated in maximum conditions. That is by

evaluating the controller performance at the maximum possible airspeed, which is about 55-60m/s. Figure 5.29 shows the launch phase response comparison between the nominal and the maximum airspeed cases G_{35A} and G_{55M}. Note that the maximum airspeed case uses the maximum X_{CG} aft position of 10mm as in the worst-case model G_{45M}. Although the air vehicle needs about 40 seconds to reach the demanded airspeed, the height response is rather acceptable even though it suffers from throttle saturation for a long period. Pitch rate response to launch is acceptable and comparable to G_{45M}.

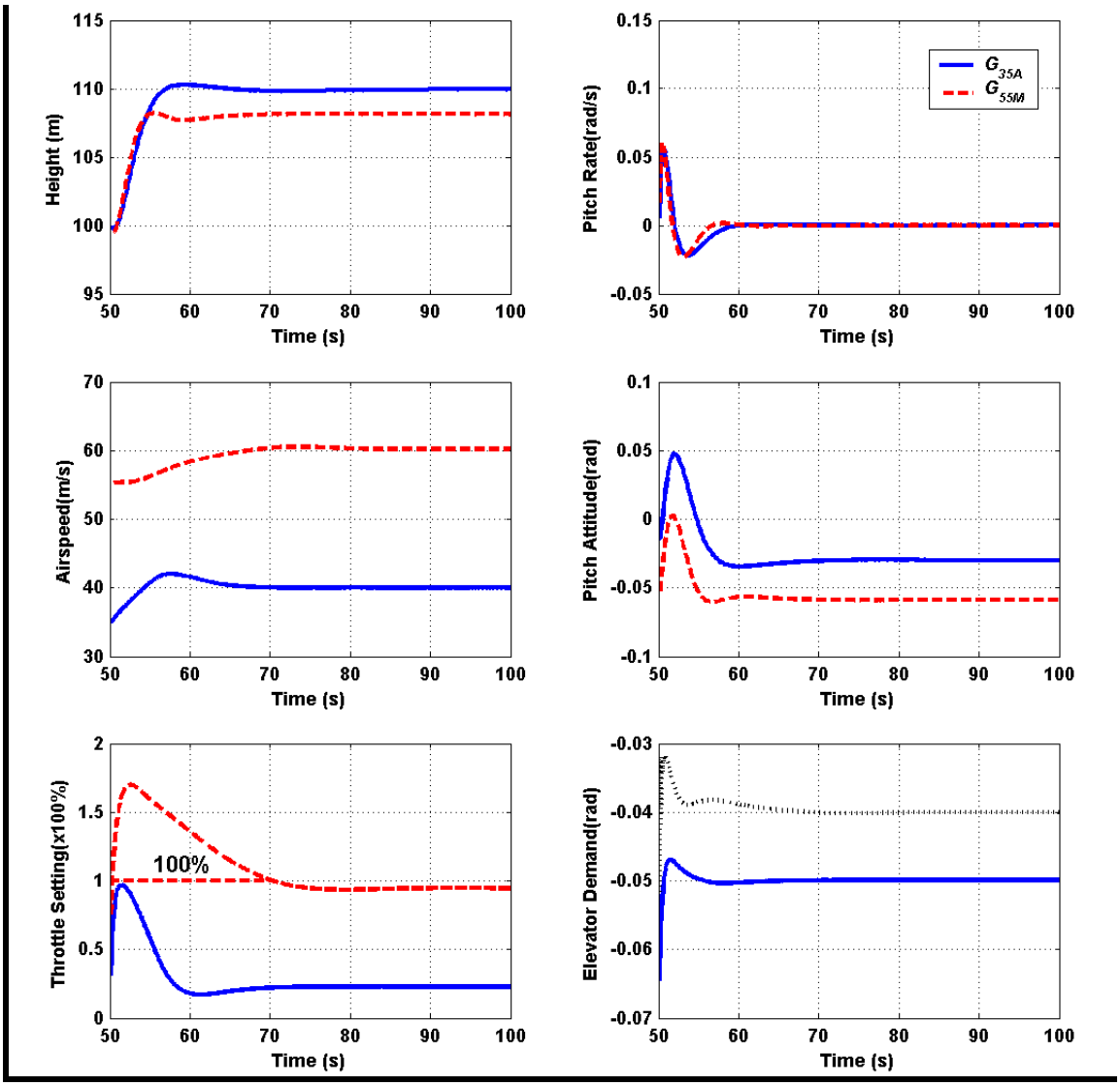

Figure 5.30: Maximum limit controller steady-state simultaneous step response

Figure 5.30 shows the response to simultaneous step inputs to airspeed and height

demands with Δu=5m/s and Δh=10m. Note that 60m/s is the maximum theoretical airspeed the air vehicle can reach. It is clear that the height response suffers from the limitations imposed by the engine full throttle available power which is just enough to over-come drag. Otherwise, the pitch rate and attitude show no signs of instability.

The longitudinal FCSD design is considered successful.

5.11 Chapter Summary

- The longitudinal air vehicle model used in the FCSD was selected based on several important factors including actuator dynamics and Padé computation delay approximation effects on modelling errors.
- LSDP was implemented in detail for the initial controller design. This included scaling, shaping, alignment, robust stabilization, and implementation configurations. The controller was then evaluated using the nominal and worst-case models of the air vehicle that represent it's operational flight envelope.
- Fine tuning process of the initial controller was performed, where the major drawbacks were overcome. This process included slight modifications to the initial LSDP for improved design clarity. The final controller was successfully evaluated against the air vehicle nominal and worst-case models.
- Implementation of the controller in the ACSL non-linear simulation environment is discussed; the FCS performance and stability were evaluated using the full flight envelope conditions. To overcome throttle saturation, the Hanus anti-windup technique was successfully implemented.
- Controller order reduction was performed on the final longitudinal control system. A maximum airspeed evaluation was successfully made in the non-linear simulation as an ultimate test of the final reduced-order controller.

Chapter 6

Lateral-Directional Flight Control System Design

In this chapter, the lateral-directional flight control system design is described using the modified LSDP. The basic steps of the longitudinal design in the last chapter will generally be followed.

6.1 Linear Model Analysis

In this section, the lateral linear model is analysed in more detail. The actuator dynamics and the computation delay effects on modelling accuracy are studied using the ν-gap metric as done in the longitudinal design. The open-loop model singular values are then investigated.

6.1.1 The ν-Gap Metric

Here, the actuators dynamics and the computation delays are treated as uncertainties and

their effects are analysed using the ν-gap metric.

Let the nominal air vehicle lateral dynamic model be G_{35Ay} which includes the aileron and rudder actuators dynamics and their respective Padé continuous approximation of their computation delay, and let the simplified model G_{35Ry}, which neglects the actuator dynamics and the computation delays represent the perturbed model. Applying the ν-gap metric to the nominal and the perturbed models we can measure the 'distance' between the two models. Table 6.1 shows the different case of neglecting actuator dynamics and/or computation delay effects.

Table 6.1: Simplification effects on Nominal Models' Accuracy

Case	Actuator Dynamics Neglected	Computation Delay Neglected	ν-Gap Metric from Nominal Model G_{35Ay}
1	Rudder	None	0.077
2	None	Rudder	0.083
3	Rudder	Rudder	0.129
4	Aileron	None	0.773
5	None	Aileron	0.801
6	Aileron	Aileron	1
7	All	All	1

Table 6.1 can be interpreted as follows:

- Case 1: Neglecting rudder actuator dynamics only has little effect on modelling accuracy(0.077).
- Case 2: Neglecting rudder computation delay only has a little more effect on modelling accuracy than the actuator dynamics(0.083 >0.077).
- Case 3: Neglecting both rudder computation delay and actuator dynamics have a significant effect on modelling accuracy(0.129) which necessitates that both should not be neglected in the control design model at the same time.
- Case 4: Neglecting aileron actuator dynamics only has much more effect on modelling accuracy than the rudder(0.773>>0.077).

- Case 5: Neglecting aileron computation delay only has the maximum single effect on modelling accuracy(0.801>0.773).
- Case 6: Neglecting both of aileron signal delay and actuator dynamics have the utmost effect (i.e. value of 1) on modelling accuracy which implies that the model can no longer represent the nominal model accurately.
- Case 7: Neglecting both rudder and aileron actuators and their respective signal delays also have the utmost effect (i.e. value of 1) on modelling accuracy as in Case 6.

Note that Cases 6 and 7 have a *v*-gap value of 1. This only implies that the perturbed models are very far from the nominal, but the *v*-gap method does not specify how far they are. In real situations, the designer is more interested in near perturbed model distances (i.e.<<1) than very far models, where the method gives adequate quantitative values.

From Table 6.1 above, it was clear that the full lateral/directional model G_{35Ay} should be used for the lateral FCSD. Although, the rudder actuator dynamics have much less effect than the aileron actuator dynamics, the gained accuracy is worth the increase in model order. For brevity, let $G:=G_{35Ay}$ represent the lateral FCSD model in the context of this chapter.

6.1.2 Open-loop Singular Values

Here, the open-loop singular values of the lateral-directional model will be presented in some detail.

Figure 6.1 below, shows the rudder input effect on all outputs individually. The following observations can be made from Figure 6.1:

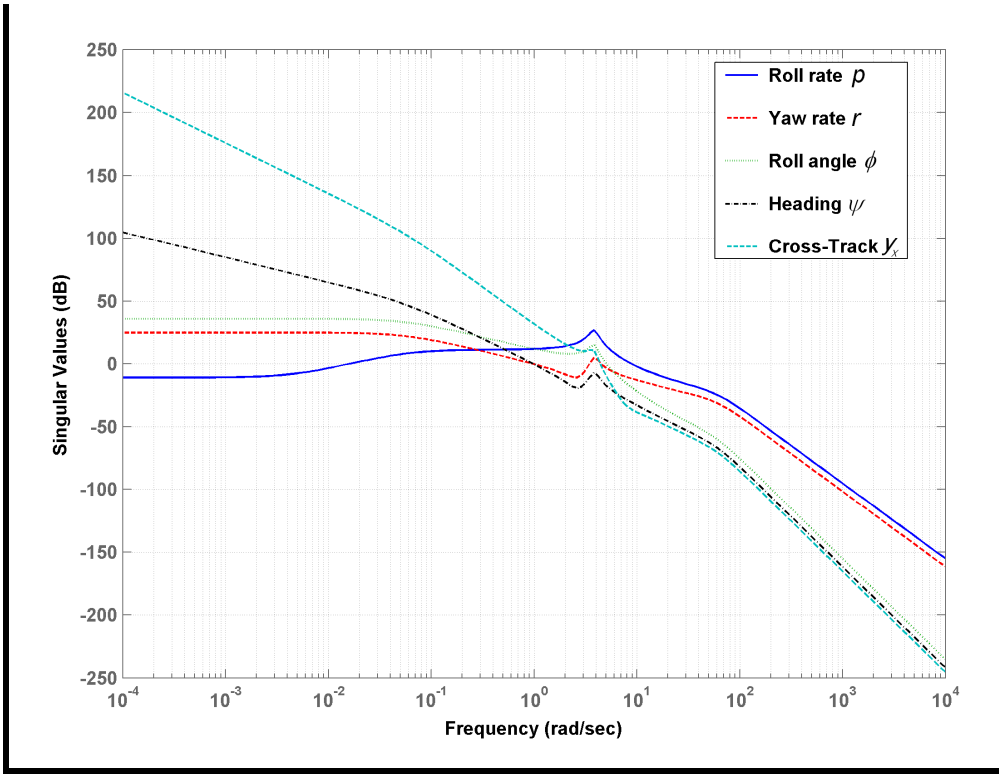

Figure 6.1: Open-loop singular values response of rudder input to each output

- Cross-track and heading gains are high at low frequencies with the expected integral action effect. This indicates that rudder input can well be used to control these outputs.
- Near gain cross-over frequency, *Dutch roll* unstable mode at $3.83 rad/s$ has a clear effect on all outputs. Heading and cross-track gains need to be pushed-up for higher bandwidths if going to be controlled by rudder.
- Roll-rate gain at frequencies $\geq 0.3 rad/s$ is higher than the yaw-rate gain, i.e. rudder is more effective in roll than in yaw in this frequency band.
- All outputs' high-frequency gain roll-off are clearly affected by the actuator and Padé delay dynamics at 41 and $100 rad/s$.

Figure 6.2 below, shows the effect of aileron input on all outputs individually. The following can be observed from Figure 6.2:

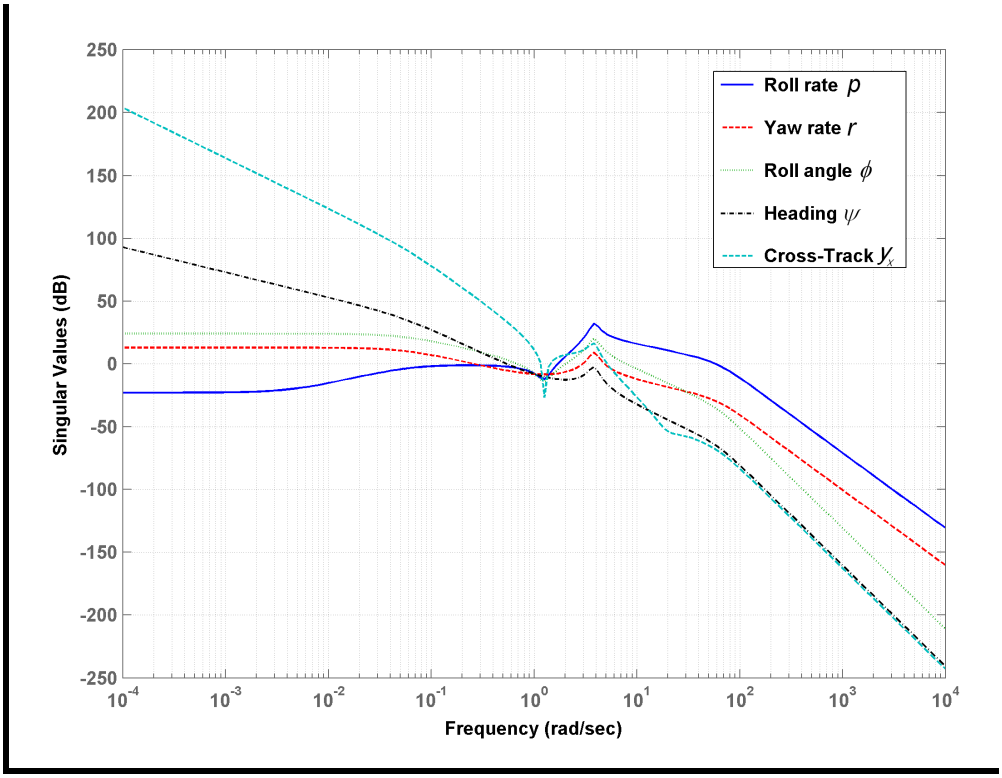

Figure 6.2: Open-loop singular values response of Aileron input to each output

- Aileron has similar frequency response gains on the outputs as the rudder, especially in the low frequency band. Hence coupling and *adverse yaw* effects are present. Consequently, aileron can also be used to control heading and cross-track effectively.
- Aileron is more effective in yaw than roll at frequencies $\leq 0.1 rad/s$.
- Roll rate high gain and wideband response is clear and needs to be reduced to improve stability and robustness. This is mainly why the lateral dynamic model is more sensitive to aileron actuator dynamics uncertainty than the rudder, as was shown in Table 6.1 earlier.
- Roll angle low frequency gain is rather low and has no slope. This indicates non-zero steady-state if not dealt with in the shaping process.

6.1.3 Robust Stabilization

The initial step in the modified LSDP is to check the ability to robustly stabilize the air vehicle model before any adjustment or modification. It is also appropriate to include

the lateral worst-case models developed in §**4.9.3** in this analysis.

Table 6.2: Lateral model robust stabilization

Model	*SM*=*b*(*G*,*K*)	*GM* (dB)	*PM* (*deg*)
G_{35Ry}	0.168	2.94	19.31
G_{35Ay}	0.148	2.58	16.99
G_{25Py}	0.151	2.64	17.37
G_{45My}	0.142	2.48	16.32

Table 6.2 above, shows the *SM*s for both the simplified and the full lateral models, i.e. G_{35Ry} and G_{35Ay}. Plus the worst-case models, i.e. the low-speed G_{25Py} and the high-speed model G_{45My}. Table 6.2 says:

- Adding the actuator and signal delay dynamics will reduce the achievable *SM*(0.148<0.168). But as was shown in Table 6.1, this is justified by the considerable effect these dynamics would have on the model uncertainty if they were neglected.
- The low *SM* of the full order lateral-directional model G_{35Ay} (i.e. $0.148<b_{min}=0.3$) also says that the bare airframe exhibits very low natural stability robustness. This is of course due to the gust insensitive configuration of the air vehicle.
- The low-speed worst-case model G_{25Py} shows more stability than the nominal model G_{35Ay} (i.e. *SM*=0.151>0.148), while the hi-speed worst-case model G_{45My} shows less stability (i.e. *SM*=0.142<0.148). These values agree with the well-known dynamics of these air vehicle models.

6.2 Input / Output Scaling

In this section the input/output scaling is applied to the lateral FCSD model. For the modified LSDP, the robust stability is also calculated to monitor the effect of scaling on the model robustness.

6.2.1 Input Scaling

For the input scaling, each input is scaled with the maximum allowed value. Although the linear model inputs are defined as the variation from the nominal trim values, it has been shown in §**4.5.2** on page 73 that the lateral-directional control inputs had approximately nil trim values at steady-state. So the allowed aileron and rudder values are defined as,

$$\begin{aligned} \xi_A &= \pm \xi_{Max} \\ \zeta_A &= \pm \zeta_{Max} \end{aligned} \qquad \textbf{6.1}$$

Given from Table 3.1on page 50,

$$\begin{aligned} \xi_{Max} &= \pm .262 \; rad \\ \zeta_{Max} &= \pm .349 \; rad \end{aligned} \qquad \textbf{6.2}$$

The initial input scaling matrix may therefore be written,

$$W_{1c} = \begin{bmatrix} 1/\xi_{Max} & 0 \\ 0 & 1/\zeta_{Max} \end{bmatrix} \cong \begin{bmatrix} 3.8 & 0 \\ 0 & 2.9 \end{bmatrix} \qquad \textbf{6.3}$$

6.2.2 Output Scaling

The output scaling is based on the maximum expected or allowed variation for each output. Initially the following values were used:

$$p = 3 \; rad/s, \; r = 0.5 \; rad/s, \; \phi = 0.5 \; rad, \; \psi = 0.3 \; rad, \; y_x = 100m \qquad \textbf{6.4}$$

$$W_{2c}\texttt{=diag([0.33 2.0 2.0 3.33 0.01])} \qquad \textbf{6.5}$$

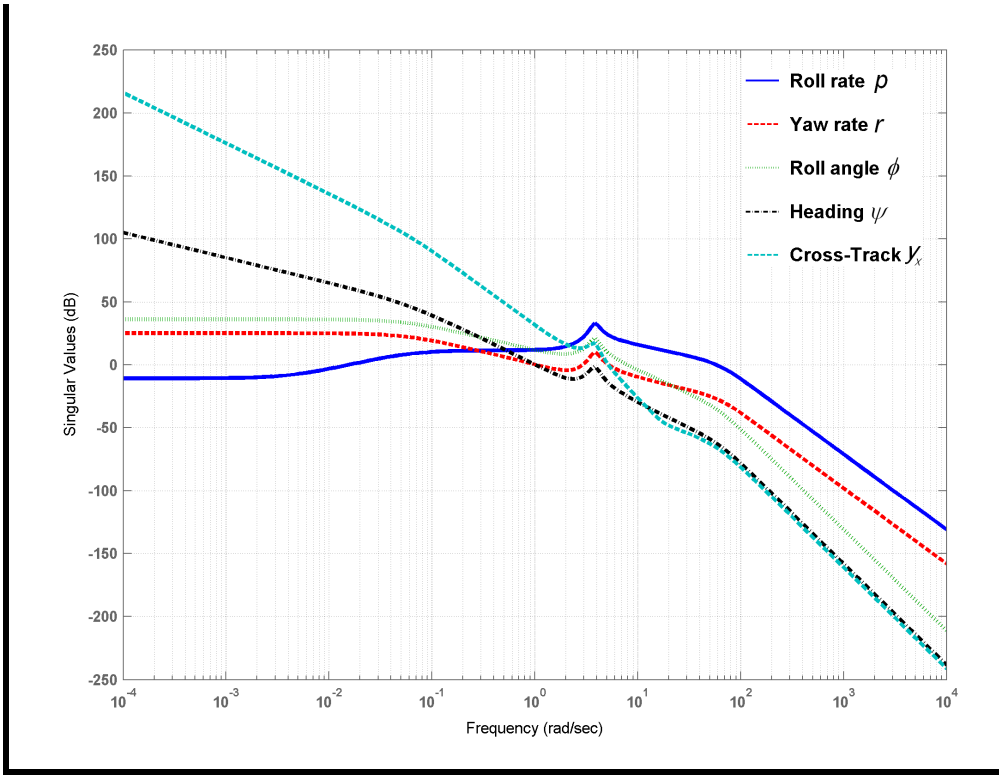

Figure 6.3: Nominal model outputs to all inputs SV

When selecting the output maximum expected values, it is important to take their frequency response gains into account, especially around the desired bandwidth (i.e. $5rad/s$)

. The following steps were taken for the output scale weight selection in Equation 6.4:

1. For the roll rate p, it is expected to have the highest value. Thus selecting a small maximum expected value would adversely affect the system robustness. It was found that increasing the maximum allowed value would increase the stability robustness of the closed-loop system.
2. For the yaw rate r, it is expected to have a much smaller value than p. Higher values did not show any improvement in robust stability.
3. For the roll angle ϕ, it is expected to reach values between p and r. It was found that increasing ϕ would improve the robust stability similar to p. The relatively small value selected was because we would like to have tight control over roll.

4. For the heading/yaw angle ψ, it is expected to have the least amplitude. Increasing the scaling value also showed a decrease in the robust stability achieved.

5. Finally, the cross-track error y_x is expected to have large values. The selected value was based on the required level of performance and on what the feedback measurement limiter may have in the non-linear simulation implementation.

6.2.3 Scaling Effect on Robust Stability

Using the scaled model G_c, a robust controller was synthesized as in §**5.5**. The achieved robust stability was:

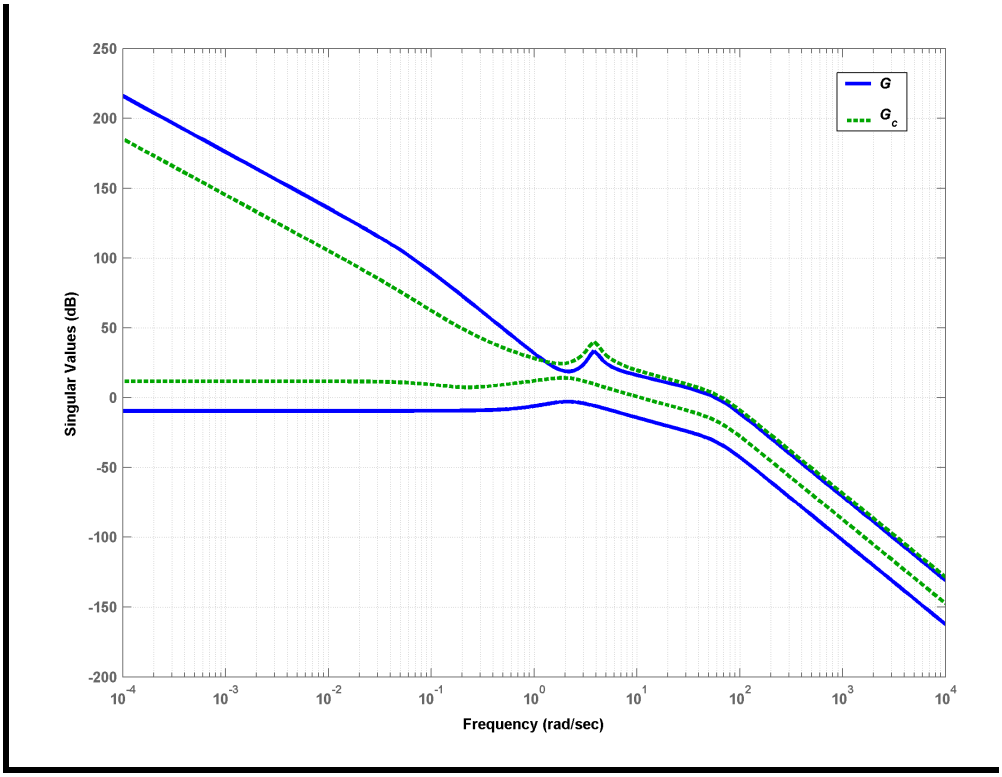

Figure 6.4: Scaling effect on lateral model principal gains

$$SM=b(K_s,G_c) = 0.23,\ GM = 4\text{dB},\ PM = 26deg \qquad \textbf{6.6}$$

Note how scaling helped increase the achievable robust stability (i.e. SM=0.23>0.148).

Figure 6.4 above, shows the effect of scaling on the principal gains of the lateral model. Notice how scaling pushed $\underline{\sigma}$ above unity gain in the low frequency band.

6.3 Shaping Weights

In this section, the shaping weights for the input and the output are selected. Note that the general rules for shaping the model open-loop SV in §**5.3** are also followed here.

6.3.1 Input Shaping Weights

For the inputs, integrators are added to boost the low frequency gain. Zeros were also added around the desired bandwidth to reduce roll-off rate at gain cross-over. The input shaping weights were initially selected as,

$$W_{1s} = \mathtt{diag}\left[\frac{s+1}{s+.001} \quad \frac{s+1}{s+.001}\right] \tag{6.7}$$

6.3.2 Output Shaping Weights

Output shaping weights usually contain functions that affect the high frequency band such as low-pass filters. Initially, the following output weighting matrix was used:

$$W_{2s} = \mathtt{diag}\left[1 \quad 1 \quad 1 \quad \frac{1}{s/10+1} \quad \frac{1}{s/10+1}\right] \tag{6.8}$$

For heading and cross-track, simple low-pass filters were added above desired bandwidth(i.e. 10>5*rad*/*s*). This was found to improve robustness and helps to reject measurement noise.

Figure 6.5 shows the effect of shaping weights on the original and scaled model open-loop principal gains, where the effect of integrators can be seen clearly.

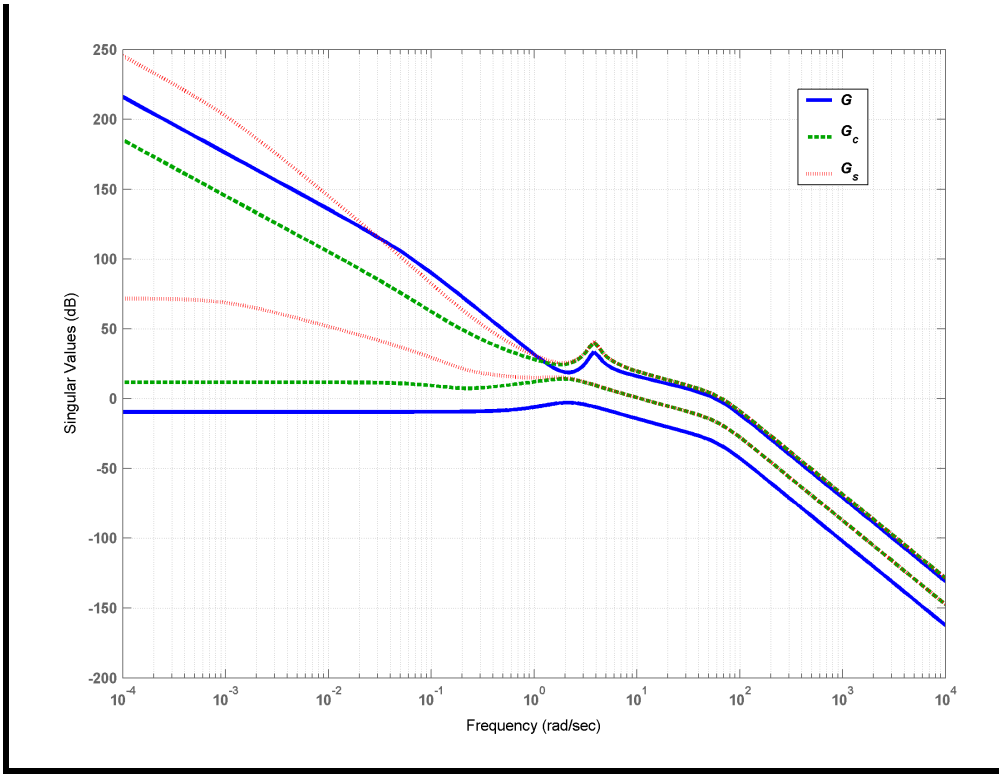

Figure 6.5: Scaling and shaping effects on model open-loop principal gains

6.3.3 Shaping Effect on Robust Stability

Using the shaped model G_s, a robust controller was synthesized. The achieved robust stability margins are,

$$SM=b(K_s,G_s) = 0.22,\ GM = 3.9\text{dB},\ PM = 25.3deg \qquad \textbf{6.9}$$

Note that shaping is expected to reduce the stability of the system. This is because it shapes the model SV for improved performance where stability would usually suffer.

6.4 Alignment and Decoupling

The coupling between the roll and yaw dynamics was shown in §4.5.2 and 4.6.2 to be significant. In this section, the MATLAB `align` algorithm is used to scale and decouple the model at the desired frequency ω_o. To align the shaped design model we have,

$$W_{a1}\big|_{2\times2} = \texttt{align}(G_s(\omega_o)\big|_{2\times2})$$
$$G_{a1}\big|_{4\times2} = G_s(\omega_o)\big|_{4\times2} W_{a1}\big|_{2\times2} \qquad \textbf{6.10}$$

where G_{a1} is the aligned model. The roll and yaw rates, p and r, are the selected outputs for decoupling in $G_s\big|_{2\times2}$ in Equation 6.10. Applying the `align` function at ω_o = 10 *rad/s* we have:

$$W_{a1} = \begin{bmatrix} 0.143 & 0.083 \\ 0.211 & 0.899 \end{bmatrix} \qquad \textbf{6.11}$$

The diagonal elements of W_{a1} in Equation 6.11 are for scaling, while the off-diagonal elements are for decoupling. Note how the aileron input was scaled-down considerably compared to the rudder input(i.e. 0.143<0.899).

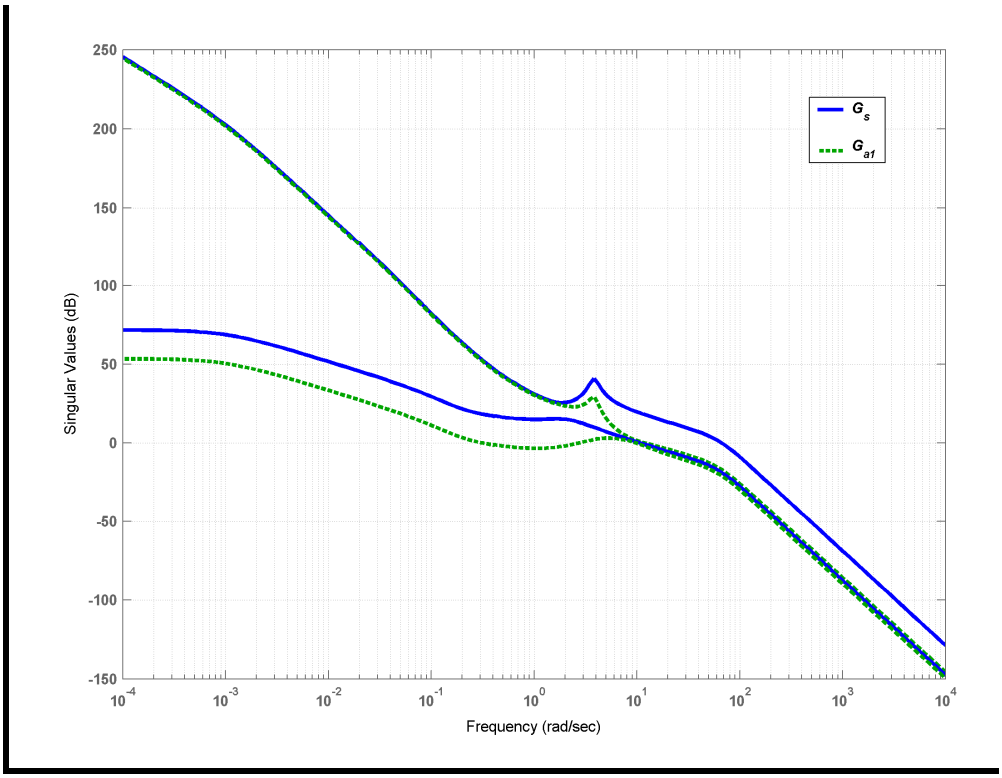

Figure 6.6: Alignment effect on shaped model principal SV

Figure 6.6 shows the effect of alignment on the open-loop principal SV of the shaped

model. It can be seen from the figure that the alignment was achieved at 10*rad*/*s* and above.

6.5 Robust Stabilization

In this section, the scaled, shaped, and aligned model, $G_w := G_{a1}$, is robustly stabilized for the final controller. Table 6.3 shows the final *SM* achieved compared to the different design stages in addition to the worst-case models.

Table 6.3: Lateral design stages robust stabilization

Stage	*SM*	*GM* (dB)	*PM* (*deg*)
Initial G	0.148	2.6	17.0
Scaling G_c	0.23	4.0	26.0
Shaping G_s	0.22	3.9	25.3
Align/final G_w	0.33	5.9	38.2
G_{25Py}	0.27	4.8	31.3
G_{45My}	0.18	3.2	20.8

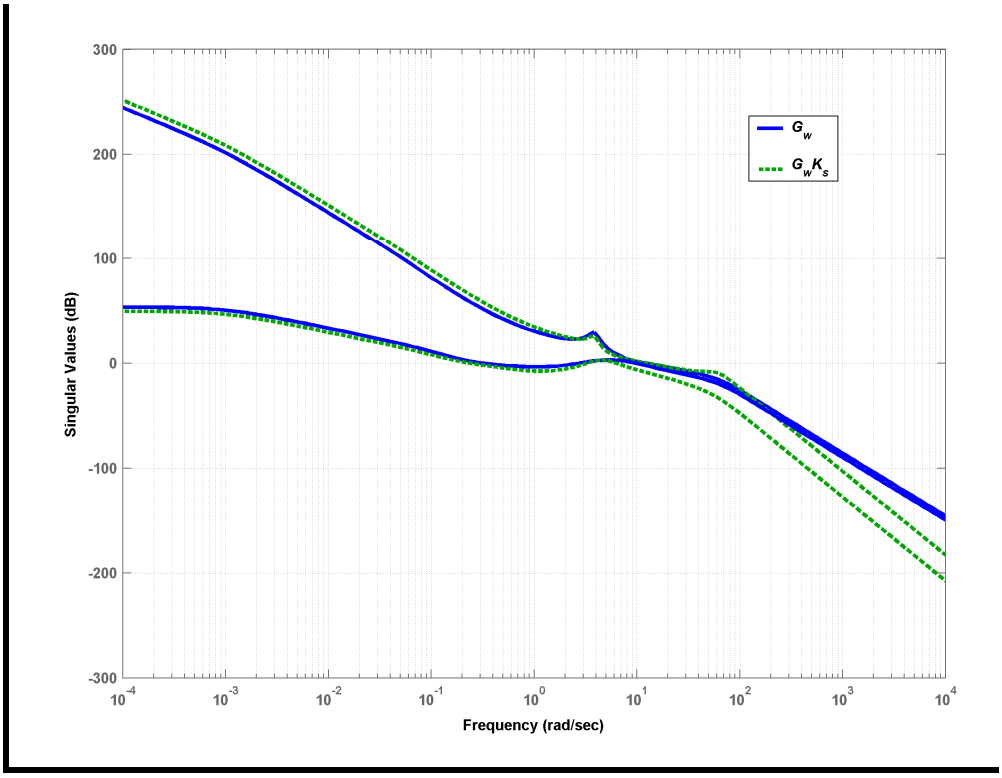

Figure 6.7: Controller effect on weighted model principal SV

Note that, as anticipated in §**4.9.2**, the lateral-directional FCSD was more challenging. The achieved stability was also less. But as an initial design, it is evaluated first and then fine-tuned if needed. Figure 6.7 above, shows how the controller had slightly altered the shaped system principal SV. Mainly, the controller has,

- added low-pass filter effect for high frequency attenuation
- slightly reduced gain cross-over slope

6.6 Controller Implementation and Evaluation

In this section, the time response of the lateral controller is evaluated using the nominal and flight envelope worst-case air vehicle models.

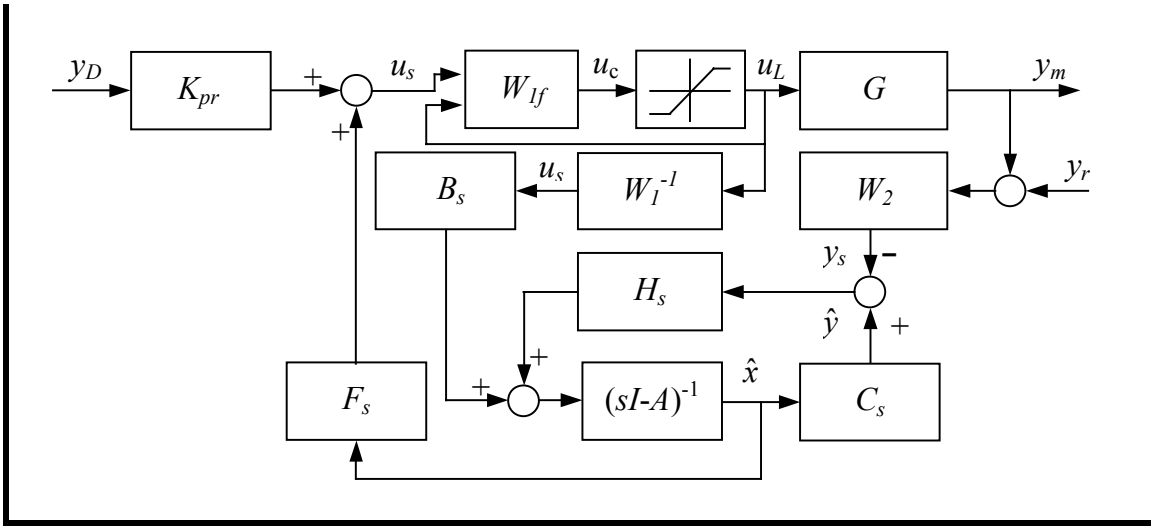

Figure 6.8: Controller implementation in Observer-form with Hanus anti-windup and demand and reference inputs y_D, y_r

But first, we quickly review the lateral-directional controller implementation. Figure 6.8 above shows, as in the longitudinal design, the observer structure used for implementation with Hanus anti-windup. Note that both demand and reference inputs, y_D and y_r, are included in the implemented structure. Note also that the pre-weight K_{pr} is scheduled as a function of airspeed to achieve unity DC gain.

6.6.1 Time Response

Here, the step response of the controlled system with the nominal and worst-case air vehicle models is evaluated.

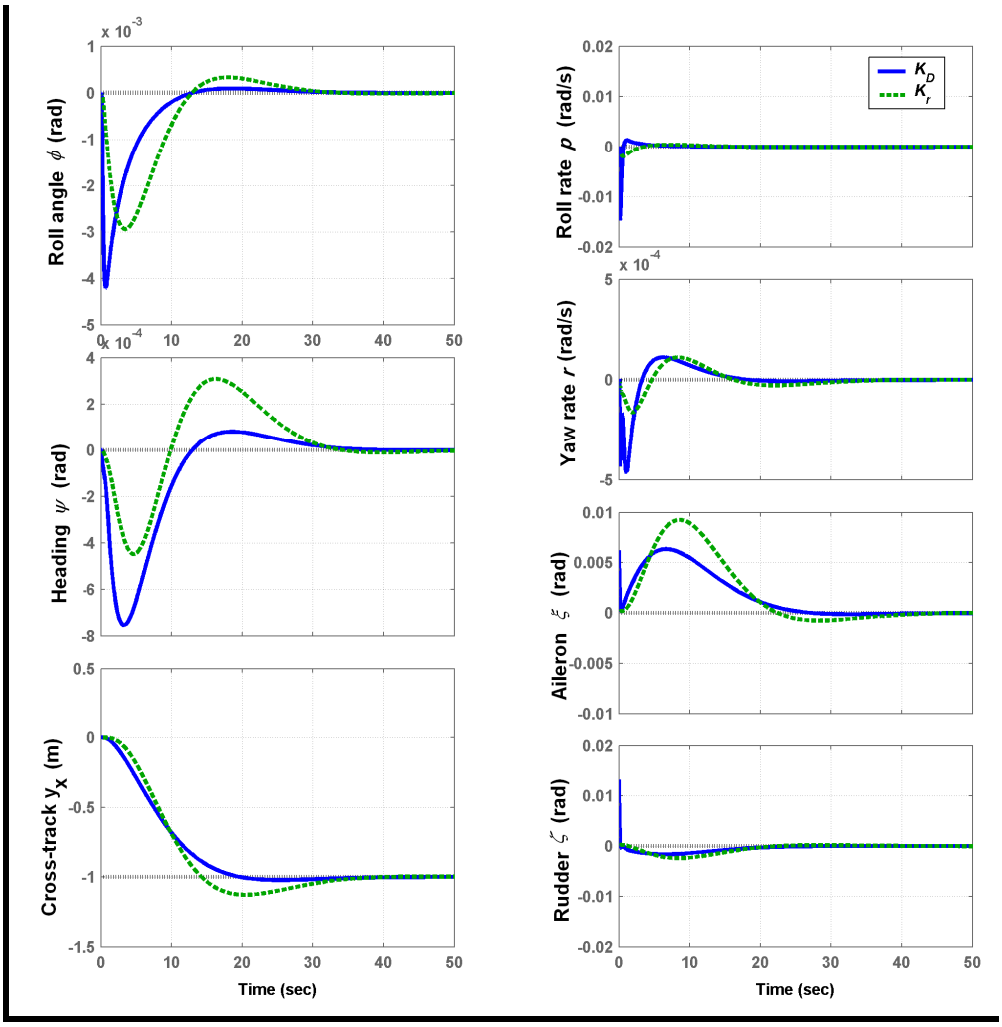

Figure 6.9: Controllers response of unit step demand and reference step cross-track inputs

Figure 6.9 above, shows the time response to both unit step inputs, demand y_D and reference y_r (represented by the controllers K_D and K_r). Although the demand step input produced better response, it required much more initial roll and yaw rates. Notice how the aileron has been mainly used for the executed manoeuvre with very little activity from the rudder.

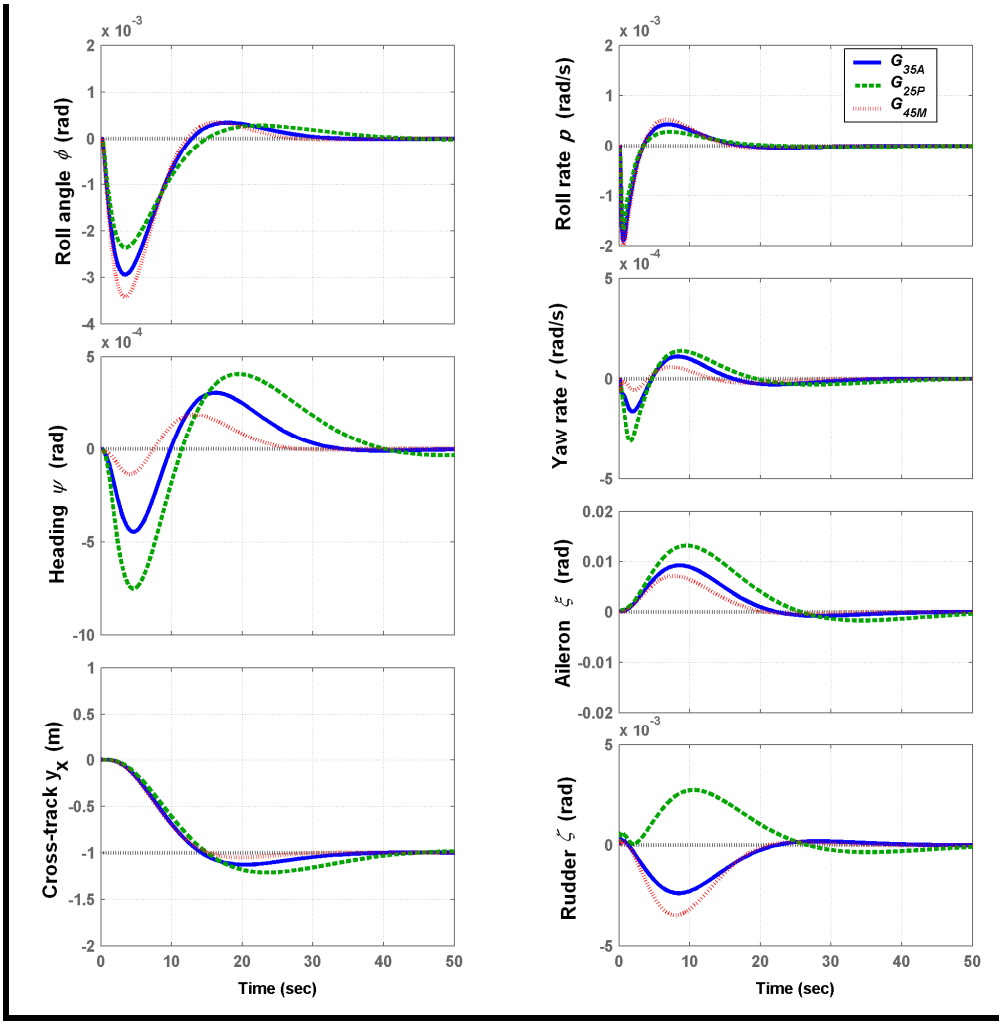

Figure 6.10: Controller response to demanded unit step cross-track with worst-case models

Figure 6.10 above, shows the controller response with the flight envelope worst-case models. Notice how the rudder was used for the low-speed worst-case model G_{25P} with an opposite sign of the other two models. This is mainly due to the fact, shown earlier in **Table 4.6**, that G_{25P} is stable in the *Dutch roll* mode, while G_{35A} and G_{45M} were unstable. This consequently changed the sign of the moment the rudder is generating to yaw the airframe; the controller was able to cope with such a condition.

The results in Figure 6.10 above, also validate the robust command-tracking performance and airframe stabilization capability of the controller. This includes the

high-speed/low stability condition represented by the high-speed worst-case model G_{45My} , where the calculated robust stability margin was low(i.e. 0.18 in Table 6.3).

6.7 Non-linear Simulation Evaluation

Here, the lateral-directional controller implementation in ACSL non-linear simulation is described. The performance of the controlled system is then evaluated for the nominal and full operational flight envelope of the air vehicle.

6.7.1 Controller Non-linear Implementation

The implementation of the lateral-directional controller follows the longitudinal controller implementation process. The main implementation steps are briefly reviewed as follows:

1. The final controller design was transformed into the state-space form:

$$\dot{x}_c = A_c x_c + B_c y_c$$
$$u_c = C_c x_c + D_c y_c$$

   where the input vector y_c includes the measurements and demands vectors as: $y_c = [y_m \; y_D]$

2. The controller was discretized at the real control system processor frequency.
3. The controller A, B, C, D matrices where exported from MATLAB to ACSL using formatted ASCII files with proper numerical formats to be read accurately by ACSL.
4. All required scheduled trim tables were generated as functions of total airspeed in ACSL including the command pre-weight K_{pr}. Note again that X_{CG} was not part of the scheduling process. So any changes in the CG position will represent an unaccounted for uncertainty.
5. The required linear feedback controller inputs were calculated in ACSL on-line, this included the measured and demanded cross-track error y_x.

6. The proper mixing strategy for the starboard- and port-actuators was implemented. For the lateral-directional case, the aileron and rudder mixing was as follows,

$$\begin{Bmatrix} \xi_{SB} \\ \xi_{P} \\ \zeta_{SB} \end{Bmatrix}_{A} = \begin{bmatrix} 1 & 0 \\ -1 & 0 \\ 0 & 1 \end{bmatrix} \begin{Bmatrix} \xi \\ \zeta \end{Bmatrix}_{D} \qquad \textbf{6.12}$$

Note that the dorsal rudder is driven by the starboard rudder command signal. This is due to the fact that the air vehicle used to have a two-rudder configuration on each of the wingtips, and was later replaced by the single dorsal rudder to improve the airframe ground handling and recovery robustness.

6.7.2 Controller Non-linear Evaluation

Here, the lateral controller is evaluated in the ACSL non-linear simulation.

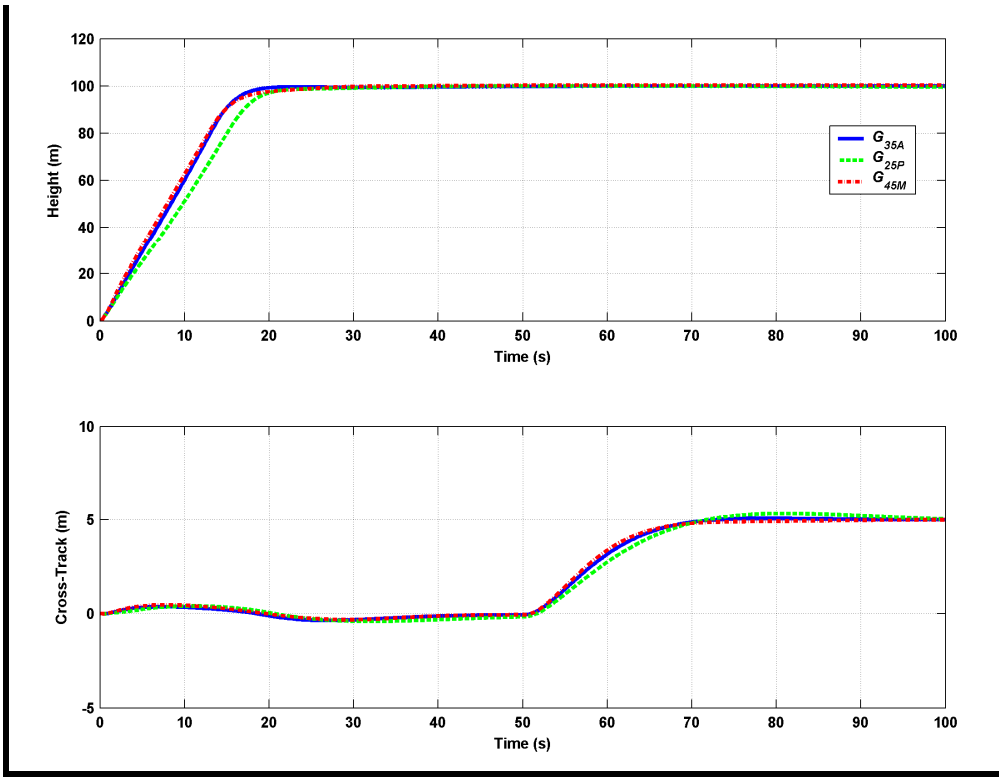

Figure 6.11: Non-linear simulation controller cross-track performance

The controller cross-track and height response are shown in Figure 6.11 using the nominal and the worst-case flight envelope models. Note that, as mentioned in the longitudinal controller design, the launch phase is the most demanding stage of the controlled flight, where considerable and simultaneous changes in air vehicle dynamic parameters take place.

Figure 6.11 also shows a cross-track step demand of $\Delta y_x = 5m$ that was executed after the air vehicle reached steady-state and level flight at 50*sec* from launch. Figure 6.11 shows that the lateral controller was fairly capable of keeping the air vehicle on straight flight path during the launch phase for the nominal and worst cases. The 5*m* step demand at 50s from launch was well tracked by the controller with no effect on the flight levels as shown in the height responses of the nominal and worst cases.

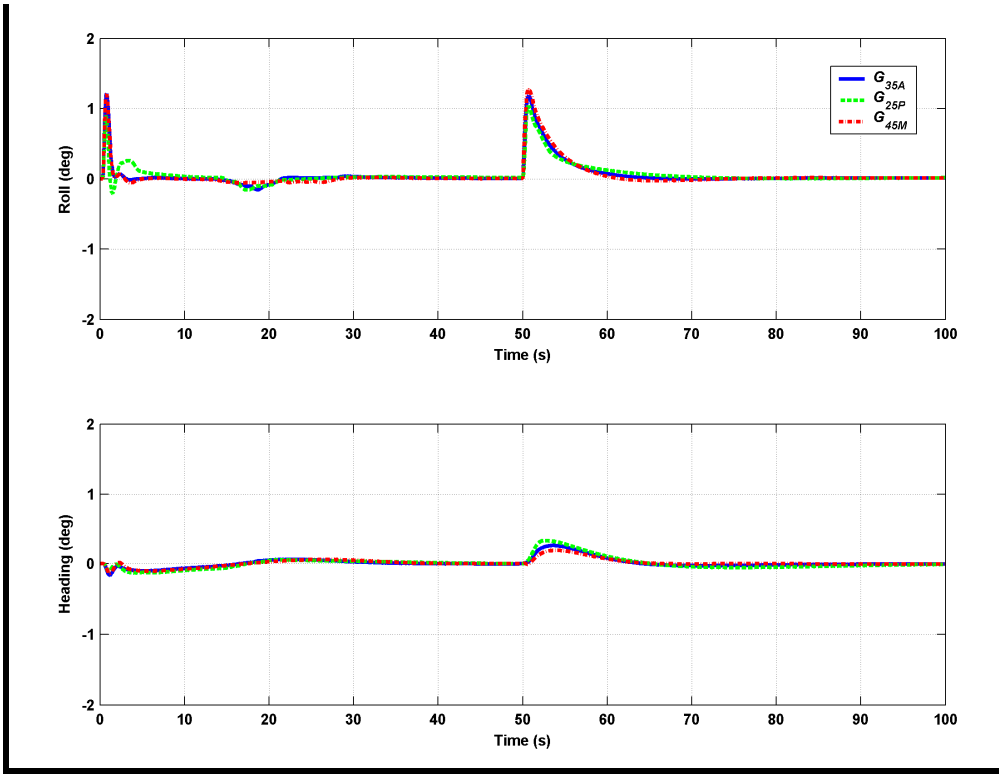

Figure 6.12: Non-linear simulation roll and heading/yaw angles control

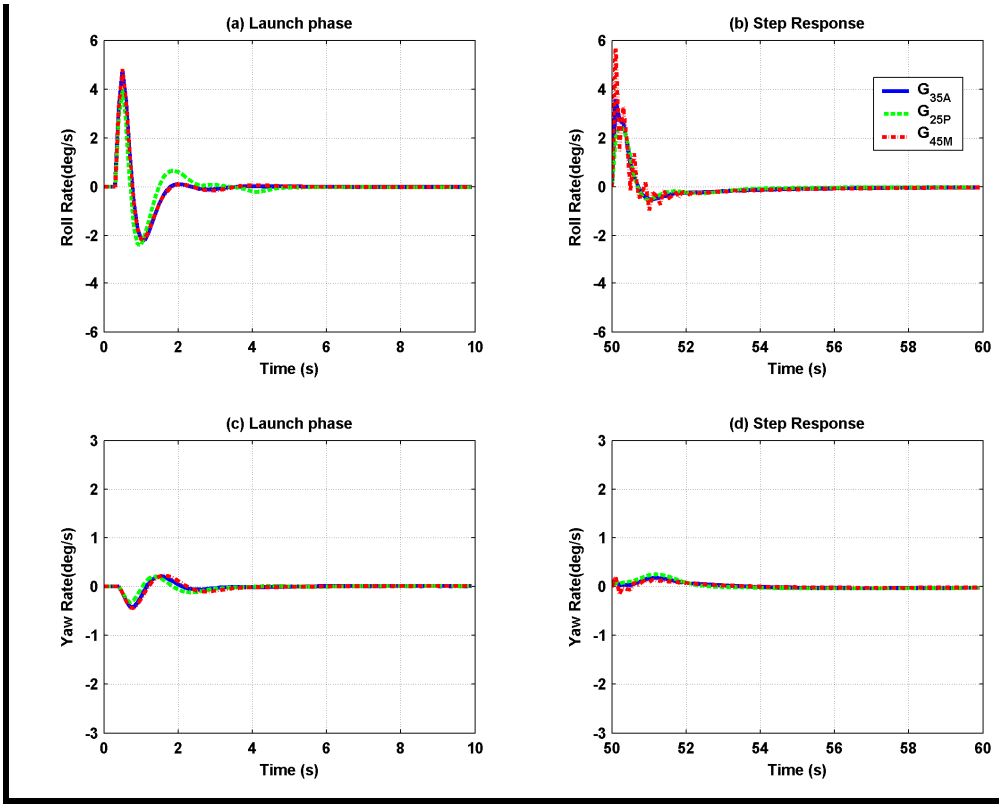

Figure 6.13: Non-linear simulation controller roll and yaw rates stabilization

Figure 6.12 shows the controlled roll and heading/yaw angles, which demonstrate the controller capability of keeping the air vehicle wing-levelled and head-on the required track during launch and in the cross-track step manoeuvre. Note how roll control was mainly used to track the cross-track step demand.

Figure 6.13 shows the roll and yaw rates during the launch and step manoeuvre phases. The sub-figures were zoomed for the first 10 seconds of each phase to emphasise the details at these critical times. Figure 6.13(b) reveals instability signs of the high-speed step manoeuvre (i.e. G_{45M}) which has the CG at the furthest aft position from the reference X_{CG}. Figure 6.13 also shows the high roll rate values reached compared to the yaw rates, as expected.

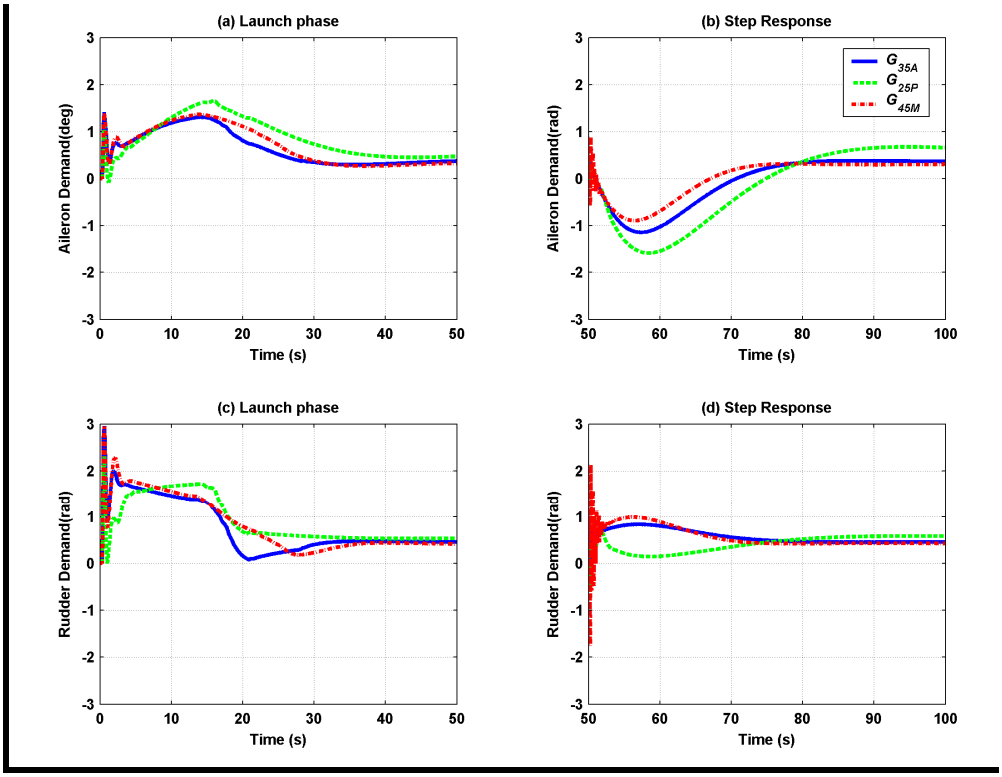

Figure 6.14: Non-linear simulation controller actuators demands

Figure 6.14 shows actuator activity for the launch and cross-track step phases. Notice the instability signs in the high-speed case (i.e. G_{45M}) for both the aileron and rudder activities in the cross-track step response phase in Figure 6.14(b) and (d). Note that the instability signs are shown in the cross-track step response and not the launch phase. This is because the air vehicle is launched at $30m/s$, while the cross-track step demand is executed when the air vehicle has reached the demanded air speed(i.e. $45m/s$).

6.7.3 Crosswind Effect Evaluation

Crosswind is well-known to have significant effect on lateral tracking performance. This is especially true for the A3 gust insensitive air vehicle, where crosswind would easily be able to slide the air vehicle laterally off-track, even while keeping the right heading.

Here, a moderate crosswind of $3m/s$ was applied in the ACSL non-linear simulation,

and the controller performance is evaluated based on the ability of keeping the air vehicle on track. Note that crosswind will be in effect from launch for the full flight time. Also note that, as in previous sections, a cross-track step demand of Δy_x=5m was executed at 50sec from launch.

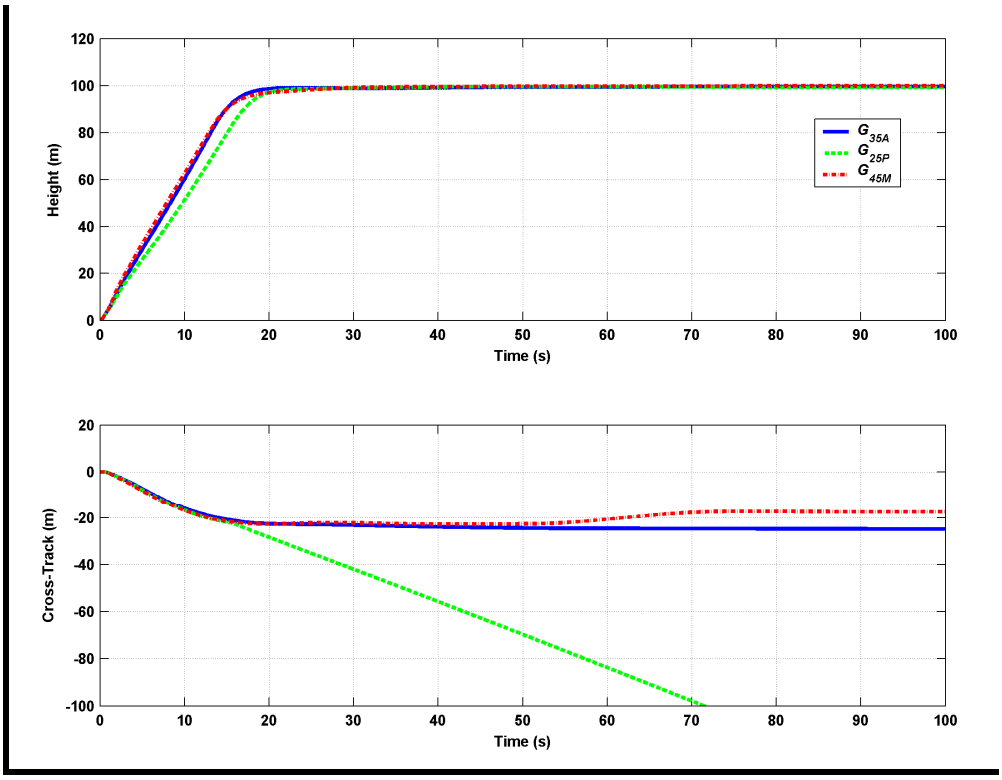

Figure 6.15: Crosswind effect on controller cross-track performance

Figure 6.15 above, shows the crosswind effect on the air vehicle cross-track performance. Although the controller was not able to put the air vehicle back on track after launch for all cases, the air vehicle was able to survive the launch phase. Although the controller was able to keep a constant distance for the nominal air speed of 35m/s and respond to the 5m step at 50s in the high speed case(i.e. G_{45M} at 45m/s), it was unable to keep the air vehicle at low air speed case(i.e. G_{25P} at 25m/s;) at a constant distance within the flight time. This is mainly due to the control power available which was not enough to overcome the crosswind effect. This is due to the fact that the aileron and rudder aerodynamic forces were reduced considerably with air speed since they are functions of the square of the total air speed. Also, the increase in the static stability due to the CG position at the most fore distance from reference, also required more force to generate the required yawing moments.

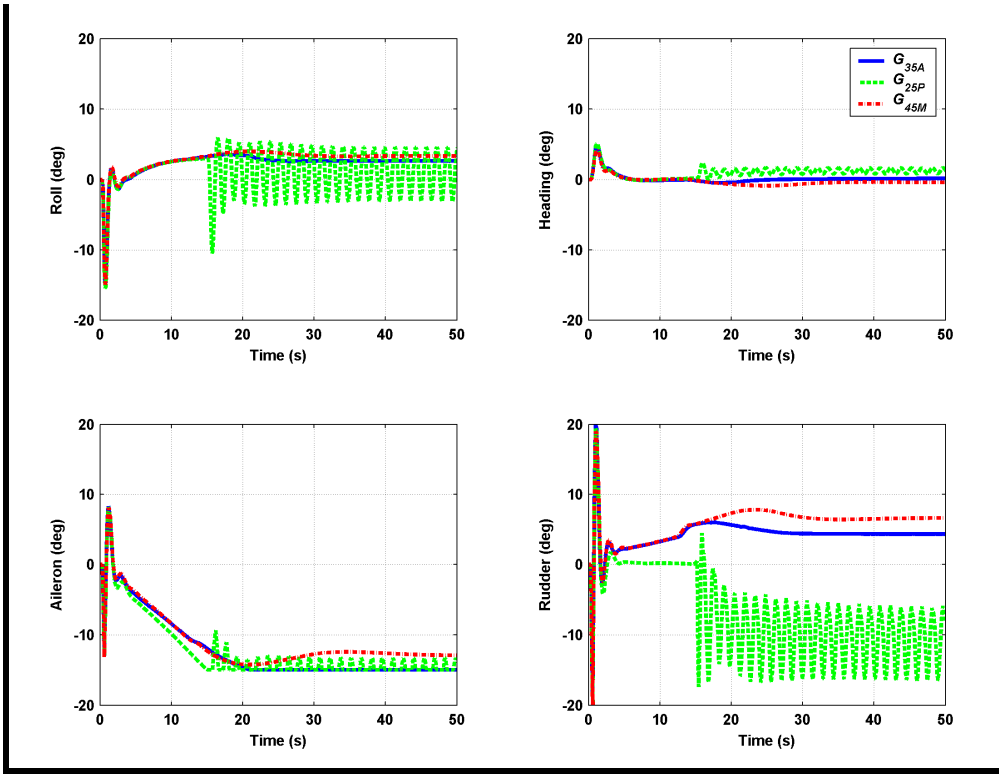

Figure 6.16: Crosswind effect on roll, heading, and actuator demands

This can easily be verified by observing the aileron and rudder activities in Figure 6.16. Notice how the aileron demand reached the limit within 15*sec* from launch, which is a major destabilizing factor, and is also reflected in the rudder response which started oscillating at the same time of aileron saturation(i.e. 15*s* from launch).

Despite the instability of the controller with G_{25P}, notice also in Figure 6.16, it is able to control the air vehicle heading error to a minimum for all cases while mainly using roll for the lateral manoeuvre.

From the above results it can be concluded that:

- A main fault in the lateral controller was that more effort was put on controlling heading error than cross-track. These two outputs are well-known to have conflicting control requirements, especially in the presence of crosswind.
- Aileron demand saturation was another main factor in destabilizing the system,

although the anti-windup technique was implemented in the controller. Using less aileron and more rudder demand would help avoid aileron saturation.

- Using roll only to overcome crosswind is the well-known "wing-down" strategy pilots practice in the final approach for landing[78]. While keeping the aeroplane heading aligned with the runway centreline, the pilot controls position across the runway(i.e. cross-track) by banking (side slipping) using rudder and aileron combination. Obviously, this strategy does not seem to be very effective for gust insensitive configured air vehicles such as the Cranfield A3 Observer.

6.8 Controller Modification

Based on the results and conclusions so far, the lateral-directional controller is modified in order to adopt a more effective control strategy in the presence of crosswind.

A major factor that affected the heading error control was the introduction of the integral action in the shaping weights for the rudder input as shown in §6.3.1 and Equation 6.7 on page 150. This is due to the fact that the integrator influences all outputs affected by the rudder input including the heading/yaw angle. Thus, to cancel this integral effect on the yaw angle, the inverse of the rudder shaping weight is used to weight the yaw angle in the output shaping function. This technique was successfully applied in the longitudinal controller design to cancel the integral effect of the elevator input on the pitch rate output. Also, the weighting function of the aileron input is reduced to avoid saturation in the presence of crosswind. After some fine tuning, the final input and output shaping weights are,

$$W_{1s} = \mathtt{diag}\left[\frac{s+2}{s+.4} \quad \frac{s+1}{s+.1}\right] \tag{6.13}$$

$$W_{2s} = \mathtt{diag}\left[1 \quad 1 \quad 1 \quad \frac{s+.1}{s+1} \quad \frac{1}{s/10+1}\right] \tag{6.14}$$

Finally, the shaped model was aligned at $7rad/s$ to help reduce the system bandwidth

and increase stability. Table 6.4 shows that the modification done on the controller has not reduced its robust stability measures.

Table 6.4: Modified controller robust stabilizations stages

Stage	*SM*	*GM* (dB)	*PM* (*deg*)
Shaping G_s	0.22	3.8	25.0
Align/final G_w	0.31	5.6	36.0
G_{25Py}	0.26	4.6	30.0
G_{45My}	0.21	3.7	24.3

6.8.1 Crosswind Effect Evaluation

The modified controller was evaluated in the ACSL non-linear simulation with the low-speed model G_{25P} and the same crosswind of $3m/s$. The following figures show the improvements achieved compared to the initial design, where K_{25P} and $K2_{25P}$ represents the initial and modified controllers respectively.

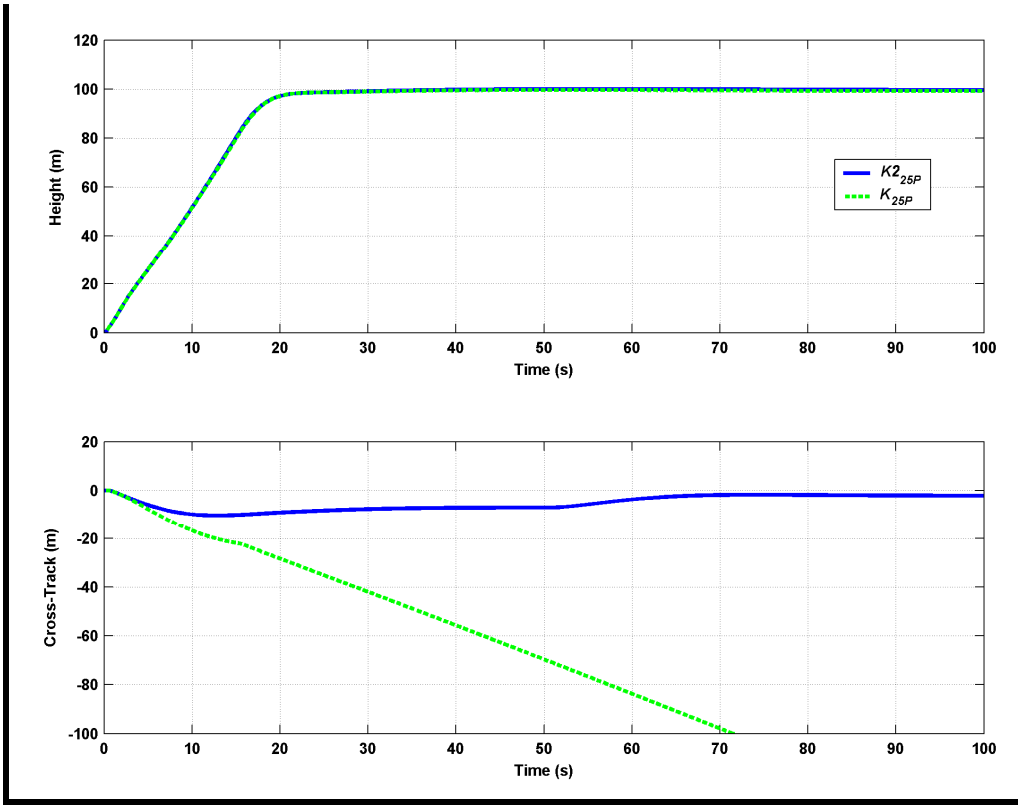

Figure 6.17: Crosswind effect on modified controller cross-track performance

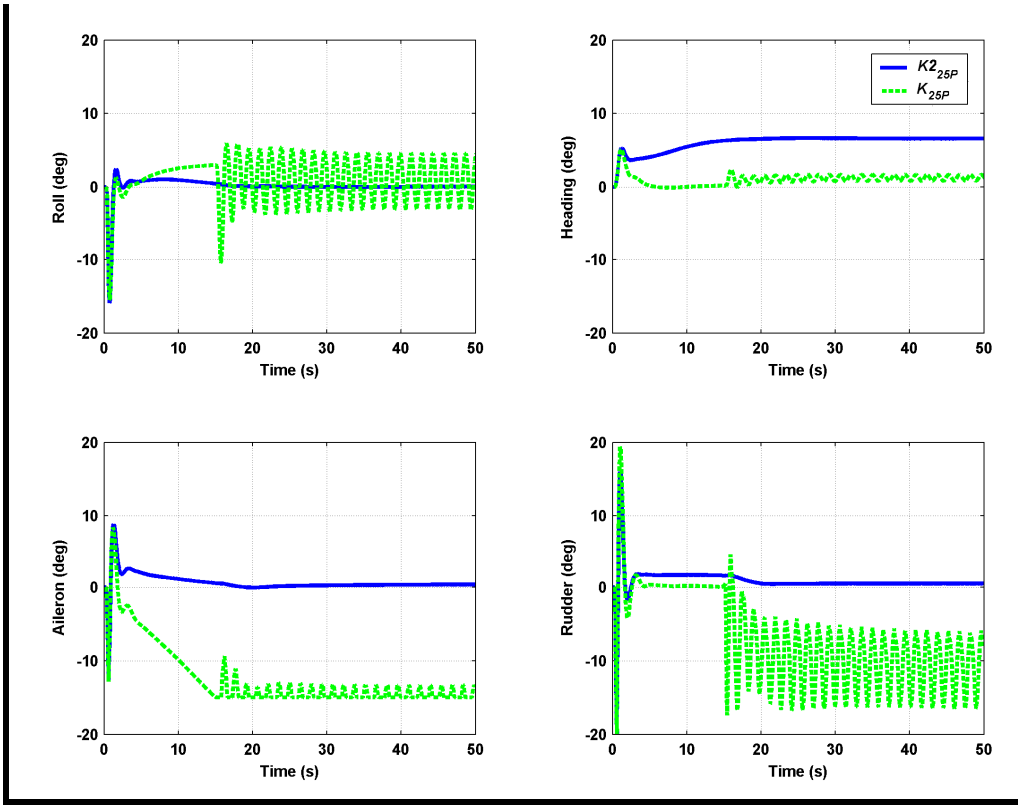

Figure 6.18: Crosswind effect on controller actuator demands

From the above results, the following is observed,

- The modified controller keeps good control over the cross-track error without sacrificing flight path height as shown in Figure 6.17.
- Aileron demand is considerably reduced in favour of rudder as shown during the first 10*s* of launch phase in Figure 6.18.
- Air vehicle is flying with a noticeable heading error which helped overcome crosswind effect on cross-track performance as required. This technique is also well-known to pilots flying a straight flight path in the presence of crosswind. They also use it in the final approach to land to keep the aeroplane in the centre of the runway and is called the "crab" method[78].

6.9 Controller Order Reduction

In this section, the order of the lateral controller is reduced following the same technique used in the longitudinal design.

The controller order can is calculated as follows:

$$n_K = n_G + 2n_{W_1} + 2n_{W_2} \quad \textbf{6.15}$$

Table 6.5 below, shows how the controller order was built-up using Equation 6.15.

Table 6.5: Controller order build-up

Model	Order	Description	Controller Order
G	14	Air vehicle lateral model with single aileron actuator	=14
W_1	2	Input weighting (i.e. integrators etc.)	+2x2 =18
W_2	2	Output weighting (i.e. low-pass filters etc.)	+2x2 =22
W_1^{-1}	2	Inverse of input weighting for Observer-form feedback	+2 =24

Applying the same reduction steps as in the longitudinal design, the 24th order observer-form controller with anti-windup was reduced to a 13th order system with the following results:

- Maximum Hankel SV truncated = 0.0041
- Full- and reduced-order systems ν-gap distance = 0.0045
- Non-linear simulation time response curves were undistinguishable and are not shown here.

6.10 Maximum Crosswind Test

The final reduced order controller was tested in the ACSL non-linear simulation to establish the maximum theoretical launch-survivable crosswind. It is vital to know the maximum crosswind any air vehicle can withstand at launch. All manned aeroplanes have the maximum crosswind component specified in the 'Flight Manual' and in the 'Pilot's Operating Handbook' that must not be exceeded during take-off or landing.

Although the A3 unmanned air vehicle is usually launched with a headwind, wind gust may reach high magnitudes with unpredictable variable directions.

From the simulation results, it was found that the maximum theoretical survivable crosswind was 17m/s which is equivalent to 33knots! Knowing that most General Aviation(GA) aeroplanes that have a weight of over 500kg have a maximum crosswind specification of about 15knots, the achieved limit is quite surprising and optimistic for such a small air vehicle. In some way it shows the limited capability of human pilots vs. the unlimited capability of autopilots.

Figure 6.19 to Figure 6.21, show the simulation results using the maximum survivable crosswind of 17m/s.

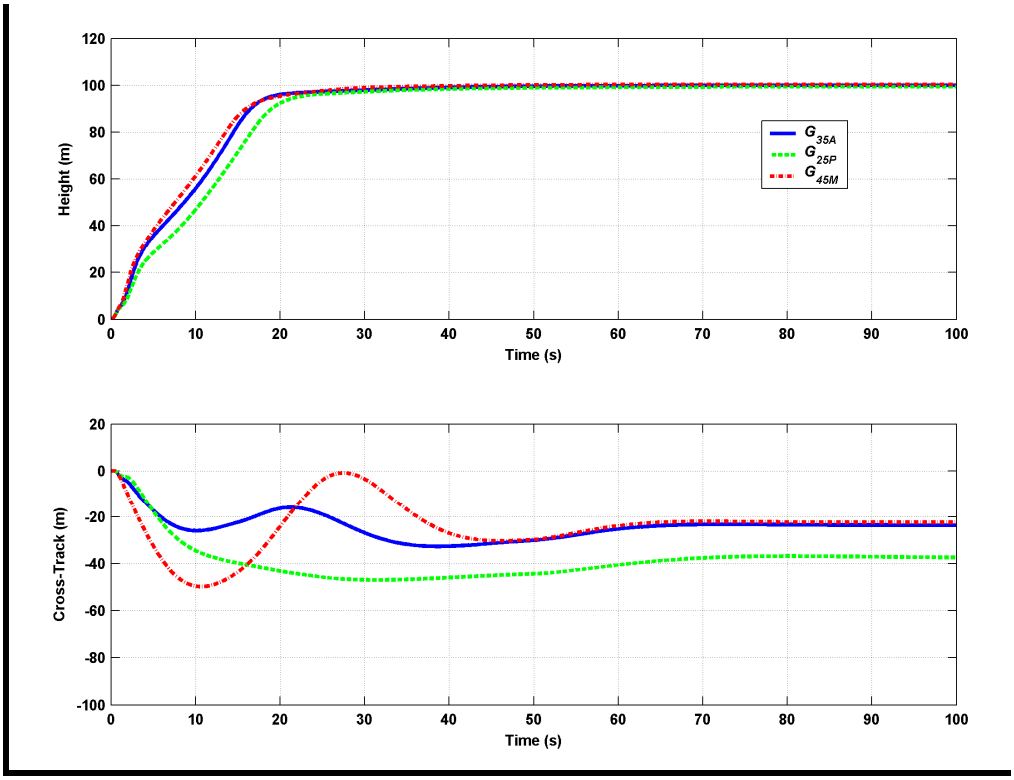

Figure 6.19: Maximum crosswind effect on controller cross-track performance with full flight envelope models: nominal G_{35A} and worst cases G_{25P} and G_{45M}

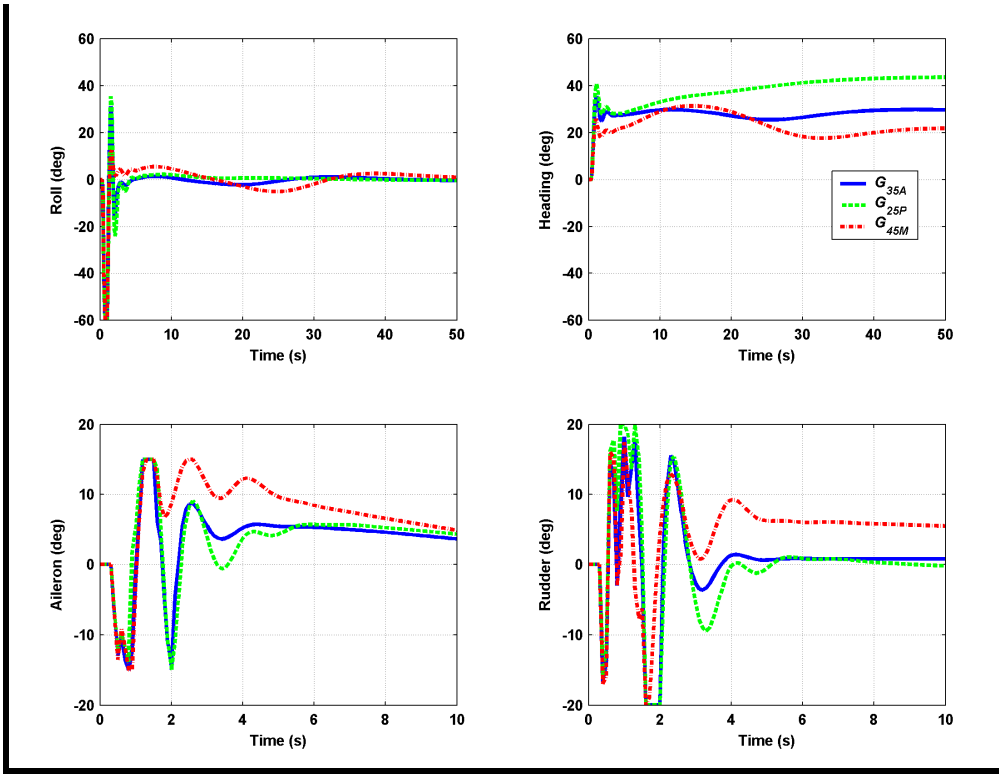

Figure 6.20: Maximum crosswind effect on roll, heading, and actuator commands

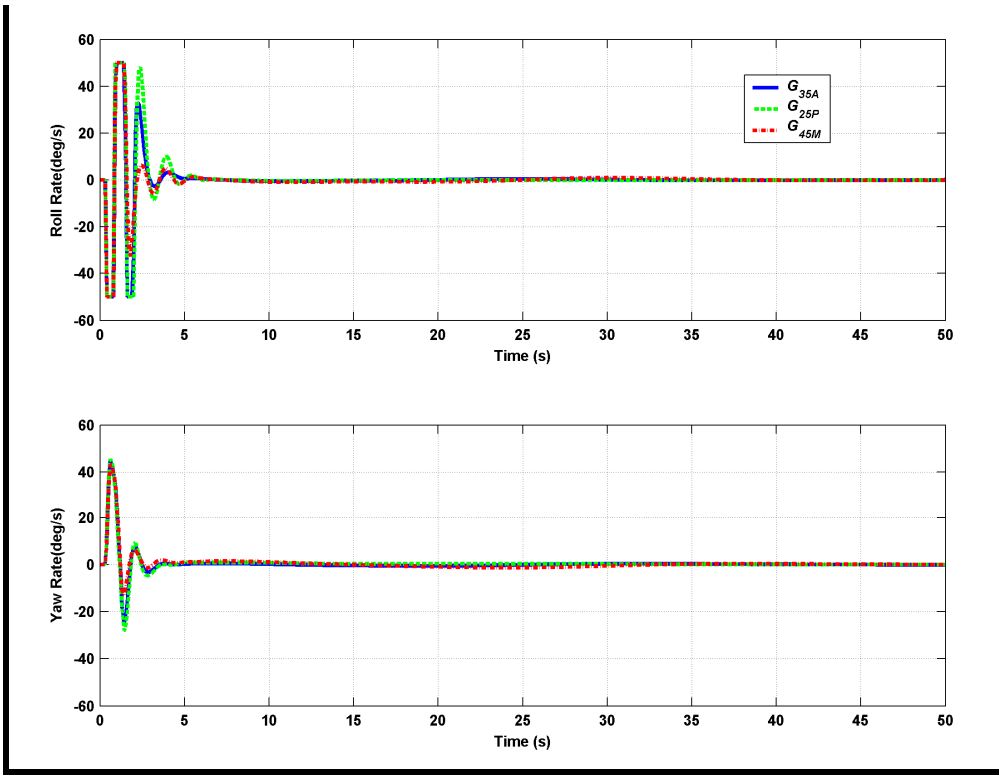

Figure 6.21: Maximum crosswind effect on controller roll and yaw rates stabilization

From the above results, the following can be observed,

- While the air vehicle survived the maximum crosswind launch with acceptable control and stabilization of roll and yaw as shown in Figure 6.20, the tracking performance was not very good. Even though is was flying a straight flight path, the steady-state cross-track error was more than 30*m* as shown in Figure 6.19. Also, in Figure 6.20, notice how the air vehicle was flying with a sideslip of over 40*deg* to overcome crosswind.

- A major limitation for the maximum crosswind control is the onboard sold-state rate gyro. The British Aerospace Vibrating Structure Gyro(VSG) was modelled in ACSL with the specified limits of ±50*deg*/*s* for all three axes. Figure 6.21 clearly shows that this limit was exceeded in roll.

- In Figure 6.20, aileron demand required was the minimum to keep the air vehicle levelled, while a noticeable rudder demand was required to overcome crosswind. Notice again that the low speed case (i.e. G_{25P}) required an opposite steady-state rudder demand compared with the nominal and high-speed worst cases(i.e. G_{35A} and G_{45M}) due to stability differences as discussed in the linear analysis in §6.6.1.

The lateral FCSD is considered successful.

6.11 Chapter Summary

- A linear lateral model was built for the FCSD which contained the models of aileron and rudder actuators to accurately represent the dynamics of the air vehicle. Aileron actuator was shown to have more effect on accuracy than rudder due to the airframe unstable roll dynamics.
- A detailed design of the lateral controller was performed using the modified LSDP by evaluating the achievable robust stability through each design stage. The worst-case models that represented the air vehicle operational flight envelope where also included in the evaluation. Linear analysis showed that the

design was successful.

- The controller was then implemented and evaluated in the ACSL non-linear simulation where it showed considerable performance degradation in the presence of moderate crosswind of $3m/s$.
- A simple but important modification was done on the first lateral-directional controller design to overcome crosswind effect on launch stability and track performance. The modification utilized the fact that side slipping was more effective than banking to overcome crosswind effect on cross-track performance.
- The modified controller order was reduced from a 24^{th} to a 13^{th} order system. It was successfully tested in the non-linear simulation for maximum crosswind launch survival of up to $17m/s$. It was also shown that this limit was mainly due to the rate gyro maximum input bound of $\pm 50deg/s$.

Chapter 7

Advanced Flight Control System Design

In Chapters 5 and 6 it was shown that designing the longitudinal and lateral-directional FCS separately is a successful design strategy. In this chapter the next logical step, to design the full flight control system in one step is described. This permits an evaluation of the advantages of taking the decoupling between the longitudinal and lateral dynamics into consideration in the design process. Also, in this chapter, the advanced technique of two degrees-of-freedom design is implemented to help improve performance and simplify the design task.

7.1 Full Linear Model Analysis

The full coupled linear model of the air vehicle, G_{35A}, is compared with the combined decoupled longitudinal and lateral-directional model G_{35AD}. Recall back in §**4.5.3** on page 75, that G_{35AD} was built as follows,

$$G_{35AD}(s) = \left[\begin{array}{c|c} G_{35Az}(s) & 0 \\ \hline 0 & G_{35Ay}(s) \end{array}\right] \qquad \textbf{7.1}$$

with

$$\begin{Bmatrix} \dot{x}_{35Az} \\ \dot{x}_{35Ay} \end{Bmatrix} = \begin{bmatrix} A_{35Az} & 0 \\ 0 & A_{35Ay} \end{bmatrix} \begin{Bmatrix} x_{35Az} \\ x_{35Ay} \end{Bmatrix} + \begin{bmatrix} B_{35Az} & 0 \\ 0 & B_{35Ay} \end{bmatrix} \begin{Bmatrix} u_{35Az} \\ u_{35Ay} \end{Bmatrix}$$
$$\begin{Bmatrix} y_{35Az} \\ y_{35Ay} \end{Bmatrix} = \begin{bmatrix} C_{35Rz} & 0 \\ 0 & C_{35Ay} \end{bmatrix} \begin{Bmatrix} x_{35Az} \\ x_{35Ay} \end{Bmatrix} \qquad \textbf{7.2}$$

where G_{35Az} and G_{35Ay} are the longitudinal and lateral dynamic models respectively. The same is repeated for the operational flight envelope worst-case models, i.e. the low speed and high speed models G_{25PD} and G_{45MD} .

7.1.1 The *v*-Gap Metric

Applying the *v*-gap metric, the combined/decoupled models are treated as uncertainties of the full/coupled models. The 'distance' between the two systems is measured as shown in Table 7.1 below.

Table 7.1: Decoupling effect on modelling accuracy

Models	*v*-Gap Metric distance
nugap(G_{35A} , G_{35AD})	0.030
nugap(G_{25P} , G_{25PD})	0.059
nugap(G_{45M} , G_{45MD})	0.027

Table 7.1 indicates that there are small but not negligible differences between the two systems and the differences(i.e. coupling) are inversely proportional to airspeed.

7.1.2 Robust Stabilization

Using the same weights as the longitudinal and lateral FCSD, the robust stabilization controller was synthesised for the full/coupled model and compared with the combined/decoupled model. The *SM*s are shown in Table 7.2 below. The table shows that the achieved robust stability is similar, although there is little advantage using the full/coupled model, i.e. G_{35A} in the design. The table also lists the achieved stability in

the longitudinal and lateral designs, i.e. G_{35Az} and G_{35Ay}. Notice that by using the combined dynamic model, i.e. G_{35AD}, the stability was reduced to the lateral system stability level.

Table 7.2: Full vs. decoupled models robust stabilization

Model	*SM*	*GM* (dB)	*PM* (*deg*)
G_{35A}	0.311	5.59	36.27
G_{35AD}	0.309	5.56	36.06
G_{35Az}	0.36	6.48	41.8
G_{35Ay}	0.31	5.6	36.0

7.1.3 Linear Simulation

Finally, the step response of the coupled and decoupled control designs are evaluated here. Note that in this analysis the controller designed using G_{35AD} and the controller designed using G_{35A}, called here K_{zy} and K_{sx} respectively, are both evaluated using G_{35A}. This is because the coupled model G_{35A} represent the real air vehicle response more accurately than the decoupled model G_{35AD}.

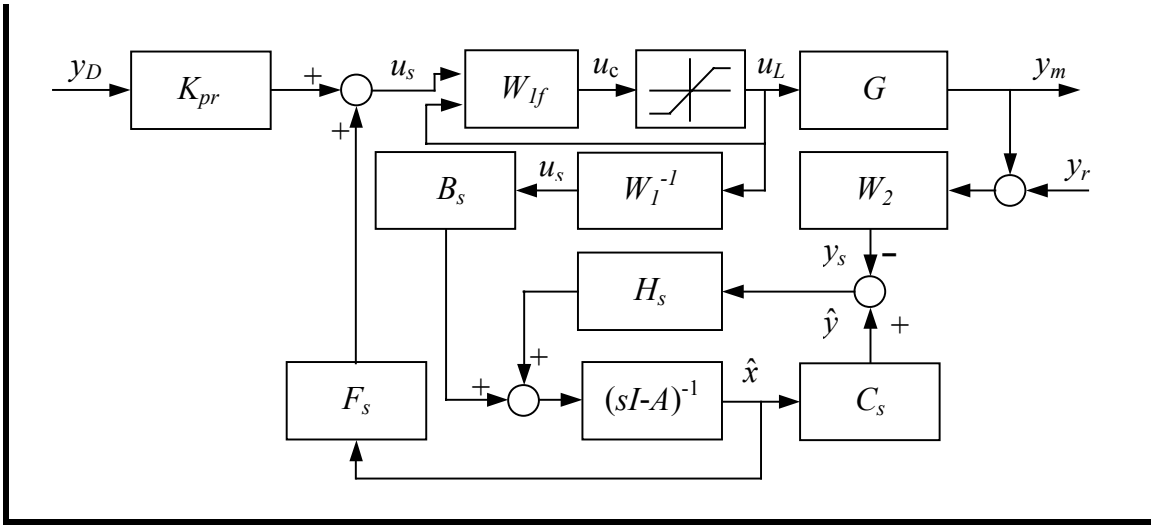

Figure 7.1: Controller 'demanded' and 'regulator feedback' inputs: y_D and y_r

Note that the step function is fed though the demanded input y_D and not the regulator output feedback y_r. Recall that the demands can be fed through either the regulator

feedback or the demanded input as was shown in both Figure 5.25 and Figure 6.8 for the longitudinal and lateral designs respectively, and repeated here for convenience in Figure 7.1.

Figure 7.2(a,b,c) show the response to a unit step demand of airspeed, height, and cross-track respectively. Figure 7.2 confirms that using either linear coupled or uncoupled models of the air vehicle in the FCSD produces very similar results; both solutions have indistinguishable responses.

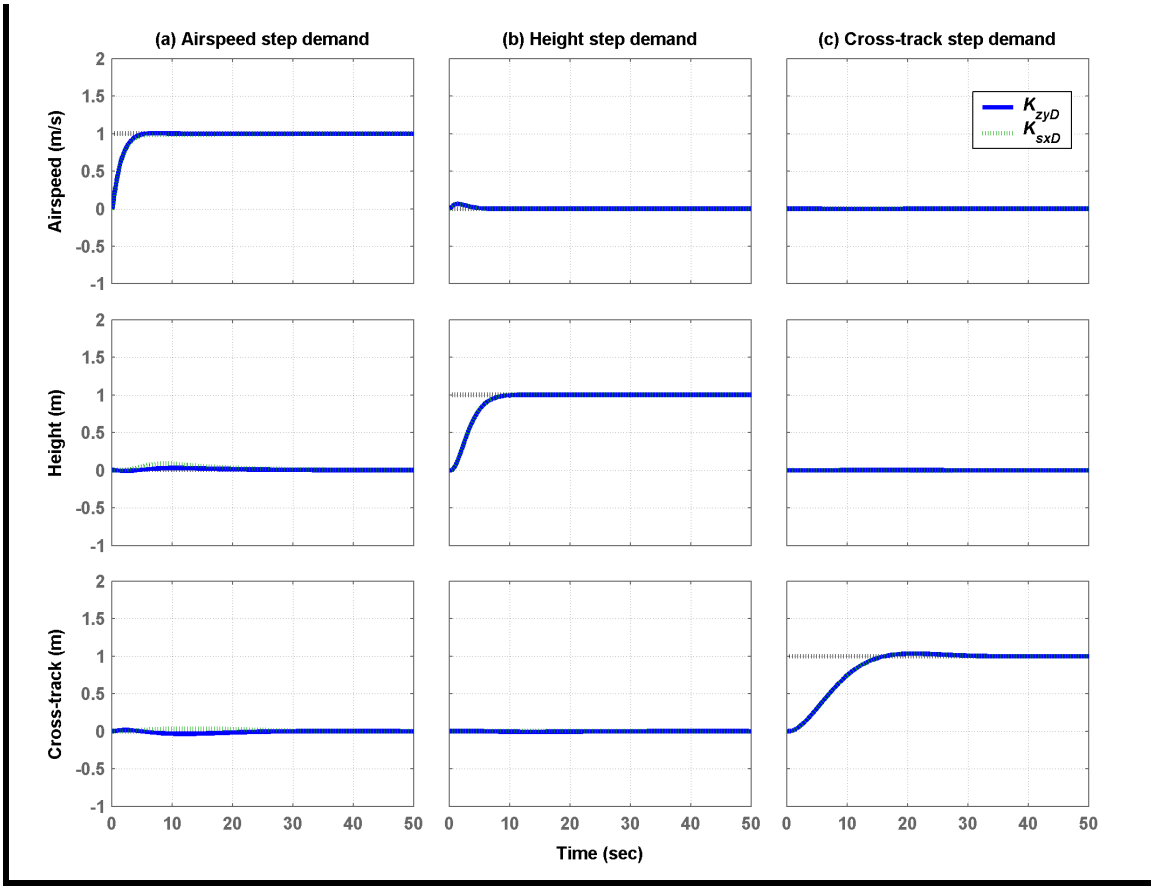

Figure 7.2: Coupled vs. uncoupled model designs step response comparison

7.2 Two Degrees-of-Freedom Design

It has been shown in the longitudinal and lateral FCSD processes that the performance requirements of tracking height and cross-track demands were achieved by altering the

open-loop SV of the air vehicle model with pre- and post weights. This was done by adding integrators to insure zero steady-state errors; adding zeros to reduce gain cross-over slopes to insure minimum phase lag, and adding low-pass filters to increase robustness to high frequency disturbances, etc. It was also shown that the observer-form configuration, shown in Figure 7.1 above, exhibits the demanded input y_D structure to give better demand tracking and decoupling than in the regulator feedback structure with input y_r . This is due to the fact that y_r is influenced by the low-pass filters in W_2 , while y_D is influenced by the integrators in W_1 only as shown in Figure 7.1. This translates into a wide-band response to the demanded inputs as shown in Figure 7.3.

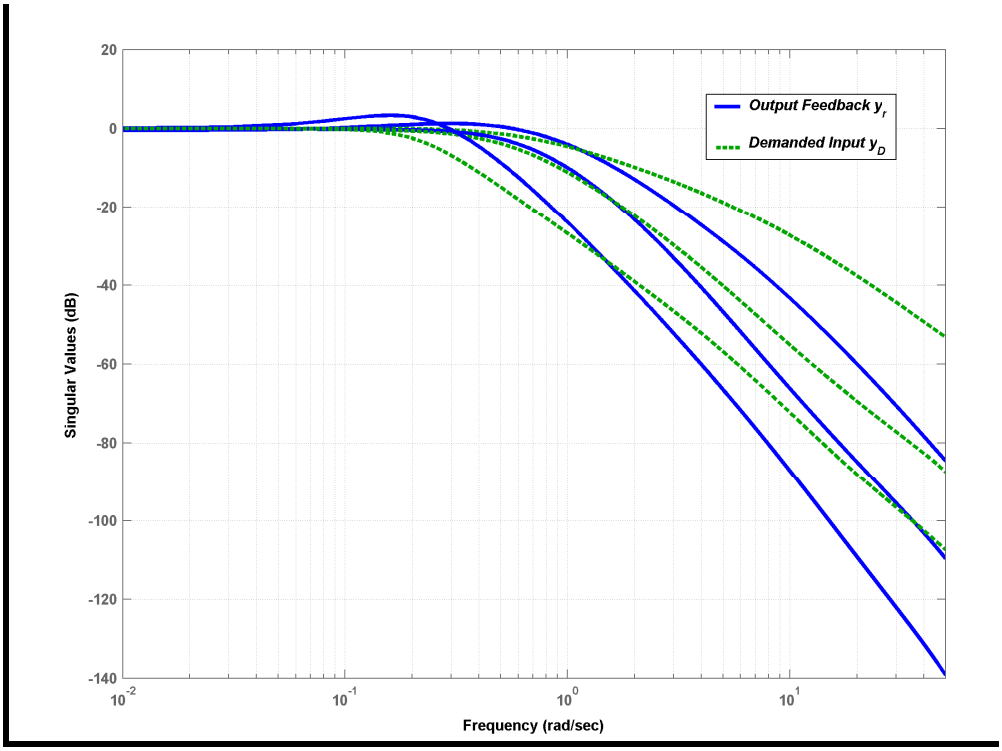

Figure 7.3: Closed-loop SV of regulator feedback and demanded inputs

Figure 7.3 also shows the effect of the pre weight, K_{pr} of Figure 7.1, on the unity feedback requirements which was achieved quite nicely. Although the demanded input has improved the performance of the tracking response of height and cross-track, it was not possible to specify this performance independently from the robust stabilization design. In other words, the robust stabilization synthesis produced one controller with two inputs, y_D and y_r, that cannot be designed independently. Furthermore, it was not

directly possible to specify any time-domain requirements for the tracking performance which is an important feature that a proper FCSD should have.

7.2.1 Controller Synthesis

Recall that in Chapter 2, the two degrees-of-freedom (TDF) controller was introduced. It was shown that it consists basically of two controllers $K=[K_1\ K_2]$ as shown in Figure 7.4. K_1 is designed to insure that y_D input response matches the dynamic model(s) defined in T_{ref} where the time responses are defined by first or second-order transfer functions with a specified time delay and, or natural frequency, and damping ratio. W_i is the pre-weight constant matrix to insure unity gain input, and W_o is the selection matrix where the required outputs for control are selected, i.e.

$$W_o = \begin{matrix} u & q & \theta & h & p & r & \phi & \psi & y_x \end{matrix} \begin{bmatrix} 1 & 0 & 0 & 0 & 0 & 0 & 0 & 0 & 0 \\ 0 & 0 & 0 & 1 & 0 & 0 & 0 & 0 & 0 \\ 0 & 0 & 0 & 0 & 0 & 0 & 0 & 0 & 1 \end{bmatrix} \begin{matrix} u \\ h \\ y_x \end{matrix} \qquad \textbf{7.3}$$

ρ is a weighting scalar that is used to place more emphasis on model matching in the optimisation at the expense of robustness. Note that $\rho \geq 1$, and if set to zero the TDF controller reduces to the ordinary robust stability problem.

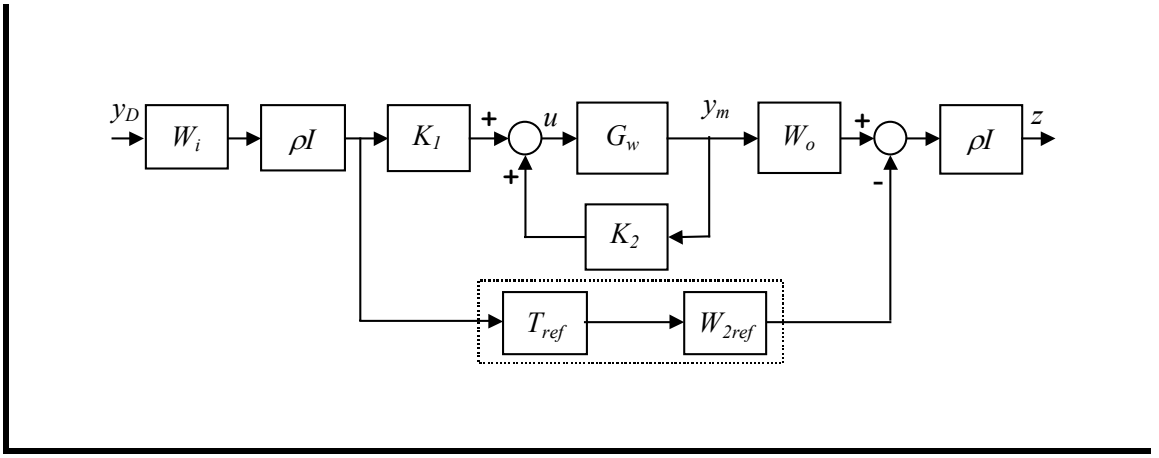

Figure 7.4: Two degrees-of-freedom controller design configuration

Note that G_w in Figure 7.4 is the weighed/shaped air vehicle model, i.e.

$$G_w = W_2 \, G \, W_1 \qquad \textbf{7.4}$$

Also note that the weighting function W_{2ref} is equal to W_2 weights of the controlled outputs only, i.e.

$$W_{2ref} = \mathtt{diag}\left[W_{2u} \quad W_{2h} \quad W_{2y_x} \right] \qquad \textbf{7.5}$$

7.2.2 Controller Design Procedure

The design procedure for the TDF controller is equivalent to that of the LSDP with the extra step of selecting the desired closed-loop transfer functions T_{ref} that represent the desired dynamic behaviour of the controlled outputs.

The initial design was based on the controller weights developed for the longitudinal and lateral-directional designs of Chapters 5 and 6. Minor modifications were made due to the fact that the command tracking performance is now achieved using the desired closed-loop transfer function T_{ref} which gives a real second degree of freedom of design. The air vehicle model used in the design is the combined/decoupled model G_{35AD} which was discussed in §7.1.2. This is because decoupled controllers are desired for their ease of design and analysis. Also, the use of the full/coupled model in the design did not show any significant advantages.

Scaling, shaping, and alignment were done in the same way as in the previous designs. The final input weights are shown in Equation 7.6. Note that the alignment weights only operate on the lateral-directional dynamics, i.e. ξ and ζ and the SVs were aligned at $7 rad/s$. Equation 7.7 shows the final output diagonal scaling and shaping weights.

$$
\begin{aligned}
W_{1c} &= \mathrm{diag}\begin{bmatrix} \tau & \eta & \xi & \zeta \\ 4.0 & 0.2 & 3.85 & 2.87 \end{bmatrix} \\
W_{1s} &= \mathrm{diag}\begin{bmatrix} 1 & \dfrac{s+0.1}{s+0.0001} & 1 & \dfrac{s+1}{s+0.1} \end{bmatrix} \\
W_{1a} &= \mathrm{diag}\begin{bmatrix} \tau & \eta & \xi & \zeta \\ 1 & 0 & 0 & 0 \\ 0 & 1 & 0 & 0 \\ 0 & 0 & -0.0855 & 0.0421 \\ 0 & 0 & -0.2345 & 0.5337 \end{bmatrix}
\end{aligned}
\qquad \textbf{7.6}
$$

$$
W_{2c} = \mathrm{diag}\begin{bmatrix} u & q & \theta & h & p & r & \phi & \psi & y_x \\ 0.04 & 3.0 & 2.0 & 0.03 & 0.333 & 3.333 & 1.429 & 1.111 & 0.033 \end{bmatrix}
$$

$$
W_{2s} = \mathrm{diag}\begin{bmatrix} 1 & \dfrac{s+0.0001}{s+0.1} & 1 & 1 & 1 & 1 & 1 & 1 & \dfrac{1}{s/10+1} \end{bmatrix}
\qquad \textbf{7.7}
$$

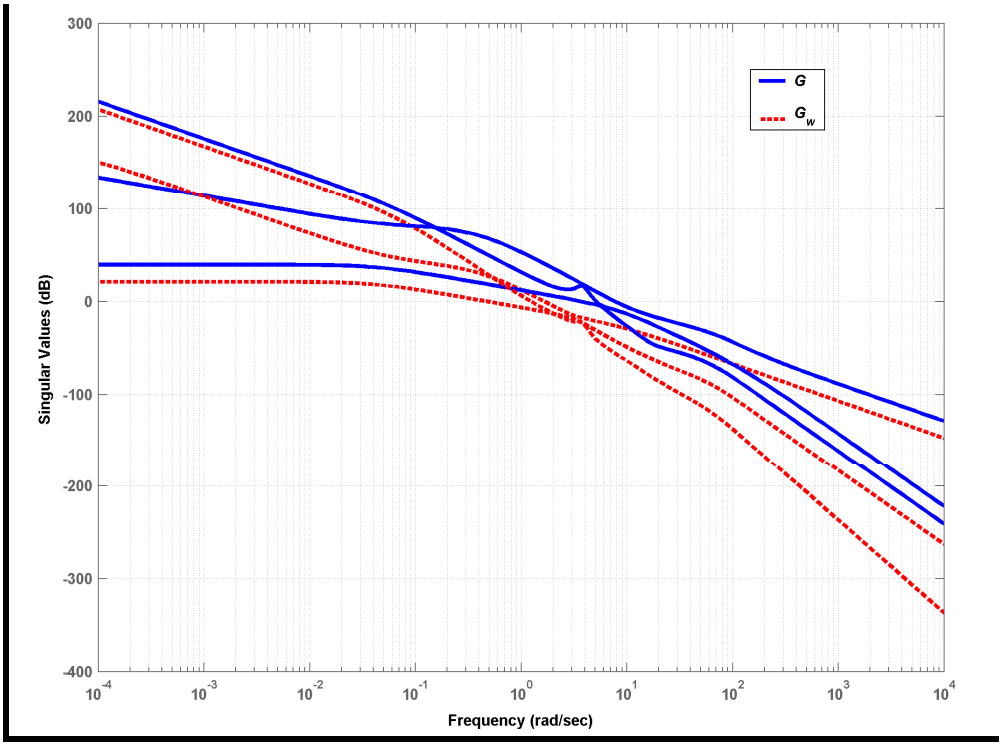

Figure 7.5: Effect of weights on model controlled outputs open-loop SV

The effect of scaling, shaping, and alignment on the air vehicle model controlled outputs (i.e. u, h, and y_x) open-loop SV is shown in Figure 7.5. The achieved stability margin for the standard LSDP was

$$SM = 0.30 \rightarrow GM = 5.42 \text{ dB}, PM = 35.18 \text{ deg} \quad \textbf{7.8}$$

The most important feature of the TDF controller design is the ability to specify dynamic reference models for the controlled outputs. These models must be realistic and obtainable. For the airspeed reference model, it must respond quickly for the launch phase. For the height reference model, it should not be as quick as the airspeed response so the air vehicle would not stall with high angles of attack, but at the same time it must be quick enough to recover the flight path height loss after launch.

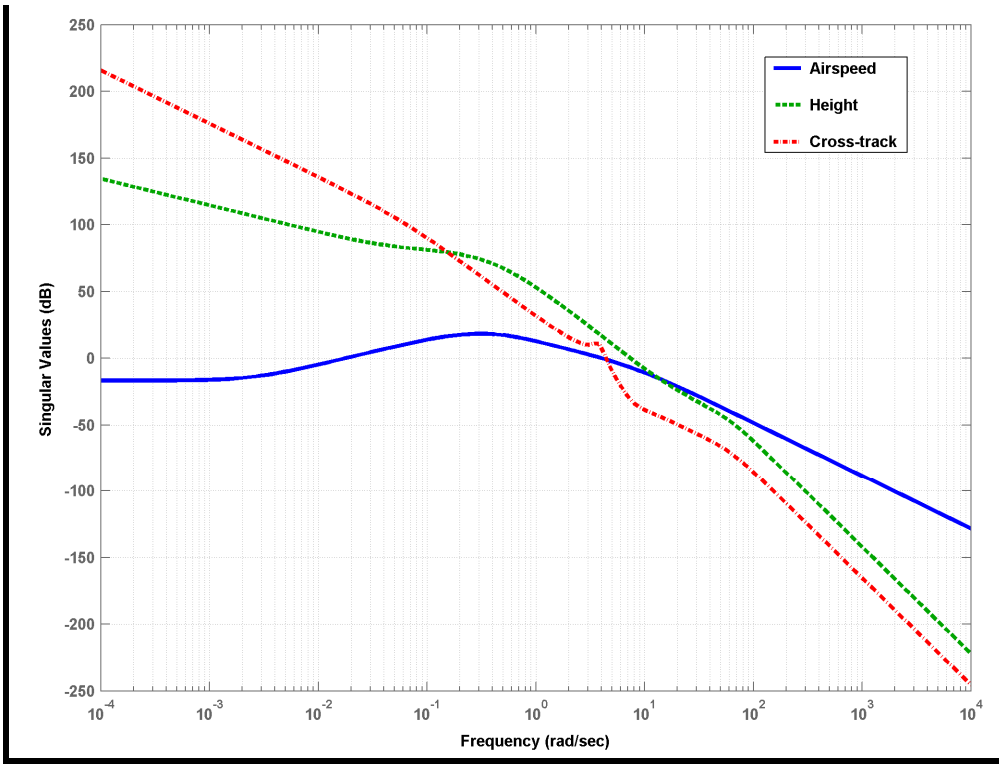

Figure 7.6: Nominal model unshaped open-loop SVs for controlled outputs

For the cross-track error reference model, it is known from the lateral-directional dynamic analysis in Chapter 4 that the cross-track has very slow response which can be

verified by the air vehicle dynamic open-loop model SV shown in Figure 7.6. Also, from the lateral FCSD in Chapter 6, it was found that using the rudder to control the cross-track is a better strategy to avoid saturation and activation of the unstable *Dutch-roll* mode. Figure 7.6 shows that this loop has a narrow bandwidth that must be taken into consideration. Equation 7.9 shows the final selected first-order reference models transfer function for the controlled outputs.

$$T_{ref} = \mathtt{diag}\left[\frac{1}{2s+1} \quad \frac{1}{3s+1} \quad \frac{1}{5s+1}\right] \tag{7.9}$$

Solving the TDF problem, the following results were obtained at $\rho = 1$,

$$\gamma = 3.55,\ SM = 0.285 \rightarrow GM = 5.1 \text{ dB},\ PM = 33.1\ deg \tag{7.10}$$

7.2.3 Controller Implementation

The TDF controller is implemented as shown in Figure 7.7 below. Notice that the controller is implemented with the two inputs y_D and y_r , where y_D contains the controlled outputs only, i.e. u, h, and y_x , while y_r contains the full output feedback vector. The Hanus anti-windup was also implemented by replacing the input weighting function W_1 with its equivalent anti-windup W_{1f} .

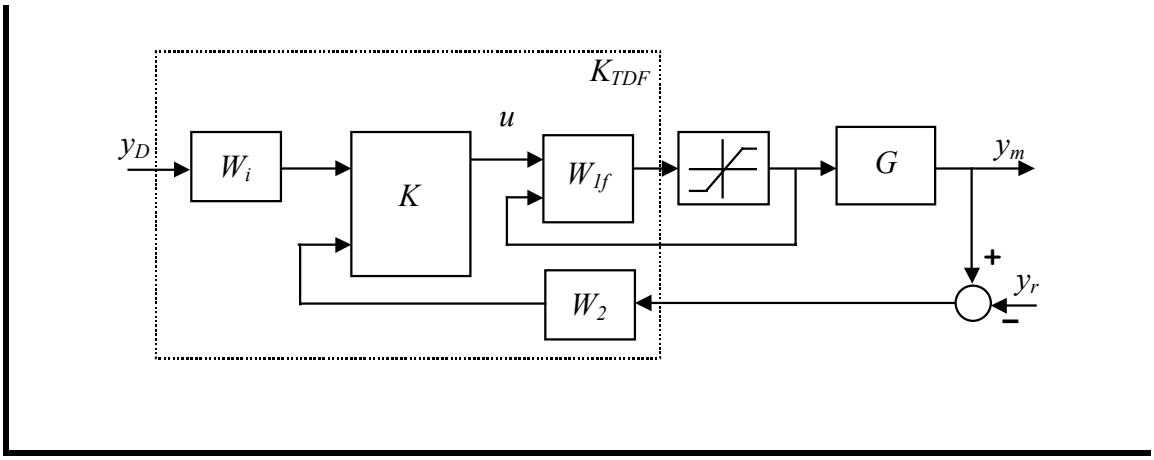

Figure 7.7: TDF controller implementation with Hanus anti-windup

7.2.4 Linear Evaluation

To evaluate the initial TDF design, a simple step was applied to the demanded inputs y_D of the system in Figure 7.7, where the coupled air vehicle linear model G_{35A} was used in the simulation.

Figure 7.8 shows the controlled output responses compared with the ideal reference model. Although the dynamic responses are not very close, the results show how the added degree of freedom can help in shaping the time response of the controlled outputs. This is quite useful if flying qualities were defined since these can be directly implemented in the TDF design. Notice in Figure 7.8 that coupling is quite eliminated between the controlled outputs, even though the linear coupled model was used in the evaluation as mentioned earlier.

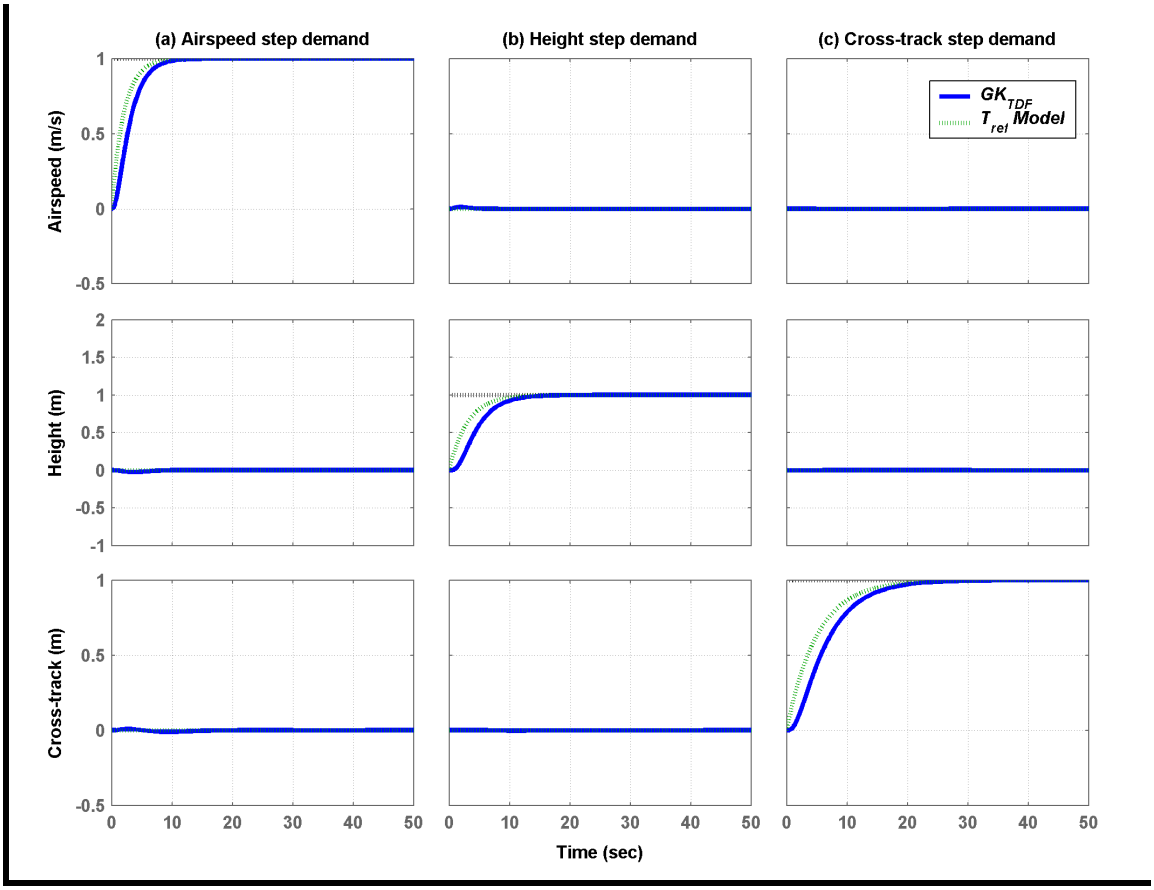

Figure 7.8: Controlled output response vs. reference model

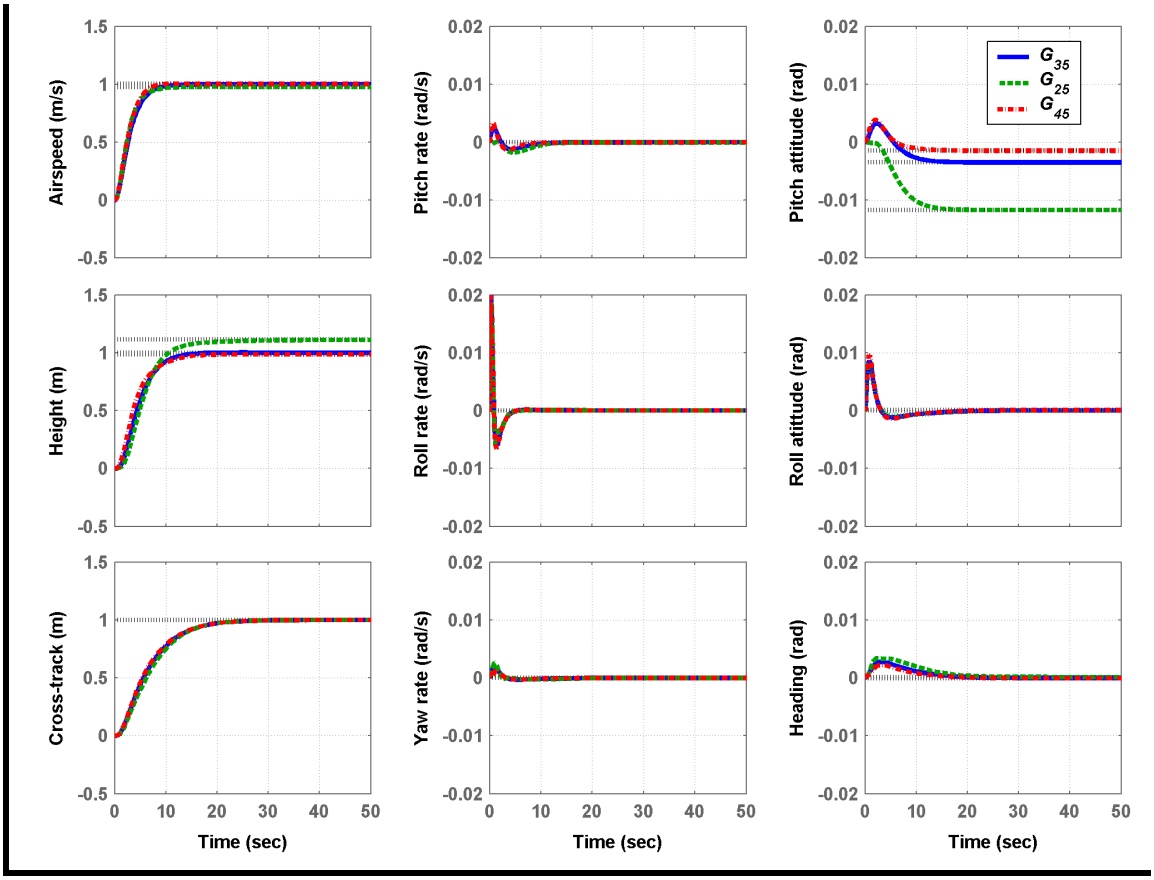

Figure 7.9: Response to simultaneous u, h and y_x unit step demand for nominal and worst-case models

Figure 7.9 above, shows the system response to the operational flight envelope nominal and worst-case models, i.e. G_{35}, G_{25}, and G_{45}. A simultaneous unit step demand input is applied to airspeed u, height h, and cross-track y_x. The results clearly show the level of performance the TDF controller achieved where the controlled outputs are almost identical for the full flight envelope conditions. Though, the effect of increased airspeed is reflected on the steady-state error of height and pitch attitude. Note that the pre-weight W_i would be scheduled as a function of airspeed to reduce the steady-state errors of the controlled outputs in the non-linear simulation as will be shown later on.

7.2.5 Non-linear Implementation

The TDF controller is implemented in the ACSL non-linear simulation following similar steps as for the longitudinal and lateral-directional designs. The main implementation steps are as follows,

1. The final controller was transformed into the stand-alone state-space form, discretized at the real control system processor frequency and exported to ACSL using formatted ASCII files.
2. All scheduled trim tables generated for the longitudinal and lateral controllers were used for the TDF FCS. The command pre-weight W_i was also scheduled as a function of airspeed. Note that scheduled W_i was also transferred to ACSL in the same controller file.
3. The required linear feedback controller inputs y_m were calculated on-line in ACSL, including the output feedback and demanded inputs, y_r and y_D .
4. The same mixing strategy for the starboard- and port-actuators of the longitudinal and lateral designs was implemented, where the combined mixing was as follows,

$$\begin{Bmatrix} \tau \\ \eta_{SB} \\ \eta_P \\ \xi_{SB} \\ \xi_P \\ \zeta_{SB} \end{Bmatrix}_A = \begin{bmatrix} 1 & 0 & 0 & 0 \\ 0 & 1 & 0 & 0 \\ 0 & 1 & 0 & 0 \\ 0 & 0 & 1 & 0 \\ 0 & 0 & -1 & 0 \\ 0 & 0 & 0 & 1 \end{bmatrix} \begin{Bmatrix} \tau \\ \eta \\ \xi \\ \zeta \end{Bmatrix}_D \qquad \textbf{7.11}$$

7.2.6 Non-linear Evaluation

Here, the TDF controller is evaluated in the ACSL non-linear simulation using the nominal and worst-case operating flight conditions, i.e. G_{35A}, G_{25P} and G_{45M}.

Figure 7.10 to Figure 7.13 show the launch phase and the simultaneous step response of 10*m*-height and 5*m*-cross-track demands at 50*s* from launch. The TDF controller performance is evaluated by the controlled outputs time response in Figure 7.10. Although the cross-track response for the three flight conditions are almost identical, the height response shows some slight differences. These differences signify the sensitivity of the controller demanded input y_D. This is due to the fact that the longitudinal control system requires the trim values for throttle, elevator and pitch attitude scheduled with

airspeed. It also requires the demanded input pre-weight W_i, which is also scheduled with airspeed only and did not take X_{CG} into account. The non-linear implementation has shown that the demanded input y_D is more sensitive to the accuracy of these parameters than the output feedback demand y_r, where the pre-weight W_i is not even required.

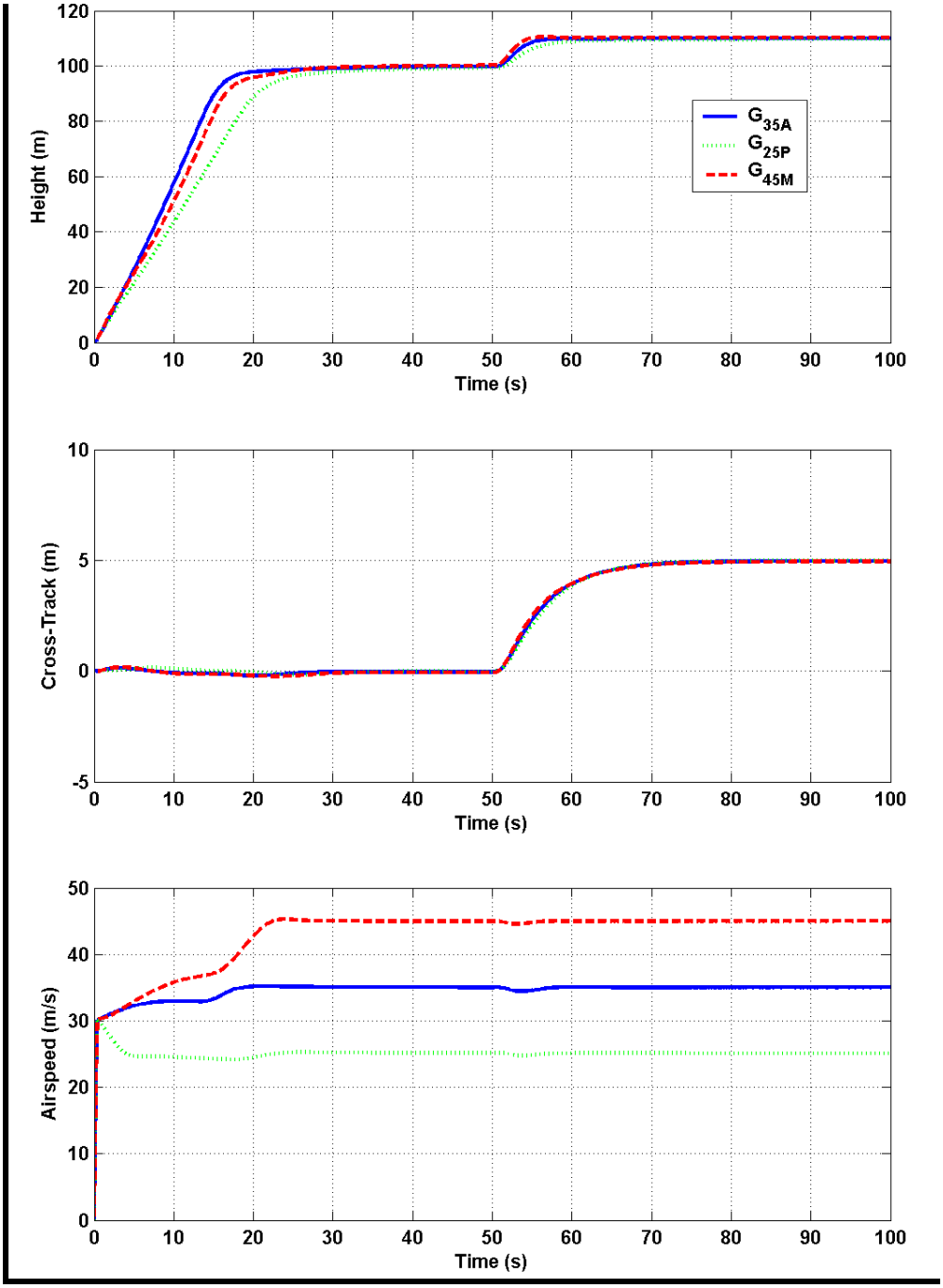

Figure 7.10: Non-linear simulation response of controlled outputs for the nominal and worst-case conditions

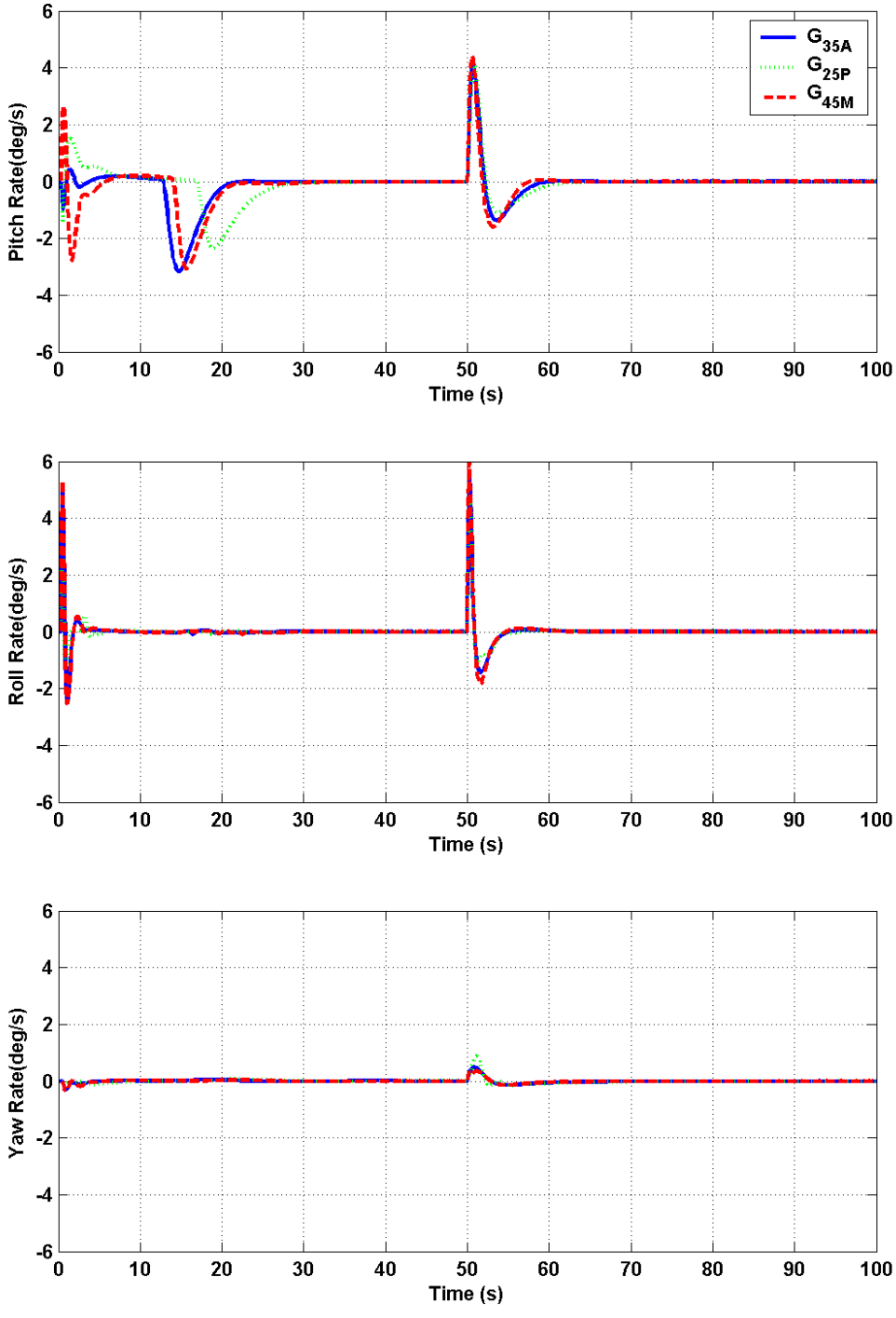

Figure 7.11: Non-linear simulation response of angular rates for the nominal and worst-case conditions

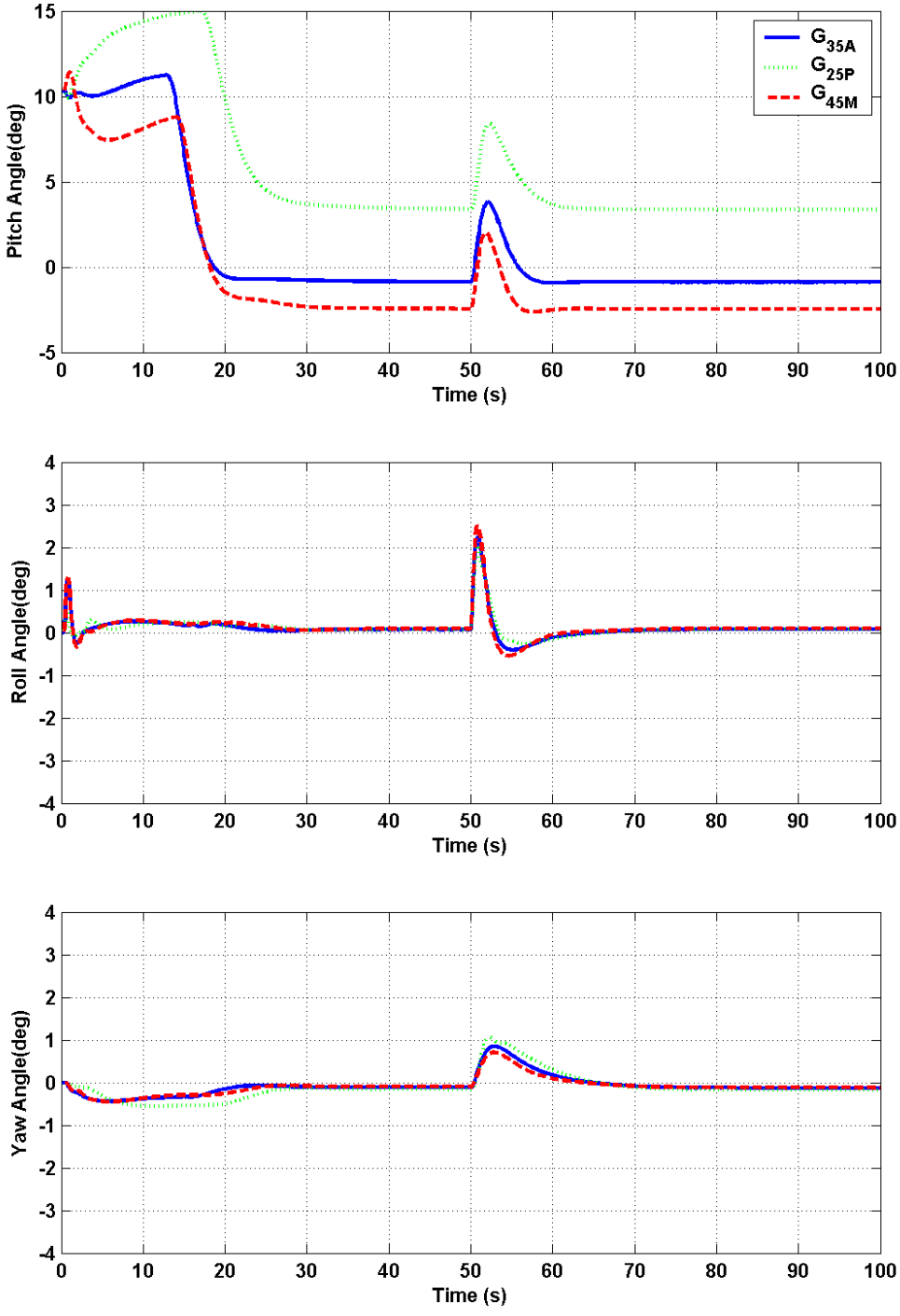

Figure 7.12: Non-linear simulation response of angular attitudes for the nominal and worst-case conditions

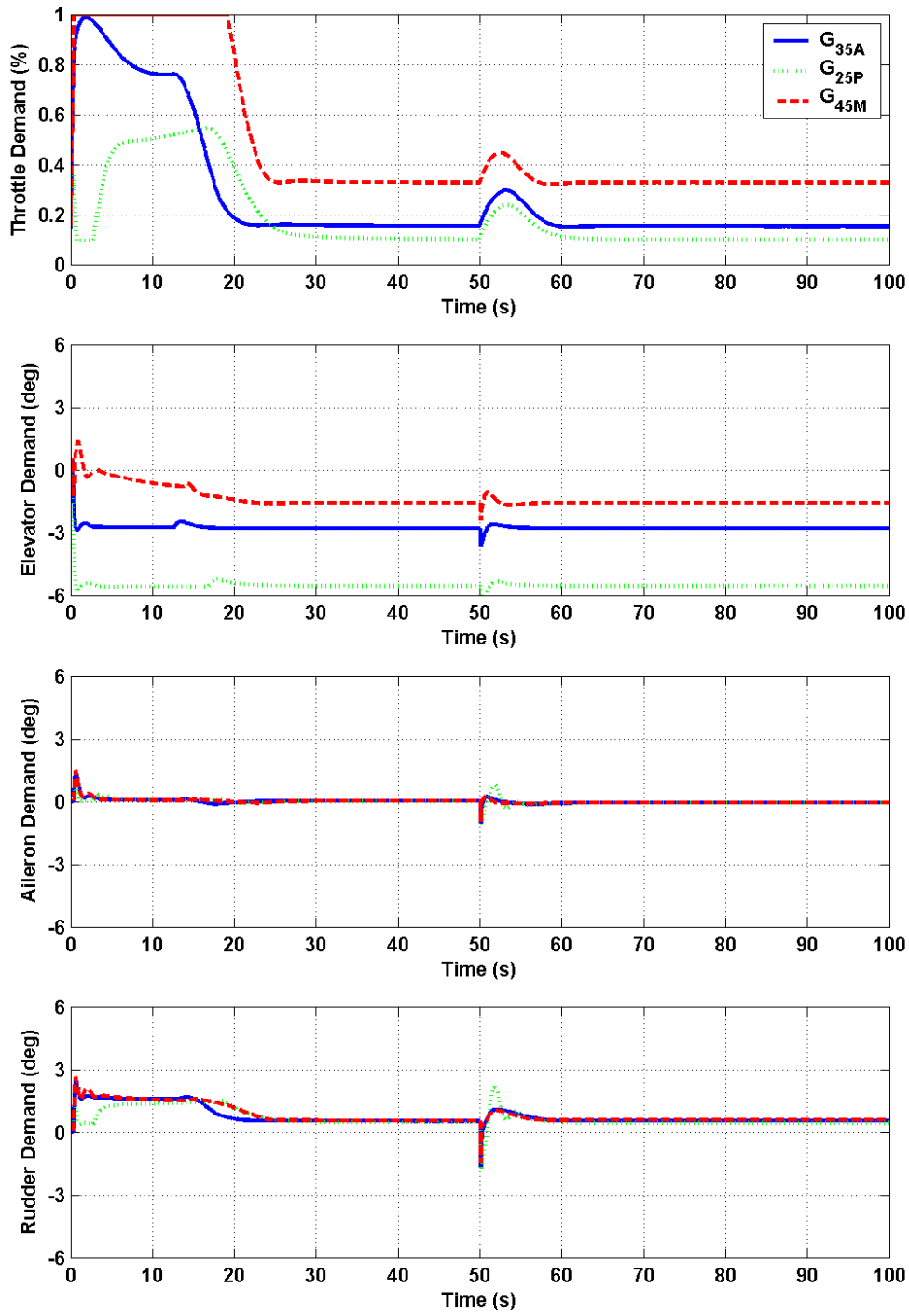

Figure 7.13: Non-linear simulation response of actuators demands for the nominal and worst-case conditions

The angular rates in Figure 7.11 show no signs of instability and have anticipated amplitudes. Similarly, Figure 7.12 shows well-accepted angular attitudes for the manoeuvres executed. Note again that the nominal and high airspeed models, i.e. G_{35A} and G_{45M}, are flying with negative pitch attitudes with respect to the air vehicle fuselage. Also note how both roll and yaw angles have null steady-state values.

Finally, the actuator commands are shown in Figure 7.13, where only throttle command hits the threshold in the high airspeed case as expected. Notice how the rudder had the same non-zero steady-state value for all cases.

7.2.6.1 Comparison with Decoupled Controller

Figure 7.14 below, shows the TDF controller K_{TDF} response vs. the combined/decoupled longitudinal and lateral controller K_{ZY} developed in Chapters 5 and 6. Notice that although K_{ZY} has a slightly better climb characteristic, it is not as good as K_{TDF} in the cross-track performance. Recall that in Chapter 6, the lateral controller was modified to overcome and survive severe cross-winds of up to $17m/s$. It is clear that this capability is at the expense of cross-track steady-state tracking performance. K_{TDF}, also shown in Figure 7.14, has a slightly better airspeed control with no over-shoots.

7.2.6.2 Maximum Cross-Wind Effect

Cross-wind of $17m/s$ (33 knots) was again applied in the ACSL simulation, with the simultaneous height and cross-track steps at $50s$ after launch.

Controlled output responses are shown in Figure 7.15 below, indicate that the TDF controller has a good level of robustness with no substantial loss of performance. Notice again that G_{45M} achieves the minimum cross-track error due to airspeed, but drifts very quickly at launch due to its instability, while the inverse happens to G_{25P}.

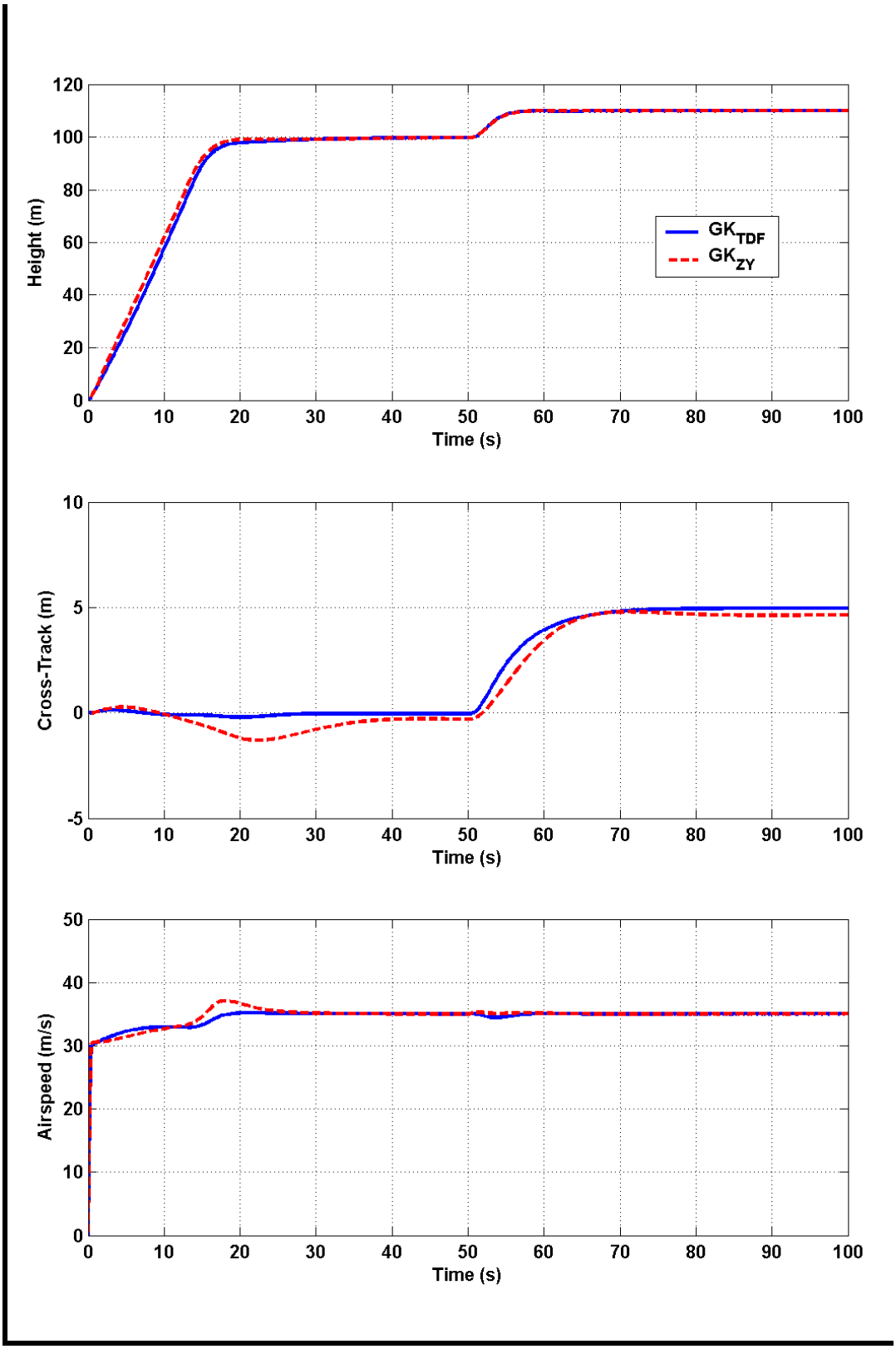

Figure 7.14: TDF controller K_{TDF}, vs. combined long./lat. controller K_{ZY}

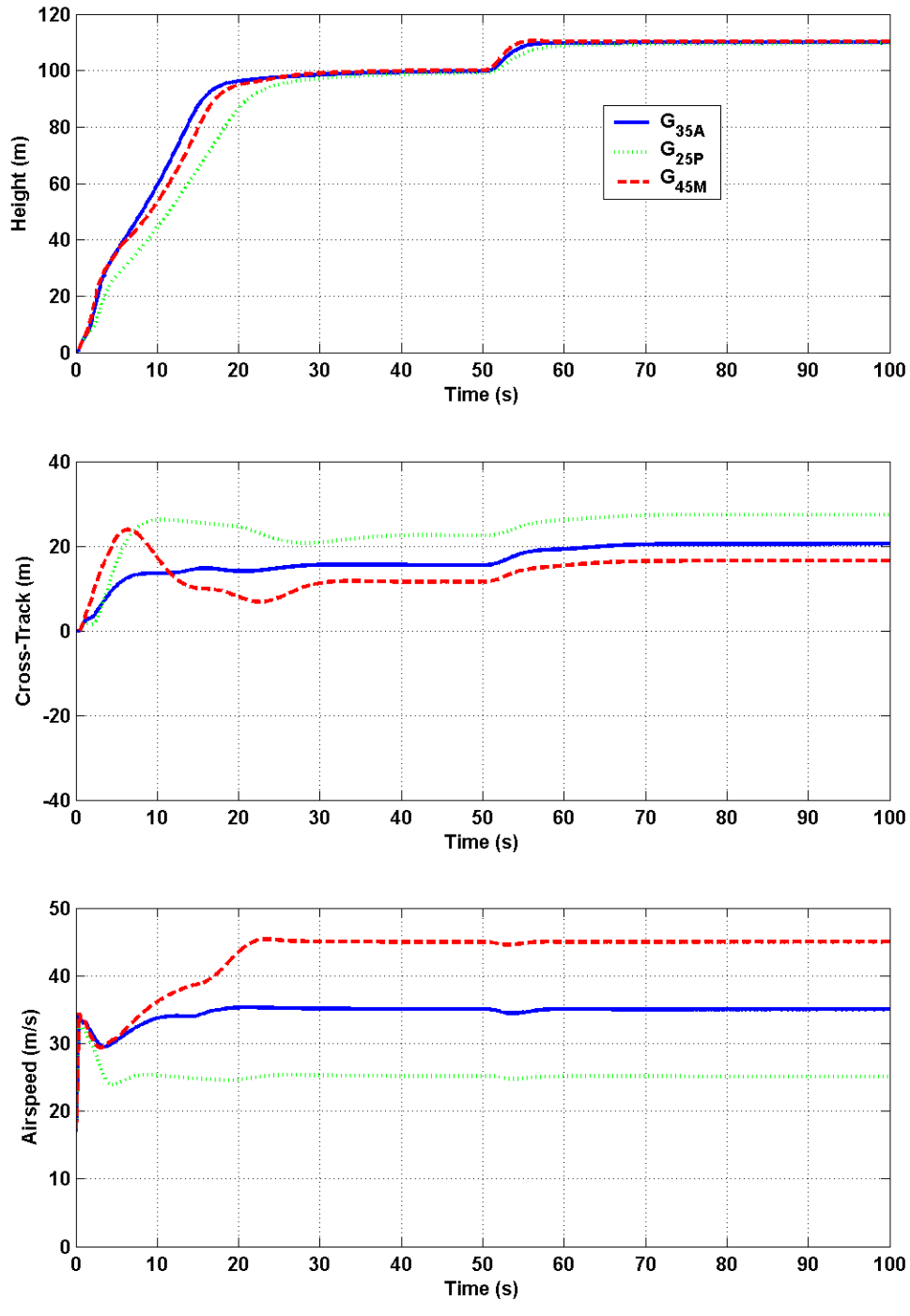

Figure 7.15: Maximum cross-wind effect for nominal and worst-case conditions

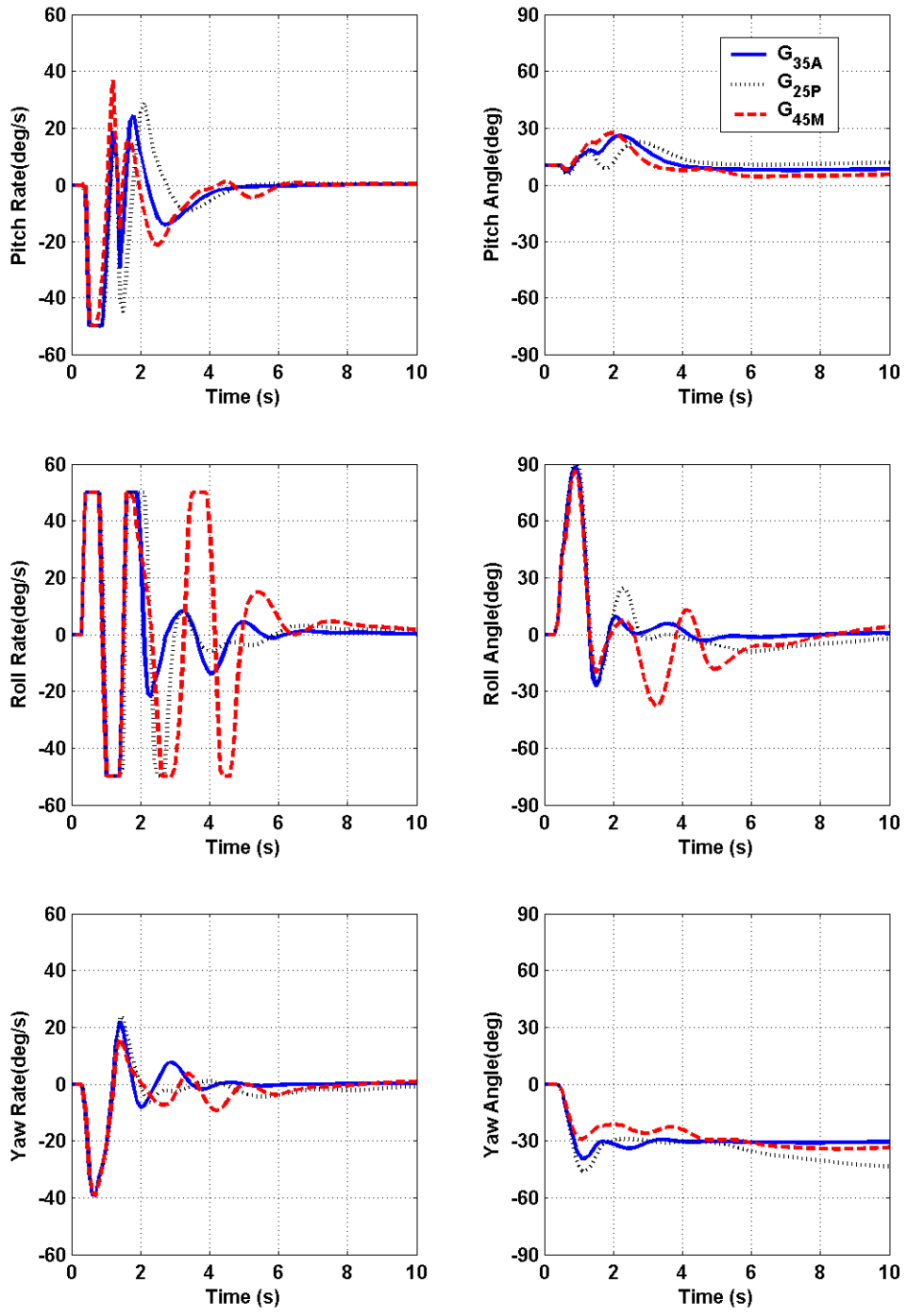

Figure 7.16: Maximum cross-wind effect on controlled angular angles and

Attitude and rate responses are shown in Figure 7.16 above. Note that only the first 10*s* are shown to emphasize the launch phase activity. Although the response curves in

Figure 7.16 above do not look very neat, they are fairly acceptable for that unrealistic launch condition. Notice again that G_{45M} has the greatest angular rate activity at launch when the rate gyro limits of 50*rad/s* are exceeded a few times at roll. Also, notice how the air vehicle recovers from the unusual attitude of 90*deg* of roll and maintains wings-level attitude later on. Notice also, that the air vehicle side-slips with high yaw angles of 30-40 *deg* to overcome the cross-wind effect, which proved again to be quite an effective tactic to adopt.

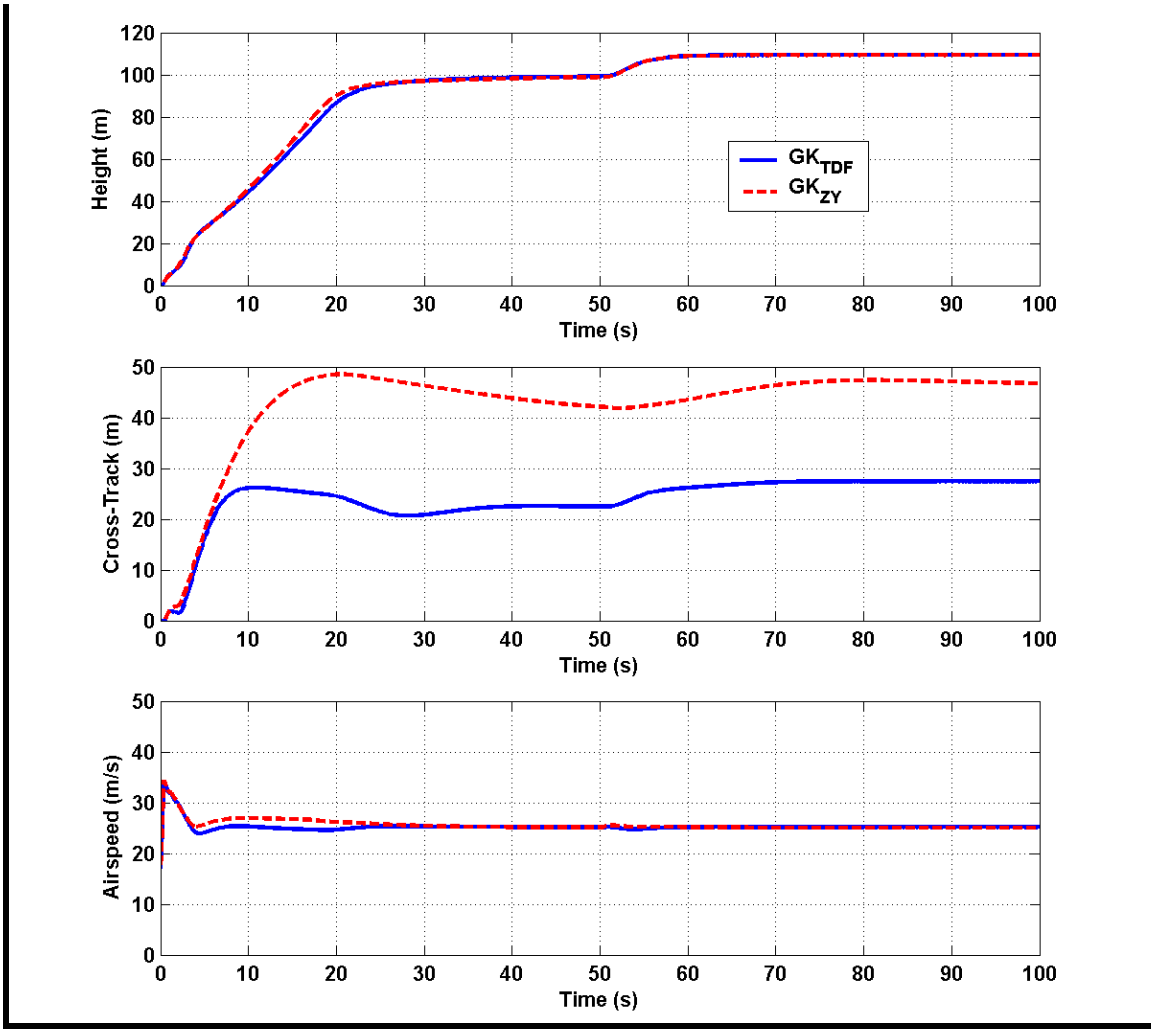

Figure 7.17: Cross-wind effect on TDF controller K_{TDF}, vs. combined long./lat. controller K_{ZY}

Finally, the TDF controller is compared to the uncoupled controller in the presence of cross-wind. Figure 7.17 above, shows the low-speed high-stability configuration G_{25P} response with the TDF controller K_{TDF} and the combined controller K_{ZY}. Although both

controllers demonstrate acceptable performance in height, K_{TDF} has a smaller cross-track error in this severe cross-wind condition. Notice how the TDF controller has a clear response to the cross-track 5*m* step demand at 50*s*.

7.2.7 Controller Order Reduction

The order of the TDF controller is reduced using the same technique as for previous designs. The controller order can be calculated as follows,

$$n_K = n_G + 2n_{W_1} + 2n_{W_2} + n_{Tref} \qquad \textbf{7.12}$$

Note that reference model order n_{Tref} is added to the controller order. Table 7.3 below, shows how the controller order was built-up using Equation 7.12.

Table 7.3: Controller order build-up

Model	Order	Description	Controller Order
G	26	Air vehicle model with single elevator and aileron actuators	=26
W_1	2	Input weighting (i.e. integrators etc.)	+(2x2) =30
W_2	2	Output weighting (i.e. low-pass filters etc.)	+(2x2) =34
T_{ref}	3+1	Reference Model+W_{2ref}	+4 =38

Applying the same reduction steps in the previous designs, the 38th order controller with anti-windup was reduced to a 23^{ed} order system with the following characteristics:

- Maximum Hankel SV truncated = 0.0005
- Full- and reduced-order systems ν-gap distance = 0
- Non-linear simulation time response curves for the full and reduced order controllers are almost identical as shown in Figure 7.18 below.

The TDF controller was found to be sensitive to order reduction. The order of the

controller had to be increased to reach the zero ν-gap distance and the very small truncated Hankel SV to keep the height responses near identical as shown in Figure 7.18 below.

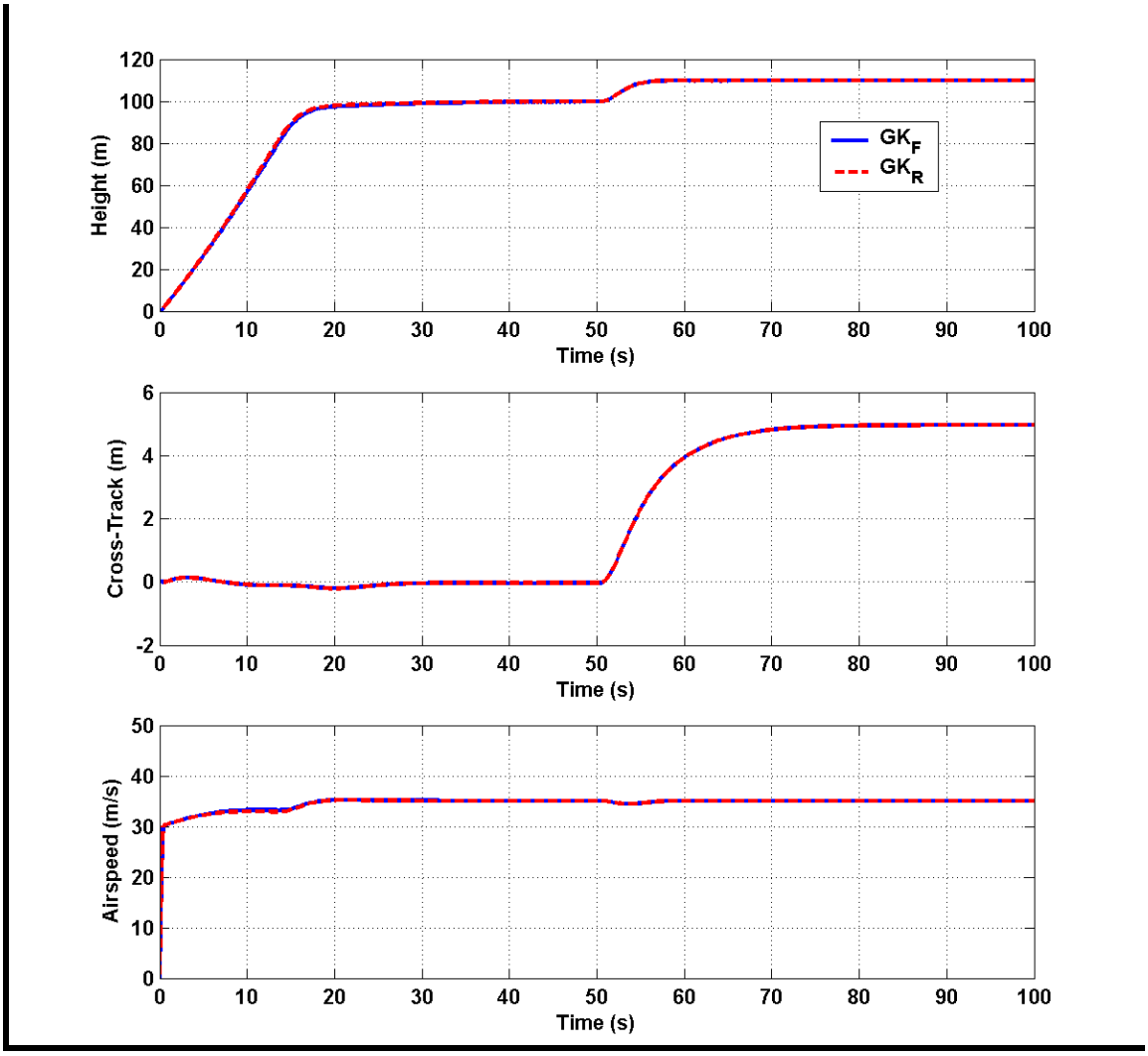

Figure 7.18: Non-linear evaluation of full order K_F vs. reduced order K_R TDF controllers

Note that the order of the combined longitudinal and lateral controllers is 10+13=23, i.e. the order of the new TDF controller is not increased even with the addition of the 3^{ed} order reference model dynamics plus the accompanied output weighting W_{2ref}. This is due to two reasons. First, the weighting functions W_1 and W_2 were simplified from a total of 7th order to 4th order system. This is due to the fact that some of the transfer functions used in the previous weighting functions were used to control the time

response of the outputs indirectly, and are not required in the new TDF design. Second, it was found from the longitudinal and lateral designs that the scheduling of the controller gains is not necessary. This is because the controllers are, as their name implies, robust enough to control the full flight operational envelope of the air vehicle and beyond. This led to the decision to not implement the new TDF controller in the observer form. This resulted in a simpler and smaller controller and removes the requirement for the addition of the inverse of the input weights W_1 for the anti-windup control command feedback.

The advanced full TDF FCSD is considered successful.

7.3 Chapter Summary

- The effect of coupling between the longitudinal and lateral-directional dynamics of the air vehicle linear models was evaluated. It was shown that the linear full/coupled model and the combined/uncoupled model have negligible effect on the FCSD. Thus, using the uncoupled linear model in the FCDS helps produce an uncoupled controller with no loss in modelling accuracy or performance.
- The TDF control design was introduced and its main advantages were emphasised. It was shown that the implementation of this advanced controller was similar to the one degree-of-freedom robust controllers designed for the longitudinal and lateral-directional systems. The main difference and advantage is the addition of the model reference, which introduced the second degree-of-freedom to control the output dynamic time response. Although this has mathematically increased the controller order and the required computations, it is more efficient and practical. As a matter of fact, the weighting functions are simpler because some of the transfer functions used in the weighting, used also to control the time response of the outputs indirectly, they were removed in the TDF. So the overall order of the new controller is not increased.
- The TDF controller was finally evaluated using the ACSL non-linear simulation with the nominal and worst-case conditions of the flight envelope, where it

showed precise control of the controlled outputs, i.e. u, h and y_x. The controller was further excised up to the maximum launch condition of $17m/s$ cross-wind, where it demonstrated a clear performance improvement over the previous designs without degradation in stability, i.e. enhanced robustness.

Chapter 8

Summary and Discussion

The three major areas that were covered in this research are:

- Air vehicle modelling
- Application of robust control in FCSD
- Non-linear implementation and evaluation

In this chapter, the main results are summarised and discussed. In addition, a comparison between the classical and robust controller designs is made. Finally, some of the research work done and not included in this thesis is reviewed.

8.1 Air Vehicle Modelling

Most FCS designs use model based controllers that rely on accurate models for the system to be controlled. In the following sections, both non-linear and linear modelling will be discussed.

8.1.1 Non-linear Modelling and Simulation

It was shown in Chapter 3 that the ACSL non-linear simulation was built around the 6DOF model of the air vehicle plus detailed modelling of the essential subsystems such as the engine/propeller, actuators, sensors etc. Realistic effects were also included such as computation delays, discretization, S/H, limiters, wind etc. It was very important to understand the full system governing equations to be able to develop the proper simplified linear models that represent the air vehicle dynamics.

Several important modifications were made to the ACSL non-linear simulation to develop the required linear models. A major modification was the replacement of the quaternion with the standard Euler angles in the DCM in §**4.5**. This has the advantage of reducing the coupling between the longitudinal and lateral-directional dynamics and non-linearity effects, and gives clearer and more logical linear model representation. This can be verified by the fact that linear models are built around small angle approximation assumption which lessens the necessity for quaternions.

Another major modification to the ACSL simulation was the selection of the linear model states that would represent the air vehicle more accurately. Several linear models were developed and evaluated, the most accurate model with the minimum states was finally introduced in §4.3.

To evaluate the derived linear models of the air vehicle, it was essential to develop an accurate model of the classical controller used in the ACSL simulation which was introduced in §3.8. Although this controller was basically linear, it was designed in the ACSL non-linear simulation environment where several non-standard non-linear functions were implemented. The controller is converted to a linear standard state-space form, as shown in §4.7, to be integrated with the air vehicle linear model in the MATLAB environment.

Comparison between the closed-loop linear and the non-linear systems in §4.8 showed

that the effort put into building an accurate linear closed-loop system that represented the non-linear air vehicle and the classical controller in ACSL was successful as was shown in **Figure 4.7**.

Note that controller measurement inputs and command outputs were restricted to the real flight control system implemented in the air vehicle on-board hardware. This was an important constraint that the robust FCSD had to cope with.

8.1.2 Linear Model Development and Analysis

Equation 8.1 represents the full linear 12-state uncoupled dynamic model of the air vehicle, with the error measurements in Equation 8.2. Actuator dynamics and computation delays are shown in the 14-state Equation 8.3.

$$\begin{Bmatrix} \dot{u} \\ \dot{w} \\ \dot{q} \\ \dot{\theta} \\ \dot{h} \\ \dot{N}_E \\ \hdashline \dot{v} \\ \dot{p} \\ \dot{r} \\ \dot{\phi} \\ \dot{\psi} \\ \dot{y}_x \end{Bmatrix} = \left[\begin{array}{cccccc:cccccc} x_u & x_w & x_q - W_0 & -g\cos\Theta_0 & 0 & x_N & & & & & & \\ z_u & z_w & z_q + U_0 & -g\sin\Theta_0 & 0 & 0 & & & & & & \\ m_u & m_w & m_q & 0 & 0 & 0 & & & & & & \\ 0 & 0 & 1 & 0 & 0 & 0 & & & \mathbf{0} & & & \\ \sin\Theta_0 & -\cos\Theta_0 & 0 & U_0\cos\Theta_0 & 0 & 0 & & & & & & \\ e_u & e_w & 0 & 0 & 0 & e_N & & & & & & \\ \hdashline & & & & & & y_v & y_p + W_0 & y_r - U_0 & g\cos\Theta_0 & 0 & 0 \\ & & & & & & l_v & l_p & l_r & 0 & 0 & 0 \\ & & & & & & n_v & n_p & n_r & 0 & 0 & 0 \\ & & & \mathbf{0} & & & 0 & \sec\Theta_0 & \tan\Theta_0 & 0 & 0 & 0 \\ & & & & & & 0 & 0 & \sec\Theta_0 & 0 & 0 & 0 \\ & & & & & & 1 & 0 & 0 & -U_0\sin\Theta_0 & U_0\cos\Theta_0 & 0 \end{array}\right] \begin{Bmatrix} u \\ w \\ q \\ \theta \\ h \\ N_E \\ \hdashline v \\ p \\ r \\ \phi \\ \psi \\ y_x \end{Bmatrix}$$

$$+ \left[\begin{array}{cc:cc} 0 & 2x_\eta & & \\ 0 & 2z_\eta & & \\ 0 & 2m_\eta & & \\ 0 & 0 & \mathbf{0} & \\ 0 & 0 & & \\ e_\tau & 0 & & \\ \hdashline & & 2y_\xi & y_\zeta \\ & & 2l_\xi & l_\zeta \\ & \mathbf{0} & 2n_\xi & n_\zeta \\ & & 0 & 0 \\ & & 0 & 0 \\ & & 0 & 0 \end{array}\right] \begin{Bmatrix} \tau_A \\ \eta_A \\ \hdashline \xi_A \\ \zeta_A \end{Bmatrix} \qquad \textbf{8.1}$$

$$\begin{Bmatrix} u_e \\ q_e \\ \theta_e \\ h_e \\ \hline p_e \\ r_e \\ \phi_e \\ \psi_e \\ y_x \end{Bmatrix} = \left[\begin{array}{cccccc|cccccc} \cos\Theta_0 & \sin\Theta_0 & [-\sin\Theta_0] & 0 & 0 & 0 & & & & & & \\ 0 & 0 & 1 & 0 & 0 & 0 & & & & & & \\ 0 & 0 & 0 & 1 & 0 & 0 & & & \mathbf{0} & & & \\ 0 & 0 & 0 & 0 & 1+\sin\Theta_0 & 0 & & & & & & \\ \hline & & & & & & 0 & 1 & 0 & 0 & 0 & 0 \\ & & & & & & 0 & 0 & 1 & 0 & 0 & 0 \\ & & \mathbf{0} & & & & 0 & 0 & 0 & 1 & 0 & 0 \\ & & & & & & 0 & 0 & 0 & 0 & 1 & 0 \\ & & & & & & 0 & 0 & 0 & 0 & 0 & 1 \end{array}\right] \begin{Bmatrix} u \\ w \\ q \\ \theta \\ h \\ N_E \\ \hline v \\ p \\ r \\ \phi \\ \psi \\ y_x \end{Bmatrix} \quad \textbf{8.2}$$

$$\begin{Bmatrix} \dot{D}_\tau \\ \ddot{D}_\tau \\ \dot{\eta}_A \\ \ddot{\eta}_A \\ \dot{D}_\eta \\ \ddot{D}_\eta \\ \hline \dot{\xi}_A \\ \ddot{\xi}_A \\ \dot{D}_\xi \\ \ddot{D}_\xi \\ \dot{\zeta}_A \\ \ddot{\zeta}_A \\ \dot{D}_\zeta \\ \ddot{D}_\zeta \end{Bmatrix} = \left[\begin{array}{cccccc|cccccccc} 0 & 1 & 0 & 0 & 0 & 0 & & & & & & & & \\ -\omega_\Delta^2 & -2\zeta_\Delta\omega_\Delta & 0 & 0 & 0 & 0 & & & & & & & & \\ 0 & 0 & 0 & 1 & 0 & 0 & & & & \mathbf{0} & & & & \\ 0 & 0 & -\omega_a^2 & -2\zeta_a\omega_a & 0 & \omega_a^2 & & & & & & & & \\ 0 & 0 & 0 & 0 & 0 & 1 & & & & & & & & \\ 0 & 0 & 0 & 0 & -\omega_\Delta^2 & -2\zeta_\Delta\omega_\Delta & & & & & & & & \\ \hline & & & & & & 0 & 1 & 0 & 0 & 0 & 0 & 0 & 0 \\ & & & & & & -\omega_a^2 & -2\zeta_a\omega_a & 0 & \omega_a^2 & 0 & 0 & 0 & 0 \\ & & & & & & 0 & 0 & 0 & 1 & 0 & 0 & 0 & 0 \\ & & & \mathbf{0} & & & 0 & 0 & -\omega_\Delta^2 & -2\zeta_\Delta\omega_\Delta & 0 & 0 & 0 & 0 \\ & & & & & & 0 & 0 & 0 & 0 & 0 & 1 & 0 & 0 \\ & & & & & & 0 & 0 & 0 & 0 & -\omega_a^2 & -2\zeta_a\omega_a & 0 & \omega_a^2 \\ & & & & & & 0 & 0 & 0 & 0 & 0 & 0 & 0 & 1 \\ & & & & & & 0 & 0 & 0 & 0 & 0 & 0 & -\omega_\Delta^2 & -2\zeta_\Delta\omega_\Delta \end{array}\right] \begin{Bmatrix} D_\tau \\ \dot{D}_\tau \\ \eta_A \\ \dot{\eta}_A \\ D_\eta \\ \dot{D}_\eta \\ \hline \xi_A \\ \dot{\xi}_A \\ D_\xi \\ \dot{D}_\xi \\ \zeta_A \\ \dot{\zeta}_A \\ D_\zeta \\ \dot{D}_\zeta \end{Bmatrix}$$

$$+ \left[\begin{array}{cc|cc} 0 & 0 & & \\ 0 & -4\zeta_\Delta\omega_\Delta & & \\ 0 & 0 & & \\ \omega_a^2 & 0 & \multicolumn{2}{c}{\mathbf{0}} \\ 0 & 0 & & \\ -4\zeta_\Delta\omega_\Delta & 0 & & \\ \hline & & 0 & 0 \\ & & \omega_a^2 & 0 \\ & & 0 & 0 \\ \multicolumn{2}{c|}{\mathbf{0}} & -4\zeta_\Delta\omega_\Delta & 0 \\ & & 0 & 0 \\ & & 0 & \omega_a^2 \\ & & 0 & 0 \\ & & 0 & -4\zeta_\Delta\omega_\Delta \end{array}\right] \begin{Bmatrix} \tau_D \\ \eta_D \\ \hline \xi_D \\ \zeta_D \end{Bmatrix} \quad \textbf{8.3}$$

Note that by representing the elevator pair and the aileron pair with single actuators in Equation 8.3, and doubling their aerodynamic coefficients in Equation 8.1, it was possible to reduce the order of the air vehicle model from 30 to 26 state equations with identical dynamics.

The effect of actuator dynamics and computation delays on modelling uncertainty was addressed in the beginning of each of the longitudinal and lateral FCSD in §5.1 and §6.1 respectively. These effects were measured using the *v*-gap metric, where it was not possible using the time or the frequency response curves.

Table 8.1 summarises the effect of neglecting the different subsystems, i.e. actuators and computation delays, on the air vehicle full linear nominal model uncertainty. Columns 2 and 3 give the *v*-gap metric distances of neglecting the actuator dynamics (at 41*rad*/*s*) or the computation delays (at 100*rad*/*s*) individually, column 4 gives the *v*-gap metric distance of neglecting both, columns 5 and 6 show the dynamic modes involved and their respective frequencies. Notice the logical proportional relation between the involved dynamic mode frequency and the measured *v*-gap metric effect on the uncertainty. In other words, as the frequency of the air vehicle dynamics increase the more they are affected by the high frequency subsystem components, i.e. the actuators and computation delays.

Table 8.1: Subsystems disregard effect on nominal model uncertainty measured by the *v*-gap metric

Command Signal	Actuator Dynamics at 41 *rad*/*s*	Computation Delay at 100 *rad*/*s*	Actuator & Computation Delay	Dominant Dynamic Mode Involved	Frequency (*rad*/*s*)
Throttle	0.085	0.080	0.165	*Phugoid*	0.20
Elevator	0.32	0.38	0.61	*Short period*	4.83
Aileron	0.773	0.801	1	*Roll subsidence*	8.17
Rudder	0.077	0.083	0.129	*Spiral mode*	0.058

8.1.3 Operational Flight Envelope

Before designing the FCS, it was important to represent the full operational flight envelope of the air vehicle adequately. A set of 9 linear models was derived from the ACSL non-linear model that represented the uncertainties that may be encountered in the real and non-linear implementation. These are mainly airspeed and CG position as shown in Figure 8.1.

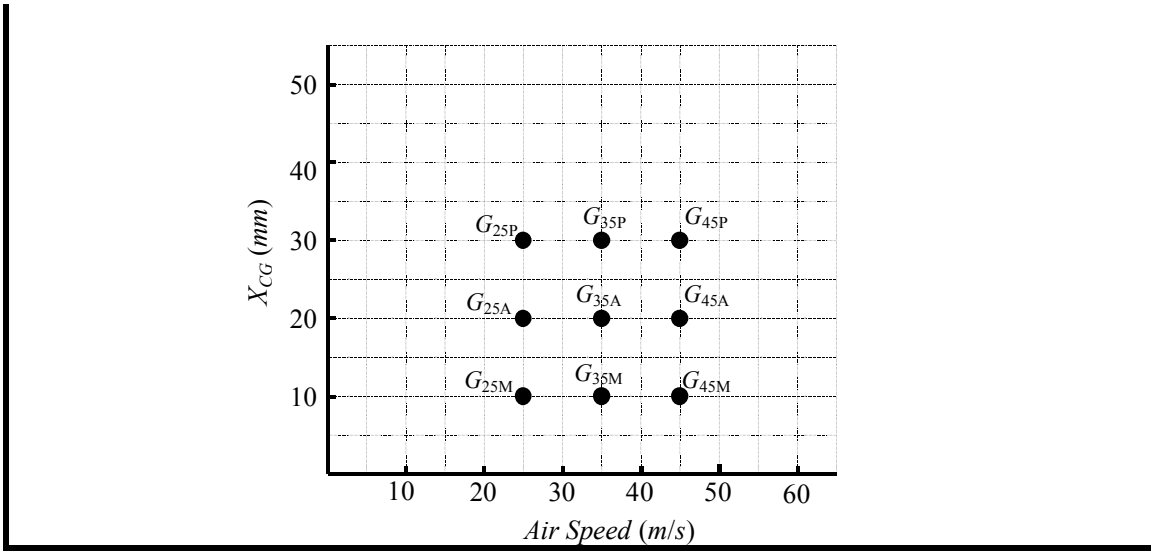

Figure 8.1: Operational flight envelope models

Although it was logical to use the middle range model, i.e. G_{35A} , to be the nominal model for the full flight envelope, the *v*-gap metric tool was used to measure the distance between these models and mathematically select the model that had the supremum (least maximum) distance from the whole set. Obviously, G_{35A} was the model selected as shown in Table 8.2, but it would not always be so clear to select the right model where the *v*-gap metric would be important as shown next.

Table 8.2 : v-Gap analysis of flight envelope models

Case	Model	*v*-Gap (max.)
1	G_{25A}	0.799
2	G_{25P} ▼	0.829
3	G_{25M}	0.793
4	G_{35A} ●	0.554
5	G_{35P}	0.567
6	G_{35M}	0.618
7	G_{45A}	0.801
8	G_{45P}	0.794
9	G_{45M} ▲	0.829

● Nominal ▼ Lower worst-case ▲ Upper worst-case

The ν-gap metric also helped in identifying the worst-case models in the operational flight envelope. These were G_{25P} and G_{45M} as shown also in Table 8.2. Although this was not as straight-forward as selecting the nominal model, these models logically represent the worst cases of the full set. That is because increased airspeed with reduced static stability will represent an upper extreme edge of the flight envelope. Reduced airspeed with increased static stability will represent the lower extreme edge. This was also verified by analysing the poles of the full flight envelope longitudinal and lateral models in §**4.9**.

To the author's knowledge, this is the first work to, intelligently and comprehensively, use the ν-gap metric in a realistic FCSD application.

8.2 Robust Control Design

Although this thesis will be submitted for a PhD degree, it was hoped to show and prove to the industrial FCS designers that *Robust Control* can be applied to real life complex projects without the need for a PhD degree to do so; can achieve comparable results with the classical designs with all the power of modern mathematical tools. Thus, throughout this work, the robust control methods used in the different designs were kept simple, effective and as practical as possible.

8.2.1 Loop-shaping Design Procedure

The loop-shaping design procedure (LSDP) was introduced in Chapter **2** with a simple example of the XRAE-1 UAV longitudinal FCSD. Detailed designs were then applied to the longitudinal and lateral FCSD of the A3 Observer UAV in Chapters 5, 6 and finally in Chapter 7 with the TDF design. These designs have proved that,

- LSDP success was partly due to its hybrid structure of mixed classical loop-shaping techniques with advanced robust stabilization synthesis.
- The new modifications implemented to the LSDP, that will be reviewed shortly, have given it the chance of success in the realistic non-linear 6DOF detailed

ACSL simulation.

- The advanced mathematics the LSDP is based on and with the wealth of tools and real application examples available , made it one of the most straight-forward and practical methods to apply in the robust control arena.

8.2.2 Robust Design Modifications

In this work, a few modifications on the LSDP were required. These modifications were mainly to assist the designer at different stages of design by having some type of evaluation and analysis that would help spot any inadequate decisions early enough and not have to wait to the end of the design process to be discovered. These modifications are as follows,

- At every design step, i.e. scaling/shaping/alignment, it was found important to calculate the closed-loop *SM* of the robust controller synthesised using the weights created so far.
- Also, observing the linear model open-loop principal gains alone in the design process will only give half of the real picture. At each design step, singular values of each significant loop should also be evaluated along with the principal gains.
- In the scaling process, when selecting the output maximum expected values, it is important to take their frequency response gains into account, especially around the desired bandwidth. This will give more realistic values and will help improve the robust stability of the controller as shown in §6.2.2.
- Alignment of the open-loop SV shown in §**5.4**, §**6.4** and later in §**7.2.2** is an effective tool that rescales and/or decouples the dynamics of the system model at the defined frequency which is usually selected at the desired bandwidth. It can be concluded here that for the alignment process to be effective: (1) it must be used to decouple comparable dynamic loops of the system for the same bandwidth, such as r/ζ with p/ξ and not r/ζ with ϕ/ξ for example, as long as the condition number is not large. (2) partial and/or multiple alignments are sometimes required to align part of the dynamic loops at the same or different

frequencies, as shown in §**7.2.2**, where the system model was effectively partially aligned to avoid the high condition number between the longitudinal and lateral-directional dynamic loops.

8.2.3 Two Degrees-of-Freedom Design

One of the most important extensions to the LSDP was the addition of the TDF design which was introduced in §2.8. This has added the ability to specify a dynamic reference model to shape the time response of the controlled outputs. The TDF controller also exhibits an inner/outer loop like structure: the inner loop K_2 is designed for control stability; the outer loop K_1 is designed for demand tracking performance, as shown in the simplified block diagram in Figure 8.2 below.

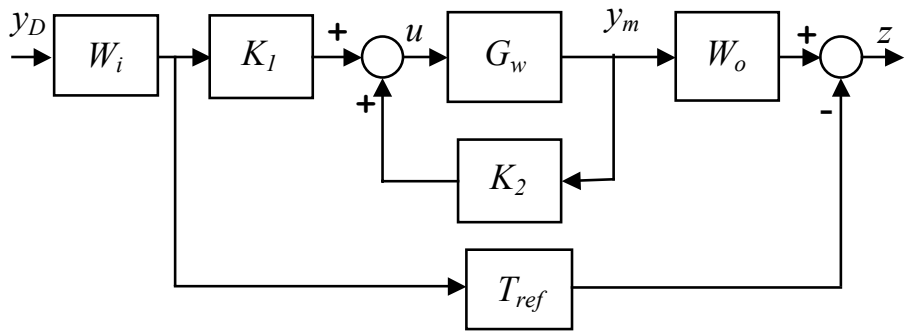

Figure 8.2: TDF with feedback measurement and model reference demand design loops

Although the TDF controller has increased the mathematical computation requirements, it was shown in Chapter **7** to be more efficient and practical by giving the designer more freedom in defining and achieving the control system requirements and objectives. The TDF controller non-linear simulation in §7.2.6 with the air vehicle full operational flight envelope showed precise control of the controlled outputs, i.e. u, h and y_x with no compromise in stability.

8.2.4 Sensitivity Analysis

The LSDP, as described and applied in this project, is concerned with shaping and weighting the open-loop gains of the system model. The rules governing the open-loop designs, described in §**5.3**, have their equivalent for the closed-loop principal gains[38, 39, 71], which are used in designs such as the Mixed-Sensitivity $\mathcal{H}_\infty$ synthesis described in §1.4.8. Such methods utilize the classical robustness measurement of the sensitivity and complementary sensitivity peaks, M_S and M_T.

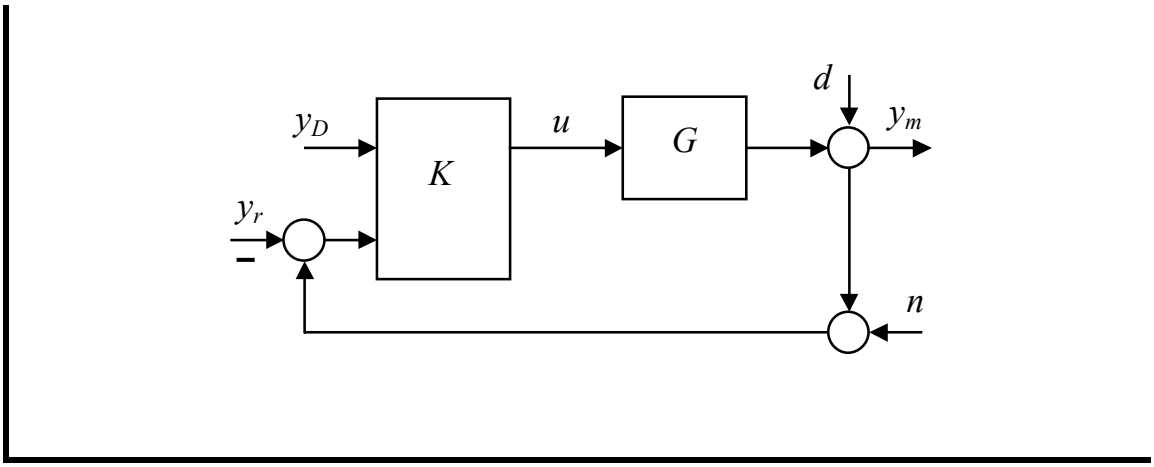

Figure 8.3: General sensitivity analysis configuration

Basically, the general closed-loop output sensitivity analysis configuration is given in Figure 8.3 above, with the disturbance and noise inputs *d* and *n*. For the regulator input y_r configuration, the sensitivity and complementary sensitivity *S* and *T* are the transfer function between y_m/d and y_m/y_r respectively. For the demanded input y_D configuration, S_D and T_D are the transfer function between y_m/d and y_m/y_D respectively.

Briefly, the governing rules for shaping *S* and *T* are,

1. For disturbance rejection: make $\bar{\sigma}(S)$ small where $\bar{\sigma}(S) << 1$.
2. For noise attenuation: make $\bar{\sigma}(T)$ small where $\bar{\sigma}(T) << 1$.
3. For tracking performance: make $\bar{\sigma}(T) \approx \underline{\sigma}(T) \approx 1$.

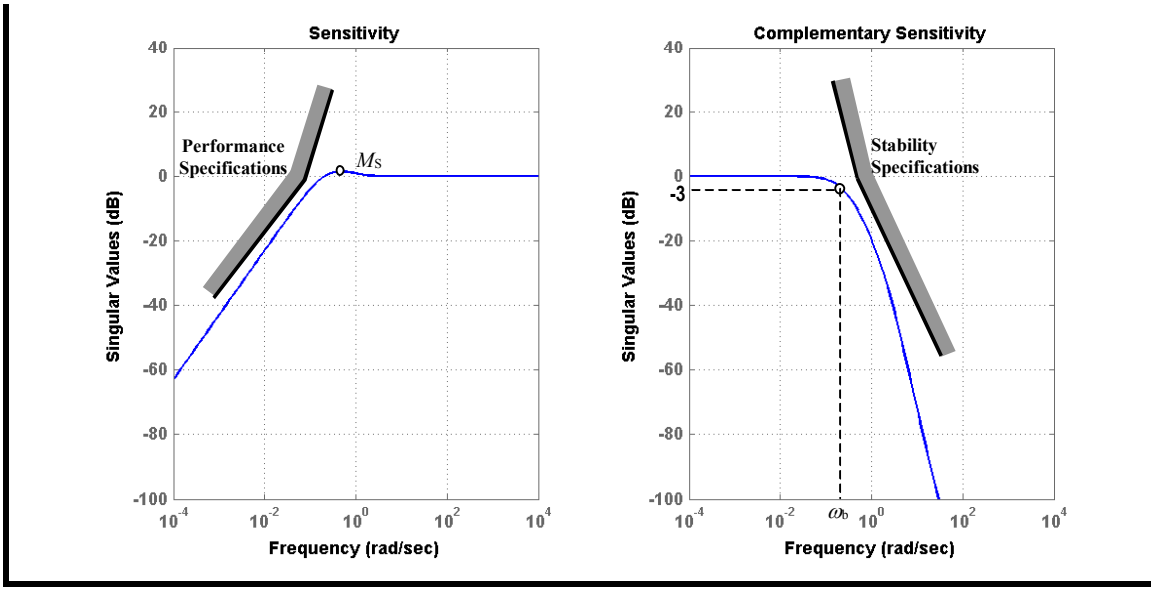

Figure 8.4: *S* and *T* shaping specifications

Figure 8.4 above, summarises these shaping rules, where M_S and M_T are the sensitivity and complementary sensitivity maximum peaks, and ω_b is the closed-loop bandwidth. Note that $M_S = \|S\|_\infty$ and $M_T = \|T\|_\infty$. From classical control,

$$GM \geq \frac{M_S}{M_S - 1}; \quad PM \geq 2\arcsin\left(\frac{1}{2M_S}\right) \qquad \textbf{8.4}$$

Recall from Equation **5.19** in §**5.5**, that the robust *SM*, was related to *GM* and *PM* by,

$$GM \geq \frac{1+SM}{1-SM}, \quad PM \geq 2\arcsin(SM) \qquad \textbf{8.5}$$

which roughly says that $2M_S \propto 1/SM$. This reveals the direct relation between the sensitivity peak M_S and the robust *SM*. It has been shown[79, 80] that this relation can be expressed more precisely if first, *M* is defined as,

$$M = \max\begin{Bmatrix} M_S \\ M_T \end{Bmatrix} \qquad \textbf{8.6}$$

then the robust *SM* can be related to the classical sensitivity functions as,

$$\frac{1}{2M-1} \geq SM \geq \frac{1}{2M} \qquad \textbf{8.7}$$

The sensitivity peak relation above can help in defining which control loop has affected the stability margin of the closed-loop system. For example, in Table 8.3, the longitudinal control design final robust *SM* achieved was 0.36; for the lateral-directional design it was 0.31. Hence, for the combined uncoupled controller K_{zy}, the *SM* of 0.31 was due to the lateral controlled system.

Table 8.3: Full vs. longitudinal / lateral robust stabilizations

Model / Controller	*SM*	*GM* (dB)	*PM* (*deg*)
G_{35A} / K_{zy}	0.311	5.59	36.27
G_{35Az} / K_z	0.36	6.48	41.8
G_{35Ay} / K_y	0.31	5.6	36.0

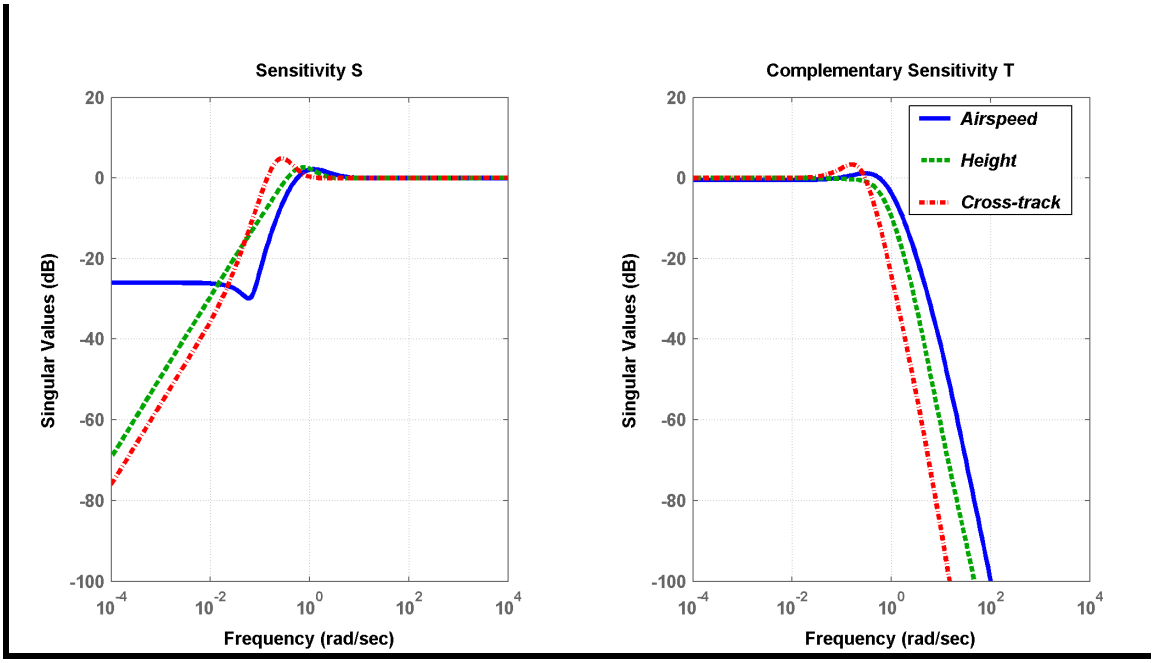

Figure 8.5:*S* and *T* of K_{zy} closed-loop controlled system

Figure 8.5 above, shows S and T for the combined decoupled control design. The lateral control loop(cross-track) is shown to have the maximum sensitivity M_S which was the main cause of the reduced SM of the full controlled system to 0.31. This is an important fact taken into account in the weighting phases of the robust control law design, which helps maximize the robust stability of the multivariable systems.

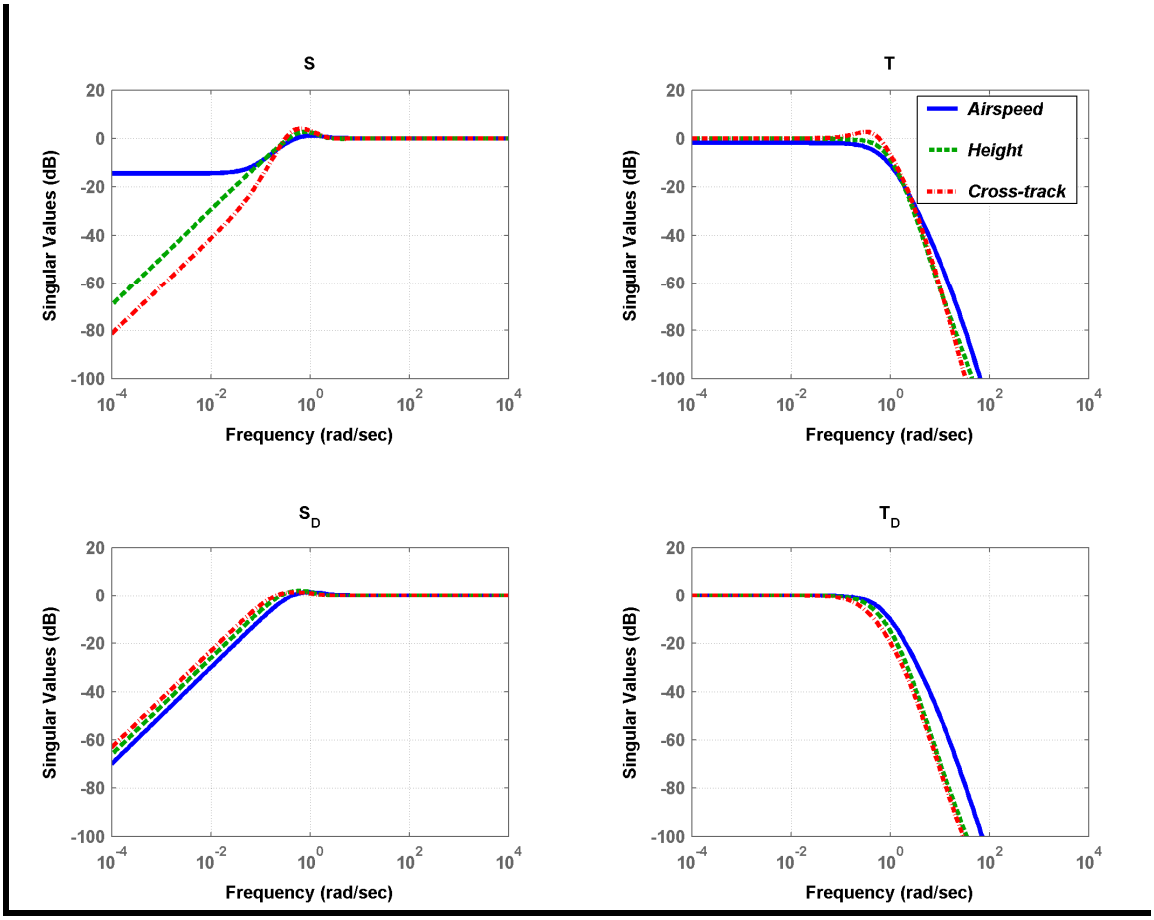

Figure 8.6: *S* and *T* of the closed-loop TDF controlled system

Finally, the demanded and regulated-input sensitivity functions, S_D/T_D and S/T, of the TDF controlled system of §7.2, are shown in Figure 8.6. Note how the demanded-input configuration S_D/T_D has vastly improved the closed-loop system performance over the regulator-input configuration S/T.

8.3 Controller Implementation

The implementation process of any FCS in a realistic and non-linear simulation environment is an essential task. The best designed FCS in the linear environment may fail in real systems and/or in non-linear simulations due to improper implementation.

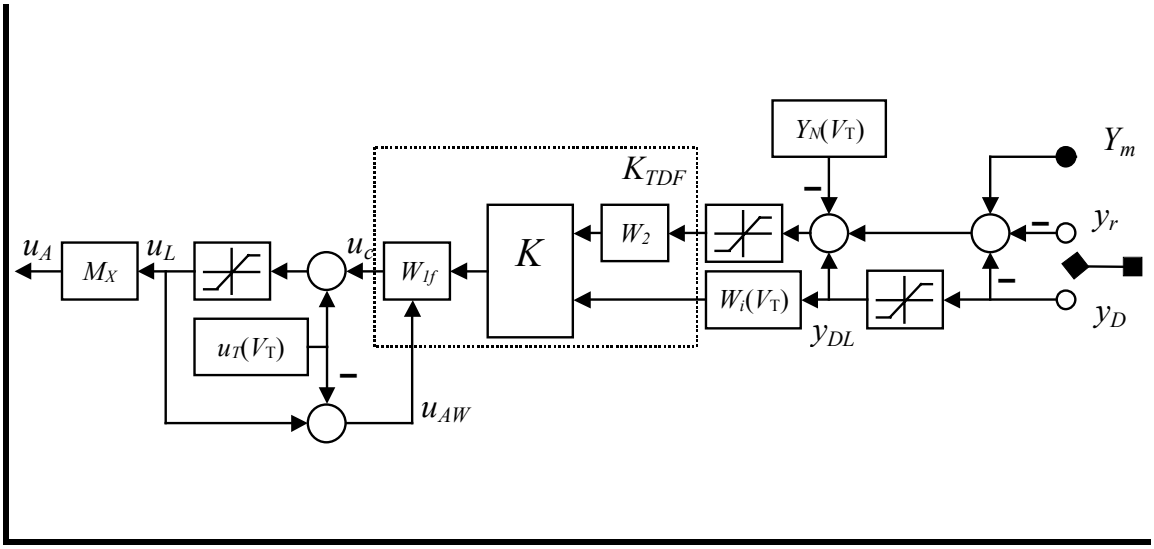

Figure 8.7: Controller non-1linear implementation

Figure 8.7 above, shows the general implementation configuration of the robust controller with the anti-windup feedback u_L, scheduled input/output nominal/trim tables ($Y_N(V_T)/u_T(V_T)$), output mixing M_x and scheduled demanded input pre-weight $W_i(V_T)$. Notice that either regulator or demanded input y_r or y_D is selected at a time. Note also that the signal lines are vectors but the nominal/trim tables, limiters, pre-weight and mixing functional blocks are only applied to the concerned variables in the signal vector. The above implementation measures are discussed in the following sections.

8.3.1 Actuator Saturation and Windup

One of the major implementations issues is the actuator saturation as discussed in §**2.9**. This is because multivariable system loop-gains have both magnitude and direction which are affected by the saturation and can lead to loss of decoupling between the controlled outputs. In the robust control design, the pre-compensator weight W_1 would also include integral action in order to reject low frequency disturbances and

uncertainty; in the case of actuator saturation the integrators will continue to integrate their input and hence cause windup problems.

Engine throttle is one of the controls that can experience command saturation and windup in real applications as was shown in §**5.9.2**, where the Hanus anti-windup was successfully implemented to solve this problem by keeping the states of W_{1f}, which replaced W_1, consistent with the actual system model at all times with the fed-back saturated demand u_L as shown in Figure 8.7.

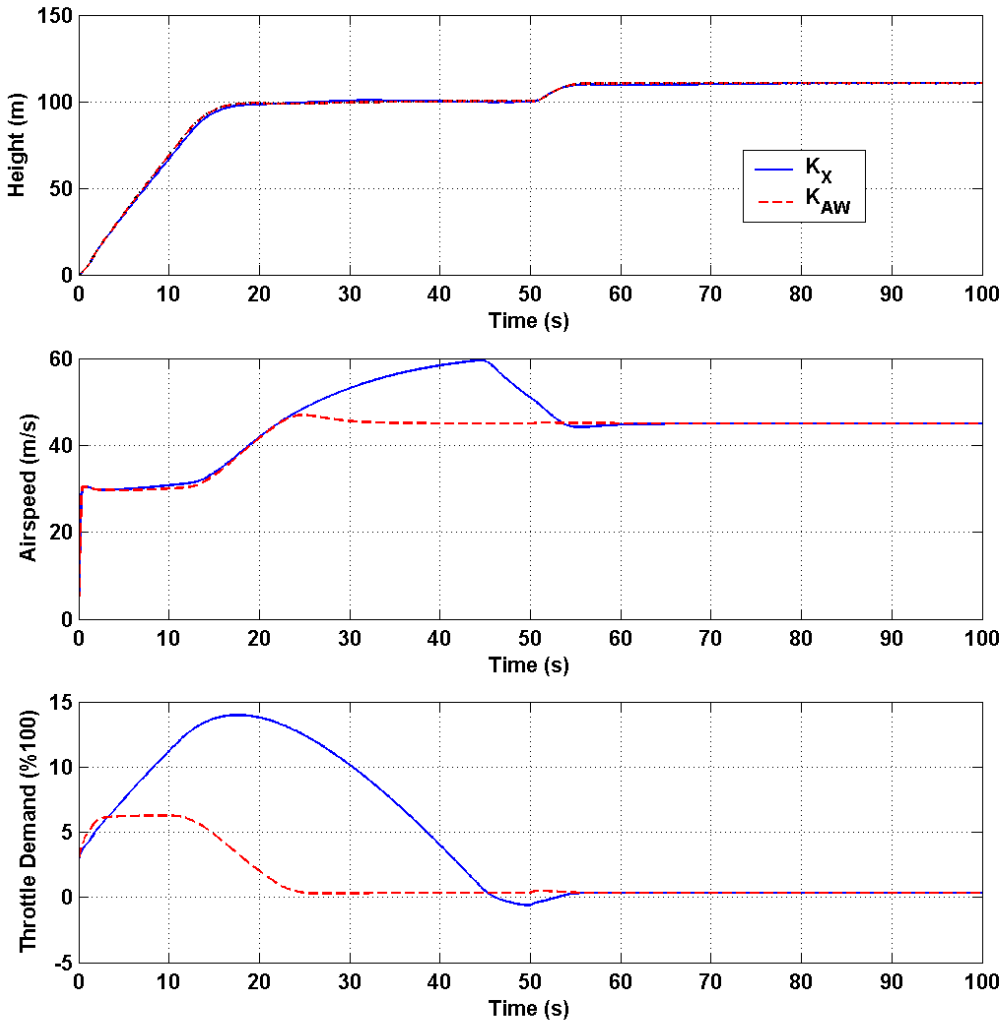

Figure 8.8: Effect of Hanus anti-windup on airspeed and throttle saturation

Figure 8.8, shows clearly how airspeed control in the ACSL non-linear simulation was improved by adding the Hanus anti-windup which also successfully reduced the throttle demand saturation and windup. Note that throttle setting of 1(100%) is the threshold allowed which was exceeded by K_x and K_{AW}.

8.3.2 Controller Input Linearization

All controllers developed in this project were based on the linear perturbed model of the air vehicle that was developed in Chapter **4** and discussed in §8.1.2. The state, input and output vectors of the linear model, repeated here in Equation 8.8, also represent the perturbed states, inputs and outputs.

$$\left.\begin{aligned} x &= \{u \;\; q \;\; \theta \;\; h \;\; p \;\; r \;\; \phi \;\; \psi \;\; y_x\}^T \\ u_e &= \{\tau_A \;\; \eta_A \;\; \xi_A \;\; \zeta_A\}^T \\ y_e &= \{u_e \;\; q_e \;\; \theta_e \;\; h_e \;\; p_e \;\; r_e \;\; \phi_e \;\; \psi_e \;\; y_x\}^T \end{aligned}\right| \qquad \textbf{8.8}$$

This implies that the controller inputs and outputs, i.e. the linear model outputs and inputs respectively, are also the perturbed values of the respected real variables from their nominal amplitudes.

The controller inputs linearization implementation is shown back in Figure 8.7. Neglecting the limiters, the simplified governing equations for the regulator demand input are,

$$\left.\begin{aligned} u_e &= U_m - U_D & \theta_e &= \Theta_m - \Theta_o(V_T) & q_e &= Q_m \\ h_e &= H_m - H_D & \psi_e &= \Psi_m - \Psi_o & p_e &= P_m \\ y_{xm} &= Y_{Xm} - Y_{XD} & \phi_e &= \Phi_m & r_e &= R_m \end{aligned}\right| \qquad \textbf{8.9}$$

where small letters denote the linear variables and the capitals for the actual magnitude variables. Subscript '*m*' denotes a measurement, '*o*' a nominal value and '*D*' denotes a

demanded value.

For tracking demand inputs, such as in the observer-form and the TDF controllers, the controller linear measurement inputs were modified as follows,

$$\left.\begin{aligned} u_e &= U_m - U_D + u_{DL} \\ h_e &= H_m - H_D + h_{DL} \\ y_{Xm} &= Y_{Xm} - Y_{XD} + y_{XDL} \end{aligned}\right| \qquad \textbf{8.10}$$

Note that all demanded inputs, i.e. u_D, h_D , y_D are limited to avoid controller saturation. This is especially true for the height demand which could easily reach values of $100m$ and above, while the measured height at launch is null. The controller measurement inputs are then adjusted to match, and to be consistent with, the limited demands as shown back in Figure 8.7 and in Equation 8.10.

8.3.3 Controller Outputs

The controller outputs are implemented following Figure 8.7 as,

$$\begin{aligned} u_A &= M_x \left[u_c + u_T \right]_L \\ \begin{Bmatrix} \tau \\ \eta_{SB} \\ \eta_P \\ \xi_{SB} \\ \xi_{SB} \\ \zeta_{SB} \end{Bmatrix}_A &= \begin{bmatrix} 1 & 0 & 0 & 0 \\ 0 & 1 & 0 & 0 \\ 0 & 1 & 0 & 1 \\ 0 & 0 & 1 & 0 \\ 0 & 0 & -1 & 0 \\ 0 & 0 & 0 & 1 \end{bmatrix} \begin{Bmatrix} \tau_c + \tau_T \\ \eta_c + \eta_T \\ \xi_c \\ \zeta_c \end{Bmatrix}_L \end{aligned} \qquad \textbf{8.11}$$

The anti-windup limited control command feedback u_{AW} is given by,

$$
\begin{aligned}
u_{AW} &= u_L - u_T \\
\begin{Bmatrix} \tau \\ \eta \\ \xi \\ \zeta \end{Bmatrix}_{AW} &= \begin{Bmatrix} \tau \\ \eta \\ \xi \\ \zeta \end{Bmatrix}_L - \begin{Bmatrix} \tau \\ \eta \\ 0 \\ 0 \end{Bmatrix}_T
\end{aligned}
\qquad \textbf{8.12}
$$

Note how the trim values were subtracted before the feedback to make the limited commands consistent with the actual commands.

8.4 Robust versus Classical Control Design

In this section the robust controller developed in this thesis, K_{TDF}, will be compared with the current classical PMC of the A3 Observer air vehicle, K_{PMC}, that was introduced in §**3.8** and §**4.7**.

8.4.1 Design Variables

Table 8.4: Classical PMC longitudinal controller design variables

Design Gains	No. of Values	Nominal / Trim Variables	No. of Values	
k_u	1	$\tau_{Tum}(\lvert\phi_D\rvert)$	9	
$k_q(V_T)$	9	$\tau_{Trim}(V_T)$	5	
$k_\theta(V_T)$	9	$\theta_L(V_T)$	1 function	
$k_{i\theta}$	1	$\theta_T(\phi_m)$	1 function	
$k_h(V_T)$	9	$\eta_{Trim}(V_T)$	9	
S_η	1			
T_h	1			
Total =	**31**	+	**25**	**= 56**
Order / States =	**2**			

Table 8.4 and Table 8.5 show the number of design gain values that the control engineer needs to manually manipulate for the PMC longitudinal and lateral-directional designs, where the total values for both designs was 31+40 = 71. The tables also shows the trim

and nominal values prepared for implementation, that were 25+9 = 34. Table 8.5 also shows the order of the controller which, in state-space form, has 4 states. Note that the PMC was scheduled with airspeed to improve its performance at the limits of the operational flight envelope.

Table 8.5: Classical PMC lateral-directional controller design variables

Design Gains	No. of Values	Nominal / Trim Variables	No. of Values	
$k_p(V_T)$	9	$\phi_{\max}(V_T)$	9	
$k_\phi(V_T)$	9			
$k_{i\phi}(V_T)$	9			
k_ψ	1			
$k_s(V_T)$	9			
S_ξ	1			
S_ζ	1			
T_m	1			
Totals =	**40**	+	**9**	**= 49**
Grand Totals =	**71**	+	**34**	**= 105**
Order / States = 2		**Full Order = 4**		

Table 8.6: Robust TDF full controller design variables

Design Gains	No. of Values	Nominal / Trim Variables	No. of Values	
W_{1c}	4	$\tau_{Trim}(V_T)$	8	
W_{2c}	9	$\theta_{Trim}(V_T)$	8	
W_{1s}	4	$\eta_{Trim}(V_T)$	8	
W_{2s}	3	W_o	1 function	
W_{1a}	1 function			
T_{ref}	3			
Total =	**24**	+	**25**	**= 49**
Order / States = 23				

Table 8.6 also shows the equivalent design variables and trim/nominal tables used in the

robust TDF controller design. Note here that the controller was robust enough to use the nominal design for the full operational flight envelope as was shown in Chapter 7 without the need of scheduling. It was possible to reduce the order of the controller to 23 states without degradation in performance or stability, as was shown in §7.2.7.

Table 8.7: Robust vs. classical controller design variables

	Robust	Classical
Design Gains	24	71
Nominal / Trim	25	34
Order / States	23	4

Table 8.7 shows that even though the robust controller relied heavily on more complex mathematical functions and has a much higher order, the number of actual design variables that needed to be manipulated manually was much less than the classical controller. This was for two main reasons. First, the robust controller eliminated the scheduling required for the classical design. Second, the robust design utilised more functions in MATLAB to produce some values automatically, such as the alignment gains and pre-demand table.

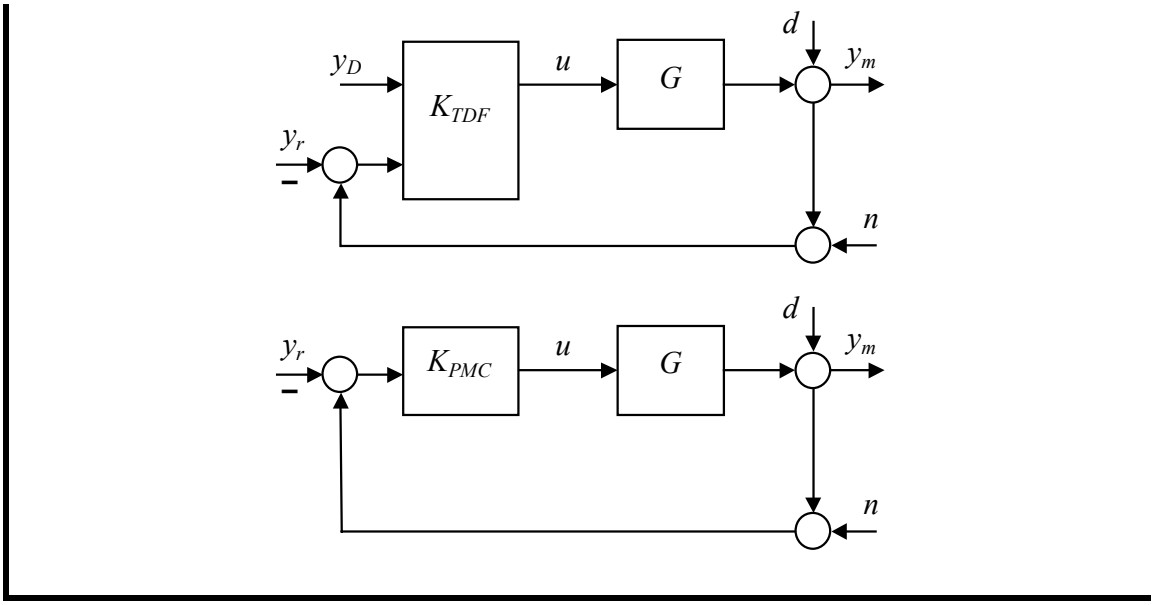

Figure 8.9: Sensitivity analysis for the robust K_{TDF} and classical K_{PMC} closed-loop systems

8.4.2 Sensitivity Analysis

Here, the closed-loop sensitivity functions S and T of the classical K_{PMC} are evaluated against the robust TDF design, where $K_{TDF/r}$ and $K_{TDF/D}$ denote the regulator and demanded input configurations as shown in Figure 8.9.

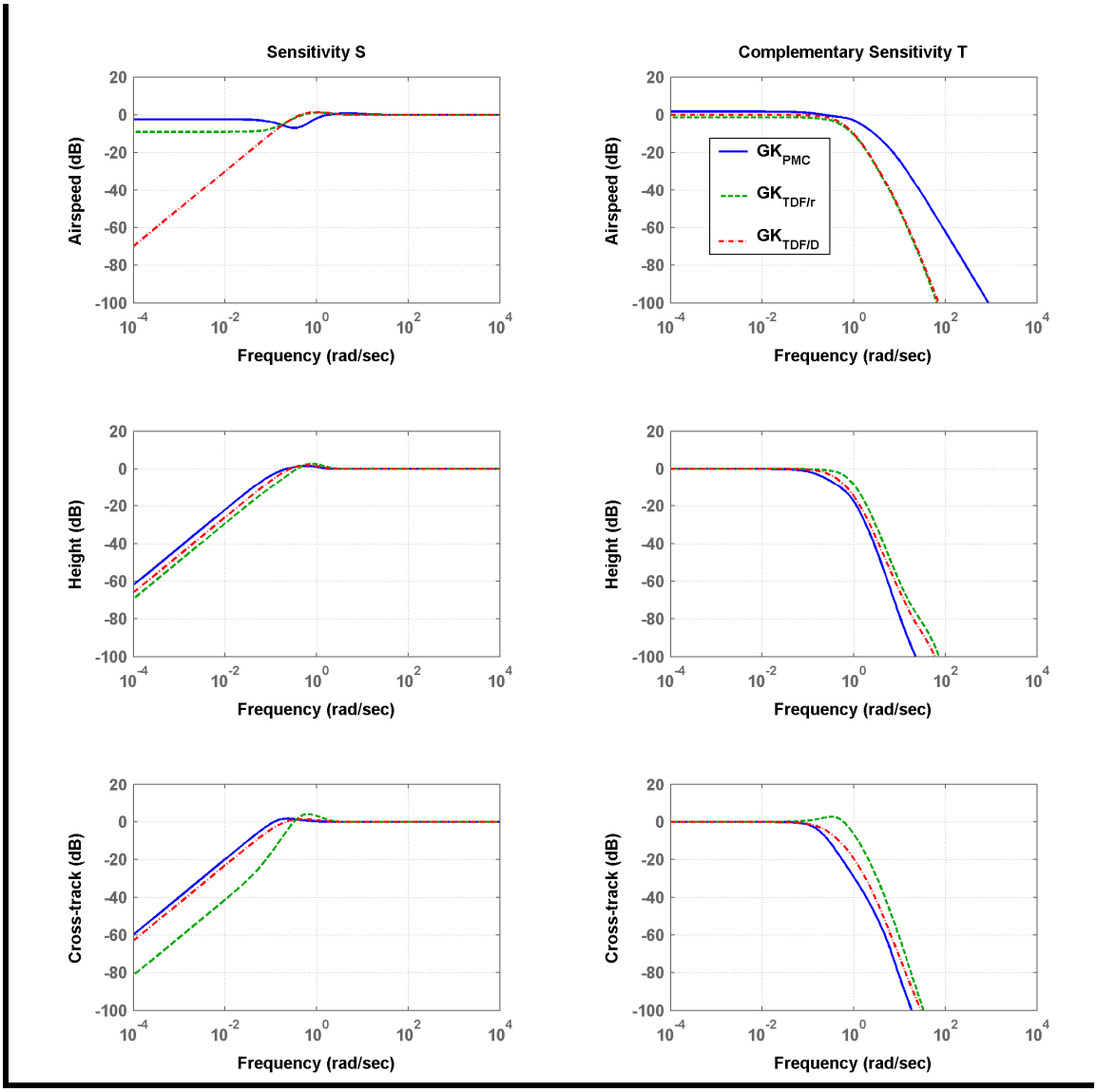

Figure 8.10: PMC vs. TDF sensitivity functions *S* and *T*

Figure 8.10, Table 8.8 and Table 8.9 compare the principal gains of S and T for the two systems. Note how the PMC airspeed sensitivity S has a high value at low frequency, which indicates the high sensitivity and increased control requirement of the loop. Also note T non-zero DC gain and high bandwidth of the PMC that indicate degraded

demand tracking and reduced noise rejection. Note also that, although K_{PMC} shows better stability (i.e. *SM*, *GM* and *PM*) in Table 8.8 tracking performance of height and cross-track loops(i.e. their bandwidths) are less than $K_{TDF/D}$, as shown in Table 8.9.

Table 8.8: Robust vs. classical controllers closed-loop stability

	$GK_{TDF/r}$	$GK_{TDF/D}$	GK_{PMC}
M_S	1.6	1.26	1.22
$SM \geq$	0.31	0.40	0.41
$GM \geq$	8.5	13.8	14.9
$PM(deg) \geq$	78	105	110

Table 8.9: Robust vs. classical closed-loop bandwidths

	$GK_{TDF/r}$	$GK_{TDF/D}$	GK_{PMC}
Airspeed(*rad/s*)	0.44	0.41	1.09
Height(*rad/s*)	0.55	0.29	0.16
Cross-track(*rad/s*)	0.78	0.18	0.14

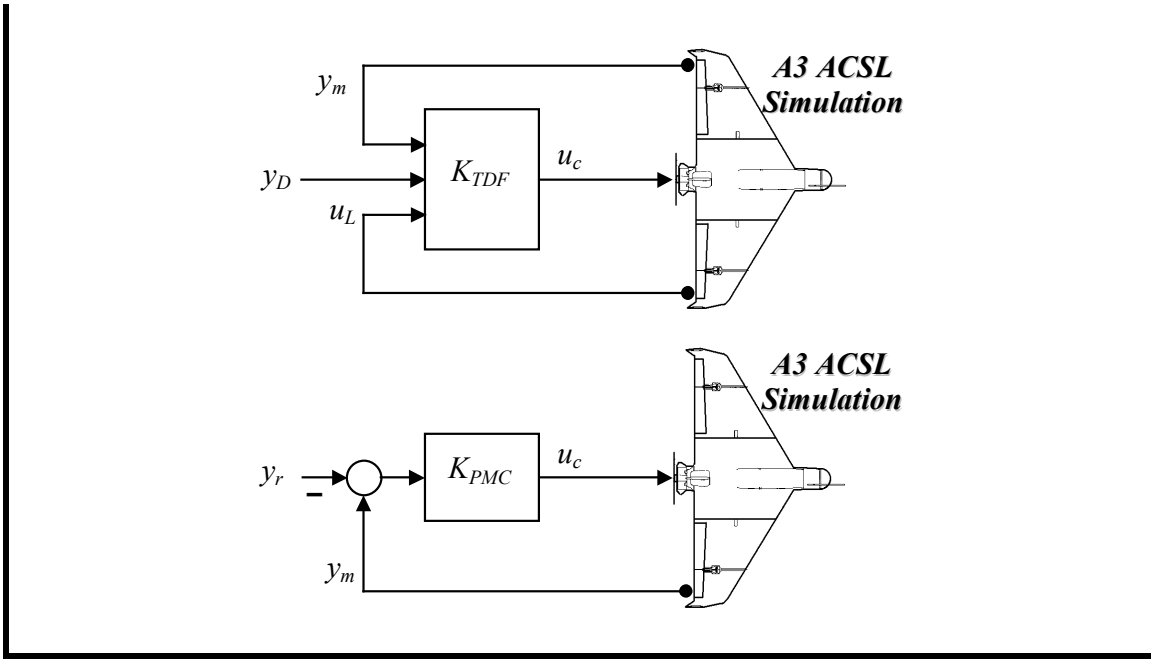

Figure 8.11: Controllers implementation in ACSL simulation

8.4.3 Non-linear Simulation

Here, the classical PMC is evaluated in the ACSL non-linear simulation using the same manoeuvres used in the robust designs in the earlier chapters. Note that The PMC is implemented in ACSL as a regulator, while the TDF was implemented as a demand tracking controller as shown in Figure 8.11 above. Figure 8.12 below, shows a comparison between PMC and TDF using the nominal flight case, i.e. G_{35}. with an initial height demand of 100m and airspeed of 35m/s, followed at 50s after launch by simultaneous step demands of 10m and 5m for height and cross-track respectively.

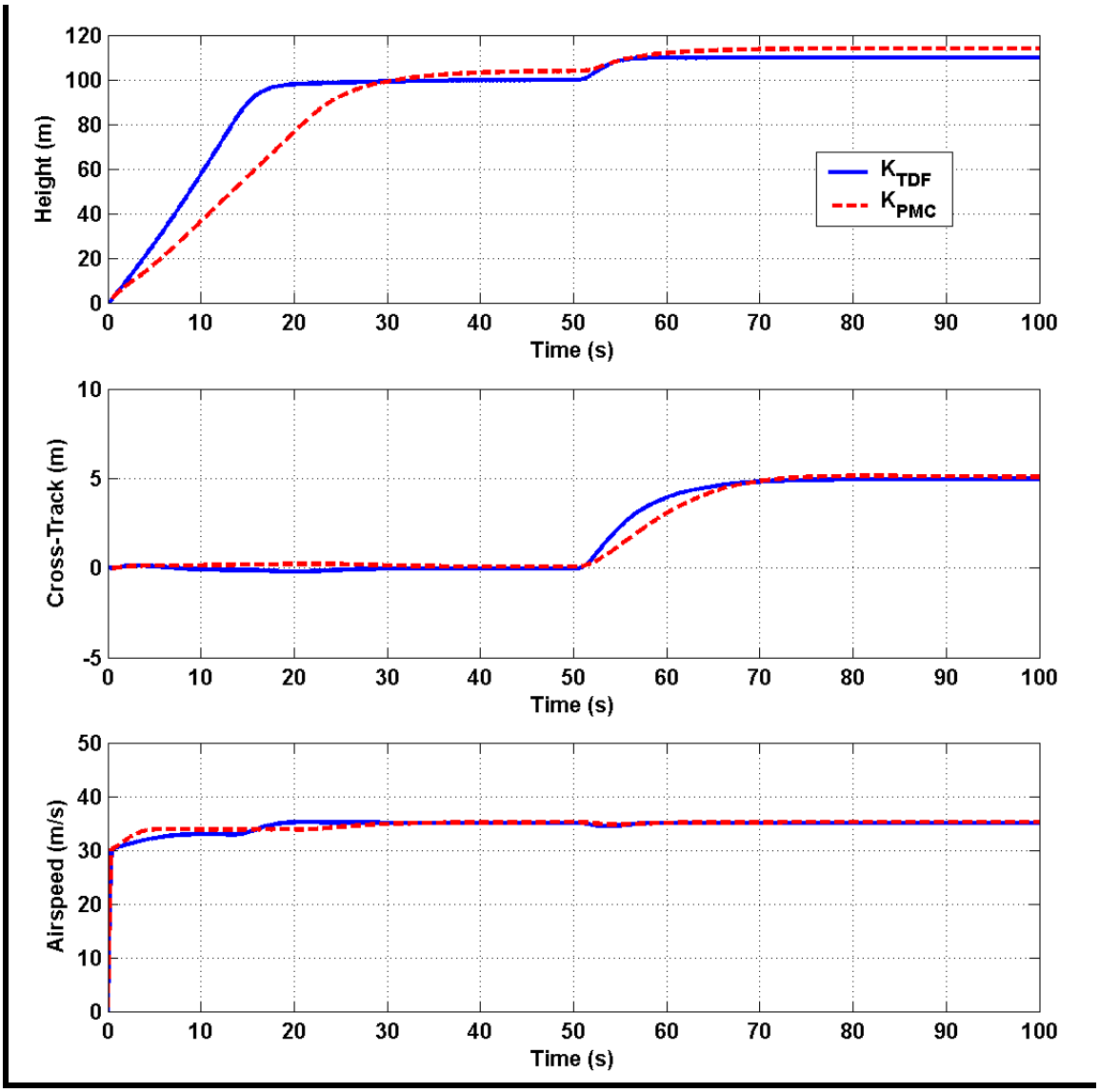

Figure 8.12: TDF vs. PMC non-linear simulation at nominal conditions

The results in Figure 8.12 verify the linear sensitivity analysis in §8.4.2. The height and cross-track loops, although show good signs of stability clearly indicate narrow-band and loose demand tracking response. Notice how the TDF airspeed control suffered in favour of the quick and precise demand tracking of height and cross-track for both launch and the 50*s* step phases. Figure 8.13 below, shows the rotational angles and their rates for the performed manoeuvres above. Notice that although the PMC was using less pitch/attitude angles, it has reached the same trim values. Also note how at launch the PMC pitch rate was negative indicating a dangerous nose down manoeuvre.

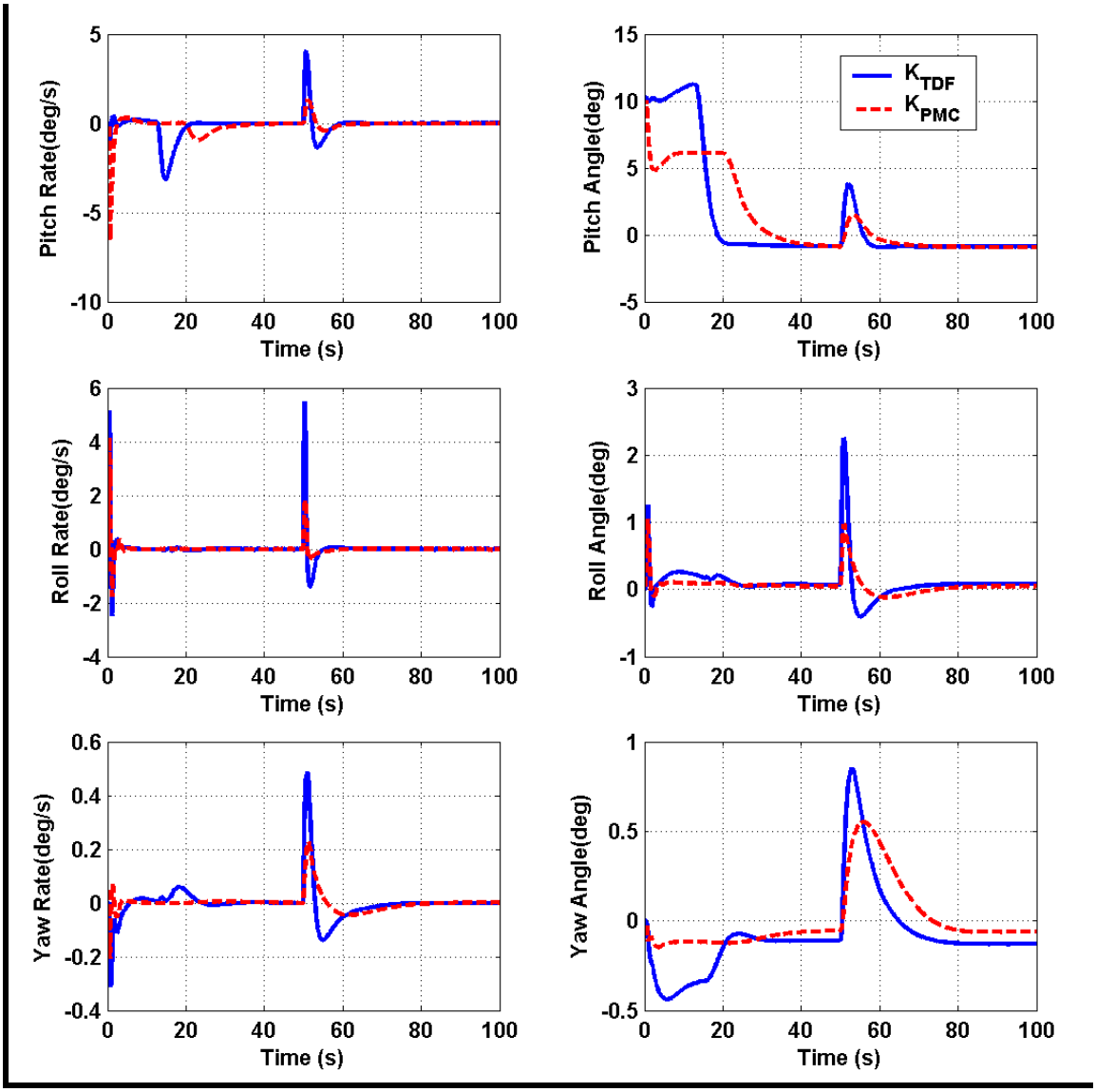

Figure 8.13:TDF vs. PMC attitude angles and rates response at the nominal condition

Figure 8.13 also shows how the PMC achieved attitude angles and rates magnitudes were less than the TDF, which indicates better stability but it was on the account of demand tracking performance as was shown earlier in Figure 8.12. Notice also how the TDF controller used more yaw for cross-track demand tracking with a slightly more relaxed wing-levelling (i.e. non-zero steady-state roll angle). Figure 8.14 below, shows the executed actuator control commands for both systems. Be aware that each control demand response was split into two subfigures to cover both the launch and the 50*s* step phases in more details.

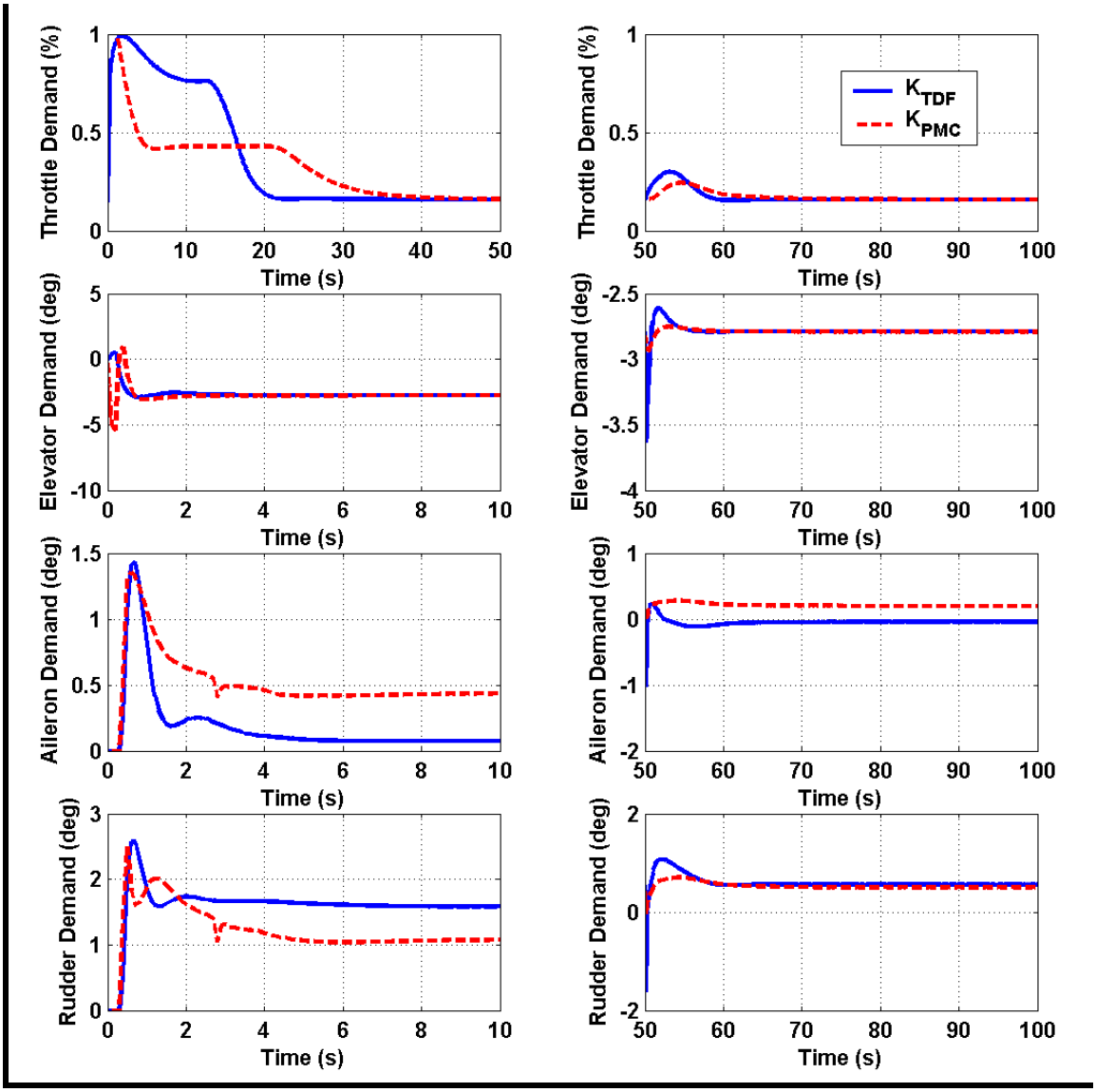

Figure 8.14:TDF vs. PMC control commands response

Figure 8.14 shows how the TDF controller used more throttle for the climb phase just like real manned aircraft pilots use, as discussed in the longitudinal design in §**5.9.2**, to reach the target height more quickly and efficiently. Notice how the PMC used more aileron for wing-levelling, but less rudder for cross-track demand tracking.

8.4.4 Maximum Crosswind Evaluation

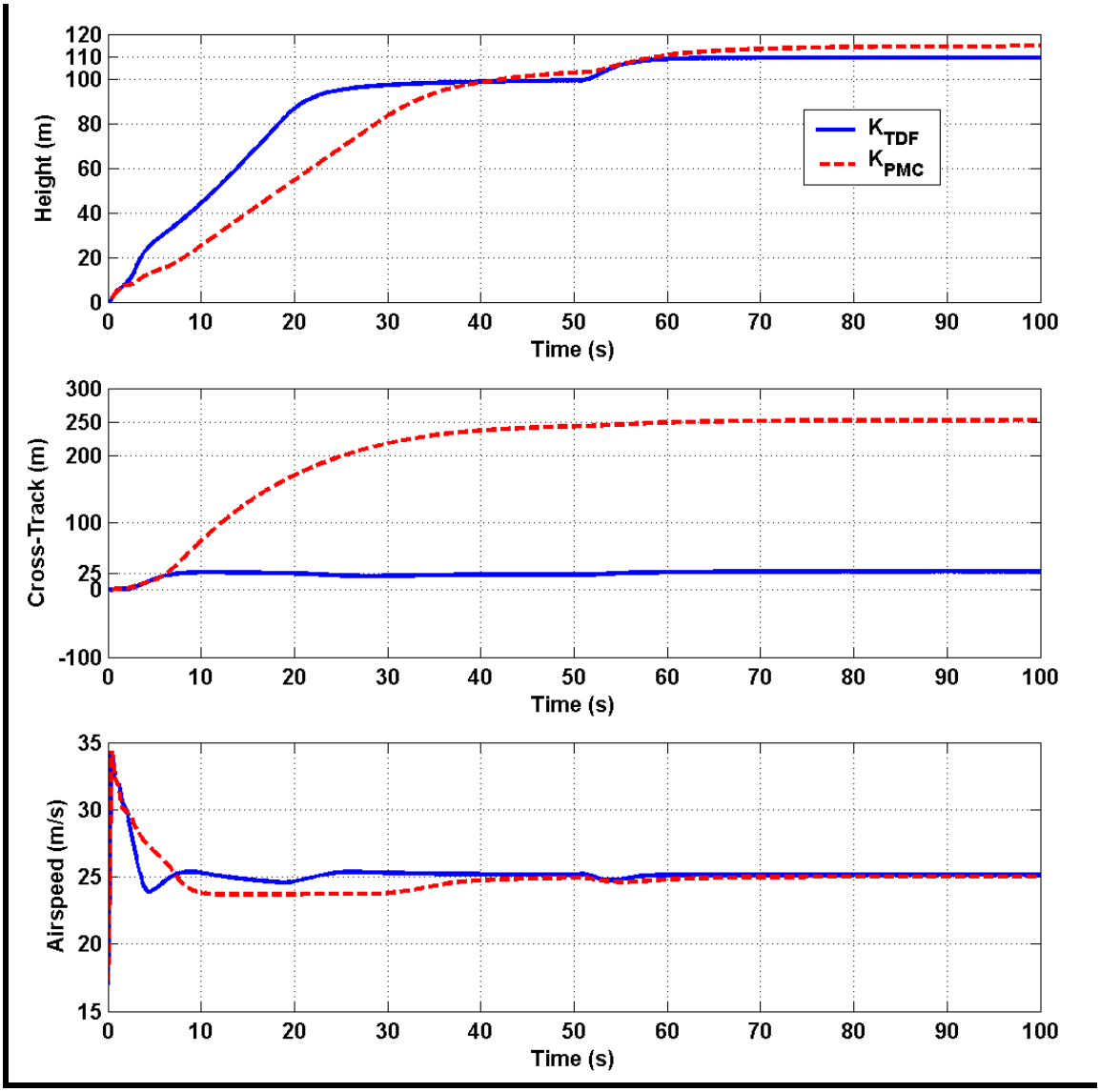

Figure 8.15: TDF vs. PMC at maximum cross-wind of 17*m/s*

Here, the PMC is evaluated in the ACSL non-linear simulation with the maximum

crosswind that the robust TDF controller was able to survive. That is, using the low airspeed/high stability G_{25P} configuration with a $17m/s$ westerly crosswind.

Figure 8.15 shows that although the PMC was able to survive the maximum crosswind launch, it was not able to keep a reasonable cross-track error. At about $250m$ vs. $25m$ for the TDF, the PMC lateral tracking performance has declined considerably. Note that both controllers were supposed to fly with zero cross-track error for the first $50s$.

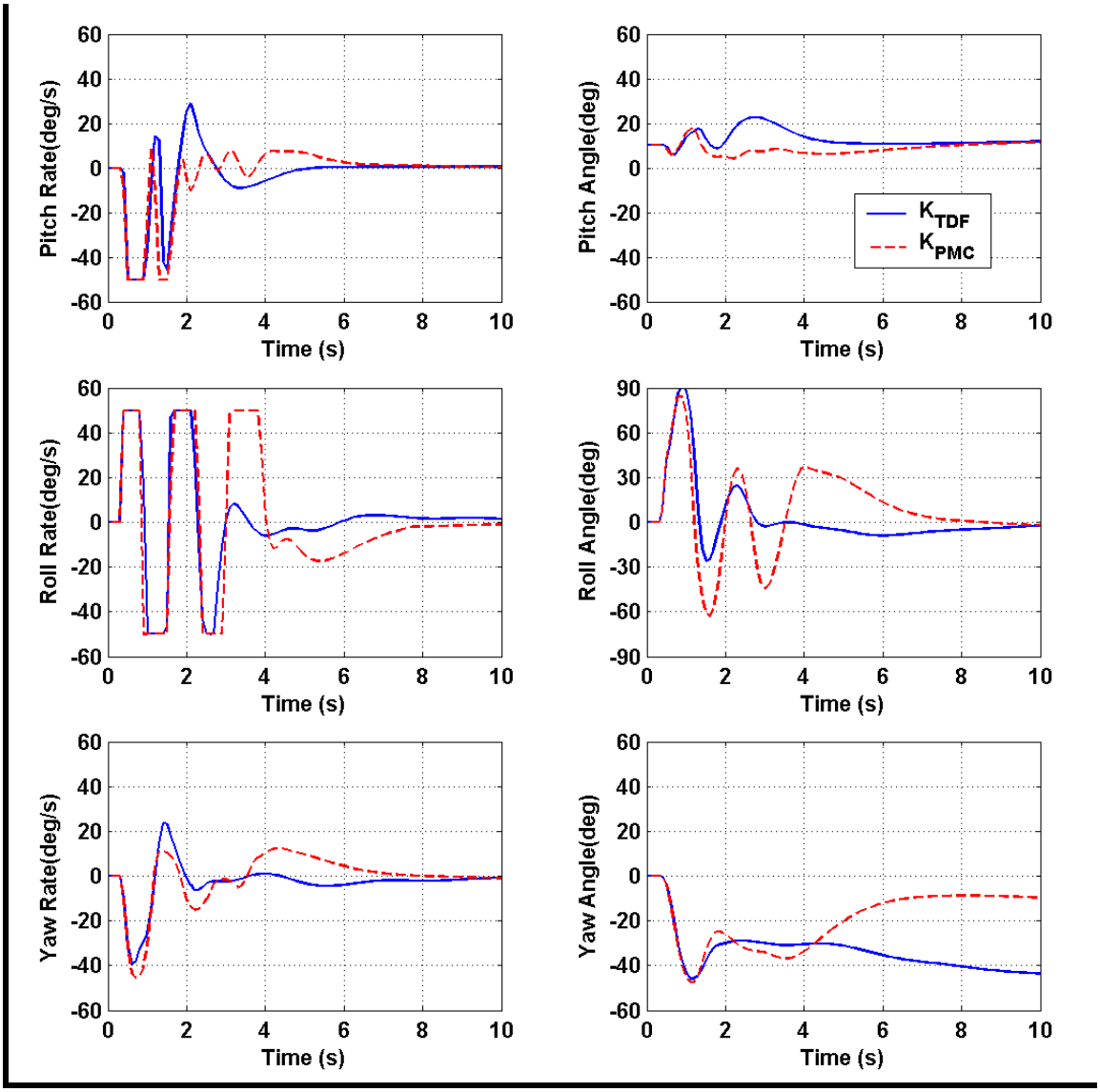

Figure 8.16: TDF vs. PMC attitude angles and rates at maximum cross-wind condition

The angular rates and attitudes are shown in Figure 8.16. Notice how the PMC exhibited more oscillations and hit the vertical gyro limits more often than the TDF controller for the pitch and roll rates. Also notice how the TDF controller used more yaw to reduce the cross-track error more than the PMC was be able to. It must be stated here that the PMC is optimised to minimize attitude angles and rates as part of the *gust insensitive* configuration and not height and cross-track.

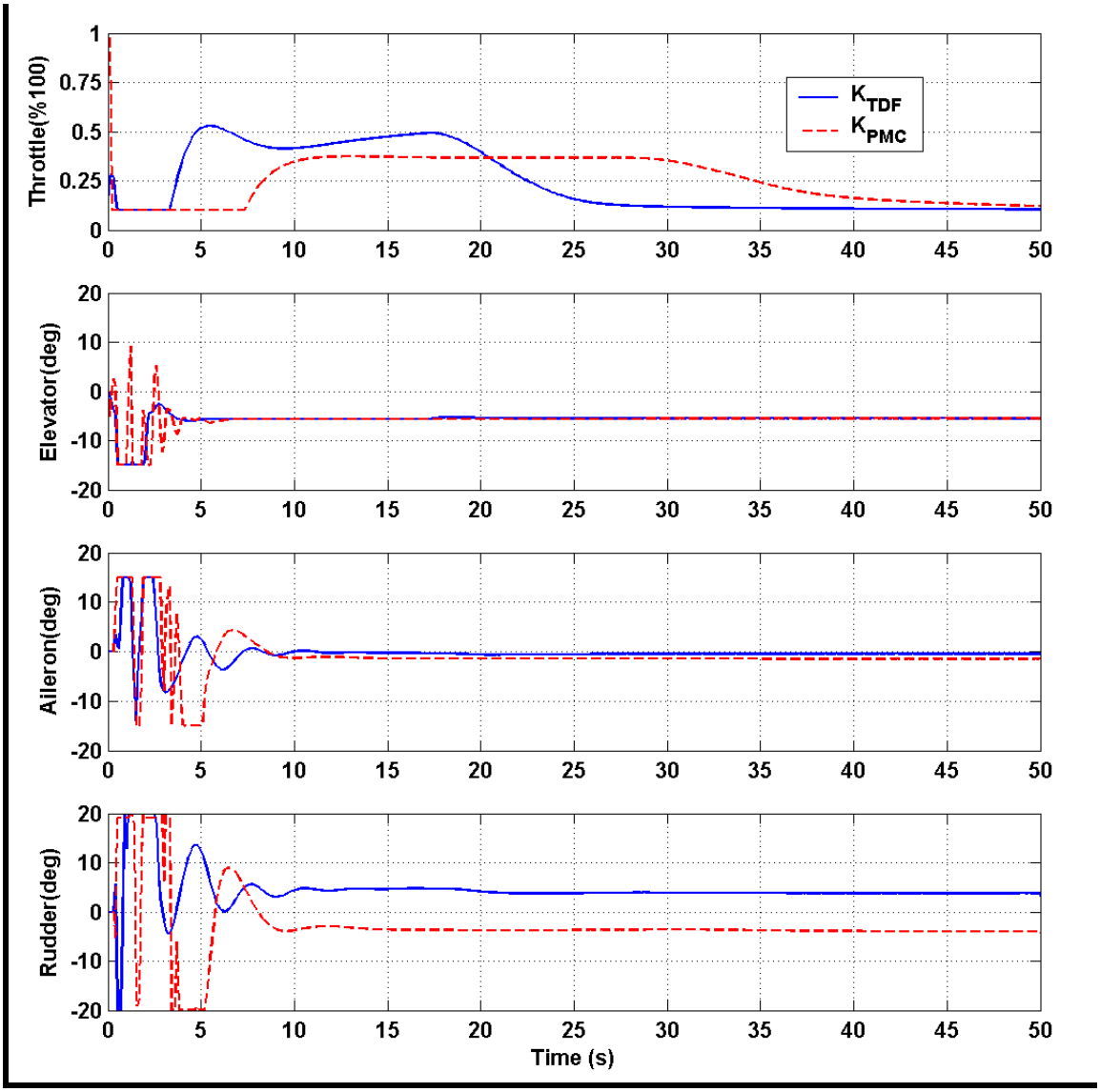

Figure 8.17: TDF vs. PMC control commands at maximum cross-wind condition

The actuator commands are compared in Figure 8.17. Only the first 50*s* of flight are

shown to emphasize the launch phase activities. The actuators response of the PMC, in Figure 8.17 reflect the angular rates response, which also exhibited more oscillations and hit the actuators limits more often than the TDF did. Note that the TDF controller implemented the Hanus anti-windup function which will significantly help in such cases by keeping the controller commands consistent with the actual executed limited commands. Notice how the PMC used negative rudder due to the mixing strategy which is aimed at decoupling the roll and yaw dynamics as described in §3.8.4, while the TDF controller used the logical positive rudder (i.e. to port) to produce the required negative heading to overcome the westerly cross-wind.

8.4.5 In Conclusion

In conclusion to this section, the classical PMC law was attractively simple and visible, designed and implemented intelligently, but required a great deal of experience and trial and error to be successful. The above evaluations showed that the PMC was optimised to minimize attitude angles and rates as part of the *gust insensitive* configuration and robust stability utilizing gain scheduling, while demand tracking performance evidently suffered.

On the other hand, the robust TDF control law required more theoretical background and mathematical tools, but would have not been successful without experience and proper implementation, and was not trial and error free. The above comparison with the classical PMC design proved the fact that the applied robust control methodology was mature enough to produce fine controllers for real life complex FCSD problems.

8.5 Alternative Research Techniques

Some of the work done in this research was not included in the main body of the thesis due to various reasons. It is thought useful to state these techniques and their outcome to be aware of what might be expected out of them and why they were not included.

8.5.1 Inner-/Outer-Loop Design

When the LSDP was applied to an inner-/outer-loop structure, one of the major problems was the considerable increase in the size of the final outer-loop controller. This is because the controller would include the inner-loop model and controller, which already in itself contains the system model and its weighting functions, plus the outer-loop weighting functions. Also, the stability margins calculated for the two loops were not sensible. That is, the inner-loop stability margin would represent the ability to stabilize the inner-loop model only, while the outer-loop stability margin would treat the inner-loop system model and controller as the system model to be controlled. Thus the actual stability margin of the whole controlled system would be the multiplication of the inner- and outer-loops stability margins which did not show any significance advantages for the increased order of the controller.

The TDF controller was able to act like an inner-/outer-loop structure while using the same system model with the minimum increase in controller order.

8.5.2 Tailless and Elevon Configurations

Removing the rudder/tail from the air vehicle has been a desire for several advantages including: reduction of number of components and weight of airframe which will increase its operational and recovery robustness, and will also help reduce its visual and radar signature for improved stealth operations. Unfortunately, although trying to utilize the considerable adverse yaw the ailerons have to generate the required yawing moment, the rolling moment generated was prohibiting the ability of the air vehicle to yaw without severe roll due to the fact that $-l_\xi >> n_\xi$ as discussed in §**4.6.2**. This in turn affected the elevators effectiveness and caused an immediate crash after launch in the non-linear simulation.

Using the outboard elevator pair as elevons and removing the inboard aileron pair and actuators would also have some of the advantages of removing the rudder. Although unlike the rudder case, the linear analysis showed acceptable results, the non-linear simulation showed undesirable coupling between the longitudinal and lateral dynamics

that resulted in degradation of performance and stability robustness for both modes. Recall that decoupled designs produce "cleaner" and more reliable controllers that the elevon configuration would not permit.

8.5.3 Dynamic Decoupling

Decoupling control is a well-known technique[18, 81, 82]. Dynamic decoupling, unlike static decoupling used in §**5.4** and elsewhere in this thesis, aims at decoupling the system model inputs and outputs at the full frequency spectrum of interest. Two methods were applied in this thesis and will be introduced here.

8.5.3.1 Dynamic Alignment

Dynamic alignment[39, 71] is based on the inverse of the system model, G^{-1}. It will decouple and scale the system model for all frequencies. The dynamic decoupling transfer matrix was derived analytically for the lateral dynamic model of the air vehicle. When applied, it was found to be as effective as the static alignment, but every time the weighting functions were modified, it was necessary to re-derive the dynamic alignment transfer matrix. Thus, compared to the static alignment, it was not worth the effort and complications to be adopted for use in the design process.

8.5.3.2 Non-Diagonal Weighting

Non-diagonal weighting[83, 84] has the advantage of dynamically decoupling the system model singular values at the input and output enabling independent shaping. Although similar to dynamic alignment, non-diagonal weighting utilizes the properties of the SVD of the nominal system model G,

$$G = U \Sigma V^{*} \qquad \textbf{8.13}$$

where U and V are matrices containing the left and right singular vectors of G, and Σ is a diagonal matrix containing the singular values of G. Thus,

$$U^{-1} G V^{-*} = \Sigma \qquad \textbf{8.14}$$

By generating U and V frequency-by-frequency for the desired frequency band, transfer matrices are found to approximate U and V that in turn are used to decouple G as in Equation 8.14.

Although the method appears attractive, it was not implemental or practical. First, when fitting a transfer matrix for U and V, only high order transfer matrices were found to fit the desired frequency band which inflated the final robust controller order considerably. Second, if spectral factorisation is applied as part of the design procedure, see [84] for more details, there will be a problem if G has a pole and/or a zero at the origin. Similarly if the pre-weight contained integrators, which was true in our case. This is due to the fact that the imaginary axis poles and zeros are not accommodated in the method used in the spectral factorisation above.

Again, the simple static alignment[71, 77] at the system bandwidth was more practical and easily implemented. This is because the effect on performance of reducing interaction and coupling is normally greatest around the system bandwidth and less elsewhere.

8.5.4 Weights Selection Optimisation

It was shown from the robust control designs in this thesis that the weighting variables that are manipulated manually need engineering sense, experience, and trial and error to achieve optimal values. Due to the large numbers of variables involved, optimisation techniques can be useful in adjusting these variables to minimize/maximize some objective function. The MATLAB Optimisation toolbox contains several techniques including unconstrained, least-squares, constrained, and multi-objective optimisations that could be utilised in this process. Recall that the multi-objective synthesis was reviewed in §**1.4.4**.

Constrained minimization was applied in the full model design in Chapter **7** to adjust the scaling and shaping weighting variables while the objective function was

minimizing the reciprocal of *SM* of the closed-loop controlled system. Although the method was successful in increasing *SM*, it did not treat the different weighting variables properly. This is because the perturbation of the cross-track scaling variable, for example, is much less sensitive than the pitch or roll rate scaling in affecting *SM*. Thus the cross-track scaling weight was not changed much from the initial condition, although the defined upper and lower bounds were wide enough for the required adjustments; only the most sensitive and influential variables were modified to improve *SM*. Also, these optimisation methods would not be adequate to use without the right weighting functions structure (such as number of integrators, low-pass and/or band-pass filters etc.), weighting variables realistic bounds and initial conditions. That is to say these optimisation methods would only be useful in fine-tuning the final weighting variables[85]. This means that most of the work needed for the weight selections and design is still required. Recall that it was decided to use the simplest and most effective methods in this thesis, the burden of learning and applying these techniques does not seem crucial; hence were not included in the main robust control design procedures.

Chapter 9

Conclusions and Future Work

In the view of the fact that "No human work is perfect or complete," it is intended in this last chapter to,

- Present the main conclusions and outcome of this research,
- Discuss the future work that time did not permit to do, but would be feasible to extend this work,
- Examine some issues that can help promote the robust control methodologies within the aerospace industry more effectively.

9.1 Conclusions

❖ Air vehicle modelling

- An effective technique is adopted to reduce the order of the air vehicle model and the related robust controller with equal dynamic behaviour. By replacing the two pairs of actuators for the elevators and ailerons with their equivalent single actuators and doubling their aerodynamic forces, it was

possible to reduce the order of the full air vehicle model from 30 to 26 states with identical dynamics. This in turn would reduce the order of the robust TDF control law by up to 8 states with exact mathematical response.

- The *v*-gap metric topology is used to assess the dynamics of coupling of the longitudinal and the lateral-directional modes of the air vehicle and the effect of the different subsystems, such as actuators and on-board processor delays, if neglected on modelling uncertainty. The results reveal how vital it is to evaluate these effects to predict and enhance the robustness of the controllers designed using such models.

❖ Robust Loop Shaping Design Procedure(LSDP)

- An important modification is adopted to the original LSDP which shows improved efficiency and visibility to the design process. The procedure is further extended by the use of the TDF design for precision demand tracking, and command signal conditioning for robust operation in actuator saturation and windup conditions.
- Piloting methods are innovatively implemented in the FCSD for the climb phase and in severe cross-wind launch conditions that proved effective and efficient.
- The robust TDF controller developed using the modified and extended design procedure was successfully applied to the unmanned, unstable, catapult launched Cranfield A3 Observer air vehicle for the whole flight phases of launch, climb, and level cruise. Robustness was demonstrated by the capability of the single-point unscheduled controller, in the high fidelity 6DOF non-linear simulation, to stabilize, control and navigate the air vehicle precisely and efficiently, and through the 3D prescribed flight path for the full operational flight envelope the air vehicle was capable of, and survive, extreme cross-wind launch conditions with exaggerated CG shifts.
- In comparison with the classical PMC design, the robust TDF controller revealed superior performance with equivalent level of stability. Although the order of the robust TDF controller was much higher, the actual number

of variables to be manipulated manually was reduced considerably due to the elimination of the scheduling process requirement.

❖ Non-linear Implementation

Several innovative ideas are implemented in the non-linear simulation to enable the "linear" robust flight control system to function more effectively and accurately in the realistic non-linear environment. As a result, the controller is able to run in demand or regulator modes or in a mix of both, and perform more accurate control command conditioning under saturation or in observer-form.

9.2 Recommendations for Future Work

❖ Real-Time GCS Evaluation

The initial aim of this thesis was to design and flight-test the developed robust controller with the A3 Observer air vehicle. The Control Systems Group at *Cranfield Aerospace Ltd* implemented the initial longitudinal controller in the GCS simulator described in Appendix A.1, where it was tested and evaluated successfully[86]. Unfortunately, due to the changes in QinetiQ plans and time limitations, it was not possible to test the robust controller in real-flight. Consequently, it was decided not to implement or test the final TDF controller in the GCS simulator.

The obvious next step is to implement and evaluate the final TDF controller in the GCS simulator, which will give more insight in its performance and stability robustness in this quite realistic environment. Ultimately, a real flight-test would be an invaluable experience.

❖ Scheduled Observer-Form TDF Design

Due to the success of the unscheduled TDF robust control design and time limitation, the observer-form described in Appendix A.3 was not implemented. However, it would be very interesting to schedule the TDF controller at the nominal and the two worst-case

model operating points using the observer-form structure. This will give the chance to evaluate the advantages scheduling may have over the single point design, and the assessment of the effort invested.

Command signal conditioning is also possible to implement in the TDF observer-form structure as shown in Appendix A.3.1. This would enhance the control law performance in actuator saturation and windup conditions as has been shown in this research work.

❖ Unconventional Control Configurations

Although, the tailless and elevon configurations were not very successful as discussed in §**8.5.2**, other possibilities and approaches exist. The control selector method described in Appendix A.2 may be used in the tailless configuration by utilizing the induced drag of both elevator and aileron that can deflect in opposite directions for each side to generate the required yawing moment with no rolling effect.

The control selector method was applied in the design of tailless aircraft control[87], and is similar to the mixing matrix idea[7, 70] used in the classical PMC design described in §3.8.4.

9.3 Industrial Promotion

❖ UAV Applications

For the UAV and missile FCSD applications, robust control has been widely accepted and employed. This is due to several factors including,

- They do not need to meet the stringent regulations that civil and military aircraft have.
- They are required to perform more complicated and sometimes not well-defined control tasks.

- The cost of the FCS failure is much less than in the military and civil applications, which encourages FCS designers to apply new methodologies.

❖ Aeronautical Industry

For the general aeronautical industry, several important steps should be taken to help employ the different advanced robust control techniques including,

- Joint effort from the scientific and industrial communities to introduce, implement, and apply these techniques to realistic problems, where the GARTEUR ACTION GROUP FM(AG08)[1] has achieved. UAVs would be excellent examples, which this thesis is considered part of, where real flight test is not out-of-reach.
- Carry out the formidable task of clearance of the these modern MIMO flight control laws. New analysis techniques for the industrial clearance process for these laws need to be explored and investigated to provide recommendations on how the current techniques should evolve in order to improve the efficiency and reliability of this process[88].
- The fact that FCSD requires high level of expertise and knowledge cannot be overlooked or overcome. The modern robust control methodologies would only contribute to escalate this level. New generations of FCS designers should be well-educated in classical and modem control theories in the under-graduate level, and in robust control in the master-degree level. This generation would be able to digest the enormous industry classical control design experience and put the new robust control techniques in full action. The robust LSDP applied in this thesis is an ideal mix of the classical and robust methodologies.

References

[1] J.-F. Magni, S. Bennani, and J. Terlouw, "Robust Flight Control: A Design Challenge," in *Lecture Notes in Control and Information Sciences; 224*. London: Springer, 1997.

[2] R. A. Hyde, *H_∞ Aerospace Control Design : A VSTOL Flight Application*. Berlin; New York: Springer, 1995.

[3] B. M. Chen, *H_∞ control and its applications*. London ; New York: Springer, 1998.

[4] R. J. Adams, *Robust Multivariable Flight Control*. London ; New York: Springer-Verlag, 1994.

[5] D. J. Dyer, R. I. Jones, and P. G. Thomasson, "The Design and Development of a Battle Group UAV Demonstrator," presented at NATO RTA Conference, Unmanned Vehicles for Aerial, Ground & Naval Military Operations, Ankara, Turkey, 2000.

[6] P. G. Thomasson, "The flight dynamics of an unstable unmanned aircraft," in *Aerospace vehicle dynamics and control*, *Institute of Mathematics and Its Applications conference series*: Oxford University Press, 1994, pp. 245-258.

[7] P. G. Thomasson, "Flight Test Experience with the Cranfield A3 Observer," presented at UAV's 15th International Conference, Bristol, UK, 2000.

[8] R. A. Walster, "Observer System Overview," Control System Group, Cranfield Aerospace Ltd, Cranfield, Bedford CA/CSG/8506, 13 September 2000.

[9] C. Doell, J.-F. Magni, G. Looye, and S. Bennani, "Robustness analysis applied to autopilot design. II - Evaluation of a new tool for μ-analysis," *ICAS, Congress, 21st, Melbourne, Australia, Sept*, 1998.

[10] S. Bennani and G. H. N. Looye, "RCAM Design Challenge Presentation Document: the μ-Synthesis Approach," GARTEUR-FM(AG08) TP-088-11, 1997.

[11] D. Moormann, A. Varga, G. Looye, and G. Gruebel, "Robustness analysis applied to autopilot design. III - Physical modeling of aircraft for automated LFT generation applied to the Research Civil Aircraft Model," *ICAS, Congress, 21st, Melbourne, Australia, Sept*, 1998.

[12] G. Papageorgiou, M. Huzmezan, K. Glover, and J. Maciejowski, "A combined *MBPC*/H_∞ automatic pilot for a civil aircraft," presented at American Control Conference, New Mexico, 1997.

[13] F. Amato, M. Mattei, S. Scala, and L. Verde, "Robust flight control design for the HIRM via linear quadratic methods," *In: AIAA Guidance, Navigation, and Control Conference and Exhibit, Boston, MA, Aug*, vol. 2, pp. 857-867, 1998.

[14] J. Markerink, S. Bennani, and B. Mulder, "Design of a Robust, Scheduled Controller for the HIRM using μ-synthesis," GARTEUR FM(AG08) TP-088-29, 1997.

[15] E. Muir, "HIRM Design Challenge Presentation Document: the Robust Inverse Dynamics Estimation approach," GARTEUR-FM(AG08) TP-088-28, 1998.

[16] G. Papageorgiou and K. Glover, "Design of a robust two degrees-of-freedom controller for an actively controlled wind tunnel model," *AIAA Guidance, Navigation, and Control Conference and Exhibit, Portland, OR, Aug*, 1999.

[17] G. Papageorgiou and K. Glover, "Design of a robust gain scheduled controller for the high incidence research model," presented at AIAA Guidance Navigation and Control Conference, Portland, 1999.

[18] A. Snell, "Decoupling of Nonminimum Phase Plants and Application to Flight Control," presented at AIAA Guidance, Navigation, and Control Conference and Exhibit, Monterey, California, 2002.

[19] H.-D. Joos, "RCAM Design Challenge Presentation Document: Multi-Objective Parameter Synthesis (MOPS)," GARTEUR-FM(088) TP-088-16, 1997.
[20] I. M. Horowitz, *Quantitative Feedback Design Theory (QFT)*. Boulder, Colorado.: QFT Publications, 1992.
[21] S. J. Rasmussen and C. H. Houpis, "Development, implementation and flight test of a mimo digital flight control system for an unmanned research vehicle designed using quantitative feedback theory," *International Journal of Robust and Nonlinear Control*, vol. 7, pp. 629-642, 1997.
[22] P. L. Fontenrose and C. E. Hall, "Development and flight testing of quantitative feedback theory pitch rate stability augmentation system," *Journal of Guidance Control and Dynamics*, vol. 19, pp. 1109-1115, 1996.
[23] "Special issue on the LQG problem," *IEEE Transaction on Automatic Control*, vol. AC-16, 1971.
[24] J. S. Jang and C. J. Tomlin, "Autopilot Design for the Stanford DragonFly UAV: Validation through Hardware-in-the-Loop Simulation," presented at AIAA Guidance, Navigation, and Control Conference and Exhibit, Montreal, Canada, 2001.
[25] J. C. Doyle and G. Stein, "Multivariable feedback design: Concepts for a classical/modern synthesis," *IEEE Transactions on Automatic Control*, vol. 26, pp. 4-16, 1981.
[26] M. Athans, "A tutorial on the LQG/LTR method," presented at American Control Conference, Seattle, WA, 1986.
[27] D. McFarlane and K. Glover, "A loop shaping design procedure using H_∞ synthesis," *IEEE Transactions on Automatic Control*, vol. 37, pp. 759-769, 1992.
[28] G. Papageorgiou, K. Glover, G. D'Mello, and Y. Patel, "Taking robust LPV control into flight on the VAAC Harrier," presented at Decision and Control, Proceedings of the 39th IEEE Conference on, Sydney, NSW, Australia, 2000.
[29] D. J. Walker and I. Postlethwaite, "Advanced helicopter flight control using two-degree-of-freedom H_∞ optimization," *Journal of Guidance, Control, and Dynamics*, vol. 19, pp. 461-468, 1996.
[30] A. Smerlas, I. Postlethwaite, D. J. Walker, M. E. Strange, J. Howitt, R. I. Horton, A. W. Gubbels, and S. W. Baillie, "Design and flight testing of an H_∞ controller for the NRC Bell 205 experimental fly-by-wire helicopter," *In: AIAA Guidance, Navigation, and Control Conference and Exhibit, Boston, MA, Aug*, vol. 2, pp. 1023-1033, 1998.
[31] M. L. Civita, G. Papageorgiou, W. C. Messner, and T. Kanade, "Design and Flight Testing of a High-Bandwidth H_∞ Loop Shaping Controller for a Robotic Helicopter," presented at AIAA Guidance, Navigation, and Control, Monterey, California USA, 2002.
[32] K. Y. Tu, A. Sideris, K. D. Mease, J. Nathan, and J. Carter, "Robust lateral-directional control design for the F/A-18," *In: AIAA Guidance, Navigation, and Control Conference and Exhibit, Portland, OR, Aug*, vol. 2, pp. 1213-1219, 1999.
[33] C.-D. Yang and C.-Y. Chang, "μ-synthesis using linear quadratic Gaussian controllers," *Journal of Guidance, Control, and Dynamics*, vol. 19, pp. 886-892, 1996.
[34] Gregory, Chowdhry, and McMinn, "Hypersonic vehicle model and control law development using H_∞ and μ synthesis," Nasa, Washington, D.C 1994.
[35] W. C. Reigelsperger, K. D. Hammett, and S. S. Banda, "Robust control law design for lateral-directional modes of an F-16/MATV using μ-synthesis and dynamic inversion," *International Journal of Robust and Nonlinear Control*, vol. 7, pp. 777-795, 1997.
[36] K. Glover and D. McFarlane, "Robust stabilization of normalized coprime factor plant descriptions with H_∞ -bounded uncertainty," *IEEE Transactions on Automatic Control*, vol. 34, pp. 821-830, 1989.

[37] D. C. McFarlane and K. Glover, *Robust controller design using normalized coprime factor plant descriptions*, vol. 138. Berlin ; New York: Springer-Verlag, 1990.
[38] K. Zhou and J. C. Doyle, *Essentials of robust control*. Upper Saddle River, N.J.: Prentice Hall, 1998.
[39] S. Skogestad and I. Postlethwaite, *Multivariable feedback control : analysis and design*. Chichester ; New York: Wiley, 1996.
[40] J. F. Whidborne, D.-W. Gu, and I. Postlethwaite, "MODCONS - a MATLAB toolbox for multi-objective control system design," presented at IEE Colloquium on Applied Control Techniques Using MATLAB, London, UK, 1995.
[41] R. Y. Chiang and M. G. Safonov, *Robust Control Toolbox*, 2 ed. Natick, MA: The MathWorks, Inc., 2001.
[42] J. M. Lipscombe, "Control Law Design for the Gust Insensitive Version of XRAE," Unpublished Report, Cranfield Institute of Technology, College of Aeronautics, Cranfield September 1986.
[43] Mitchell and Gauthier, "ACSL MODEL: Reference Manual," 11 ed. Concord: MGA Software, 1995.
[44] J. Sefton and K. Glover, "Pole/zero cancellations in the general H_∞ problem with reference to a two block design," *Systems & Control Letters*, vol. 14, pp. 295-306, 1990.
[45] R. A. Hyde, "An H_∞ loop-shaping design for the VAAC Harrier," in *Flight Control Systems: practical issues in design and implementation*, *Control Engineering Series 57*, R. Pratt, Ed.: IEE, 2000, pp. 348-373.
[46] N. Aouf, D. G. Bates, and I. Postlethwaite, "Observer-Form Scheduling of H_∞ Loopshaping Integrated Flight and Propulsion Control Law," presented at AIAA Guidance, Navigation, and Control Conference, Montreal, Canada, 2001.
[47] R. A. Hyde and K. Glover, "Meeting VSTOL aircraft performance requirements using scheduled H_∞ controllers," 1991.
[48] R. A. Hyde and K. Glover, "The Aapplication of Scheduled H_∞ Controllers to a VSTOL Aircraft," *IEEE Transactions on Automatic Control*, vol. 38, pp. 1021-1039, 1993.
[49] I. Postlethwaite, D. J. Walker, and A. J. Smerlas, "Robust control law design for the Bell-205 helicopter," *In: European Rotorcraft Forum, 21st, St. Petersburg, Russia, Aug*, vol. 2, pp. 7, 1995.
[50] G. Vinnicombe, *Uncertainty and feedback : H_∞ loop-shaping and the ν-gap*. London: Imperial College Press, 2001.
[51] D. J. Hoyle, R. A. Hyde, and D. J. N. Limebeer, "AN H_∞ APPROACH TO TWO DEGREE OF FREEDOM DESIGN," presented at Proceedings of the 30th IEEE Conference on Decision and Control, Brighton, United Kingdom, 1991.
[52] D. J. N. Limebeer, E. M. Kasenally, and J. D. Perkins, "On the design of robust two degree of freedom controllers," *Automatica*, vol. 29, pp. 157-168, 1993.
[53] G. J. Balas, J. C. Doyle, K. Glover, A. K. Packard, and R. Smith, *μ-Analysis and Synthesis Toolbox*, 3 ed. Natick, MA: The MathWorks, Inc., 2001.
[54] R. Hanus, M. Kinnaert, and J. L. Henrotte, "Conditioning Technique, a General Anti-Windup and Bumpless Transfer Method," *Automatica*, vol. 23, pp. 729-739, 1987.
[55] R. G. Ford and K. Glover, "An application of coprime factor based anti-windup and bumpless transfer control to the spark ignition engine idle speed control problem," presented at Decision and Control, Proceedings of the 39th IEEE Conference on, Sydney, NSW, Australia, 2000.
[56] R. Hanus and P. Bogaerts, "'Feedback' and 'feedforward' conditioning techniques," *European Journal of Control*, vol. 6, pp. 421-434, 2000.
[57] Y. B. Peng, D. Vrancic, R. Hanus, and S. S. R. Weller, "Anti-windup designs for multivariable controllers," *Automatica*, vol. 34, pp. 1559-1565, 1998.

[58] S. Miyamoto and G. Vinnicombe, "Robust control of plants with saturation nonlinearity based on coprime factor representations," presented at Proceedings of the 35th IEEE Decision and Control, Kobe , Japan, 1996.
[59] A. El-Sakkary, "The gap metric: Robustness of stabilization of feedback systems," *Automatic Control, IEEE Transactions on*, vol. 30, pp. 240-247, 1985.
[60] G. Vinnicombe, "Measuring The Robustness of Feedback Systems," in *Department of Engineering*. Cambridge: University of Cambridge, 1992, pp. 112.
[61] G. Vinnicombe, "Frequency Domain Uncertainty and the Graph Topology," *IEEE Transactions on Automatic Control*, vol. 38, pp. 1371-1383, 1993.
[62] P. G. Thomasson, "The Use of Simulation in the Development of a Gust Insensitive Aircraft," presented at UKSC Conference on Computer Simulation, Brighton, UK, 1990.
[63] P. G. Thomasson, "Modelling a Gust Insensitive Aircraft," in *Aerogram*, vol. 6. Cranfield: Cranfield Institute of Technology, 1990, pp. 11-14.
[64] P. G. Thomasson, "The Flight Dynamics of a Gust Insensitive Unmanned Aircraft," *IEE Colloquium*, 1995.
[65] Zipfel, *Modelling and simulation of aerospace vehicle dynamics*. Reston, VA: AIAA, 2000.
[66] L. Mangiacasale, *Flight Mechanics of a μ-Airplane*. Milan: Libreria CLUP, 1998.
[67] M. V. Cook, *Flight Dynamics Principles*. London: Arnold, 1997.
[68] D. McLean, *Automatic flight control systems*. New York: Prentice Hall, 1990.
[69] B. L. Stevens and F. L. Lewis, *Aircraft control and simulation*. New York: Wiley, 1992.
[70] P. G. Thomasson, "Control Mixing Strategy," Cranfield College of Aeronautics, Cranfield 2000.
[71] J. M. Maciejowski, *Multivariable feedback design*, First ed: Addison-Wesley, 1989.
[72] Futaba, "http://www.futaba-rc.com/servos/."
[73] L. Mangiacasale, *Airplane Control Systems μ-Synthesis with Matlab*. Turin: Libreria CLUP, 1996.
[74] B. Kouvaritakis, "COMPLEX ALIGN : A technique for the characteristic locus method of design," *IEE Proc., Control Theory and Applications*, vol. 129, Part D, pp. 1-5, 1982.
[75] J. Edmunds and B. Kouvaritakis, "Extensions of the frame alignment technique and their use in the characteristic locus design method," *International Journal of Control*, vol. 29, pp. 787-796, 1979.
[76] A. G. J. MacFarlane and B. Kouvaritakis, "A design technique for linear multivariable feedback systems," *International Journal of Control*, vol. 25, pp. 837-874, 1977.
[77] B. Kouvaritakis, "Theory and practice of the characteristic locus design method," *IEE Proc., Control Theory and Applications*, vol. 126, pp. 542-548, 1979.
[78] T. Thom, *The air pilot's manual*, 4th rev. ed. Shrewsbury: Airlife, 1999.
[79] K. J. Astrom, "Model Uncertainty and Robust Control." Lund,Sweden: COSY, 2000, pp. 63-100.
[80] H. Panagopoulos, K. J. Astrom, and T. Hagglund, "Design of PID controllers based on constrained optimisation," *Control Theory and Applications, IEE Proceedings-*, vol. 149, pp. 32-40, 2002.
[81] Q.-G. Wang, *Decoupling control*. New York: Springer, 2002.
[82] A. Snell, "Decoupling Control Design with Applications to Flight," *Journal of Guidance, Control, and Dynamics*, vol. 21, pp. 647-655, 1998.
[83] G. Papageorgiou, "Robust Control System Design: H_∞ Loop Shaping and Aerospace Applications," in *Darwin College, Engineering Department*. Cambridge: Cambridge University, 1998, pp. 206.
[84] G. Papageorgiou and K. Glover, "A systematic procedure for designing non-

diagonal weights to facilitate H_∞ loop shaping," presented at Decision and Control, Proceedings of the 36th IEEE Conference on, San Diego, CA, USA, 1997.
[85] J. King, "Robust multivariable control law design for missile autopilots," in *Department of Aerospace and Guidance Systems*. Shrivenham: Royal Military College of Science, 1997, pp. 194.
[86] R. A. Walster, "Robust Control Implementation in the CGI SIM," Cranfield Aerospace Ltd, Internal Report, Cranfield, 2001.
[87] A. D. Ngo, W. C. Reigelsperger, S. S. Banda, and J. A. Bessolo, "Tailless aircraft control law design using dynamic inversion & μ-synthesis," presented at Control Applications, Proceedings of the 1996 IEEE International Conference on, Dearborn, MI, USA, 1996.
[88] C. Fielding, *Advanced techniques for clearance of flight control laws*. Berlin ; London: Springer, 2002.
[89] R. J. Adams and S. S. Banda, "Robust flight control design using dynamic inversion and structured singular value synthesis," *IEEE Transactions on Control Systems Technology*, vol. 1, pp. 1063, 1993.
[90] D. J. Walker, "On the structure of a two-degree-of-freedom H_∞ loop shaping controller," *International Journal of Control*, vol. 63, pp. 1105-1127, 1996.

Appendix

A.1 Real-Time Ground Control Station Simulator

Figure A.1: A3 Observer Ground Control Station

The in-house Ground Control Station(GCS) real-time simulator at *Cranfield Aerospace Ltd* is aimed at simulating the actual GCS shown in Figure A.1, where the basic layout is shown in Figure A.2. The simulator contains the full non-linear simulation of the A3 Observer air vehicle that the ACSL simulation has. In addition, it is capable of simulating most of the air vehicle on-board equipments including GPS, camera payload and virtual views, and all guidance and navigation functions, all in real-time. This system is considered the nearest thing to reality, where it must verify all control, navigation, and tracking function prior to any flight test.

The Control Systems Group at *Cranfield Aerospace Ltd* implemented and tested the initial longitudinal controller in the GCS simulator. The evaluation was successful[86] and very similar to the ACSL non-linear simulation results.

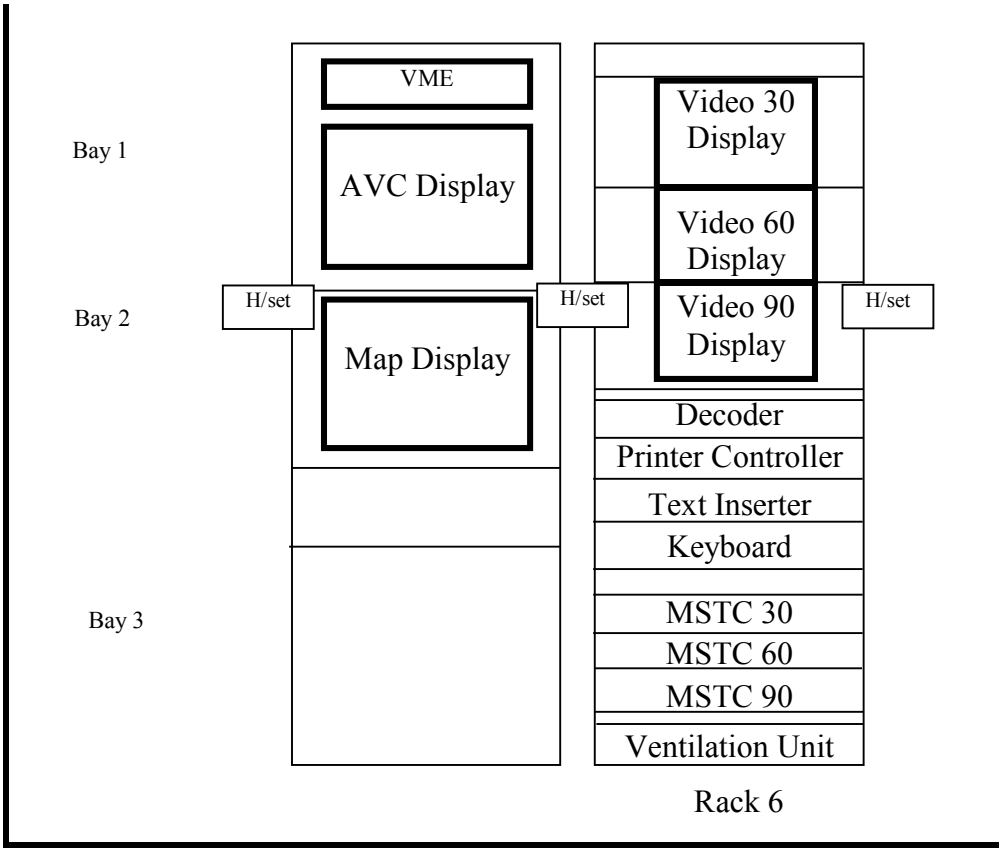

Figure A.2: Basic GCS console layout[8]

A.2 The Control Selector Design

Multivariable control design has the ability to deal with and utilize the different control fins configurations an air vehicle such as the Cranfield A3 Observer has. The control selector design[4, 35, 89] accomplishes two functions. First, it normalizes control effectiveness by transforming generalized rotational rate commands into actuator position commands. Second, it takes the advantages of available control redundancy by allowing for control redistribution without changing the linear closed-loop performance. The basic idea of the control selector is in redefining the control contribution to the state equation

$$B\delta = B^{*}\delta^{*} \qquad \text{A.1}$$

B and δ are the actual control effectiveness matrix and control vector. B^* and δ^* are the generalized control effectiveness matrix and control vector. The actual control can now be defined in terms of the generalized control

$$\delta = T\delta^* \tag{A.2}$$

The transformation T is the control selector defined by

$$T = N(BN)^{\#}B^* \tag{A.3}$$

where $(\ )^{\#}$ is a pseudoinverse and N is a matrix that may be used to combine controls or emphasize a control channel in the case of redundant effectors. Note that the control selector T in Equation A.3 is function of the B matrix, which in turn is a function of the flight condition.

A.3 Observer-form Structure

By deriving the state-space representation of the TDF sub-optimal controller, Walker[90] has shown that the loop-shaping controller also has an observer-form structure which depends on one algebraic Riccati equation[51]. By considering the system model,

$$G_s \overset{S}{=} \left[\begin{array}{c|c} A_s & B_s \\ \hline C_s & 0 \end{array}\right]$$

and the desired reference model

$$T_r \overset{S}{=} \left[\begin{array}{c|c} A_r & B_r \\ \hline C_r & 0 \end{array}\right]$$

Walker showed that a stabilizing controller $K = [K_1\ K_2]$ has the following equations:

$$\begin{aligned}\dot{\hat{x}}_s &= A_s\hat{x}_s + H_s(C_s\hat{x}_s - y_s) + B_s u_s \\ \dot{x}_r &= A_r x_r + B_r y_D \\ u_s &= F_s\hat{x}_s + F_r x_r\end{aligned} \qquad \textbf{A.4}$$

where,

$$\begin{aligned}H_s &= -Z_s C_s^T \\ F_s &= -B_s^T X_{\infty 11} \\ F_r &= -B_s^T X_{\infty 12}\end{aligned} \qquad \textbf{A.5}$$

$X_{\infty 11}$ and $X_{\infty 12}$ are the elements of,

$$X_\infty = \begin{bmatrix} X_{\infty 11} & X_{\infty 12} \\ X_{\infty 21} & X_{\infty 22} \end{bmatrix}$$

which has been partitioned conformably with,

$$A = \begin{bmatrix} A_s & 0 \\ 0 & A_r \end{bmatrix}$$

This structure shown in Figure A.3, shares the important advantages such as gain-scheduling and anti-windup as the one degree-of-freedom controller. The reference model can be fixed for all operating points for gain-scheduled controllers. These features have significant advantages in implementation over standard form controllers.

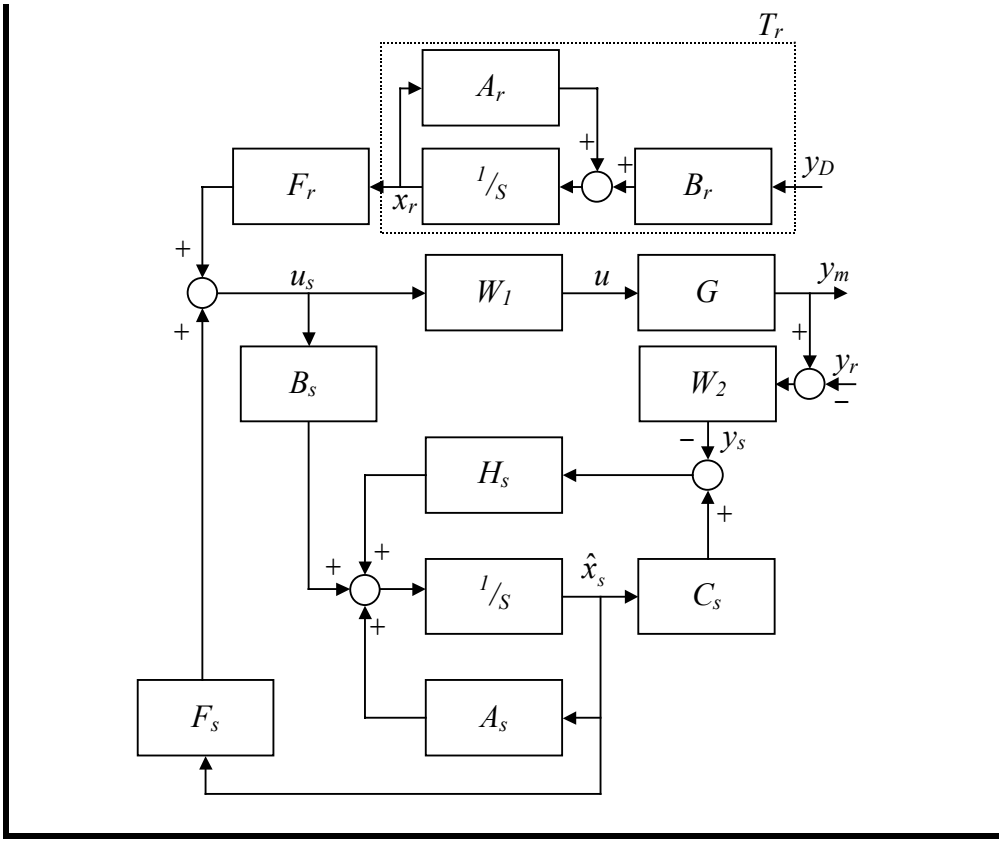

Figure A.3: Observer-form TDF controller

A.3.1 Combined Hanus and TDF Observer-Form Structure

Combining the TDF controller with the Hanus anti-windup structure allows the advantages of both forms to be utilised in one system. As in the one degree-of-freedom self-conditioned observer structure, the input u_a is used to drive both of pre-weight W_{1f} and the observer. This in turn will ensure that the controller states remain consistent with the system model states, while the Hanus form keeps W_{1f} from winding up at saturation. Figure A.4 shows the anti-windup and TDF implementation in the observer-form structure.

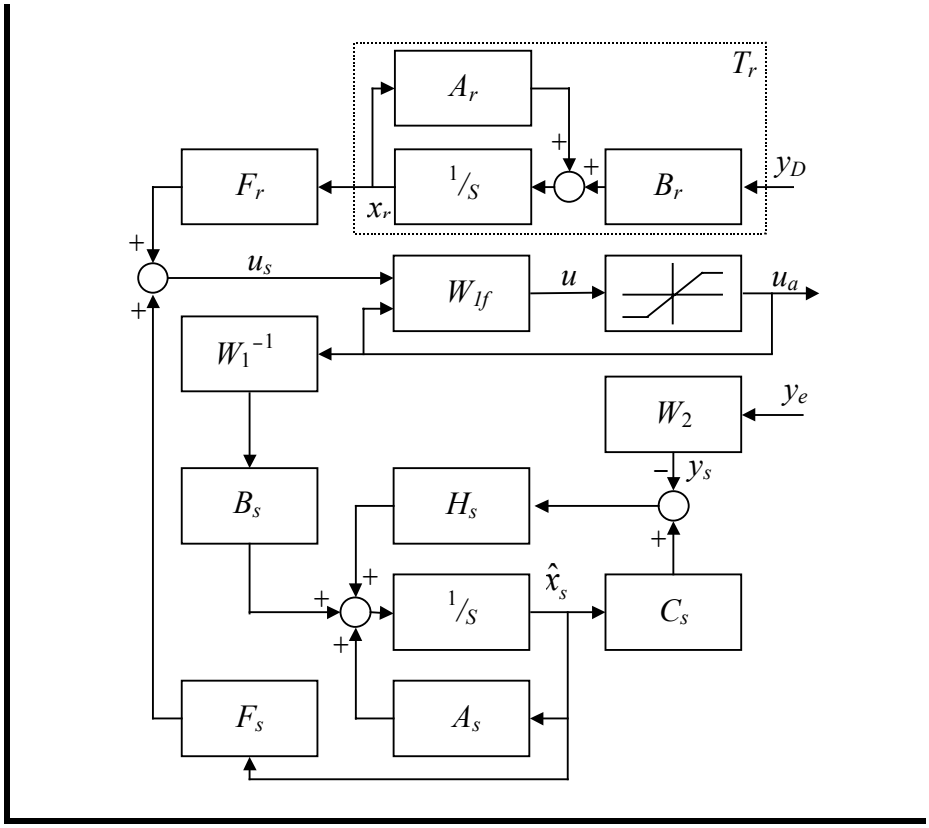

Figure A.4: Anti-windup and TDF implementation in observer-form